

Nanomaterials based on magnetic switchable molecules for hybrid devices



Universitat de València

Instituto de Ciencia Molecular (ICMol)

Memoria presentada por Ramón Torres Cavanillas para aspirar al grado de
Doctor en Nanociencia y Nanotecnología

Dirigida por el Prof. Eugenio Coronado Miralles y la Dra Alicia Forment
Aliaga

Abril 2021

D. EUGENIO CORONADO MIRALLES, catedrático del Departamento de Química Inorgánica de la Universitat de València y director del ICMol Instituto de Ciencia Molecular de la Universitat de València, y DÑA. ALICIA FORMENT ALIAGA, profesora titular por la Universitat de València y actualmente investigadora en el Instituto de Ciencia Molecular de la Universitat de València,

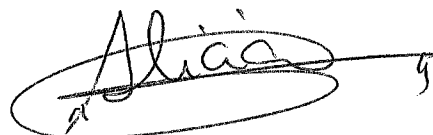
CERTIFICAN:

Que la memoria presentada por D. RAMÓN TORRES CAVANILLAS con título “Nanomaterials based on magnetic switchable molecules for hybrid devices” corresponde a su Tesis Doctoral y ha sido realizada bajo su dirección en el Instituto de Ciencia Molecular, autorizando mediante este escrito la presentación de la misma para optar al grado de Doctor.

En Paterna, a 16 de abril de 2021.



Prof. Eugenio Coronado Miralles



Dra. Alicia Forment Aliaga

List of publications

During the development of this Ph.D. thesis, my work has given rise to the following publications:

“Self-assembled monolayers on a ferromagnetic permalloy surface” M. Mattera, R. Torres-Cavanillas, J. Pablo Prieto-Ruiz, H. Prima-Garcia, S. Tatay, A. Forment-Aliaga, E. Coronado. *Langmuir* **2015**, 31, 19, 5311–5318.

“Near room-temperature memory devices based on hybrid spin-crossover@SiO₂ nanoparticles coupled to single-layer graphene nanoelectrodes”. A. Holovchenko, J. Dugay, M. Gimenez-Marques, R. Torres-Cavanillas, E. Coronado, H.S.J. van der Zant. *Advanced Materials* **2016**, 28, 33, 7228-7233.

“Charge Mobility and Dynamics in Spin-Crossover Nanoparticles Studied by Time-Resolved Microwave Conductivity”. J. Dugay, W. Evers, R. Torres-Cavanillas, M. Giménez-Marqués, E. Coronado, H. S. J. Van der Zant. *Journal of Physical Chemistry Letter* **2018**, 9, 19, 5672–5678.

“Sensing of the Molecular Spin in Spin-Crossover Nanoparticles with Micromechanical Resonators”. J. Dugay, M. Giménez-Marqués, W. J. Venstra, R. Torres-Cavanilla, U. N. Sheombarsing, N. Manca, E. Coronado, H. S. J. van der Zant. *Journal of Physical Chemistry C* **2019**, 123, 11, 6778–6786.

“Halide-Mediated Modification of Magnetism and Electronic Structure of α -Co(II) Hydroxides: Synthesis, Characterization, and DFT+U Simulations”. V. Oestreicher, D. Hunt, R. Torres-Cavanillas, G. Abellán, D. A. Scherlis, M. Jobbágy. *Inorganic Chemistry* **2019**, 58, 14, 9414–9424.

“Downsizing of robust Fe-triazole@SiO₂ spin-crossover nanoparticles with ultrathin shells”. R. Torres-Cavanillas, L. Lima-Moya, F. D. Tichelaar, H.W. Zandbergen, M. Giménez-Marqués, E. Coronado. *Dalton Transactions* **2019**, 48, 15465-15469. (Chapter 4)

“Design of Bistable Gold@Spin-Crossover Core-Shell Nanoparticles Showing Large Electrical Responses for the Spin Switching”. R. Torres-Cavanillas, R. Sanchis-Gual, J. Dugay, M. Coronado-Puchau, M. Giménez-Marqués, E. Coronado. *Advanced Materials* **2019**, 31, 27, 1900039. (Chapter 5)

“Reinforced Room-Temperature Spin Filtering in Chiral Paramagnetic Metallopeptides”. R. Torres-Cavanillas, G. Escorcia-Ariza, I. Brotons, R. Sanchis-Gual, P. Chandra Mondal, L. E. Rosaleny, S. Giménez-Santamarina, M. Sessolo, M. Galbiati, S. Tatay, A. Gaita-Ariño, A. Forment-Aliaga, S. Cardona-Serra. *Journal of American Chemical Society* **2020**, 142, 41, 17572–17580. (Chapter 2)

“The design of magneto-plasmonic nanostructures formed by magnetic Prussian Blue-type nanocrystals decorated with Au nanoparticles”. R. Sanchis-Gual, I. Susic, R. Torres-Cavanillas, D. Arenas-Esteban, S. Bals, T. Mallah, E. Coronado. *Chemical Communications* **2021**, 57(15), 1903-1906..

“Smart molecular/MoS₂ Heterostructures Featuring Light and Thermally-Induced Strain Driven by Spin Switching”. R. Torres-Cavanillas, M. Morant-Giner, G. Escorcia-Ariza, J. Dugay, J. Canet-Ferrer, S. Tatay, S. Cardona-Serra, M. Giménez-Márquez, M. Galbiati, A. Forment-Aliaga, E. Coronado. *ChemRxiv. Preprint*, **2020**. chemrxiv.12664799.v1 (Chapter 7)

“Fast Polymeric Functionalization Approach for the Covalent Coating of MoS₂ Layers”. I. Gómez-Muñoz, S. Laghouati, R. Torres-Cavanillas, M. Morant-Giner, A. Forment-Aliaga, M. Giménez Marqués. *ChemRxiv. Preprint, 2021. chemrxiv.14124137.v1*

“Plasmon assisted spin transition in gold nanostars@Spin Crossover heterostructures”. R. Torres-Cavanillas, R. Sanchis-Gual, M. Coronado-Puchau, M. Giménez-Marqués, E. Coronado. *Submitted 2021. (Chapter 5)*

*One of the great challenges in life is knowing enough to think
you're right but not enough to know you're wrong*

Neil Degrasse Tyson

A mi familia y todos los que confiaron en mi

List of abbreviations

| | |
|---------------------------|--|
| 1L | Single layer |
| 1T-MoS₂ | Tetragonal Molybdenum disulfide polytype |
| 2D | Two-dimensional materials |
| 2H-MoS₂ | Hexagonal Molybdenum disulfide polytype |
| γ_{HS} | High-Spin fraction |
| $\zeta\text{-pot}$ | Zeta-potential analysis |
| λ | photoelectrons inelastic mean free path |
| μ | shear modulus of the quartz crystal |
| ρ | Density |
| χ_{M} | Molar magnetic susceptibility |
| a | electrode active area |
| A | Asymmetric parameter |
| AFM | Atomic Force Microscopy |
| Ala-X | SH-(CH ₂) ₂ NH-(Ala-Aib) _x |
| AOT | Dioctyl sulfosuccinate sodium salt |
| Au NSs | Gold Nanostars |
| Au/TbLBT | Self-assembled monolayer of LBT terbium complex on gold |
| Au/Tb | Gold substrate incubated in a terbium solution |

| | |
|---------------------------|--|
| Au/YLBT | Self-assembled monolayer of LBT Yttrium complex on gold |
| Au@SCO | Gold nanospheres@Fe(Htrz) ₂ (trz)(BF ₄) |
| BE | binding energy |
| CE | Counter electrode |
| ce-MoS₂ | Chemically exfoliated Molybdenum disulfide |
| CISS | Chiral-induced spin selectivity |
| CP-AFM | Conductive-probe atomic force microscope |
| <i>d</i> | Self-assembled monolayer thickness |
| D | Dextrogire |
| DI | Deionized water |
| DFT | Density-functional theory |
| DLS | Dynamic light scattering |
| DSC | Differential scanning calorimetry |
| EC | Electro dichroism |
| EDS | Energy dispersive X-ray spectroscopy |
| EGaIn | Gallium indium eutectic alloy |
| EIS | electrochemical impedance spectroscopy |
| EtOH | Ethanol |
| <i>f</i> | uartz crystal resonant frequency |

| | |
|----------------------|--|
| HEPES | 4-(2-hydroxyethyl)-1 piperazineethanesulfonic acid |
| HS | High-Spin |
| Htrz | Triazole |
| I | Photo emitted electrons intensity |
| I₊ | electron counts with the spin parallel with the movement |
| I₋ | electron counts with the spin antiparallel with the movement |
| ICP-OES | Inductively coupled plasma optical emission spectrometry |
| IPTS | (3-iodopropyl)trimethoxysilane |
| I-V | Current vs voltage |
| J | Electronic current density |
| L | Laevogire |
| LBT | Lanthanide Binding Tag |
| LS | Low-Spin |
| LSPR | Localized surface plasmon resonance |
| MALDI-TOF | Matrix-assisted laser desorption/ionization-time of flight |
| n-BuLi | n-butyl lithium |
| NIR | Near infrared radiation |
| NSs | Gold Nanostars |
| NSs@SCO | Gold Nanostars@Fe(Htrz) ₂ (trz)(BF ₄) |

| | |
|--|--|
| NPs | Nanoparticles |
| PCT | Platinum electrode |
| PL | Photoluminescence |
| PTS-MoS₂ | Propyltrimethoxysilane functionalized MoS ₂ |
| PVP | Poly(vinylpyrrolidone) |
| PXRD | Powder X-ray diffraction |
| QMC | Coverage evaluation using quartz crystal microbalance |
| RE | Reference electrode |
| RMS | Root Mean Square Roughness |
| SAM | Self-assembled monolayers |
| SCE | Saturated calomel electrode |
| SCO | Spin-crossover |
| SCO@SiO₂ | Fe(Htrz) ₂ (trz)(BF ₄)@SiO ₂ |
| SCO/MoS₂ | MoS ₂ decorated with spin crossover nanoparticles |
| SCO/MoS₂ | MoS ₂ decorated with spin crossover nanoparticles |
| SEM | Scanning electron microscopy |
| SiO₂ | Silica |
| Si/SiO₂ | Silicon/Silica substrates |
| SiO₂/MoS₂ | MoS ₂ decorated with silica nanoparticles |

| | |
|-------------------------------------|--|
| SP | Spin Polarization |
| STEM | Scanning transmission microscopy |
| T | Temperature |
| T_{1/2}^{HS} | High spin transition temperature |
| T_{1/2}^{LS} | Low spin transition temperature |
| TbLBT | Complex of Terbium and Lanthanide Binding Tag |
| TCEP | tris(2-carboxyethyl) phosphine |
| TEM | Transmission electron microscopy |
| TEOS | tetraethyl orthosilicate |
| TGA | Thermogravimetric analysis |
| TMDC | Transition metal dichalcogenides |
| UV-VIS | Ultraviolet–visible spectroscopy |
| WE | Working electrode |
| XAS | X-ray absorption spectroscopy |
| XPS | X-ray photoelectron spectroscopy |
| Z | Atomic number |
| Z_I | Resistance measured by electrochemical impedance |
| Z_I' | Real part of impedance |
| Z_I'' | Imaginary part of impedance |

Summary and organization

In the last 50 years unprecedented technological advances have been experienced in our world. One of the main reasons is the progressive miniaturization of components for practical electrical devices, which has improved efficiencies while minimizing costs. In this sense, the bulk nature of the components of conventional devices is leading us into a plateau in this downsizing race. A possible solution to overcome this problem relies on developing devices based on molecular components. Due to their molecular nature, these components can be integrated in nanodevices. Even more, thanks to their chemical versatility, it is possible to form hybrid structures, combining different molecular compounds to obtain multifunctional nanostructures. In this thesis we look forward to the development of new hybrid and multifunctional nanostructures that in the future could act as molecular components for practical devices. In this context, we explore the synthesis of hybrid materials based on molecular monolayers ,part I, nanoparticles (NPs), part II, or 2D compounds ,part III. The thesis is divided into three parts, which face three different topics in the field of nanomaterials: (I) The use of chiral self-assembled molecular monolayers as active components for spintronics; (II) The synthesis of core@shell nanoparticles based on the spin-crossover (SCO) compound $[\text{Fe}(\text{Htrz})_2(\text{trz})](\text{BF}_4)$, (Htrz =1,2,4-triazole, trz = 1,2,4-triazolate); (III) The Modulation of ultrathin MoS_2 electrical and optical properties via molecular strain engineering.

Beginning with part I, we explore the potential of metallic complexes of lanthanide binding tag polypeptides as spin filters in order to generate spin-polarized currents. These chiral biomolecules are chemically designed to

coordinate metallic atoms, specially lanthanoids, introducing other functionalities into the molecular biosystems and boosting the peptide's spin filtering effect. Thus, we produced highly oriented monolayers of a member of this family, coordinating paramagnetic terbium or diamagnetic yttrium, to study the spin selectivity as a function of the coordinated atom. Part I is organized as follows: in chapter 1, the state of the art of the spin-dependent electronic scattering of chiral molecules and a summary of the main techniques employed to explore it are presented. After this general introduction, the results obtained in this thesis are discussed in chapter 2, which includes: (i) A detailed description of the preparation and characterization of chiral self-assembled monolayers (SAMs) based on Tb^{3+} and Y^{3+} bio complexes on gold and on a ferromagnetic substrate. (ii) The study of the spin filtering properties of both films by spin-dependent electrochemistry in solution and electrical transport in solid-state.

In Part II the synthesis of two core@shell SCO systems is presented. On the one hand, we study the downsizing of the core@shell system $[Fe(Htrz)_2(trz)](BF_4)@SiO_2$, where the SCO core is wrapped with a thin silica shell, which increases the stability of the core against oxidation. On the other hand, to face the high insulating nature of this coordination polymer, a second core@shell nanostructure based on a metallic gold core, and the $[Fe(Htrz)_2(trz)](BF_4)$ compound as the shell is synthesized. This topic is organized as follows: firstly, the SCO concept and the technique employed to synthesize SCO NPs are introduced in chapter 3. Later, the results of this thesis are presented in chapters 4 and 5, where the two hybrids mentioned above are described. In chapter 4 we focus on the synthesis of

the $[\text{Fe}(\text{Htrz})_2(\text{trz})](\text{BF}_4)@\text{SiO}_2$ and the tuning of their size by playing with some synthetic parameters. Then, in chapter 5, the synthesis of $\text{gold}@[\text{Fe}(\text{Htrz})_2(\text{trz})](\text{BF}_4)$ SCO NPs using gold nanospheres as core and $[\text{Fe}(\text{Htrz})_2(\text{trz})](\text{BF}_4)$ as shell is presented, followed by a study of the current vs voltage (IV) of the hybrid as a function of the temperature. Finally, this synthetic protocol is expanded to other gold nanostars as the core, and the number of iron centers susceptible to switch their spin state is maximized.

In part III, a manner to reversible modulate the bandgap of layers of the 2D semiconductor MoS_2 via strain engineering is presented. In this work, the mechanical stress will be induced by the same SCO NPs synthesized in chapter 4 and attached to the 2D system. The hybrid structure takes advantage of the mechanical deformation provoked by the NPs when they change their spin state to alter the physical properties of the 2D material reversibly. Part III is organized as follows: in chapter 6, a brief introduction of the transition metal dichalcogenides family (TMDCs) and the effect of dimensionality in their physical properties is presented. From this family, MoS_2 properties depending on the number of layers, the polymorph, the exfoliation protocols, and the strain engineering are discussed in detail. Next, the results obtained in this thesis are discussed in Chapters 7, presenting the synthesis of MoS_2 layers covalently functionalized with SCO NPs. Then we study the effect of the reversible strain applied by SCO NPs as a function of their spin state. At the same time that the strain is tuned by playing with the degree of coverage and the size of the NPs.

Part I

| | |
|---|----|
| 1. Introduction to chirality induce spin selectivity | 1 |
| 1.1. Chirality | 2 |
| 1.2. Spin selectivity of chiral molecules in gas phase | 4 |
| 1.3. Chiral self-assembled monolayers as spin-filters | 6 |
| 1.4. Spin selectivity characterization | 8 |
| 1.4.1. Optical induction | 9 |
| 1.4.2. Electronic induction | 10 |
| 1.5. Bibliography | 15 |
| 2. Reinforced Spin Filtering in chiral Metallopeptides | 21 |
| 2.1. Motivation | 22 |
| 2.2. Introduction | 22 |
| 2.2.1. Lanthanide Binding Tags ³ | 22 |
| 2.2.2. Spin dependency with the coordinated atom | 24 |
| 2.3. Results and discussion | 24 |
| 2.3.1. TbLBT solution | 25 |
| 2.3.2. TbLBT self-assembled monolayer on gold | 26 |
| 2.3.3. Role of the coordinated metal in the Spin-filtering | 34 |
| 2.4. Conclusions and perspectives | 45 |

Table of contents

| | |
|---|-----------|
| 2.5. Bibliography | 48 |
| 2.6. Experimental section | 51 |
| 2.6.1. Equipment | 51 |
| 2.6.2. Methods | 53 |
| Part II | |
| 3. Introduction to Spin Crossover | 55 |
| 3.1. Spin Crossover | 56 |
| 3.2. Types of Spin Crossover | 57 |
| 3.3. Spin Crossover detection | 58 |
| 3.3.1. Magnetic Susceptibility | 58 |
| 3.3.2. Vibrational Spectroscopy | 60 |
| 3.3.3. Heat Capacity | 60 |
| 3.3.4. Optical properties | 61 |
| 3.3.5. Electrical response | 62 |
| 3.3.6. X-ray Structural Studies | 63 |
| 3.4. Bibliography | 65 |
| 4. Downsizing [Fe(Htrz)₂(trz)](BF₄) Core@Shell Nanoparticles | 69 |
| 4.1. Motivation | 70 |
| 4.2. Introduction | 71 |

| | |
|--|-----------|
| 4.2.1. [Fe(Htrz) ₂ (trz)](BF ₄) | 72 |
| 4.2.2. [Fe(Htrz) ₂ (trz)](BF ₄) nanoparticles | 74 |
| 4.2.3. Reverse micelle technique | 74 |
| 4.2.4. [Fe(Htrz) ₂ (trz)](BF ₄)@SiO ₂ | 78 |
| 4.3. Results and discussion | 80 |
| 4.3.1. Tuning the [Fe(Htrz) ₂ (trz)](BF ₄)@SiO ₂ NPs size | 81 |
| 4.3.2. Stability and structure of the [Fe(Htrz) ₂ (trz)](BF ₄)@SiO ₂ | 84 |
| 4.3.3. Thickness of the silica shell in [Fe(Htrz) ₂ (trz)](BF ₄)@SiO ₂ | 85 |
| 4.3.4. [Fe(Htrz) ₂ (trz)](BF ₄)@SiO ₂ size magnetic dependency | 87 |
| 4.4. Conclusions and perspectives | 88 |
| 4.5. Bibliography | 89 |
| 5. Design of bistable gold@spin crossover nanoparticles | 94 |
| 5.1. Motivation | 95 |
| 5.2. Introduction | 95 |
| 5.2.1. Spin Crossover electrical devices | 95 |
| 5.2.2. [Fe(Htrz) ₂ (trz)](BF ₄)@SiO ₂ based devices | 97 |
| 5.2.3. Hybrids with conductive materials | 98 |
| 5.3. Results and discussion | 102 |
| 5.3.1. Core@shell based on gold nanospheres | 103 |

Table of contents

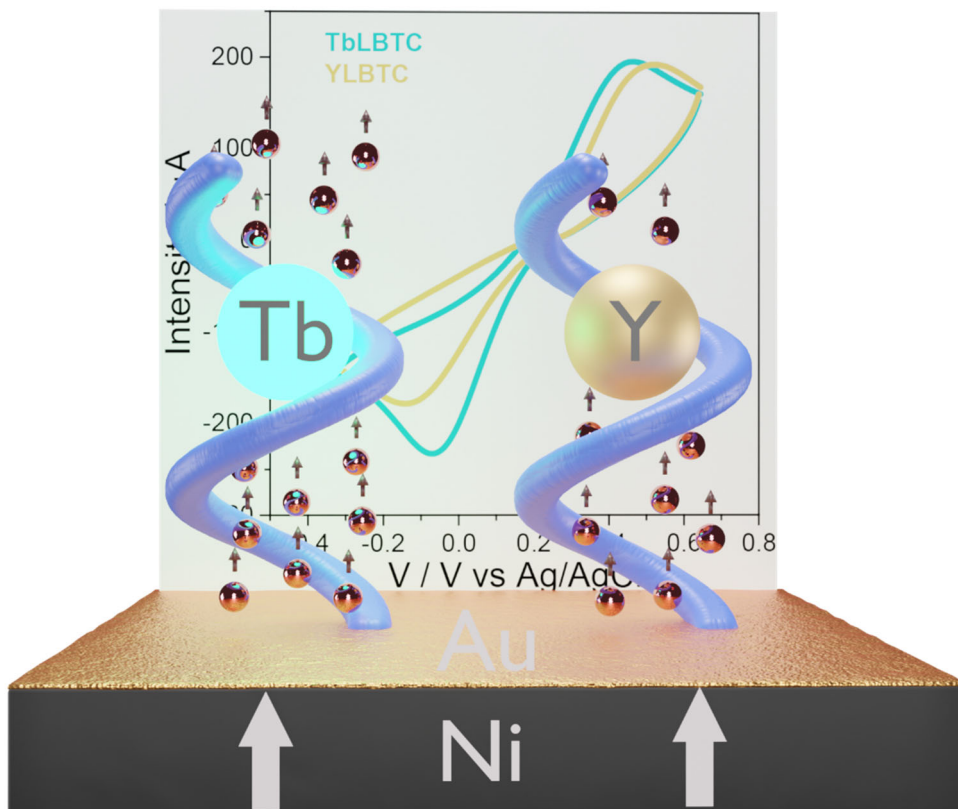
| | |
|--|-----|
| 5.3.2. Optimization of the Fe ²⁺ in the shell | 117 |
| 5.3.2. Core@shell based on gold nanostars | 118 |
| 5.4. Conclusions and perspectives | 124 |
| 5.5. Bibliography | 125 |
| 5.6. Experimental section | 131 |
| 5.6.1. Equipment | 131 |
| 5.6.2. Methods | 132 |
| Part III | |
| 6. Introduction to MoS₂ strain engineering | 136 |
| 6.1. 2D materials | 137 |
| 6.2. Transition metal dichalcogenides | 138 |
| 6.2.1. Crystalline phase | 139 |
| 6.3. Molybdenum disulfide | 141 |
| 6.3.1. Exfoliated 2H-MoS ₂ | 141 |
| 6.3.2. Exfoliated 1T-MoS ₂ | 142 |
| 6.4. From bulk to single layer | 143 |
| 6.4.1. Ion intercalation-Assisted Liquid Exfoliation | 144 |
| 6.5. Functionalization of chemically exfoliated MoS ₂ | 145 |
| 6.5.1. Non-covalent functionalization | 146 |

| | |
|---|------------|
| 6.5.2. Covalent functionalization | 147 |
| 6.6. Phase engineering | 149 |
| 6.6.1. Strain engineering | 150 |
| 6.6.2. S vacancies induction | 152 |
| 6.6.3. Chemical/electrochemical intercalation | 152 |
| 6.6.4. Electron injection | 153 |
| 6.6.5. Chemical induced phase transition | 154 |
| 6.7. Bibliography | 154 |
| 7. Spin Crossover assisted MoS₂ strain engineering | 169 |
| 7.1. Motivation | 170 |
| 7.2. Introduction | 170 |
| 7.3. Results and discussion | 172 |
| 7.3.1. MoS ₂ Chemical exfoliation | 173 |
| 7.3.2. Silane functionalized MoS ₂ | 174 |
| 7.3.3. Anchoring Fe(Htrz) ₂ (trz)@SiO ₂ to the MoS ₂ | 177 |
| 7.3.4. MoS ₂ Phase | 180 |
| 7.3.5. SCO/MoS ₂ spin transition | 190 |
| 7.3.6. MoS ₂ electrical dependency of the nanoparticles spin state | 192 |
| 7.3.7. Piezoresistivity | 199 |

Table of contents

| | |
|---------------------------------------|------------|
| 7.3.8. Spin dependant optical bandgap | 200 |
| 7.4. Conclusions and perspectives | 207 |
| 7.5. Bibliography | 208 |
| 7.6. Experimental section | 217 |
| 7.6.1. Equipment | 217 |
| 7.6.2. Methods | 219 |
| 8. General Conclusions | 223 |
| Resumen en castellano | 226 |

PART I



1

**INTRODUCTION TO
CHIRALITY INDUCED SPIN
SELECTIVITY**

1.1. Chirality

The term chirality derives from the Greek 'cheir' for hand. Many organic molecules are chiral, which means that they present neither a symmetry plane nor an inversion center. A chiral molecule cannot be superposed on its mirror image by any combination of rotation and translation, Figure 1.

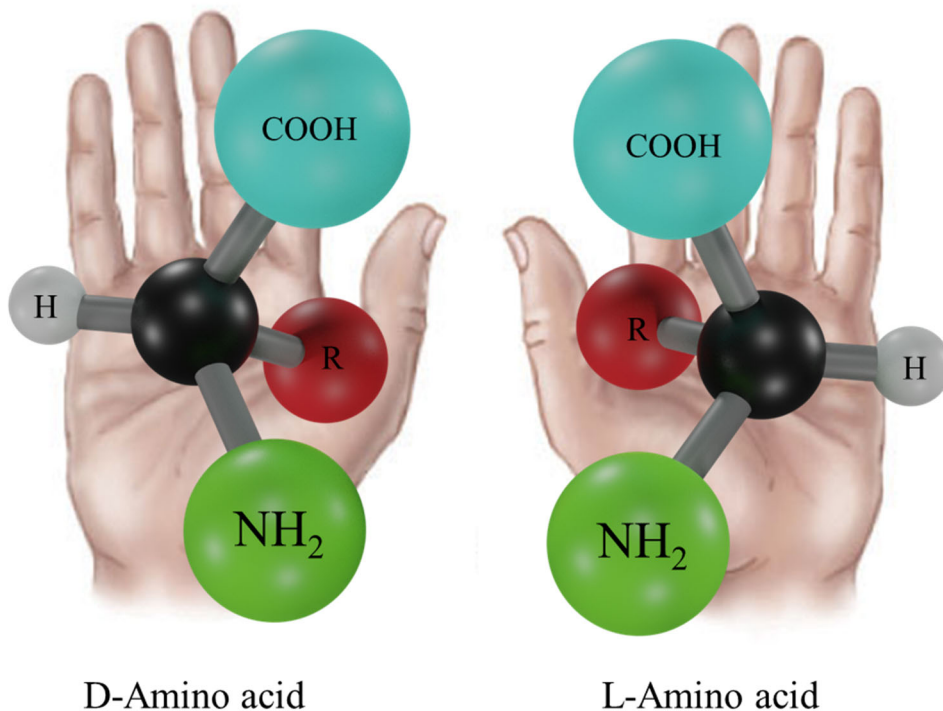


Figure 1. Representation of two generic chiral amino acids

Since the discovery of chiral molecules in 1848, their exciting interaction with light has been widely investigated by the scientific community.¹ In particular, a rotation of the polarization plane of an incoming beam of polarized light has been discovered, Figure 2. This effect has been used to classify the chiral molecules as laevo (from left, L) and dextro (from right,

D), depending on the clockwise or counterclockwise light polarization induced by the molecule.

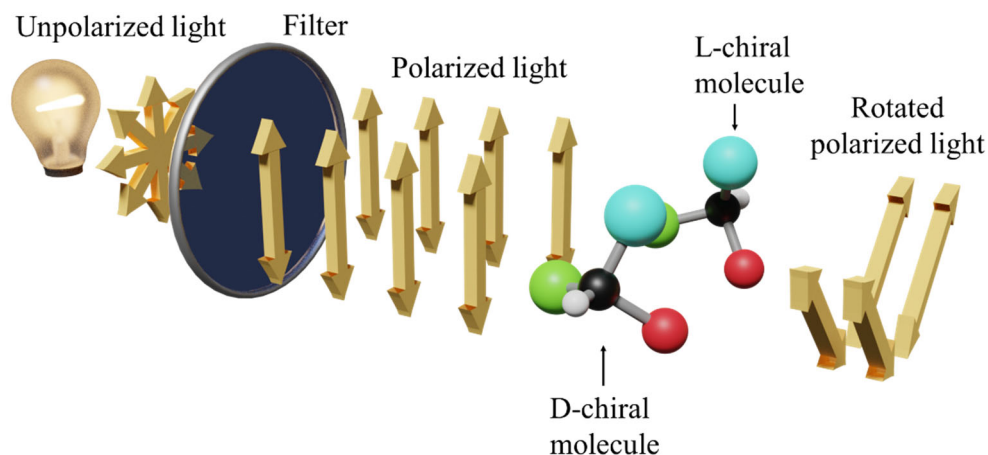


Figure 2. Scheme of the polarized light rotation induced by chiral molecules.

In the past few years, the chiral-light interaction has been expanded to electronic currents. Note that moving spins may be also seen as chiral due to their mirror-reflection asymmetry depending on the relative momentum and spin orientations, Figure 3.^{2,3} This allows chiral objects to couple to the moving spins. Consequently, spins with a specific handedness can travel through chiral molecules with the same handedness longer distances than for the opposite, leading to spin-polarized currents.⁴

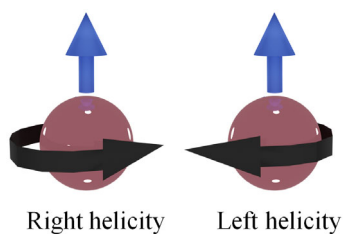


Figure 3. Schematics of the chiral nature of moving spins. The electrons are the burgundy spheres, the blue arrow represents the direction of the moving electrons, and the black curved arrows their spins.

Several authors have probed the influence of chirality in the electronic scattering of spin-polarized currents. This electro dichroism (EC) permits chiral molecules to act as spin-filters.

1.2. Spin selectivity of chiral molecules in gas phase

The EC provoked by chiral systems is a complex phenomenon that has been probed for different chiral molecules. To the best of our knowledge, one of the first experiments of spin-polarized electronic scattering was carried out by Farago et al. in the 1980s.⁵⁻⁷ They measured the transmitted spin-polarized electrons through a cell with D and L camphor molecules in gas phase. Later, the difference between each electronic polarization was quantified by the asymmetry parameter A through eq. 1, where I_+ is the counts of transmitted electrons with spin parallel to the electron velocity and I_- the antiparallel one.

$$A = \frac{I_+ - I_-}{I_+ + I_-} \quad \text{eq.1}$$

The results obtained in this work were close to the detection limit of the detector, and even if the authors claimed to obtain A values between 10^{-3} - 10^{-5} , these results could not be reproduced by other groups.⁸

In this context, some theoretical works suggested that the addition of heavy atoms with high atomic numbers (Z) in the chiral structure amplifies the spin selectivity.^{9,10} To experimentally prove it, the spin selectivity of bare camphor and camphor coordinated with ytterbium was investigated by the same technique. While the chiral camphor showed A values close to the detection limit of the detectors, the Yb-camphor exhibited a low but measurable spin selectivity of 1 electron each 10000 at best, Figure 4.⁸

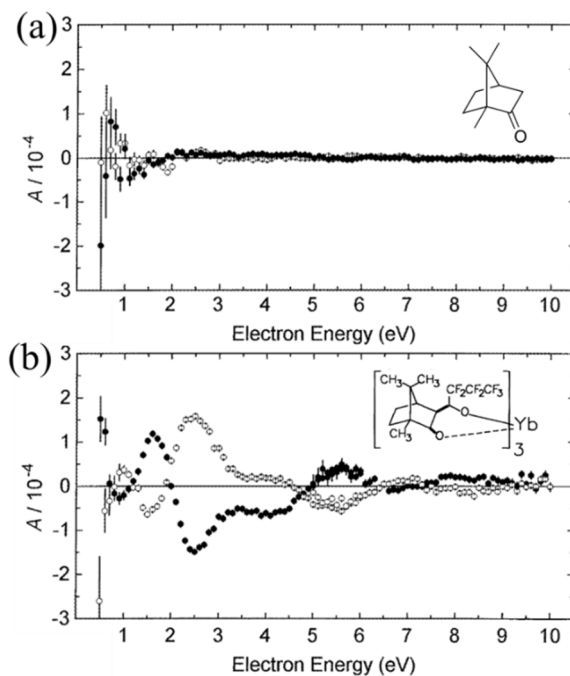


Figure 4. (a) Transmission asymmetry A measured for D (filled circles) and L (empty circles)-camphor vs electron energy. (b) The same measurement but for D -Yb-camphor, (filled circles) and L -Yb-camphor (open circles). The structure of both compounds is indicated in the inset. Adapted from Ref 11.

This concept was later expanded, coordinating camphor with other lanthanoids: Praseodymium, Europium, or Erbium. The EC response, accounted by the A factor, was observed to vary with the atomic number of the metal.¹² In more recent studies of EC in gas phase, Br-camphor and I-camphor, exhibited a dependent spin selectivity with Z , being roughly larger for the heavier compound (I-camphor).¹³

As the nature of the phenomenon is not well understood, the underlying causes of the A dependence with Z remain unclear. Nevertheless, it has been speculated that it is related to the spin-orbit coupling scale with Z , enhancing the interaction between the chiral molecule and the incoming electron and

improving the spin selectivity.¹⁰ However, this is not an isolated factor, and structural effects due to the inclusion of heavy atoms can also play a major role.¹⁴

Although the EC has been observed and amplified for chiral molecules with heavy atoms, the values are still far from their use in practical devices. This is probably caused by the free rotation in gas phase of the molecules.

1.3. Chiral self-assembled monolayers as spin-filters

As has been commented, one of the main handicaps of spin filtering in gas phase is the random orientation of their molecules. In this context, a preferential orientation of the chiral molecules concerning the incoming electrons should maximize their spin selectivity, Figure 5.¹⁵⁻¹⁷

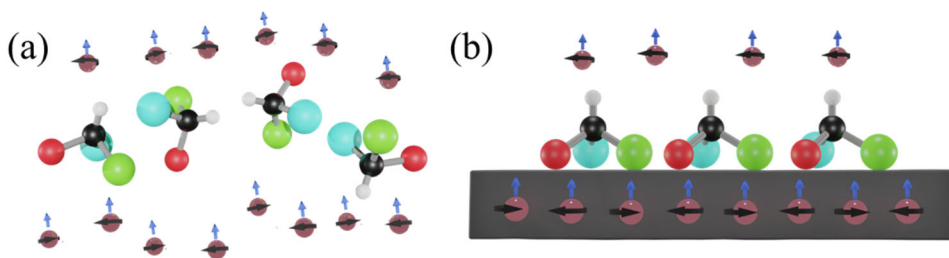


Figure 5. Representation of the spin filtering induced by chiral molecules in gas phase and by oriented chiral molecules on a substrate, a and b, respectively.

In this line, in 1999, Ray et al. produced highly oriented L- or D-stearoyl lysine films on a gold substrate. Firstly, films of 2, 3, and 5 layers were prepared through Langmuir Blodgett deposition.¹⁸ Remarkably, the A factor in this experiment was a thousand times higher than the one exhibited by chiral compounds in gas phase for a 5 layers peptidic film.¹⁸ This work proved that oriented chiral molecules could boost the spin selectivity while showing the high potential of biomolecules as spin-filters.

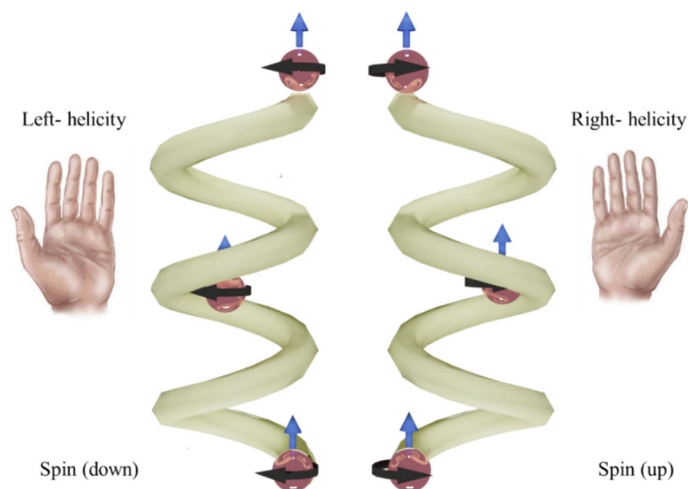


Figure 6. Schematics of the chiral dependence spin selectivity. Electrons of a specific spin orientation move preferentially through one of the helices. Left-handed helix exhibits less resistance to the movement of spin-down electrons. This behaviour is reversed in the right-handed.

In this sense, more experiments of films based on biomolecules like DNA or bacteriophages, among others, have been carried out, exhibiting similar results.¹⁹ For some of these molecules, the chirality arises from their helicoidal structure. Recent works suggested that helical geometry can induce a coupling between the spin orientation of the electrons and their flow direction.²⁰ Electrons moving in one direction have one preferred spin alignment, and those moving in the opposite direction have the opposite desired spin alignment.^{20,21}

Therefore, in oriented helicoidal biomolecules, the electrons of a certain spin are preferentially scattered in one direction. Thus, choosing the handedness is possible to select the outgoing spin current, Figure 6.²² Due to all the advantages and possibilities of using oriented biomolecules as spin-filters, this phenomenon has been coined as Chiral Induced Spin Selectivity (CISS).²¹

Noticeably, the chemical versatility of these helicoidal biocompounds permit their synthesis with different lengths and helicities. In this sense, the spin polarization of double-stranded DNA molecules with helixes ranging from 20 to 80 base pairs on Au(111) was explored by Göhler et al.²³ Interestingly, the resulting spin polarization ranged from 0 to ~50% depending on the length of the chiral DNA, being maximum for the longest strand. These observations suggest that spin filtering can be maximized by increasing the molecule length and helicity.

1.4. Spin selectivity characterization

Two main approaches can be used to examine the spin polarization of chiral self-assembled monolayers (SAMs) depending on how the electrons flow is generated. Thus, the electrons can be produced by the photoelectric effect or by applying a voltage to the substrate where the chiral molecules have been attached. We named these two approaches optical induction (Figure 7a) and electrical induction (Figure 7b), respectively.

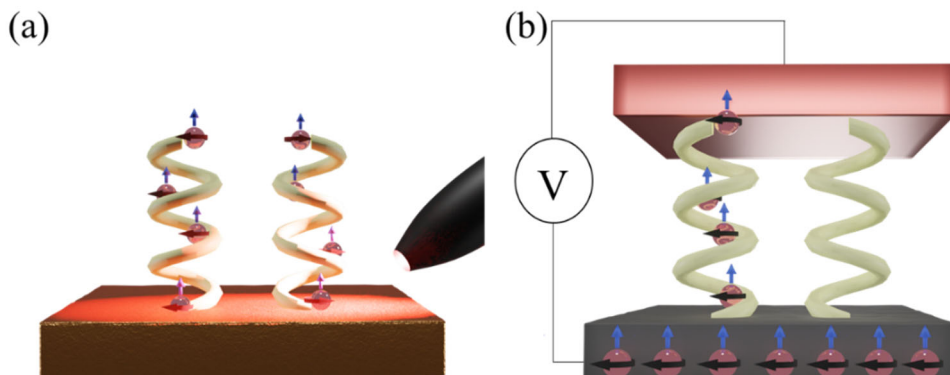


Figure 7. Scheme of the optical (a) and electrical induction (b) of polarized electrons flow.

1.4.1. Optical induction

As has been previously commented, the first work related to the study of chiral biomolecular thin films was developed by growing L- or D-stearoyl lysine films (2, 3- and 5-Layers) on gold.¹⁸ It is known that there is a spin polarization of photoemitted electrons by some metals, like gold, upon the irradiation with circularly polarized light.^{6,24} Thus, when an additional chiral film is formed on top of the gold, it is possible to infer its spin-dependent electronic scattering by switching the polarization of the light and monitoring the intensity of ejected photoelectrons. It must be noticed that the spin selectivity depends on the peptide's helicity; thus, when the spin-polarization of the ejected photoelectrons matches with the chirality of the film, the intensity is maximized, Figure 8. This methodology has been widely used for DNA, proteins, or oligomers.^{17,25,26} Nevertheless, this is an indirect probe of the spin selectivity, where its value is inferred from the number of photoemitted electrons that reach the detector.

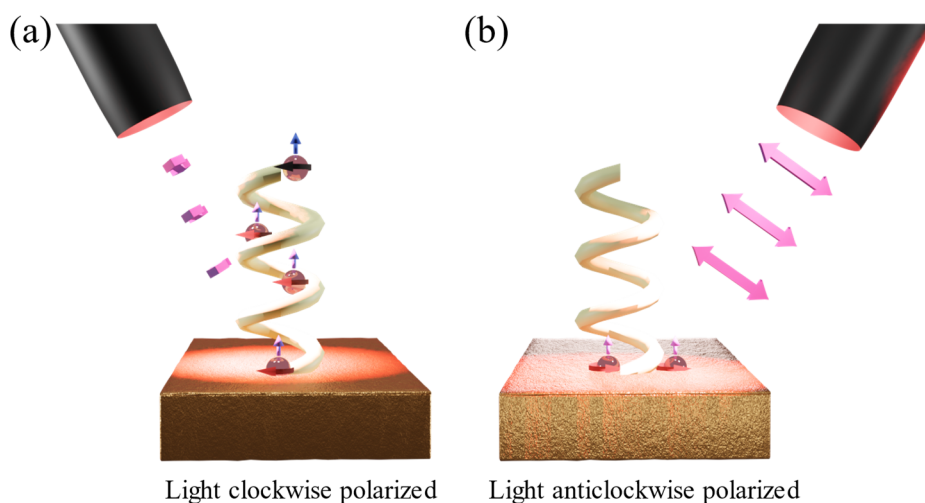


Figure 8. Irradiation of a left-handed SAMs anchored on gold with polarized light, clockwise (a) and anticlockwise (b).

A more direct method consists of using a Mott polarimeter to determine the spin orientation of photoemitted electrons with unpolarized light. In this context, the spin filtering of different proteins, oligomers, and helicenes organized on different metallic surfaces, like Au, Ag, or Cu, has been demonstrated.^{23,27–30}

1.4.2. Electrical induction

An alternative manner to investigate the spin selectivity of chiral SAMs is the study of their electrical properties. However, such measurements can be complicated due to the instability and high insulating nature of organic SAMs. For these reasons, the typical techniques used to electrically investigate the CISS effect consist of strategies that minimize the damage suffered by the film during the characterization. Those methodologies include modified magnetoresistance studies, the use of a conductive-probe atomic force microscope (CP-AFM), or spin-dependent electrochemistry.

1.4.2.a. Magnetoresistance

The most common magnetoresistance measurements are based on nonmagnetic films between two ferromagnetic electrodes. In such devices, the electrical current is recorded as a function of an external magnet orientation. In a recent experiment, Ravi et al. deposited a monolayer of DNA between two ferromagnetic electrodes in a sandwich-like configuration.³¹ In this work, a spin-filtering of ~30% was calculated from the magnetotransport measurements.

1.4.2.b. CP-AFM

CP-AFM has been widely used to investigate the electrical properties of SAMs or thin films locally.^{32,33}

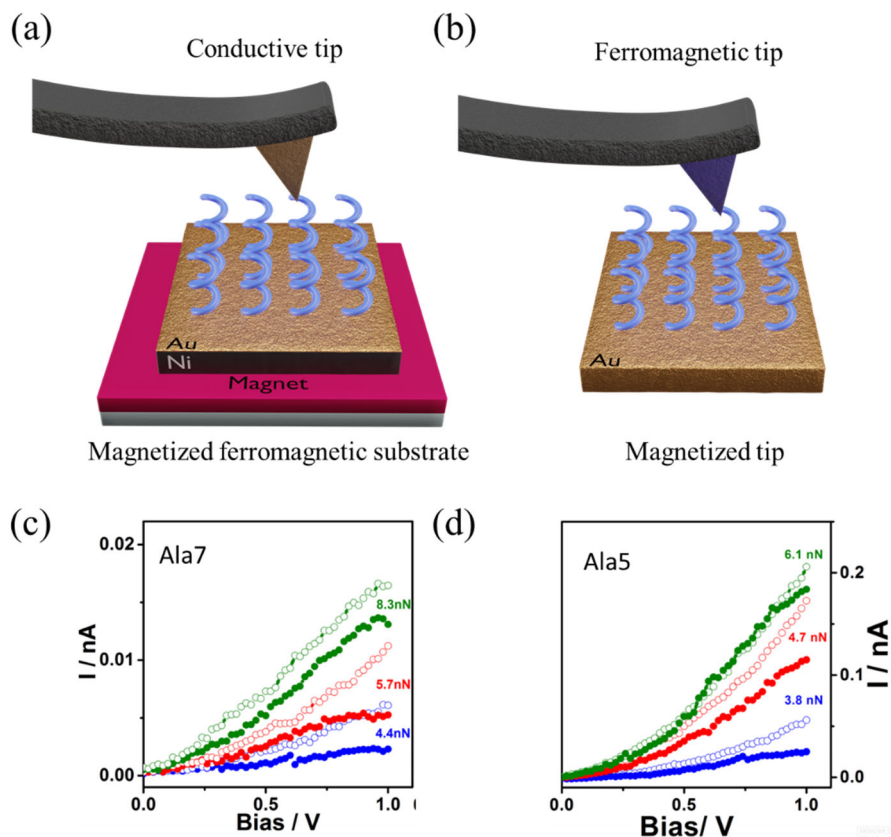


Figure 9. Schematic representation of the CP-AFM measuring a chiral SAM, injecting the polarized electrons from a magnetized substrate (a) or tip (b). (c-d) I - V data obtained for Ala7 (c) and Ala5 (d) recorded under various tip loading forces. b and c Extracted from 34.

This useful technique can be easily adapted to study the CISS effect of chiral SAMs, by using magnetized ferromagnetic substrates and measuring the polarized currents with a conductive tip, Figure 9a, or by using a ferromagnetic tip and non-magnetic substrates, Figure 9b.³⁴⁻³⁶

For instance, the oligopeptides $\text{SH}-(\text{CH}_2)_2\text{NH}-(\text{Ala-Aib})_x$ with x equal to 5 and 7 (Ala=alanine, and Aib=2 aminoisobutyric acid), abbreviated Alax, have been electrically characterized by CP-AFM, as a function of the tip magnetization and the load force, Figure 9c-d. As was expected, a more significant spin polarization was exhibited by the larger peptide.³⁴

1.4.2.c. Spin-dependent electrochemistry

Electrochemistry consists of following a redox process by studying the current as a function of an applied voltage inside an electrochemical cell. A typical liquid electrochemical cell comprises a working electrode (WE), a counter electrode (CE), and a reference electrode (RE). Upon applying a voltage between the working and counter electrode in a liquid medium, the reduction/oxidation process of an electroactive component is followed.³⁷

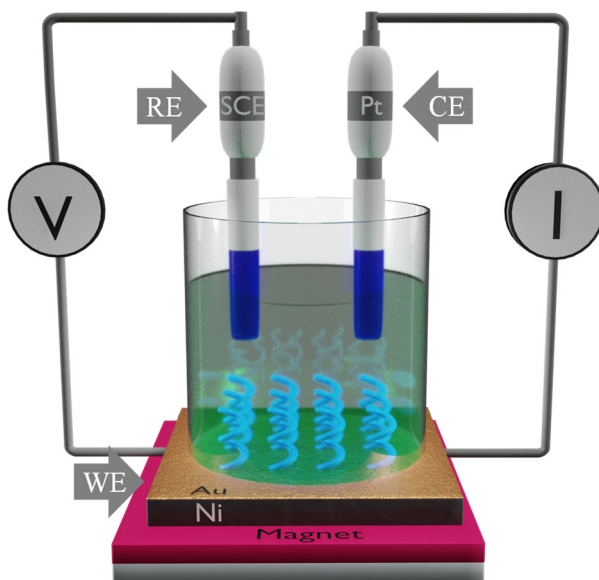


Figure 10. a) Schematic diagram illustrating the spin-dependent electrochemistry setup where a Ni electrode, platinum, and saturated calomel electrode (SCE) were used as the working electrode (WE), counter electrode (CE), and reference electrode (RE), respectively.

The basic setup is adjusted to perform spin-dependent measurements using a ferromagnetic working electrode modified with the chiral molecule, Figure 10. Then, the redox process occurring in an electroactive chiral SAM, or in an external probe (if the SAM is not electroactive) is followed as a function of the external magnetic field.^{38,39}

The most common manner to investigate spin-dependent electrochemistry is by performing cyclic voltammetry in the modified cell, Figure 11.

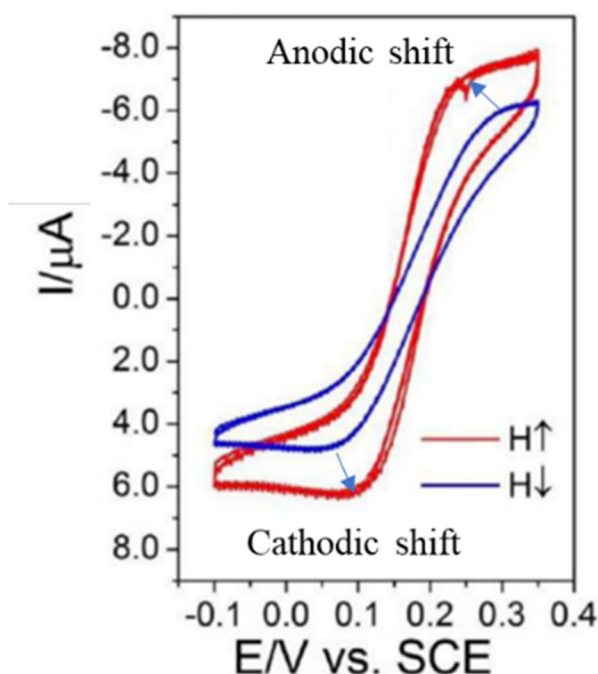


Figure 11. Cyclic voltammetry of a chiral bacteriophage thin-film physisorbed on a Ni working electrode. Red indicates the magnet pointing up and the blue down. Taken from 27.

For this measurement, two parameters must be considered to quantify the CISS effect. The first one is the intensity of the faradaic current; more intense redox peaks are related to an easier electron transfer from the WE to the

redox-active unit under study. Secondly, the anodic (oxidation) and cathodic (reduction) peaks position. Peaks with a lower separation between the anodic and cathodic signals also indicate a higher electron flow. Therefore, when the injected electronic spin matches the SAM's polarization, the electron conduction is maximum, exhibiting more intense peaks and lower peak separation. In contrast, in the reverse scenario, the peak separation increases and shows lower current intensity, Figure 11.

The spin polarization (SP) is quantified by applying the eq 2. Where, I_+ is the faradaic current at the maximum of the redox peak when transmitted electrons have their spin parallel to the electron movement and I_- antiparallel.

$$SP = \frac{I_+ - I_-}{I_+ + I_-} \text{ eq.2}$$

1.5. Bibliography

1. Pasteur, L. Memoires sur la relation qui peut exister entre la forme cristalline et al composition chimique, et sur la cause de la polarization rotatoire. *Compt. rend.* **26**, 535–538 (1848).
2. Cheng, T.-P. & Li, L.-F. Gauge Theory of Elementary Particle Physics: Problems and Solutions. *Oxford Univ. Press.* (2000).
3. Peskin, M. An introduction to quantum field theory. *CRC Press* (2018).
4. Yang, S. H. Spintronics on chiral objects. *Appl. Phys. Lett.* **116**, 120502 (2020).
5. Campbell, D. M. & Farago, P. S. Electron optic dichroism in camphor. *J. Phys. B* **20**, 5133 (1987).
6. Meier, F. & Pescia, D. Band-Structure Investigation of Gold by Spin-Polarized Photoemission. *Phys. Rev. Lett.* **47**, 374–377 (1981).
7. Campbell, D. M. & Farago, P. S. Spin-dependent electron scattering from optically active molecules. *Nature* **318**, 52–53 (1985).
8. Mayer, S. & Kessler, J. Experimental Verification of Electron Optic Dichroism. *Phys. Rev. Lett.* **74**, 4803–4806 (1995).
9. Blum, K. & Thompson, D. Spin-dependent electron scattering from oriented molecules. *J. Phys. B At. Mol. Opt. Phys.* **22**, 1823–1844 (1989).
10. Rich, A., Van House, J. & Hegstrom, R. A. Calculation of a Mirror Asymmetric Effect in Electron Scattering from Chiral Targets. *Phys.*

- Rev. Lett.* **48**, 1341 (1982).
11. Mayer, S., Nolting, C. & Kessler, J. Electron scattering from chiral molecules. *J. Phys. B At. Mol. Opt. Phys.* **29**, 3497–3511 (1996).
 12. Nolting, C., Mayer, S. & Kessler, J. Electron dichroism-new data and an experimental cross-check. *J. Phys. B At. Mol. Opt. Phys.* **30**, 5491 (1997).
 13. Dreiling, J. M., Lewis, F. W. & Gay, T. J. Spin-polarized electron transmission through chiral halocamphor molecules. *J. Phys. B At. Mol. Opt. Phys.* **51**, 21LT01 (2018).
 14. Scheer, A. M., Gallup, G. A. & Gay, T. J. An investigation of electron helicity density in bromocamphor and dibromocamphor as a source of electron circular dichroism. *J. Phys. B At. Mol. Opt. Phys.* **39**, 2169–2181 (2006).
 15. Blum, K. & Thompson, D. G. *Chiral Effects in Electron Scattering by Molecules. Advances in Atomic, Molecular and Optical Physics* vol. 38 (Elsevier Masson SAS, 1998).
 16. Yeganeh, S., Ratner, M. A., Medina, E. & Mujica, V. Chiral electron transport: Scattering through helical potentials. *J. Chem. Phys.* **131**, 014707 (2009).
 17. Vager, Z., Carmeli, I., Leitus, G., Reich, S. & Naaman, R. Surprising electronic-magnetic properties of closed packed organized organic layers. *J. Phys. Chem. Solids* **65**, 713–717 (2004).
 18. Ray, K., Ananthavel, S. P., Waldeck, D. H. & Naaman, R.

- Asymmetric scattering of polarized electrons by organized organic films of chiral molecules. *Science*. **283**, 814–816 (1999).
19. Wei, J. J. *et al.* Molecular chirality and charge transfer through self-assembled scaffold monolayers. *J. Phys. Chem. B* **110**, 1301–1308 (2006).
 20. Michaeli, K. & Naaman, R. Origin of Spin-Dependent Tunneling Through Chiral Molecules. *J. Phys. Chem. C* **123**, 17043–17048 (2019).
 21. Naaman, R. Chiral-induced spin selectivity effect. *J. Phys. Chem. Lett.* **3**, 2178–2187 (2012).
 22. Naaman, R., Paltiel, Y. & Waldeck, D. H. Chiral molecules and the electron spin. *Nat. Rev. Chem.* **3**, 250–260 (2019).
 23. Göhler, B. *et al.* Spin selectivity in electron transmission through self-assembled monolayers of double-stranded DNA. *Science*. **331**, 894–897 (2011).
 24. Borstel, G. & Wöhlecke, M. Spin polarization of photoelectrons emitted from nonmagnetic solids. *Phys. Rev. B* **26**, 1148 (1982).
 25. Carmeli, I., Naaman, R., Leitun, G., Reich, S. & Vager, Z. New electronic and magnetic properties of monolayers of thiols on gold. *Isr. J. Chem.* **43**, 399–405 (2003).
 26. MacLaren, D. A. *et al.* Asymmetric photoelectron transmission through chirally-sculpted, polycrystalline gold. *Phys. Chem. Chem. Phys.* **11**, 8413–8416 (2009).

27. Mishra, D. *et al.* Spin-dependent electron transmission through bacteriorhodopsin embedded in purple membrane. *Proc. Natl. Acad. Sci. U. S. A.* **110**, 14872–14876 (2013).
28. Naaman, R. & Waldeck, D. H. "The Chiral Induced Spin Selectivity (CISS) Effect". 235–270 (2018).
29. Kettner, M. *et al.* Spin Filtering in Electron Transport Through Chiral Oligopeptides. *J. Phys. Chem. C* **119**, 14542–14547 (2015).
30. Kettner, M. *et al.* Chirality-Dependent Electron Spin Filtering by Molecular Monolayers of Helicenes. *J. Phys. Chem. Lett.* **9**, 2025–2030 (2018).
31. Ravi, S., Sowmiya, P. & Karthikeyan, A. Magnetoresistance and spin-filtering efficiency of dna-sandwiched ferromagnetic nanostructures. *Spin* **3**, 1350003 (2013).
32. Ishida, T. *et al.* Conductive Probe AFM Measurements of Conjugated Molecular Wires. *Ann. N. Y. Acad. Sci.* **1006**, 164–186 (2003).
33. Kim, B., Beebe, J. M., Jun, Y., Zhu, X. Y. & Frisbie, G. D. Correlation between HOMO alignment and contact resistance in molecular junctions: Aromatic thiols versus aromatic isocyanides. *J. Am. Chem. Soc.* **128**, 4970–4971 (2006).
34. Kiran, V., Cohen, S. R. & Naaman, R. Structure dependent spin selectivity in electron transport through oligopeptides. *J. Chem. Phys.* **146**, 092302 (2017).
35. Kiran, V. *et al.* Helicenes - A New Class of Organic Spin Filter. *Adv.*

- Mater.* **28**, 1957–1962 (2016).
36. Xie, Z. *et al.* Spin specific electron conduction through DNA oligomers. *Nano Lett.* **11**, 4652–4655 (2011).
37. Allen, J. B. & Larry, R. F. *Electrochemical methods: Fundamentals and Applications.* John Wiley & Sons (2001).
38. Mondal, P. C., Fontanesi, C., Waldeck, D. H. & Naaman, R. Spin-Dependent Transport through Chiral Molecules Studied by Spin-Dependent Electrochemistry. *Acc. Chem. Res.* **49**, 2560–2568 (2016).
39. Fontanesi, C. Spin-dependent electrochemistry: A novel paradigm. *Curr. Opin. Electrochem.* **7**, 36–41 (2018).

2

Reinforced Spin Filtering in Chiral Metallopeptides

R. Torres-Cavanillas, G. Escorcía-Ariza, I. Brotons, R. Sanchis-Gual, P. Chandra Mondal, L. E. Rosaleny, S. Giménez-Santamarina, M. Sessolo, M. Galbiati, S. Tatay, A. Gaita-Ariño, A. Forment-Aliaga, S. Cardona-Serra. *Journal of American Chemical Society* **2020**, 142, 41, 17572–17580.

2.1. Motivation

The work described in part I was motivated to study the effect of coordination in the spin filtering of helicoidal peptidic SAMs. As has been already proved, the spin selectivity of chiral molecules in gas phase is enhanced by their coordination with heavy atoms.

Herein, we expanded this concept to SAMs of metal coordinated peptides. Because the current in peptides has been known to flow through the backbone chain, the interaction of the metal and the incoming current can be maximized, permitting the tuning of the spin selectivity by using different metallic centers.

2.2. Introduction

As chiral systems, we choose a member of the helical peptide family known as Lanthanide Binding Tags (LBTs)¹⁻⁴, with paramagnetic Tb³⁺ or diamagnetic Y³⁺ ions.

2.2.1. *Lanthanide Binding Tags*

We choose LBTs as helicoidal peptides, because of their binding affinity for lanthanoid ions, through the carboxylate groups in the peptidic backbone, Figure 1. From the perspective of chirality, these biomolecules autonomously fold into a helical structure, making them ideal candidates to exhibit CISS effect. From crystallographic studies, the ternary structure of the LBT remains the same despite the coordinated cation.⁵ For this reason, its structure can be considered independent of the coordination, being ideal systems to compare de CISS effect as a function of the coordinated metal. Recently, our group has

shown that LBTs can be used as spin tags to open a fruitful playground in the field of molecular spin qubits, thanks to their synthetic versatility.⁶

Sequence = YIDTNNDGWYEGDEL C

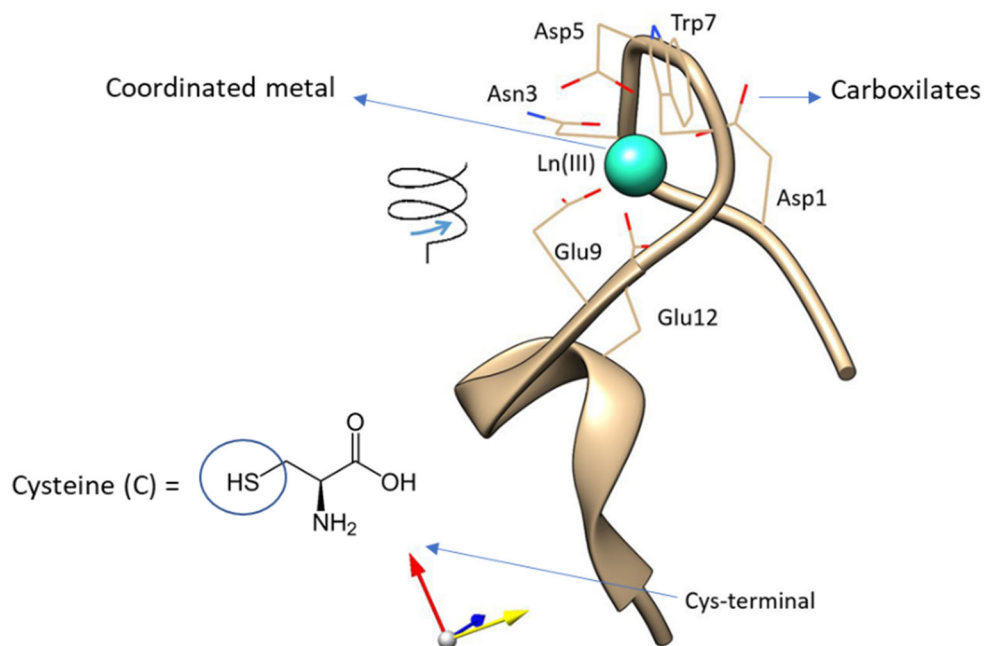


Figure 1. Structure of the LBT sequence employed in this work.

The sequence of the peptide employed in this thesis is shown in Figure 1. It is formed by 16 amino acids with the sequence YIDTNNDGWYEGDEL C. The cysteine residue (C) in the tail is used to attach the biomolecule onto the metallic surface. The metallic coordination occurs through the monodentate oxygen ligands (red sticks, Figure 1) of Asp1, Asn3, and Asp5, the bidentate carboxylate ligands from Glu9 and Glu12, and the backbone carbonyl group of Trp7. At the same time, the indole group of the Trp7 permits the Tb^{3+} (Turquoise sphere, Figure 1) detection via photoluminescence emission in the

coordinated state.⁷ It must be noticed that our LBT sequence exhibits 1.5 helices and only coordinates one cation.

2.2.2. *Spin dependency with the coordinated atom*

Based on the pioneer work of Mayer et al.,⁸ we thought that the nature of the coordinated atom could alter the helicoidal polypeptide filtering effect. For these chiral biocompounds, the electrons have known to flow through the backbone chain,⁹ hence, if the orbitals of the metal overlap with the orbitals of the backbone, a stronger interaction between the incoming current and the metallic center than the already reported can be expected.

Even more, we also speculated that thanks to this strong coupling, the modulation of the spin filtering via metallic exchange was possible. Two main reasons have accounted for this. On the one hand, due to the influence of Z, coordinating heavier atoms would lead to larger spin selectivity. On the other hand, the electronic signature may also play a role, exhibiting different overlapping with the backbone depending on the coordinated atom.

These assumptions are confronted in this thesis as a proof of concept for their future use on metallic biocomplexes based spintronic devices.

2.3. Results and discussion

In this chapter the results are presented as follows: first, the formation of LBT SAMs on gold, with and without complexing a lanthanoid cation, are explored in detail; next, the spin-selectivity ability of the LBT SAMs coordinating Tb³⁺ or Y³⁺ were inspected. To do so, both SAMs are studied by wet spin-dependent electrochemistry or by using liquid-metal drop contacts, to locally measure the SAMs spin-dependent electrical conductivity, Figure 2.

The growth of the LBT coordinating Tb^{3+} (TbLBT) was done by a simple immersion protocol of a Si/SiO₂ (285 nm) substrate, in which 200 nm of gold had previously been evaporated. We chose gold as an anchoring surface for two reasons: its high stability and high affinity with thiols, which ensures a strong bond between the cysteine (last amino acid in the polypeptide sequence) and the substrate. Therefore, the synthetic protocol begins with preparing a TbLBT solution, where the Au substrate was be incubated overnight at 4°C.

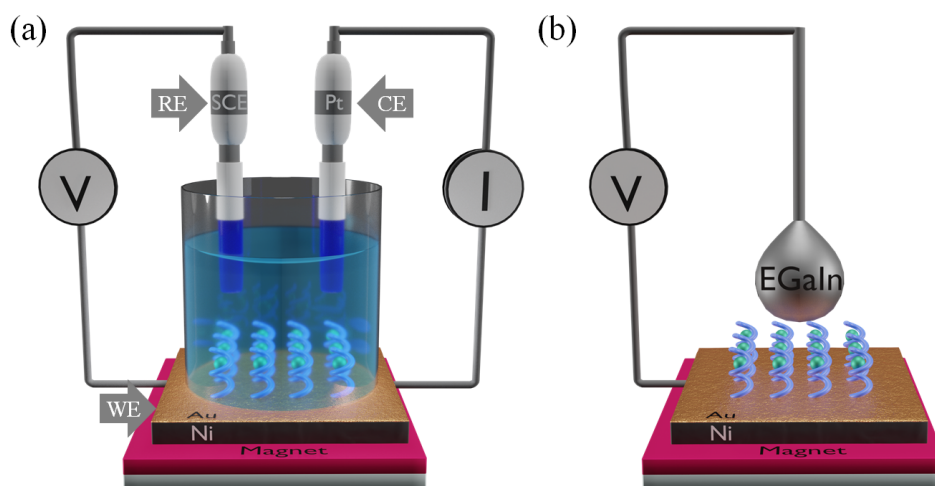


Figure 2. Scheme of the two experimental setups used to study the spin polarization of the SAMs. (a) Spin-dependent electrochemistry and (b) spin-dependent conductivity measured by liquid-metal drop contacts.

2.3.1. TbLBT solution

The cation coordination is performed by mixing a solution of Tb^{3+} with the buffered peptide (see the experimental section 2.5). Under the particular coordination environment produced by the peptide, the coordinated Tb^{3+} exhibits a distinctive light emission after its excitation with 280 nm light.¹⁰As Figure 3 shows, after the excitation, an intense peak appears at 550 nm in the

Tb³⁺ complex. Once the ratio LBT:Tb³⁺ 1:1 was achieved, the maximum intensity remains constant, indicating that all the LBTs coordinate a Tb³⁺ cation.

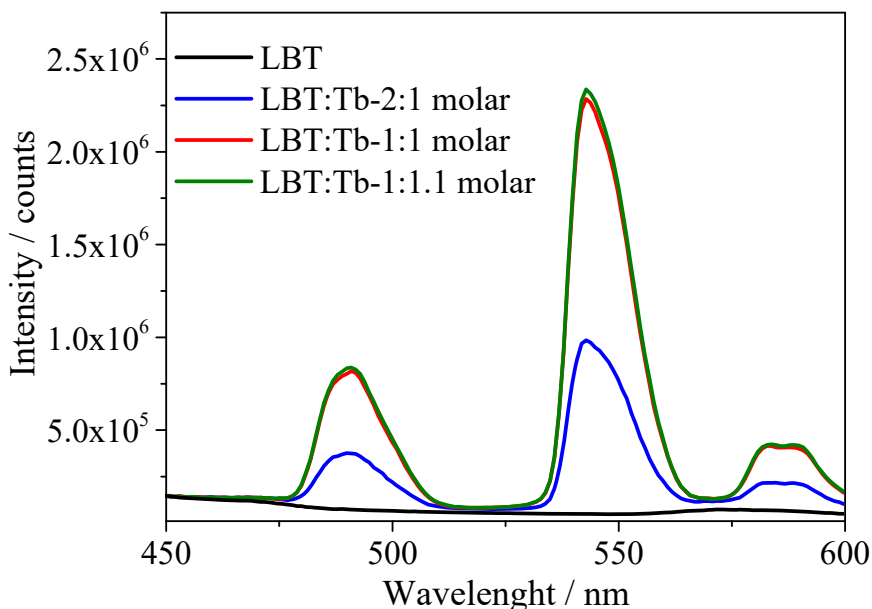


Figure 3. Luminescence spectra (280 nm excitation wavelength) of LBT after the addition of a solution of TbCl₃. Pure LBT (black line), with a ratio 2:1 of LBT:Tb (blue), 1:1 (red), and 1:1.1 (green).

2.3.2. TbLBT self-assembled monolayer on gold

Later, a freshly evaporated Au substrate was immersed overnight in a 0.1 mM TbLBT solution at 4°C. After its functionalization (Au/TbLBT), the topography of the gold surface was checked by Atomic Force Microscopy (AFM). As shown in Figure 4, the roughness after the anchoring remained similar to bare evaporated Au, suggesting that the SAM grows following the roughness of the substrate, which is typical of well-packed SAMs. The figure of merit of the roughness is the Root Mean Square (RMS) value presented in the right corner of the AFM images, Figure 4.

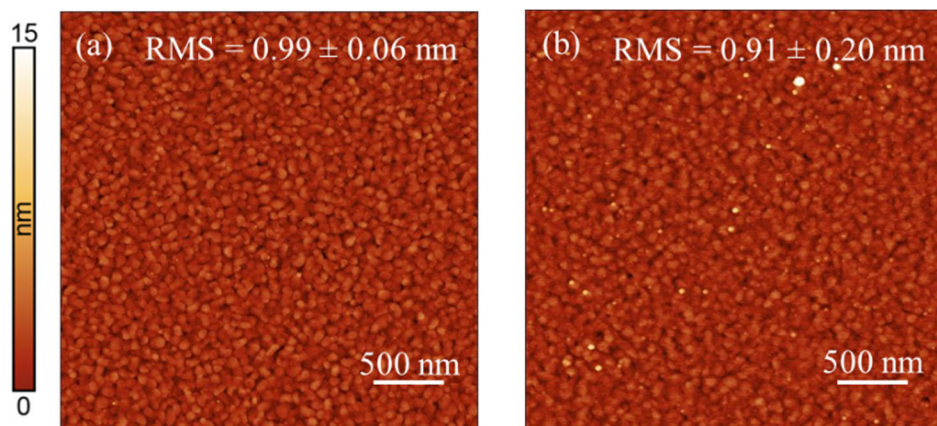


Figure 4. Topography images measured by AFM of bare gold and Au/TbLBT, a, and b, respectively. RMS value in the right corners.

2.3.2.a. Presence of LBT on gold

The peptide presence on the gold surface was proved by matrix-assisted laser desorption/ionization-time of flight (MALDI-TOF) mass spectrometry. MALDI is a soft ionization technique commonly used for mass spectrometry analysis of bio- and large organic molecules. The spectrum shows charged fragments of the macromolecule obtained after ionizing the sample in the presence of a matrix.

The matrix ensures the +1 charge in the molecular fragments via protonation or charge compensation with Na^+ or K^+ cations. As shown in Figure 5, the main fragment of the SAM appeared at 1630 m/z (Peak A); there was also a smaller peak at 1929 m/z (Peak B). Peak A belongs to the fragment DTNNDGWYEGDEL C and represent the main fracture point after the ionization. The minor peak B corresponds to the molecular weight of the complete LBT with an additional Na^+ . Unfortunately, the entire peptide coordinating the Tb^{3+} could not be observed. It must probably be due to the weak coordination of the carboxylates and the Tb^{3+} .

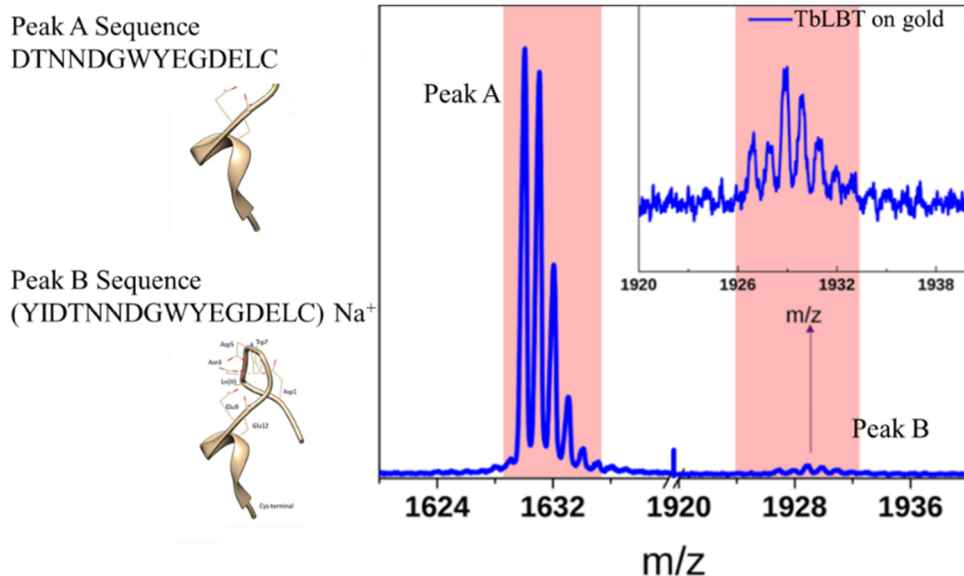


Figure 5. MALDI-TOF spectrum of Au/TbLBT.

From this result, we concluded that the peptide located on top of the metallic surface was firmly anchored on the substrate, most probably via S-Au bonds coming from the cysteine amino acid. Also, the integrity of the LBT was confirmed by the detection of the complete sequence in the spectrum, Peak B.

2.3.2.b. Presence and coordination of the Tb^{3+}

In order to prove the presence of the Tb^{3+} in Au/TbLBT, the sample was analysed by X-ray photoelectron spectroscopy (XPS). This is a surface-sensitive technique based on the extraction of the core electrons to quantify their binding energies (BE), which is characteristic of each element, oxidation state, and coordination environment. Therefore, by XPS, it is possible to accurately determine the presence of Tb^{3+} in the SAM and even the existence of S-Au bonds. As shown in Figure 6, the electronic signature of the lanthanide in the surface was evidenced by the presence of $Tb3d_{5/2}$ (1242 eV)

and Tb3d_{3/2} peaks (1277 eV). The LBT presence was also confirmed by the S2p (~162.5 eV, thiol bonded to Au) and N1s (400 eV, amino groups) peaks coming from the aminoacids, Figure 6.

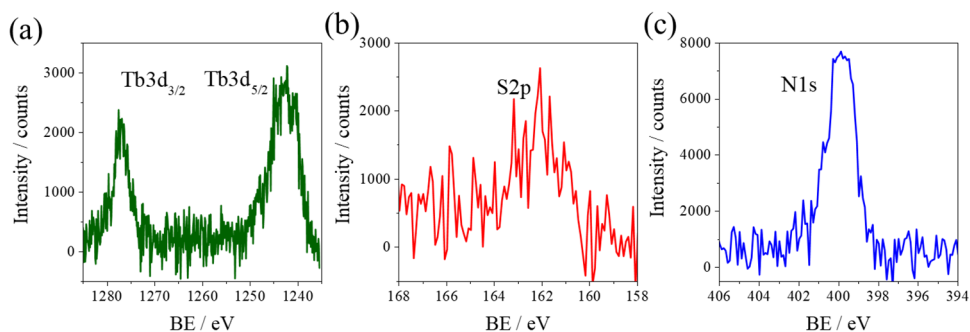


Figure 6. XPS spectrum of Tb (green), S (red), and N (blue) of TbLBTC SAM on Au surface.

Due to the extremely high affinity of the LBT for Tb³⁺ ions,¹¹ it was fair to assume that LBT coordinates them. Still, we investigated the photoluminescence of the Au/TbLBT to ensure it. Therefore, the photoluminescence of the functionalized Au substrate was recorded under excitation with a 254 nm wavelength source.

First, to validate the measurements, we characterize a solution of LBT, Tb³⁺, and TbLBT. As shown in Figure 7, all the samples presented a baseline attributed to light partially reflected from the source into the detector. However, it is clear that the TbLBT exhibits a huge light emission after the excitation. Similarly, the Au/TbLBT was compared with two different reference substrates: clean Au (Au) and Au incubated in Tb³⁺ solution and copiously rinsed (Au/Tb). It should be noticed that for these samples, the reduced amount of material and the increased background coming from the highly reflective gold led to smaller differences between the baseline and the

signal. However, as in solution, Au/TbLBT displayed a slight increase in the recorded light by the camera. This fact supports the claim that Tb^{3+} is indeed coordinated by the SAM.

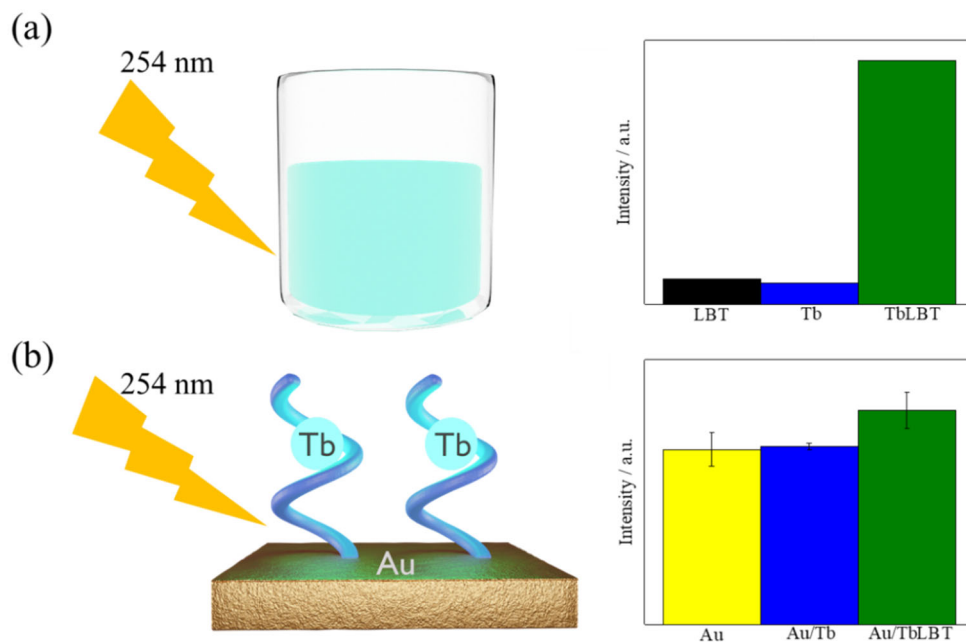


Figure 7. Photoluminescence signal recorded by the digital camera of the optical microscope (a) for solutions of LBT, YLBT, Tb^{3+} , and TbLBT and (b) for clean Au (Au), Au incubated in Tb^{3+} solution and copiously rinsed (Au/Tb), and Au with a TbLBT SAM (Au/TbLBT).

2.3.2.c. Coverage evaluation using quartz crystal microbalance

To quality and packing of the SAM is evaluated with a quartz crystal microbalance (QCM), monitoring its formation. The experiment consists of a freshly cleaned Au covered piezoelectric quartz crystal immersed in a liquid cell where a flow of different liquids at controlled rates was pumped. Then, the oscillation frequency of the crystal was continuously recorded.

Therefore, after adding the TbLBT solution to the cell, the SAM is formed on the piezoelectric. This affects its oscillation due to the increase in weight on top, being a direct proof of the amount of material deposited on top of the Au/quartz crystal.

Several cycles of pure water and aqueous buffered solution flowed in a standard experiment until the signal's frequency was stabilized (Figure 8a, water in blue, buffer in red). Later, right after a buffered solution step, a TbLBT solution was injected during ca. 30 min to ensure a constant frequency value (in green). Finally, a flow of the buffered aqueous solution was flowed to remove the physisorbed TbLBT on the crystal.

From the frequency difference, we estimated the mass loaded in the electrode through Sauerbrey's equation, eq. 1.

$$\Delta f = -\frac{2f_0^2}{A\sqrt{\rho\mu}}\Delta m \quad \text{eq.1}$$

where f_0 is the resonant frequency of QCM, Δf is the change in the resonant frequency of the quartz microbalance due to the electrodes mass change (Δm), A is the active area, ρ is the density, and μ is the shear modulus of the quartz crystal.

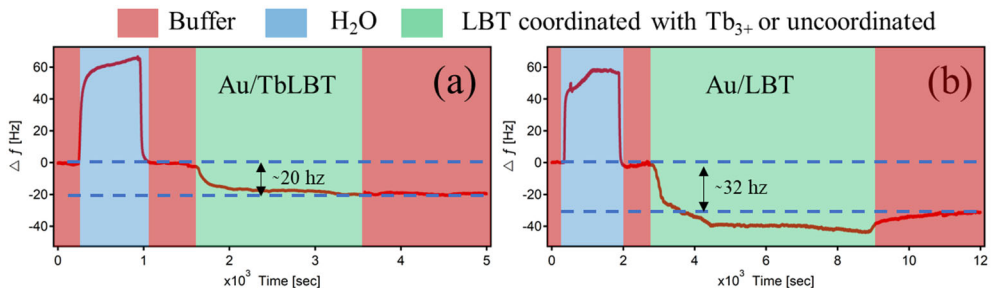


Figure 8. Quartz crystal microbalance measurements of LBT coordinating Tb^{3+} (a) and LBT uncoordinated (b).

Once the Δm was calculated and knowing that the LBT is a globular peptide with a diameter of ~ 1.6 nm, we could estimate the surface coverage. This was done by calculating the number of peptides covering the gold substrate thanks to the measured Δm and the already known molecular weights of the TbLBT ($2065 \text{ g} \cdot \text{mol}^{-1}$). Nevertheless, it is essential to clarify that the molecular weight is not precise, since the number and kind of counterions are unknown. Therefore, the calculated coverages may be overestimated, as the most straightforward situation where protons compensate the negative charges of the polypeptide was considered.

According to our calculation, the coverage of TbLBT ranged between 80-120%. From this result, we concluded that a monolayer was probably obtained in the case of TbLBT.

The same experiment was carried out but flowing an uncoordinated LBT solution (Figure 8b), leading to a more extensive coverage that ranges between 145-189%. This larger frequency shift in the absence of the Tb^{3+} indicates or (i) stronger intermolecular polypeptide-polypeptide interactions, forcing a less globular shape and permitting a more compact packing at the surface, or (ii) the formation of a multilayer. From our perspective, the second option is less probable as there is no reason to think that a second layer can be formed with LBT, but it does not happen with TbLBT. In conclusion, we believe that a cation is required to maintain the chirality in LBT SAMs, and hence the CISS effect.

2.3.2.d. SAM thickness

XPS can be used to determine the overlayer thickness of SAMs by different methodologies. The most straightforward approach assumes that an

increasing overlayer thickness causes an exponential attenuation of the photoelectron signal coming from the substrate that can be described by¹²:

$$I = I_0 \exp(-d/\lambda) \text{ eq. 2}$$

Where I_0 is the signal coming from the substrate in the absence of the overlayer, d is the overlayer thickness, and λ the inelastic mean free path (IMFP) of the photoelectrons crossing the overlayer.

I and I_0 were determined by measuring the intensity of the Au $4f_{7/2}$ peak at 84.4 eV on Au/TbLBT before and after removing the SAM. To remove the SAM, successive Ar ion gun etching cycles (1000 eV and 30 s) were done until an invariable Au signal was obtained. Figure 9 shows the initial and final Au $4f_{7/2}$ signal.

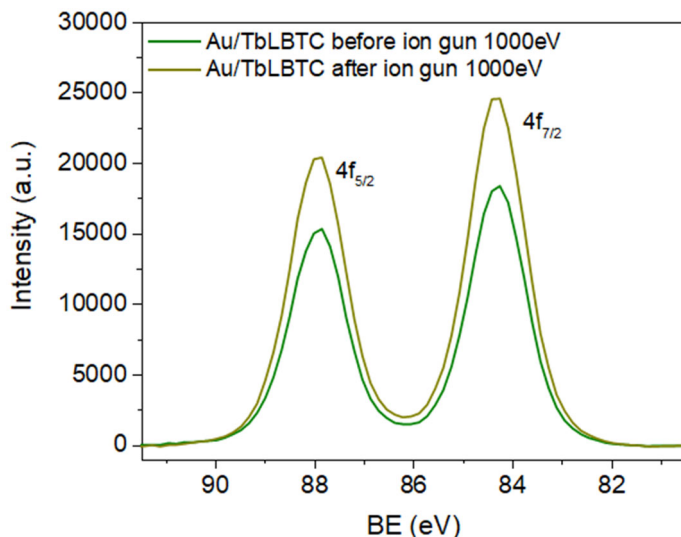


Figure 9. Au $4f$ XPS spectra of TbLBT SAM on a Au surface, before (dark green) and after (light green) ion etching

A value of $\lambda = 58.0 \text{ \AA}$ was estimated from the NIST Electron Inelastic-Mean-Free-Database, using the Gries equation, which utilizes the molecular formula of the compound and its density.¹³ The molecular formula used was

that of the LBT peptide coordinating one Tb^{3+} ($\text{TbC}_{82}\text{H}_{113}\text{N}_{19}\text{O}_{32}$). The monolayer density, $\sim 1,1 \text{ g}\cdot\text{cm}^{-3}$, was extracted from de QCM measurements, assuming a full coverage of the substrate. Finally, equation 2 was applied, and the thickness calculated is $\sim 1.7 \text{ nm}$ for Au/TbLBT, which is in good agreement with the formation of a TbLBT monolayer, considering that the diameter of the LTB is around 1.6 nm .

2.3.3. Role of the coordinated metal in the Spin-filtering effect

Once the possibility of assembling metallo-complexes onto metallic surfaces was demonstrated, the spin filtering of the monolayers coordinating Tb^{3+} or Y^{3+} was investigated.

To examine the spin polarization electrically, it is necessary to introduce charge carriers with a particular spin orientation. In this thesis, we used a ferromagnetic nickel electrode protected with 5 nm gold as a source of spin-polarized electrons, Ni/Au. The presence of gold is of capital importance because it acts as a better anchoring surface, while protecting Ni from oxidation.

The Ni/Au electrode magnetization was achieved by placing a permanent magnet under the substrate. The magnetic field was manually flipped by changing the orientation of the magnet, Figure 10. This allows the injection of spin-polarized electrons from the ferromagnetic electrode. As a matter of convenience, we will refer to the magnetic field pointing "down" or "up" when the magnet north pole points towards or opposite the substrate, respectively, Figure 10.

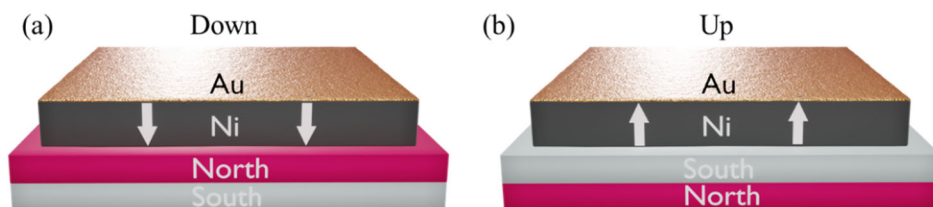


Figure 10. Scheme of the magnet orientation under the Ni/Au substrate with the magnetic field "down" or "up" when the north pole points towards or opposite to the substrate.

Following this idea, a similar synthetic protocol used to grow TbLBT on gold was expanded to Ni/Au substrates and to form YLBT SAMs by coordinating Y^{3+} instead of Tb^{3+} (experimental section 2.5.). The SAM of Y^{3+} was developed to compare the spin-filtering with the different metallic centers.

We chose Y^{3+} because it exhibits a similar atomic radius than the Tb^{3+} (180 and 175 pm, respectively); thus, a similar packing is expected. The main difference between both metals is their atomic number, Z_{at} , and their electronic signature. Tb^{3+} ($Z_{at}=65$) is paramagnetic, having its orbitals partially filled ($S=5/2$), while Y^{3+} ($Z_{at}=39$) is diamagnetic, having them fully occupied ($S=0$). It is important to remark that the only difference between the SAMs growth process on Au or Ni/Au was that the incubation of the magnetic substrate was performed under an inert atmosphere to minimize the Ni oxidation (for more information about the synthetic protocol, see experimental section 2.5.). Figure 11 shows the topography of both SAMs. As can be seen, the roughness remains similar for TbLBT and YLBT, suggesting a similar packing. Once the SAMs were formed, the spin polarization was studied by wet electrochemistry and spin-dependent conductivity.

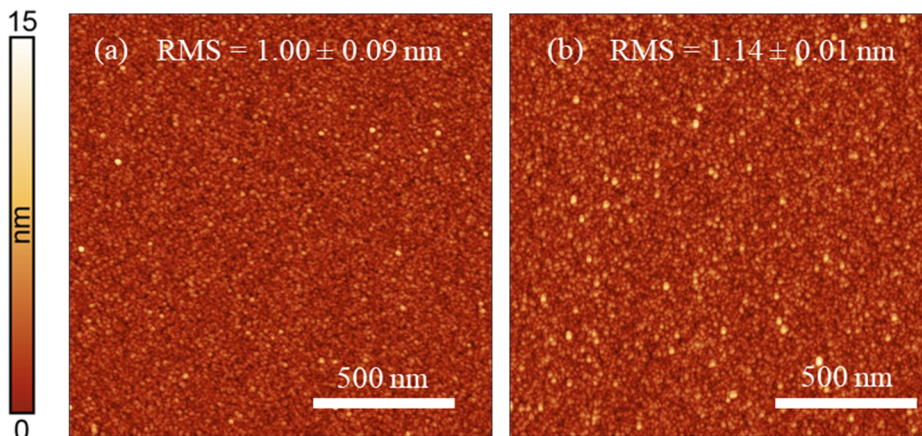
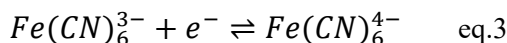


Figure 11. (a,b) Topography images measured by AFM of Ni/Au/TbLBT and Ni/Au/YLBT, respectively.

2.3.3.a. Tb and YLBTC Cyclic voltammetry

The study of chiral SAMs spin filtering properties has been widely studied in the literature by electrochemistry. This approach consists of following the faradaic current of a redox process while an external magnetic field with different orientations is applied.¹⁴ In our particular scenario, due to the non-electroactive nature of our metallo-peptidic SAMs, we used $K_4Fe(CN)_6/K_3Fe(CN)_6$ as a redox-active external probe. The redox reaction involves the reduction and oxidation of Fe^{3+} and Fe^{2+} , eq. 3.



The experimental setup is shown in Figure 12a, where the Ni/Au was used as working electrode (WE) with a Ag/AgCl reference electrode (RE), a Pt wire as counter electrode (CE), and a solution of the buffer containing $K_4Fe(CN)_6/K_3Fe(CN)_6$ in contact with the electrodes as a redox probe. Next, to perform the spin-dependent cyclic voltammetry measurements, a permanent magnet ($H = 350$ mT) is placed underneath the WE. The

measurements were carried out by Isaac Brotons and Prakash Mondal, see experimental section 2.5.

Cyclic voltammograms of the $\text{Fe}^{3+}/\text{Fe}^{2+}$ process were recorded for three WE: bare Ni/Au (as reference experiment), Ni/Au/TbLBT, and Ni/Au/YLBT. The bare Ni/Au exhibited the highest faradaic current, and the difference between the anodic and cathodic peaks was the lowest (0.29V), Figure 12b. This matches perfectly with a good contact and electron flow between the WE and the $\text{K}_4\text{Fe}(\text{CN})_6/\text{K}_3\text{Fe}(\text{CN})_6$ solution. Even more, the redox process was independent of the magnet orientation placed underneath, which was accounted for the perfect overlap of the current vs. voltage plot at the two magnetic orientations. In contrast, when the Ni/Au/TbLBT or Ni/Au/YLBT modified substrates were used as WE, the faradaic current decreased substantially, Figure 12c-d.

Additionally, the distance between the anodic and cathodic peaks increased. This is a strong indication of the presence of a well-packed insulating SAM. Comparable values were obtained for both samples, supporting the similar quality of the SAMs.

Regarding the redox process as a function of the magnetic field, clear changes occurred in the modified electrodes. In good agreement with reported results,¹⁵ Ni/Au/TbLBT and Ni/Au/YLBT electrodes displayed a higher faradaic current with the external magnetic field pointing "down" compared to "up". Furthermore, a shift in the anodic (to lower voltages), and cathodic (to higher voltages) potentials was evidenced when the magnetic field pointed down (Figure 12d, blue lines). Therefore, we concluded that depending on the orientation of the external magnet, the SAM electrical resistance changes,

being lower when the magnetic field points down (North pole towards the substrate).

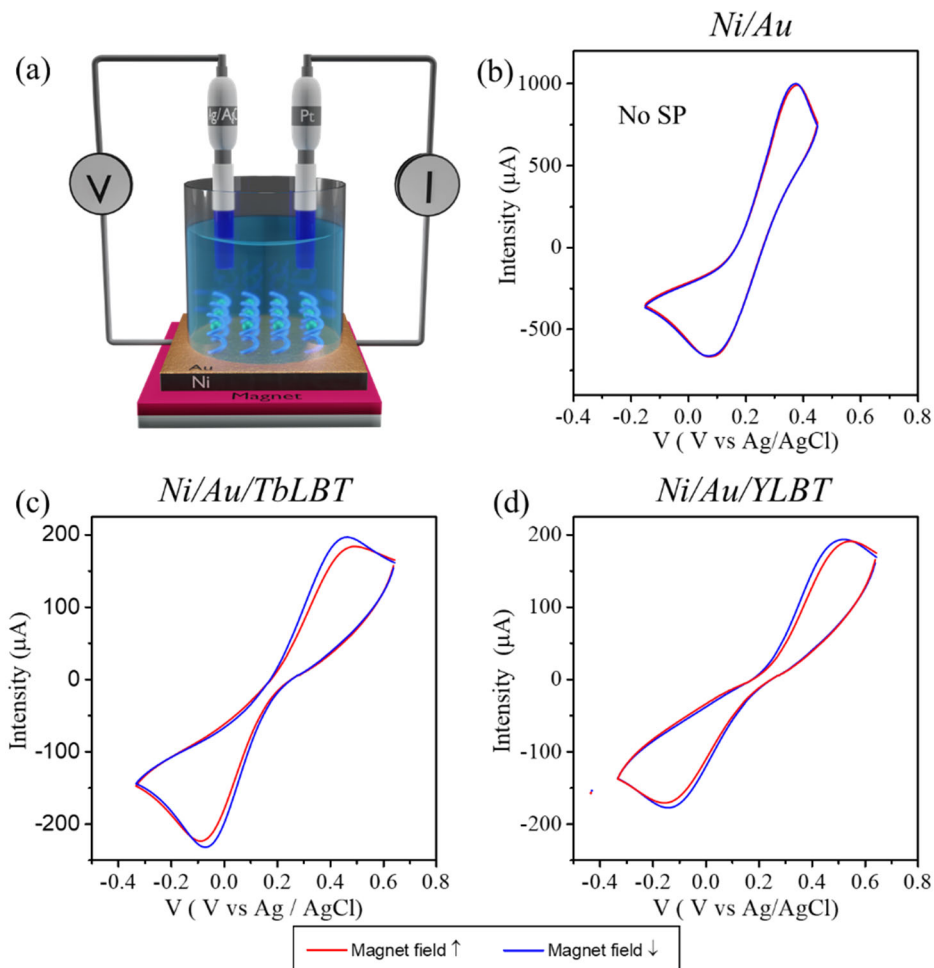


Figure 12. (a) Scheme of the experimental setup used to perform the spin-dependent electrochemistry measurements. (b–d) Spin-dependent cyclic voltammograms of an $\text{Fe}^{2+}/\text{Fe}^{3+}$ solution using different working electrodes: Ni/Au (b), TbLBTC SAM modified Ni/Au (c), and YLBT SAM modified Ni/Au (d). Voltammograms are recorded at 20 mV/s under an external magnetic field pointing "up" (solid red line) or "down" (solid blue line); four cycles are averaged.

These magnetic current and voltage dependences are a result of the SAM spin selectivity. Remarkably, the peaks position shifts, and their intensity

varied from the Ni/Au/TbLBT to the Ni/Au/YLBT. Thus, a more in-depth study on these two samples was required to cast light on the spin-polarization dependence on the coordinated cation. In this context, we calculated the Spin Polarization (SP) of the SAMs through eq 4.:

$$SP = \frac{I_{up} - I_{down}}{I_{up} + I_{down}} \times 100 \quad \text{Eq. 4}$$

where I_{up} and I_{down} stand for the current at the maximum of the redox peak. For the Ni/Au/TbLBTC, we obtained a $SP = -3.3(\pm 0.2)\%$ at +460 mV and a $SP = -1.9(\pm 0.2)\%$ at -70 mV. Moreover, comparing the anodic and cathodic peak positions, when the magnetic field was pointing down, a shift of -28 (anodic potential) and 20 mV (cathodic potential) was recorded, Figure 12c. Interestingly, when the Y^{3+} center replaced the Tb^{3+} , the SP effect slightly decreased, displaying a SP of $-0.6(\pm 0.2)\%$ measured at +515 mV and $-1.9(\pm 0.2)\%$ at -140 mV. Additionally, the anodic and cathodic shifts of the oxidation and reduction potential also decreases compared with its paramagnetic counterpart, -21 (anodic) and 11 mV (cathodic), Figure 12d. This experimental observation suggests an increase in the filtering of the TbLBT SAM. Nevertheless, due to the high voltages applied during the measurements, modification in the SAM packing can occur, which complicates the quantitative comparison of the SP between samples.

2.3.3.b. Tb and YLBTC Electrochemical impedances

To avoid the degradation of the SAMs, we decided to investigate the SP by electrochemical impedance spectroscopy (EIS). This is a non-destructive technique that can corroborate the results obtained by cyclic voltammetry while minimizing the fatigue associated with the applied voltage.

The EIS is a powerful technique to characterize electrochemical charge-transfer processes. This technique expands the concept of resistance from direct to alternating current circuits (DC and AC, respectively).¹⁶ In this technique, a low alternative current potential (AC potential) is applied on an electrochemical cell while monitoring the current (eq.5).

$$V_{AC} = I_{AC}Z_I \quad \text{Eq. 5}$$

where Z_I corresponds to the impedance, a property that represent the opposition that the circuit presents to the current produced by the AC potential. Notice that Z_I is more complicated than the typical electrical resistance measured in DC. Indeed, it is a complex number composed by a real part, Z_I' , and an imaginary part, Z_I'' (eq. 6).

$$Z_I = Z_I' + iZ_I'' \quad \text{Eq. 6}$$

The real part, Z_I' , is related to the electronic resistivity and is independent of the AC frequency. In contrast, Z_I'' is associated with capacitive effects and depends on the frequency. Therefore, when Z_I'' is equal to 0 it is fair to assume that $Z_I = Z_I'$ in such way that it can be considered the resistivity of the circuit to a specific electrochemical process, being analogue to the classical electrical resistance R. Therefore, Z_I' is extracted at $Z_I''=0$ in the plot of Z_I'' as a function of Z_I' over a range of frequencies (Nyquist plot).

Therefore, an AC potential of 10 mV in the range of frequencies 10^5 to 10^0 Hz was applied at the open circuit potential (~ 0.2 V), following the $\text{Fe}^{2+}/\text{Fe}^{3+}$ reaction. These measurements were carried out by Roger Sanchis, supporting information 2.5. As for the cyclic voltammetry, we measured a Ni/Au reference and the two SAMs, Ni/Au/TbLBT and Ni/Au/YLBT.

In all the samples, two semicircles were visible. The first at higher frequencies (Figure 13, a-c inset) corresponds to the charge transfer resistance of the WE, and the second one at lower frequencies is related to the resistance at the metallic interphase (Figure 13). Therefore, the second semicircle was the one potentially affected by the SAM and the magnet orientation.

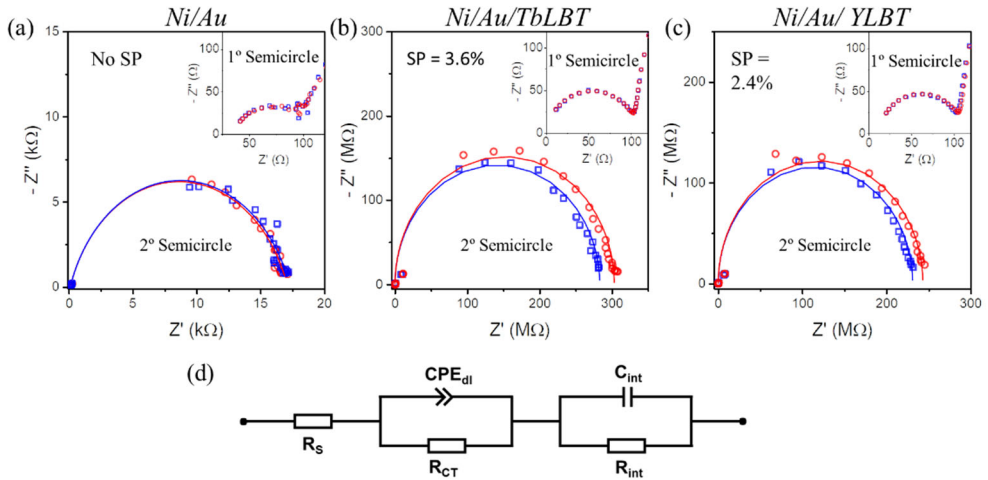


Figure 13. (a–c) Imaginary (Z'') vs real (Z') impedance components of an Fe^{2+}/Fe^{3+} solution using a Ni/Au (a), TbLBT SAM on Ni/Au (b), and YLBT SAM on Ni/Au (c) as working electrodes, respectively. An external magnetic field pointing "up" (red \circ) or "down" (blue \square) is applied during the measurements. Zooms of the corresponding plots in the high-frequency region (from 10^5 to 10^3 Hz) are shown in the insets. Solid lines in the (a–c) plots are the EIS fits obtained using the equivalent circuit (d).

As expected, the first semicircle exhibits the same value of $\sim 100 \Omega$ at $Z''=0$ for all the samples, which is also independent of the magnet orientation. Looking at the cutting of the plot on the x-axis, the empty Ni/Au exhibits a resistance to the electronic transfer which is three orders of magnitude lower, around 18 k Ω , than the SAM modified analogous (~ 270 , and ~ 240 M Ω for the Ni/Au/TbLBT and Ni/Au/YLBT, respectively). This is caused by the insulating nature of the SAM located at the Ni/Au interphase.

Focusing now on the magnet flipping effect, the SAM modified WEs displays an explicit Z_I' dependency, in contrast to the unaffected Z_I' value for Ni/Au WE,. In both cases, the second semicircle is suppressed when the magnetic field is pointing "down", which indicates a lower charge transfer resistance. Thus, a reduction of the resistance is exhibited by changing the external magnetic field from "up" to "down". The SP of both samples was calculated using eq. 4 and converting the resistance extracted from Z_I' at the cutting x-axis into conductance. Remarkably, a SP of $-3.6(\pm 0.2)$ % was determined for the Ni/Au/TbLBTC and $-2.4(\pm 0.2)$ % for the Ni/Au/YLBTC. These results are in good agreement with those extracted from the cyclic voltammetry and point out to the active role of the metallic center in the spin selectivity.

2.3.3.c. Spin-dependent electrical conductivity

Once cyclic voltammograms and impedance measurements demonstrated the spin selectivity, we advanced toward a dry spin-dependent characterization closer to a practical device.

To do so, we performed magnetic field-dependent charge-transport measurements through the Ni/Au/TbLBT or YLBT using a gallium indium eutectic alloy (EGaIn) as a liquid-metal electrode (Figure 14). Liquid-metal drop local transport in solid-state devices has been widely used in electronic current transport measurements in organic layers.¹⁷ Here, we extended it to CISS measurements by including an additional static magnetic field.

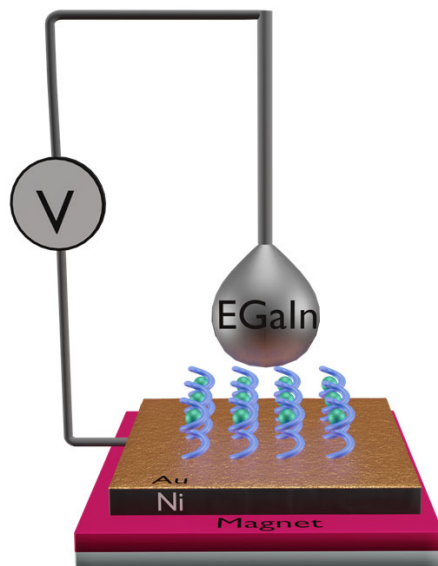


Figure 14. Scheme of the experimental setup used to perform the spin-dependent electrical conductivity through the liquid-metal contact of EGaIn.

It must be noticed that the same magnet of the electrochemistry measurements to magnetize the Ni/Au substrate was used in this setup. First, as a reference and to validate our experimental setup, two analogous devices, including well-studied chiral and achiral SAMs were measured, Figure 15. The achiral molecule was octadecanethiol (C18SH), and the chiral reference was the right-handed HS-CH₂-CH₂-NHCO(Ala-AiB)₈-NH₂ (Ala₈),¹⁴ where Ala was alanine and AiB is 2-aminoisobutyric acid. The choice of the reference molecules was not arbitrary. On the one hand, SAMs based on C18SH are probably the most studied in the literature, and liquid-metal contacts have already been used to investigate their conductivity.¹⁷ On the other hand, Ala₈ has been widely investigated as a spin filtering SAM.^{14,18}

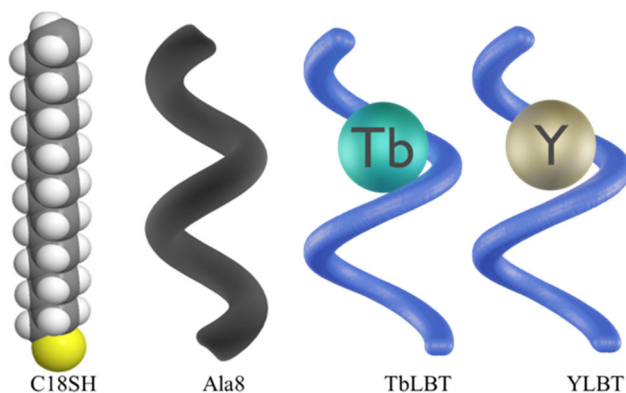


Figure 15. Schematic representation of molecules used to form SAMs on Ni/Au electrodes, in order to measure and compare their spin-dependent electronic conductivity.

Figure 16-top shows current density histograms in the range ± 0.2 V for opposite directions of the external magnet. In the achiral C18SH SAMs, no difference in the current density histograms was observed, $SP = 2 \pm 2\%$ (Figure 16a). In contrast, the Ala8 SAM exhibits a negative SP of $40 \pm 15\%$, Figure 16b. These results proved the feasibility of the setup. It must be noticed that similar to Ala8 SAMs, the complexed LBT chirality was expected to be right-handed and thus to provide the same SP sign.¹⁹

The dry spin-dependent conductivity of TbLBT and YLBT, corroborated the electrochemical measurements i.e., a higher SP for the Tb^{3+} complex than for Y^{3+} . In both cases, negative SPs were recorded. However, the filtering effect displayed by the Tb SAM is considerably larger than that stated by Y ($SP = -50 \pm 20\%$ for YLBTC and $SP = -70 \pm 10\%$ for TblBTC, Figure 16d).

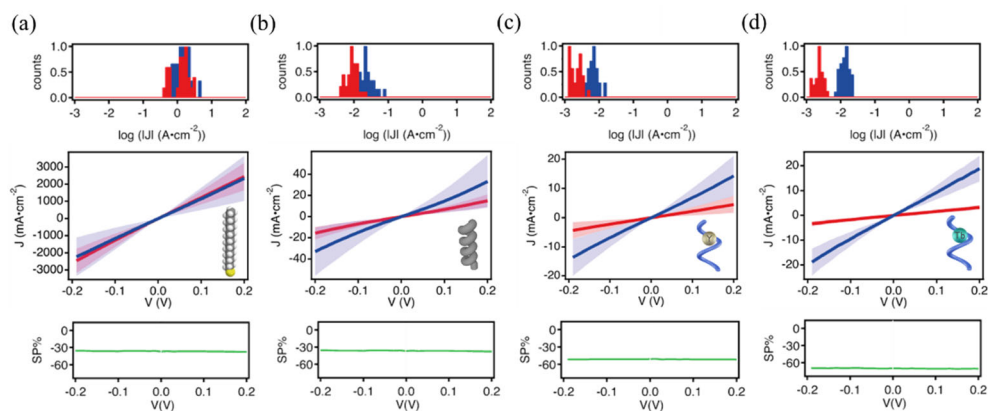


Figure 16. Magnetic field-dependent liquid-metal transport experiments measured for (a) C18S, (b) Ala8, (c) YLBT, and (d) TbLBT. Current density histograms measured at ± 0.15 V (top) and averaged current density versus voltage curves (middle) measured under an external magnetic field pointing "up" (red) or "down" (blue). SP polarization as a function of the bias voltage calculated from the measured averaged current density (bottom).

Noticeably, SP values measured employing liquid-metal contacts were of the same sign but nearly one order of magnitude larger than those obtained by electrochemical measurements. We attributed this fact to the more local nature of this technique. The unavoidable presence of pin-holes in the SAM should result in a supply of unpolarized electrons that will contribute to the total measured current. In turn, this will account for a reduction of the SP, in the electrochemical measurements, due to the larger contact surface, which was about 1500 times the contact area generated with EGaIn.²⁰

2.4. Conclusions and perspectives

In this part of the thesis, the potential of lanthanide binding peptides as effective spin filtering units has been demonstrated. To the best of our knowledge, this work represents the first attempt to electrically explore the

CISS effect in a system combining chiral SAMs with a coordinated metallic center.

These, two different metallic ions have been incorporated in the bio-SAMs, Tb^{3+} and Y^{3+} . The polypeptidic complexes have been anchored on a ferromagnetic Ni/Au substrate to investigate their spin-filtering properties by electrochemistry (cyclic voltammetry and EIS) and solid-state electrical conductivity. For the first time, EIS and electrical conductivity measured by liquid contacts have been proposed to study the CISS effect as a suitable alternative to typical cyclic voltammetry. From the point of view of EIS and in contrast with the usual electrochemical methodologies, the fatigue of the SAM is minimized, increasing the reproducibility and facilitating the SP quantification. Regarding the electrical conductivity measured in solid state, the more local character of the liquid contact has permitted to minimize the pin-holes, recording more efficiently the CISS effect.

In the three techniques, an apparent SP is displayed by the chiral SAMs. Remarkably, the SP was reinforced in the TbLBT, Figure 1. The reason for this improvement is still not clear, but we speculate that can be attributed to two main reasons. On the one hand, the higher spin-orbit coupling of the incoming electrons with the helicoidal TbLBT, induced by the larger Z of Tb ($Z=65$), compared with the Y ($Z=39$). On the other hand, it could exist a more efficient overlapping of the Tb^{3+} orbitals with the peptidic backbone. It is tempting to correlate this difference with the spin state of the metallic center. This issue will be confronted in the future by performing similar experiments in Fe^{2+} chiral bio complexes, which can exhibit a change in its spin state, from a diamagnetic low spin state ($S=0$), into a paramagnetic high spin state ($S=2$).

This will allow the spin filtering study in the diamagnetic low-spin and the paramagnetic high-spin, while Z is constant.

2.5. Bibliography

- (1) Silvaggi, N. R.; Martin, L. J.; Schwalbe, H.; Imperiali, B.; Allen, K. N. Double-Lanthanide-Binding Tags for Macromolecular Crystallographic Structure Determination. *J. Am. Chem. Soc.* **2007**, *129* (22), 7114–7120.
- (2) Nitz, M.; Sherawat, M.; Franz, K. J.; Peisach, E.; Allen, K. N.; Imperiali, B. Structural Origin of the High Affinity of a Chemically Evolved Lanthanide-Binding Peptide. *Angew. Chemie* **2004**, *116* (28), 3768–3771.
- (3) Nitz, M.; Franz, K. J.; Maglathlin, R. L.; Imperiali, B. A Powerful Combinatorial Screen to Identify High-Affinity Terbium(III)-Binding Peptides. *ChemBioChem* **2003**, *4* (4), 272–276.
- (4) Daughtry, K. D.; Martin, L. J.; Sarraju, A.; Imperiali, B.; Allen, K. N. Tailoring Encodable Lanthanide-Binding Tags as MRI Contrast Agents. *ChemBioChem* **2012**, *13* (17), 2567–2574.
- (5) Barb, A. W.; Ho, T. G.; Flanagan-Steet, H.; Prestegard, J. H. Lanthanide Binding and IgG Affinity Construct: Potential Applications in Solution NMR, MRI, and Luminescence Microscopy. *Protein Sci.* **2012**, *21* (10), 1456–1466.
- (6) Rosaleny, L. E.; Cardona-Serra, S.; Escalera-Moreno, L.; Baldoví, J. J.; Gołębiewska, V.; Wlazło, K.; Casino, P.; Prima-García, H.; Gaita-Ariño, A.; Coronado, E. Peptides as Versatile Platforms for Quantum Computing. *J. Phys. Chem. Lett.* **2018**, *9* (16), 4522–4526.
- (7) Franz, K. J.; Nitz, M.; Imperiali, B. Lanthanide-Binding Tags as

- Versatile Protein Coexpression Probes. *ChemBioChem* **2003**, *4* (4), 265–271.
- (8) Mayer, S.; Kessler, J. Experimental Verification of Electron Optic Dichroism. *Phys. Rev. Lett.* **1995**, *74* (24), 4803–4806.
- (9) Sek, S.; Misicka, A.; Swiatek, K.; Maicka, E. Conductance of α -Helical Peptides Trapped within Molecular Junctions. *J. Phys. Chem. B* **2006**, *110* (39), 19671–19677.
- (10) Clark, I. D.; Hill, I.; Sikorska-Walker, M.; MacManus, J. P.; Szabo, A. G. A Novel Peptide Designed for Sensitization of Terbium (III) Luminescence. *FEBS Lett.* **1993**, *333* (1–2), 96–98.
- (11) Martin, L. J.; Sculimbrenne, B. R.; Nitz, M.; Imperiali, B. Rapid Combinatorial Screening of Peptide Libraries for the Selection of Lanthanide-Binding Tags (LBTs). *QSAR Comb. Sci.* **2005**, *24* (10), 1149–1157.
- (12) Snow, A. W.; Jernigan, G. G.; Ancona, M. G. Packing Density of HS(CH₂)NCOOH Self-Assembled Monolayers. *Analyst* **2011**, *136* (23), 4935–4949.
- (13) Gries, W. H. A Universal Predictive Equation for the Inelastic Mean Free Pathlengths of X-Ray Photoelectrons and Auger Electrons. *Surf. Interface Anal.* **1996**, *24* (1), 38–50. h
- (14) Mondal, P. C.; Fontanesi, C.; Waldeck, D. H.; Naaman, R. Spin-Dependent Transport through Chiral Molecules Studied by Spin-Dependent Electrochemistry. *Acc. Chem. Res.* **2016**, *49* (11), 2560–2568.

- (15) Kiran, V.; Mathew, S. P.; Cohen, S. R.; Hernández Delgado, I.; Lacour, J.; Naaman, R. Helicenes - A New Class of Organic Spin Filter. *Adv. Mater.* **2016**, *28* (10), 1957–1962.
- (16) Ciureanu, M.; Mikhailenko, S. D.; Kaliaguine, S. PEM Fuel Cells as Membrane Reactors: Kinetic Analysis by Impedance Spectroscopy. *Catal. Today* **2003**, *82* (1–4), 195–206.
- (17) Simeone, F. C.; Yoon, H. J.; Thuo, M. M.; Barber, J. R.; Smith, B.; Whitesides, G. M. Defining the Value of Injection Current and Effective Electrical Contact Area for Egain-Based Molecular Tunneling Junctions. *J. Am. Chem. Soc.* **2013**, *135* (48), 18131–
- (18) Kiran, V.; Cohen, S. R.; Naaman, R. Structure Dependent Spin Selectivity in Electron Transport through Oligopeptides. *J. Chem. Phys.* **2017**, *146* (9), 092302.
- (19) Naaman, R. Chiral-Induced Spin Selectivity Effect. *J. Phys. Chem. Lett.* **2012**, *3* (16), 2178–2187.
- (20) Kettner, M.; Göhler, B.; Zacharias, H.; Mishra, D.; Kiran, V.; Naaman, R.; Fontanesi, C.; Waldeck, D. H.; Sek, S.; Pawowski, J.; Juhaniewicz, J. Spin Filtering in Electron Transport Through Chiral Oligopeptides. *J. Phys. Chem. C* **2015**, *119* (26), 14542–14547.

2.6. Experimental section

2.6.1. Equipment

X-ray Photoelectron Spectroscopy (XPS): Samples were analyzed *ex-situ* at the X-ray Spectroscopy Service at the Universidad de Alicante using a K-ALPHA Thermo Scientific spectrometer. All spectra were collected using Al K α radiation (1486.6 eV), monochromatized by a twin crystal monochromator, yielding a focused X-ray spot (elliptical in shape with a major axis length of 400 μ m) at 30 mA and 2 kV. The alpha hemispherical analyzer was operated in the constant energy mode with survey scan pass energies of 200 eV to measure the whole energy band and 50 eV in a narrow scan to selectively measure the particular elements. Charge compensation was achieved with the system flood gun that provides low energy electrons and low energy argon ions from a single source.

Luminescence. The luminescence of the complexed Tb was recorded on a PTI fluorescence instrument equipped with: a GL-3300 Nitrogen Laser, a GL-302 Dye laser and a photomultiplier detection system, over quartz cuvettes filled with 0.1M TbLBT solution, under 280 nm laser excitation. The luminescence of the SAMs was measured with an optical microscope NIKON Eclipse LV-100, equipped with a digital camera: Nikon, D7000 AF-S DX NiKKOR 18-105mm f/3.5-5.6G ED VR. An UV lamp was used as a source of the 254 nm excitation wavelength. Photoluminescence intensity was recorded by the digital camera of the optical microscope and quantified from the integrated density of pixels through the ImageJ software

Spin-Dependent Cyclic Voltammograms. LBTC grafted on 5 nm Au overlayers onto a 200 nm Ni (Ni/Au) was used as working electrode, and Pt and Ag/AgCl were used as counter and reference electrodes, respectively. Freshly prepared and deoxygenated 5 mM Fe²⁺/Fe³⁺ solutions in HEPES buffer were used as the redox mediator, and the oxidation/reduction currents were monitored under an external magnetic field of 0.35 T applied underneath the TbLBTC-modified ferromagnetic Ni.

Electrochemical Impedance Spectroscopy (EIS). The same electrochemistry setup was used in EIS, but using a Gamry 1000E and Gamry 5000E potentiostat/galvanostat controlled by Gamry software. An AC voltage of 10 mV in the frequency range of $10^0 - 10^5$ Hz at the OCP was applied. EIS data were analyzed and fitted by means of Gamry Echem Analyst v. 7.07 software.

EGaIn Measurements. Spin-Dependence by the EGaIn Method. Target molecule grafted on 5 nm Au overlaid onto a 200 nm Ni (Ni/Au) was used as the bottom electrode and EGaIn drop as the top contact. Six junctions were measured with 16 I–V curves between -0.2 and 0.2 V for a magnetic field applied of 0.35 and -0.35 T by a permanent magnet placed under the metallic surface.

Matrix-assisted laser desorption/ionization-time of flight (MALDI-TOF). Analyzed in a 5800 MALDI TOF instrument (ABSciex) in positive reflectron mode (3000 shots every position) in a mass range of $150-3000$ m/z. Previously, the plate and the acquisition method were calibrated with a CalMix solution. The analysis was carried out at the Proteomics Unit in the SCIE of the Universitat de València.

Atomic Force Microscopy (AFM). The substrates were imaged with a Digital Instruments Veeco Nanoscope IVa AFM microscope in tapping and contact mode. Silicon tips with natural resonance frequency of 300 kHz and with an equivalent constant force of 40 N/m were used. Gwyddion software was used to process the obtained images

Quartz Crystal microbalance. All the QMCD measurements were carried out with a 400 Electrochemical Quartz Crystal Microbalance (CHI Instruments) consisting of a potentiostat/galvanostat (CHI440), an external box with oscillator circuitry and EQCM cell. The Quartz crystal microbalance results were extracted from the comparison of a reference frequency (~ 8 MHz) and the recorded during the experiment.

2.6.2. *Methods*

Materials. Dimethylformamide, TbCl_3 , YCl_3 , 1-octadecanethiol and Gallium Indium Eutectic (Sigma-Aldrich) and Ethanol (Honeywell), are commercially available and were used without any further purification. Poly(L-alanine) with sequence $[\text{SHCH}_2\text{CH}_2\text{CO}-\{\text{Ala-Aib}\}_8-\text{COOH}]$ was bought from Genemed Synthesis, Inc. and the lanthanide binding tag of sequence YIDTNNDGWYEGDEL (LBT) was purchased from GenScript USA Inc.

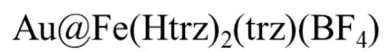
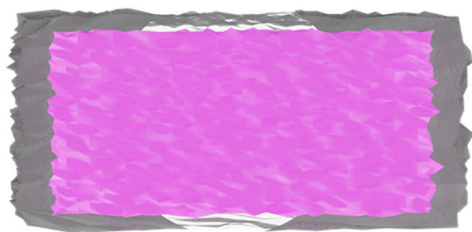
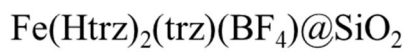
LBT solution. Aqueous buffered solutions of LBT were prepared by solving 1.9 mg of the LBT on 10 ml of buffered solution 10 mM HEPES, 1 mM TCEP, and 100 mM NaCl. After the solution was filtered and stored at -4°C .

MLBT solution. The MLBT solution was done by mixing 1 ml of the previously prepared LBT solution with 11 μL of 0.1M aqueous $\text{TbCl}_3/\text{YCl}_3$ solutions.

Au/TbLBT. The metalloprotein-based SAMs were prepared following a strategy similar to the typical growth in solution method used for alkanethiol SAMs on gold. Substrates made 200 nm thermally evaporated gold on a Si/SiO₂ wafer were washed with acid piranha to activate the metallic surface, followed by their immersed during 24 h in a 0.1 mM buffered solution of 0.1 mM TbLBT. This procedure ensures formation of a monolayer with high surface coverage.

Ni/Au/MLBT. This SAM was prepared analogously than Au/TbLBT but using a substrate of Ni (200 nm)/Au (5nm) thermally evaporated on Si/SiO₂. To grow a TbLBT SAM the substrate Ni/Au substrate was incubated in 0.1 mM TbLBT solution, while for the YLBT SAM in 0.1 mM of YLBT. Another important difference was that to avoid the Ni oxidation all the manipulation needs to be carried out under N₂ atmosphere.

PART II



3

**INTRODUCTION TO SPIN
CROSSOVER**

3.1. Spin Crossover

The spin-crossover phenomenon is one of the most spectacular examples of molecular bistability, which is displayed by some octahedrally coordinated transition metal atoms ($3d^4$ - $3d^7$).¹ In an octahedral coordination, the d orbitals of the transition metal ion split into a subset of three degenerated orbitals, t_{2g} , and a subset of two degenerated orbitals, e_g , which is known as ligand field splitting, Δ (Figure 1).² The Δ value depends on the coordinated metal, the nature of the ligand, and the distance between them. Therefore, depending on the magnitude of Δ , two configurations are possible. For energy splitting larger than the electronic repulsion, all the electrons are located in the t_{2g} levels, called the low spin state (LS). For the reverse scenario, the electrons fill the five d orbitals; according to Hund's rule, this is known as high spin state (HS). Noticeably, the physical properties of the material strongly differ depending on the spin state.¹

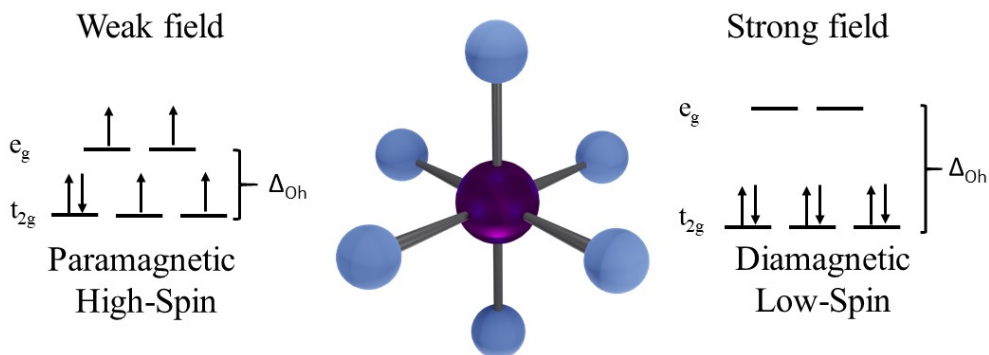


Figure 1. Scheme of the two possible electronic states for Fe^{2+} in an octahedral complex.

Remarkably, for Δ values close to the electronic repulsion, it is possible to change between the two electronic states upon applying an external stimulus

as temperature, light, or pressure.³⁻⁶ This electronic state switching is the so-called spin-crossover (SCO) or spin transition.

3.2. Types of Spin Crossover

Typically, the spin-crossover phenomenon is monitored by plotting the spin state vs the external stimulus used to induce the spin transition. The most common example is the HS fraction representation, γ_{HS} , as a function of the temperature (Figure 2). In this context, depending on the magnitude of the interaction between metallic centers, called cooperativity, different curves can be seen. For instance, a progressive transition is recorded for weakly-cooperative systems, called gradual transition, Figure 2a. In contrast, a strong cooperative system exhibits a sharp interconversion in a few degrees, called abrupt transition, Figure 2b. The last example shown in Figure 2c represents a sample with exceptionally high cooperativity, in which case the system displays hysteresis. This last scenario is the most interesting and one of the most significant aspects of the whole spin-crossover phenomenon. The appearance of hysteresis reflects bistability on the system and thus a memory effect opening the door to their use as molecular switches.

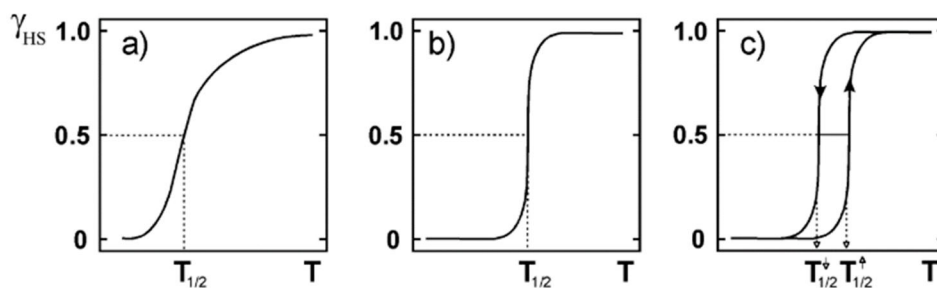


Figure 2. The main types of thermal spin transitions plotted as high spin fraction, γ_{HS} , as a function of the temperature, called: (a) gradual; (b) abrupt, and (c) hysteretic. Figure extracted from 5

3.3. Spin Crossover detection

Due to the different physical properties exhibited by both spin states, several techniques permit the study of the SCO phenomenon by plotting a physical magnitude that can be correlated with the γ_{HS} . Some of the main techniques used to study this phenomenon are explained below.

3.3.1. *Magnetic Susceptibility*

While the LS state is diamagnetic or weakly paramagnetic, the HS state exhibits a strong paramagnetism, which is clearly reflected in its molar magnetic susceptibility (χ_M).^{1,5} χ_M is calculated by measuring the magnetization of the sample under a certain magnetic field and applying eq.1. Where M is the sample magnetization, H the applied magnetic field, Mw the molecular weight of the samples, and Sw the sample weight.

$$\chi_M = \left(\frac{M}{H}\right) \cdot \left(\frac{MW}{SW}\right) \text{ eq.1}$$

Therefore, to investigate the spin transition, the temperature (T) dependence of $\chi_M \cdot T$ product is typically plotted, $\chi_M T$ vs T, which is analogue to the γ_{HS} vs T plot.

The magnetic characterization of the spin transition is exemplified by the Fe^{2+} complexes, which change from diamagnetic in LS state (S=0) to paramagnetic in the HS state (S=2). For instance, the magnetic plot of the strongly cooperative $[Fe(Htrz)_2(trz)](BF_4)$ bulk SCO polymer, where Htrz is the ligand 1,2,4-triazole and trz the deprotonated triazole, is shown in Figure 3. As we can see, this compound exhibits a broad thermal hysteresis, which is proof of its high cooperativity. Due to the Fe^{2+} LS diamagnetic nature, a 0 $cm^3 \cdot mol^{-1} \cdot K$ $\chi_M T$ value is expected at low temperatures. Nonetheless, we can

see a value close to $0.2 \text{ cm}^3 \cdot \text{mol}^{-1} \cdot \text{K}$ at 300 K. This paramagnetic residue comes from the iron atoms at the surface, which have an incomplete coordination sphere, presenting a weaker ligand field splitting at the same time that are more susceptible to oxidize, giving rise to Fe^{2+} HS or paramagnetic Fe^{3+} impurities.

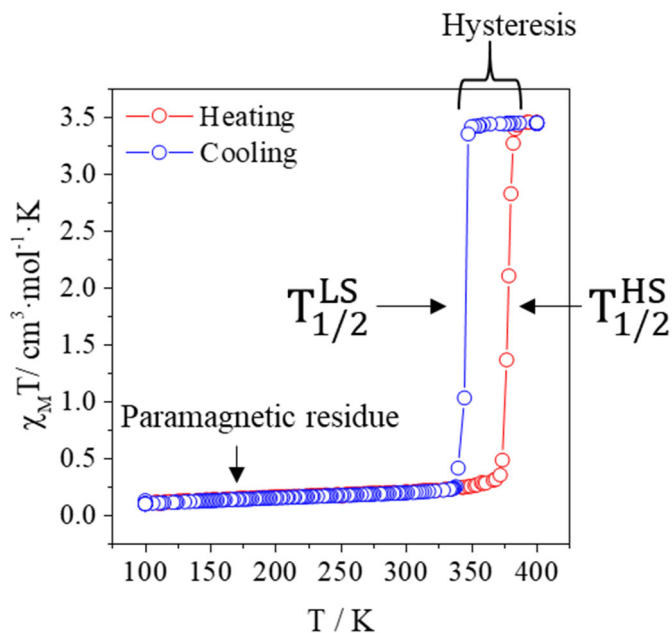


Figure 3. $\chi_M T$ plot as a function of the temperature for $[\text{Fe}(\text{Htrz})_2(\text{trz})](\text{BF}_4)$ bulk material, recorded at $1 \text{ K} \cdot \text{min}^{-1}$.

When the $\chi_M T$ is recorded during the heating process, the paramagnetic residue remains similar till $\sim 380 \text{ K}$. Around this temperature, the $\chi_M T$ value increases abruptly because the transition from diamagnetic LS to paramagnetic HS state, exhibiting a value of $\sim 3.5 \text{ cm}^3 \cdot \text{mol}^{-1} \cdot \text{K}$ at 400 K. The transition temperature accounted by $T_{1/2}^{\text{HS}}$, is defined as the temperature at which half of the iron centers have reached the HS state in the heating mode.

Later, during the cooling process, an abrupt decrease in $\chi_M T$ occurs at ~340 K. This is provoked by the recovery of the LS state. The transition temperature from HS to LS is defined by $T_{1/2}^{LS}$, which is the temperature at which half of the iron centers are still in HS state in the cooling process.

3.3.2. Vibrational Spectroscopy

Due to the different bond lengths in each spin state, their vibrational energy differs. Therefore, by infrared or Raman spectroscopy, it is possible to distinguish the spin state.^{1,5} For instance, Figure 4 shows the Raman spectrum of the SCO compound $[\text{Fe}(\text{Htrz})_2(\text{trz})](\text{BF}_4)$ as a function of the temperature. As can be seen, the vibrational modes of the Fe-N bond are at lower wavenumber in the HS state, Figure 4 inset.

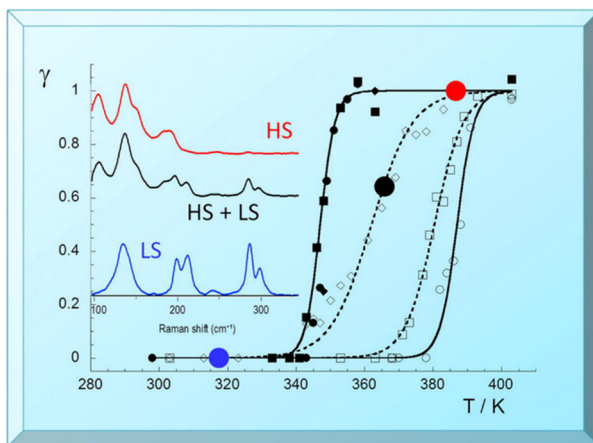


Figure 4. Raman spectra of the SCO compound $[\text{Fe}(\text{Htrz})_2(\text{trz})](\text{BF}_4)$ at different temperatures showing the different spin states. Extracted from reference 7

3.3.3. Heat Capacity

The SCO is a first-order transition,^{8,9} which means that the spin change involves an absorption or heat release; thus, calorimetric measurements can

be used to detect the spin transition.^{1,5} In this context, the LS to HS crossover absorbs heat while releasing for the reverse scenario. Therefore, plotting the first derivative of the heat flow vs the temperature is possible to extract the transition temperatures from the maximum ($T_{1/2}^{LS}$) and the minimum ($T_{1/2}^{HS}$) of the plot. This technique is called Differential Scanning Calorimetry (DSC).

For instance, the $[\text{Fe}(\text{Htrz})_2(\text{trz})](\text{BF}_4)$ DSC plot is shown in Figure 5. Two clear peaks can be discerned during the heating (red) and the cooling (blue), associated with the endothermic and exothermic processes occurring for the spin transition. The endothermic peak is related to the transition from LS to HS, while the exothermic peak is assigned to the LS recovery.

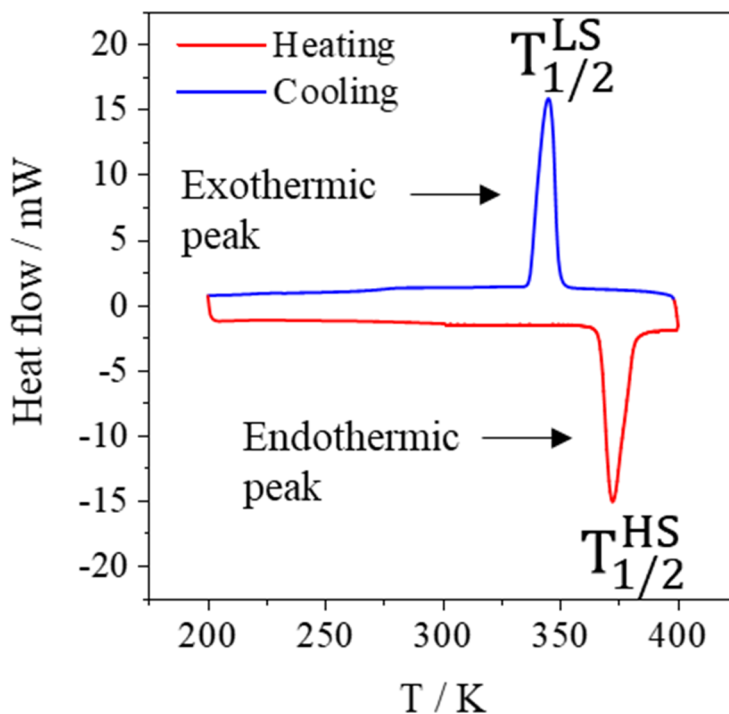


Figure 5. DSC curves in the heating (red) and cooling mode (blue) of $[\text{Fe}(\text{Htrz})_2(\text{trz})](\text{BF}_4)$, recorded at $10 \text{ K}\cdot\text{min}^{-1}$.

3.3.4. Optical properties

The spin state, in most cases, defines the colour of the compound.^{1,10} An example of this is accounted for the different UV-VIS spectra of the Fe^{2+} SCO compound, $[\text{Fe}(\text{Htrz})_3](\text{ClO}_4)$, in both spin states, Figure 6. The LS state shows a band around 550 nm, which shifts to 800 nm in the HS state. Even more, the real part of the refractive index between both spin states varies in the range between $\Delta n = 0.01 - 0.1$.^{8,9,11} These facts allow the determination of the spin state by monitoring the optical properties of the material.

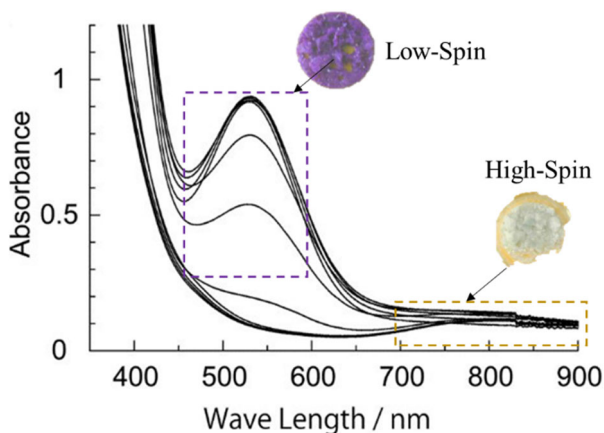


Figure 6. UV-spectra of the spin-crossover compound $[\text{Fe}(\text{Htrz})_3](\text{ClO}_4)$ suspended in 1,2,4-trichlorobenzene at different temperatures. Figures extracted from reference 10,12

3.3.5. Electrical response

SCO materials are known to display a spin-state dependence electrical conductivity.^{13,14} This has been widely investigated to characterize their spin state. Thus, it is well known that generally, these materials exhibit a more conductive LS than HS state, Figure 7.¹⁵ Interestingly, this spin-dependent electrical response has permitted the development of electrical devices, where the SCO compound is used to convert the external stimuli that induce the

transition into an electrical output.^{13,16} However, the major drawback for their electrical use as switchers is the highly insulating nature of many of these coordination polymers, making them nearly perfect dielectrics.

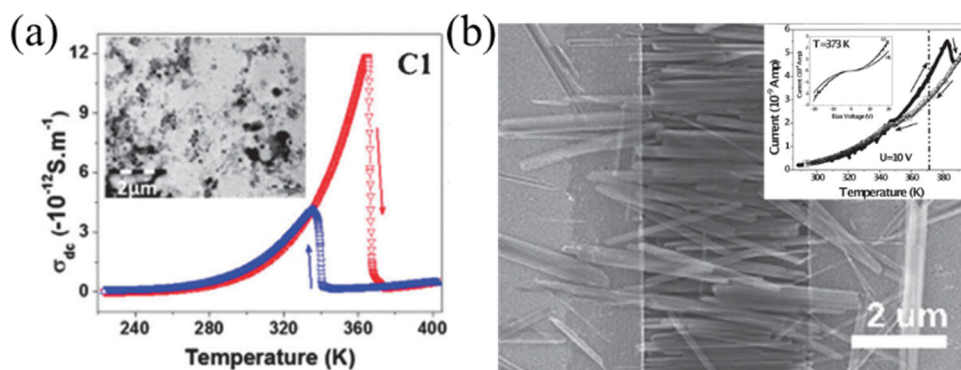


Figure 7. Conductivity as a function of the temperature for nanoparticles of $[\text{Fe}(\text{Htrz})_2(\text{trz})](\text{BF}_4)$ (a), nanorods of the same material aligned between interpenetrated electrodes (b). Extracted from 15,17.

3.3.6. X-ray Structural Studies

Generally, metal-ligand bonds of complexes in HS state are substantially larger than those in LS. This is due to the simple fact that in the HS, two of the six d electrons occupy the e_g orbitals, which are antibonding, whereas, in the LS state, all six d-electrons reside in the essentially nonbonding t_{2g} orbitals. For instance, the Fe-N bond length in the LS ranges between 1.95-2.00 Å, while in the HS state, it is around 2.12-2.18 Å. Thus, commonly, in the HS state the SCO systems display ~ 0.2 Å longer bonds than in the LS states.⁵ Therefore, upon the spin transition from LS to HS, the metal to ligand distance increases, changing the SCO total volume. This modulation depends on the material structure, ranging between 3-11%.^{5,18,19}

Due to this enlargement, the metal coordination sphere changes may provoke a significant crystal lattice modification. As Figure 8a,b show, in the

X-Ray powder diffraction spectra, the shape and peak positions of the already mentioned $[\text{Fe}(\text{Htrz})_2(\text{trz})](\text{BF}_4)$ system differ depending on the spin state. Hence, this permits the SCO investigation by monitoring its crystal structure as a function of the temperature (Figure 8a,b). This exciting property has been widely employed to transduce thermal, optical, or chemical stimuli into useful mechanical work, making these ideal materials as sources of mechanical strain, Figure 8c,d.^{20–24}

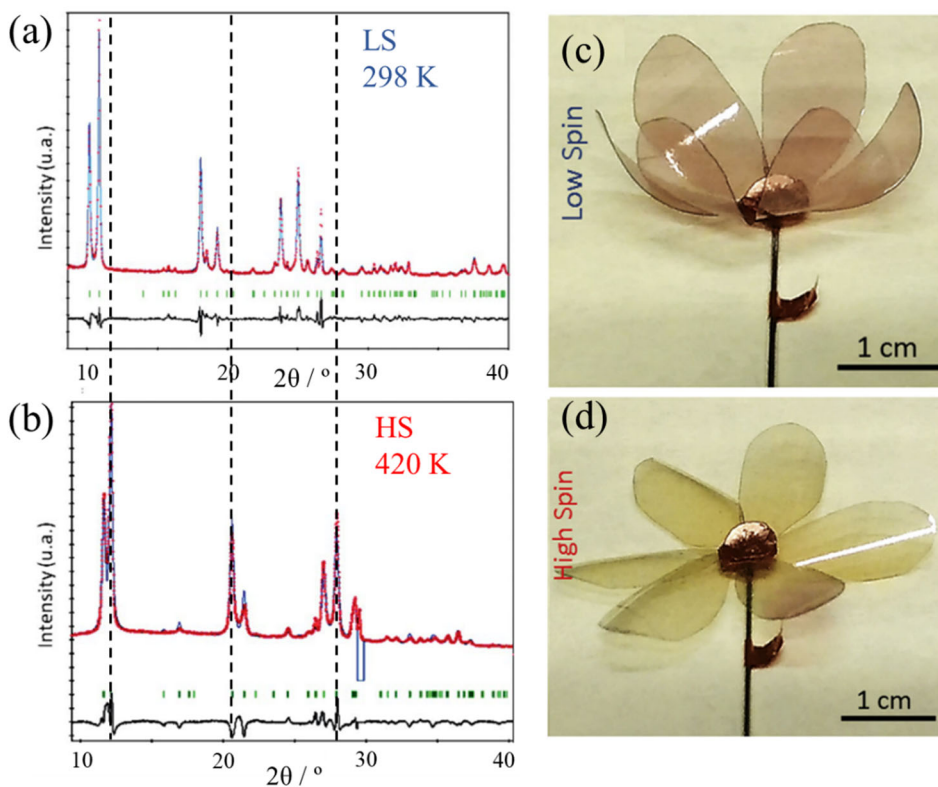


Figure 8. (a,b) $[\text{Fe}(\text{Htrz})_2(\text{trz})](\text{BF}_4)$ X-Ray powder diffraction pattern in the LS state at 298 K and the HS state at 420 K. The red dots represent the experimental data, while the theoretical fitting is plotted in blue. (c,d) Artificial muscles made with the same SCO compound over a plastic flower. The flower opens or closes the petals depending on the spin state. Figure extracted from 19,23.

3.4. Bibliography

- (1) Halcrow, M. A. *Spin-Crossover Materials: Properties and Applications*; 2013.
- (2) Hauser, A. Ligand Field Theoretical Considerations. **2004**, 49–58.
- (3) Gütllich, P.; Garcia, Y.; Woike, T. *Photoswitchable Coordination Compounds*; 2001; Vol. 219–221.
- (4) Létard, J.-F.; Guionneau, P.; Goux-Capes, L. Spin Crossover in Transition Metal Compounds III. **2004**, *1*, 221–249.
- (5) Chemistry, C. *Spin Crossover in Transition Metal Compounds I*; 2004.
- (6) Hauser, A. Spin Crossover in Transition Metal Compounds II. **2004**, 155–198.
- (7) Guillaume, F.; Tobon, Y. A.; Bonhommeau, S.; Létard, J. F.; Moulet, L.; Freysz, E. Photoswitching of the Spin Crossover Polymeric Material [Fe(Htrz) 2(Trz)](BF₄) under Continuous Laser Irradiation in a Raman Scattering Experiment. *Chem. Phys. Lett.* **2014**, *604*, 105–109.
- (8) Loutete-Dangui, E. D.; Codjovi, E.; Tokoro, H.; Dahoo, P. R.; Ohkoshi, S. I.; Boukheddaden, K. Spectroscopic Ellipsometry Investigations of the Thermally Induced First-Order Transition of RbMn [Fe (CN) 6]. *Phys. Rev. B - Condens. Matter Mater. Phys.* **2008**, *78* (1), 1–9.
- (9) Boukheddaden, K.; Loutete-Dangui, E. D.; Koubaa, M.; Eypert, C. First-Order Phase Transitions of Spin-Crossover and Charge Transfer Solids Probed by Spectroscopic Ellipsometry. *Phys. Status Solidi Curr. Top. Solid State Phys.* **2008**, *5* (5), 1003–1006.
- (10) Gütllich, P.; Gaspar, A. B.; Garcia, Y. Spin State Switching in Iron Coordination Compounds. *Beilstein J. Org. Chem.* **2013**, *9* (li), 342–391.
- (11) Loutete-Dangui, E. D.; Varret, F.; Codjovi, E.; Dahoo, P. R.; Tokoro, H.; Ohkoshi, S.; Eypert, C.; Létard, J. F.; Coanga, J. M.; Boukheddaden, K. Thermal Spin Transition in [Fe (N H₂ -Trz)₃] Br₂ Investigated by Spectroscopic Ellipsometry. *Phys. Rev. B - Condens. Matter Mater. Phys.* **2007**, *75* (18), 1–7.

- (12) Tanaka, D.; Aketa, N.; Tanaka, H.; Tamaki, T.; Inose, T.; Akai, T.; Toyama, H.; Sakata, O.; Tajiri, H.; Ogawa, T. Thin Films of Spin-Crossover Coordination Polymers with Large Thermal Hysteresis Loops Prepared by Nanoparticle Spin Coating. *Chem. Commun.* **2014**, 50 (70), 10074–10077.
- (13) Molnár, G.; Rat, S.; Salmon, L.; Nicolazzi, W.; Bousseksou, A. Spin Crossover Nanomaterials: From Fundamental Concepts to Devices. *Adv. Mater.* **2018**, 30 (5), 1–23.
- (14) Lefter, C.; Davesne, V.; Salmon, L.; Molnár, G.; Demont, P.; Rotaru, A.; Bousseksou, A. Charge Transport and Electrical Properties of Spin Crossover Materials: Towards Nanoelectronic and Spintronic Devices. *Magnetochemistry* **2016**, 2 (1), 18.
- (15) Rotaru, A.; Gural'skiy, I. A.; Molnár, G.; Salmon, L.; Demont, P.; Bousseksou, A. Spin State Dependence of Electrical Conductivity of Spin Crossover Materials. *Chem. Commun.* **2012**, 48 (35), 4163–4165.
- (16) Lefter, C.; Tan, R.; Tricard, S.; Dugay, J.; Molnár, G.; Salmon, L.; Carrey, J.; Rotaru, A.; Bousseksou, A. On the Stability of Spin Crossover Materials: From Bulk Samples to Electronic Devices. *Polyhedron* **2015**, 102, 434–440.
- (17) Rotaru, A.; Dugay, J.; Tan, R. P.; Gural'skiy, I. A.; Salmon, L.; Demont, P.; Carrey, J.; Molnár, G.; Respaud, M.; Bousseksou, A. Nano-Electromanipulation of Spin Crossover Nanorods: Towards Switchable Nanoelectronic Devices. *Adv. Mater.* **2013**, 25 (12), 1745–1749.
- (18) Urakawa, A.; Van Beek, W.; Monrabal-Capilla, M.; Galán-Mascarós, J. R.; Palin, L.; Milanese, M. Combined, Modulation Enhanced X-Ray Powder Diffraction and Raman Spectroscopic Study of Structural Transitions in the Spin Crossover Material [Fe(Htrz)₂(Trz)](BF₄). *J. Phys. Chem. C* **2011**, 115 (4), 1323–1329.
- (19) Grosjean, A.; Négrier, P.; Bordet, P.; Etrillard, C.; Péchev, S.; Lebraud, E.; Létard, J.; Grosjean, A.; Négrier, P.; Bordet, P.; Etrillard, C.; Mondieig, D. Crystal Structures and Spin Crossover in the Polymeric Material [Fe(Htrz)₂(Trz)](BF₄) Including Coherent-Domain Size Reduction Effects *European Journal of Inorganic Chemistry*, 2013(5-6), 796-802.

-
- (20) Manrique-Juárez, M. D.; Rat, S.; Salmon, L.; Molnár, G.; Quintero, C. M.; Nicu, L.; Shepherd, H. J.; Bousseksou, A. Switchable Molecule-Based Materials for Micro- and Nanoscale Actuating Applications: Achievements and Prospects. *Coord. Chem. Rev.* **2016**, *308*, 395–408.
- (21) Manrique-Juarez, M. D.; Rat, S.; Mathieu, F.; Saya, D.; Séguy, I.; Leïchlé, T.; Nicu, L.; Salmon, L.; Molnár, G.; Bousseksou, A. Microelectromechanical Systems Integrating Molecular Spin Crossover Actuators. *Appl. Phys. Lett.* **2016**, *109* (6).
- (22) Shepherd, H. J.; Gural'Skiy, I. A.; Quintero, C. M.; Tricard, S.; Salmon, L.; Molnár, G.; Bousseksou, A. Molecular Actuators Driven by Cooperative Spin-State Switching. *Nat. Commun.* **2013**, *4*, 1–9.
- (23) Manrique-Juárez, M. D.; Mathieu, F.; Laborde, A.; Rat, S.; Shalabaeva, V.; Demont, P.; Thomas, O.; Salmon, L.; Leichle, T.; Nicu, L.; Molnár, G.; Bousseksou, A. Micromachining-Compatible, Facile Fabrication of Polymer Nanocomposite Spin Crossover Actuators. *Adv. Funct. Mater.* **2018**, *28* (29), 1–7.
- (24) Dugay, J.; Giménez-Marqués, M.; Venstra, W. J.; Torres-Cavanillas, R.; Sheombarsing, U. N.; Manca, N.; Coronado, E.; Van Der Zant, H. S. J. Sensing of the Molecular Spin in Spin-Crossover Nanoparticles with Micromechanical Resonators. *J. Phys. Chem. C* **2019**, *123* (11), 6778–6786.

4

Downsizing $[\text{Fe}(\text{Htrz})_2(\text{trz})](\text{BF}_4)$ Core@Shell Nanoparticles

R. Torres-Cavanillas, L. Lima-Moya, F. D. Tichelaar, H.W. Zandbergen, M. Giménez-Marqués, E. Coronado. *Dalton Transactions* **2019**, 48, 15465-15469.

4.1. Motivation and goals

The interest in miniaturizing hybrids spin-crossover nanostructures have been increasing since the discovery of the first SCO NPs in 2007,¹ Figure 1. This interest in the possible applications of these nanoswitchers in molecular switching nanodevices.

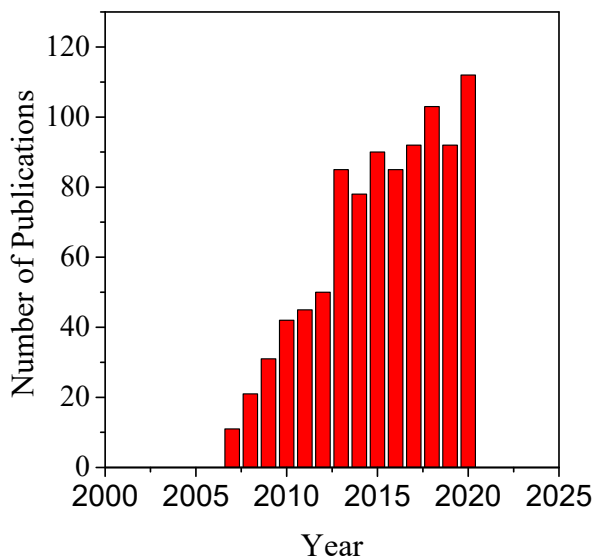


Figure 1. Publications of nanostructured SCO since 2007.

In chapter 4 we focus on the study of the synthetic parameters that control the size of the $[\text{Fe}(\text{Htrz})_2(\text{trz})](\text{BF}_4)@\text{SiO}_2$ core@shell nanostructure. Two main goals were pursued in this thesis: (1) Unravel the most relevant parameters that influence the dimensions of synthesized nanoparticles. In order to fine-tune their size further than the already reported for this system. (2) Incorporation of thin silica shells, keeping the protection provided by the silica, while minimizing the isolation of the core.

4.2. Introduction

The control of the dimensionality of SCO materials has proven to be challenging due to its rapid formation and precipitation as microparticles. The scenario gets even more complex due to the drastic effect of the downsizing over the spin transition. It has been broadly observed that the cooperativity decreases as the size of the nanostructures does, shortening or even quenching their hysteretical behaviour.² Clear examples of the cooperativity dependence with the miniaturization can be seen in Figure 2, where two SCO materials were magnetically characterized for nanoparticles (NPs) of different sizes.^{3,4} For Fe(pz)[Pt(CN)₄], where pz is pyrazine (Figure 2a), the downsizing provoked the complete loss of cooperativity between metallic centers.⁴ For Fe(Htrz)₂(trz)(BF₄) (Figure 2 b), the hysteresis was maintained but decreasing its broadness.³

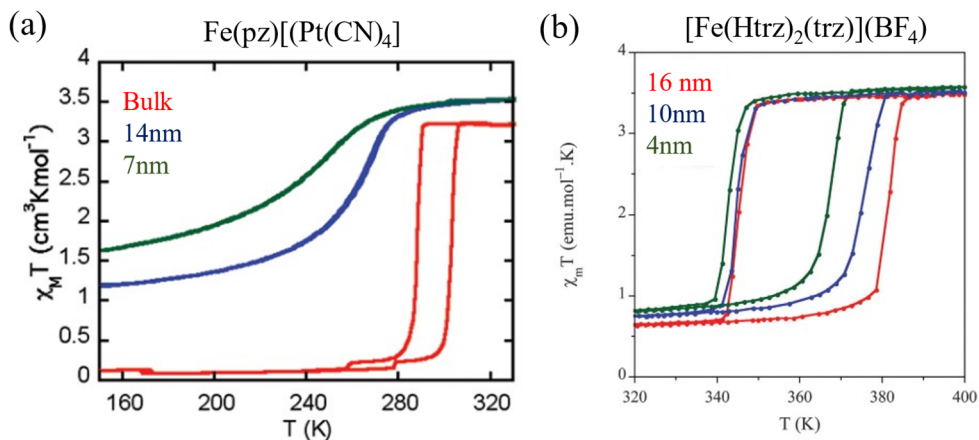


Figure 2. $\chi_M T$ plot as function of the temperature for Fe(pz)[Pt(CN)₄] (a) and [Fe(Htrz)₂(trz)](BF₄) (b) of different sizes. Extracted from reference 3,4

Even more, the downsizing also increases the instability of these molecular materials, making them more susceptible to oxidize or suffer from fatigue after successive spin transitions. For this reason, the protection of the

nanostructures with surfactants, polymers, or rigid shells has been proposed as a manner to increase the resilience of SCO NPs.^{5–10}

4.2.1. $[\text{Fe}(\text{Htrz})_2(\text{trz})](\text{BF}_4)$

We selected the $[\text{Fe}(\text{Htrz})_2(\text{trz})](\text{BF}_4)$ system as SCO material because it is one of the most studied and has proved to be very robust, versatile, and with a considerable modulation of its physical properties upon the spin transition. It exhibits one of the strongest cooperativities recorded for SCO compounds, having a hysteresis of 40 K above room temperature (between 380 K–340 K). As Figure 2b shows, even if the cooperativity is affected by the downsizing, it is partially maintained even for nanostructures of 4 nm.^{1,3,11} These features make it an ideal system to obtain low-dimensional nanostructures that preserve the spin transition.

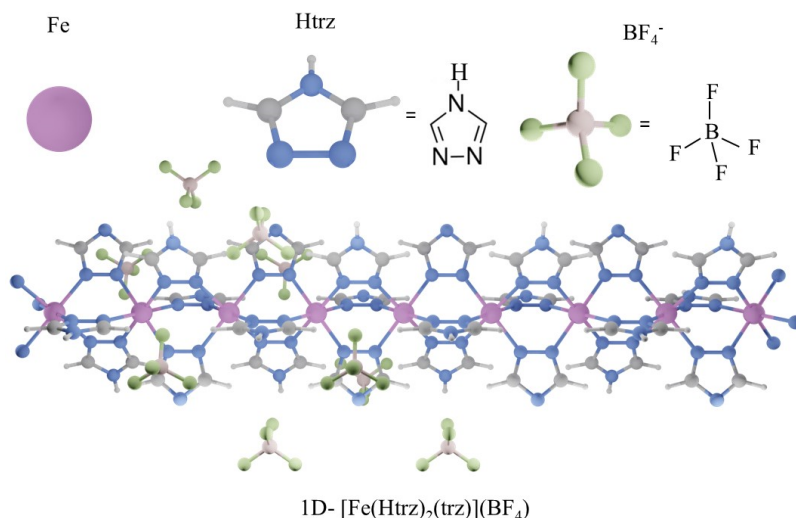


Figure 3. Structure of the 1D $[\text{Fe}(\text{Htrz})_2(\text{trz})](\text{BF}_4)$ polymer, N (blue), C (gray), H (white), Fe (purple), F (green) and B (beige).

The underlying reason for this particular strong cooperativity seems to relay in its low dimensional structure. As can be seen in Figure 3, it is based

on infinite 1D chains of Fe ions, strongly linked via 2 triazole (Htrz) and 1 triazolate (trz) bridges, while the BF₄⁻ electrostatically packs the chains. Due to the rigidity of the triazole bridges in one dimension, the metallic centers are strongly connected.^{12,13} This accounts for the broad hysteresis maintained even in nanostructures.

Remarkably, by changing the triazole ligand for another triazole derivative, like 4-Amino-4H-1,2,4-triazole (NH₂trz), the cooperativity and transition temperatures can be tuned. For instance, in Figure 4 the $\chi_M T$ vs T of the compound [Fe(Htrz)_{3-3x}(NH₂trz)_{3x}](BF₄)₂ (with the full range between 3x = 0-2) is shown. As can be seen, the transition temperature shifts to lower values as the amount of NH₂trz increases. That is so because of the lower field splitting caused by the NH₂trz compared with the Htrz. This proves the chemical versatility of this particular SCO family.

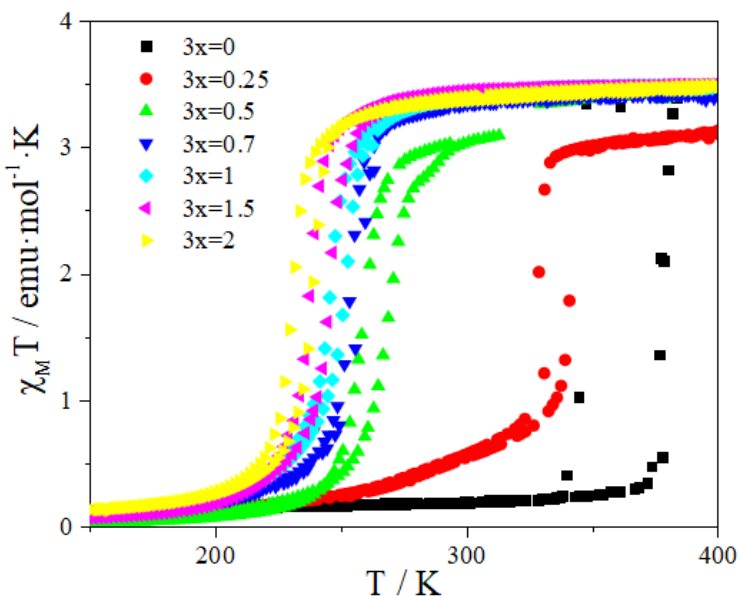


Figure 4. $\chi_M T$ plot as function of the temperature for bulk [Fe(Htrz)_{3-3x}(NH₂trz)_{3x}](BF₄)₂, with 3x from 0 to 2.

4.2.2. *[Fe(Htrz)₂(trz)](BF₄) nanoparticles*

From the point of view of its nanostructuration different approaches have been developed over the years to limit the $[\text{Fe}(\text{Htrz})_2(\text{trz})](\text{BF}_4)$ size, e.g.: the use of matrices or templates to confine the growth;^{6,14,15} direct synthesis in high concentration;^{16,17} or the most common reverse micelle technique.^{1,3} During this thesis, this last approach has been employed due to its simplicity, versatility, and easy NPs size tuning by acting over some crucial synthetic parameters.

4.2.3. *Reverse micelle technique*

The reverse micelle protocol consists of blending two separate microemulsions of the metal and the ligand to use the micelles of the microemulsions as nanoreactors, Figure 5.¹⁸⁻²⁰ The microemulsions are formed as follows. Firstly, two solutions made of a surfactant (and sometimes a cosurfactant to stabilize the micelles) and an organic solvent are prepared, called the organic phase. Later, aqueous solutions of the ligand and the metal are independently prepared, also called the aqueous phases. Once the solutions are ready, the metal solution is added into one of the organic phases and the ligand solution into the other. In this step, due to the surfactant amphoteric character, the hydrophilic head stays in contact with the water from the aqueous phase, while the hydrophobic tail points to the organic solvent. This leads to the formation of two microemulsions containing water micelles with the metal or the ligand inside, Figure 5i.

Finally, the two microemulsions are mixed. When the two micelles collide, the water from one flows inside the other, mixing their content. When this exchange occurs with micelles containing metal and ligand, both precursors

are in contact, and the reaction begins. This step is called micellar exchange (Figure 5ii). Then due to the reaction of the ligand and the metal in the micellar water pool, the material is formed inside the micelle, Figure 5iii. In this way, the NPs size is limited by the water pool diameter.

Therefore, by playing with the parameters which determine the micelle size and amount of material it is possible, not only to obtain nanostructures of [Fe(Htrz)₂(trz)](BF₄), but also to fine-tune their sizes. Therefore, the main parameters that can be controlled are reaction time, temperature, precursors, micellar composition, and the molar ratio between water:surfactant (called ω parameter).

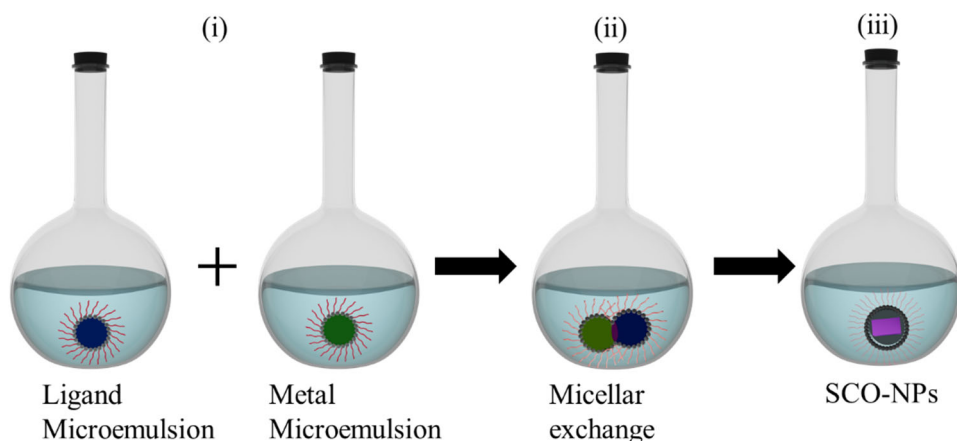


Figure 5. Scheme of the experimental process for the synthesis of SCO NPs by the reverse micelle approach. First, the microemulsions of ligand and metal are formed by adding an aqueous solution on an organic phase with a surfactant (i). Later both microemulsions are mixed, beginning the micellar exchange (ii). Finally, the reaction leads to the NPs formation (iii).

4.1.3.a. Micellar composition

The surfactant selected, as well as the organic solvent and the presence or absence of a co-surfactant, determines the size and stability of the microemulsion; hence, the size and morphology of the resulting NPs.

For instance, using the same synthetic parameters with Triton X-100, a derivative of polyethylene glycol, (hexanol as cosurfactant and cyclohexane as organic phase) or AOT as surfactant (octane as organic phase), NPs with completely different sizes and morphologies can be obtained. As transmission electron microscopy (TEM) images show when using Triton X-100 NPs of ~300 nm are synthesized, while with AOT the size is limited to ~30 nm, Figure 6a.

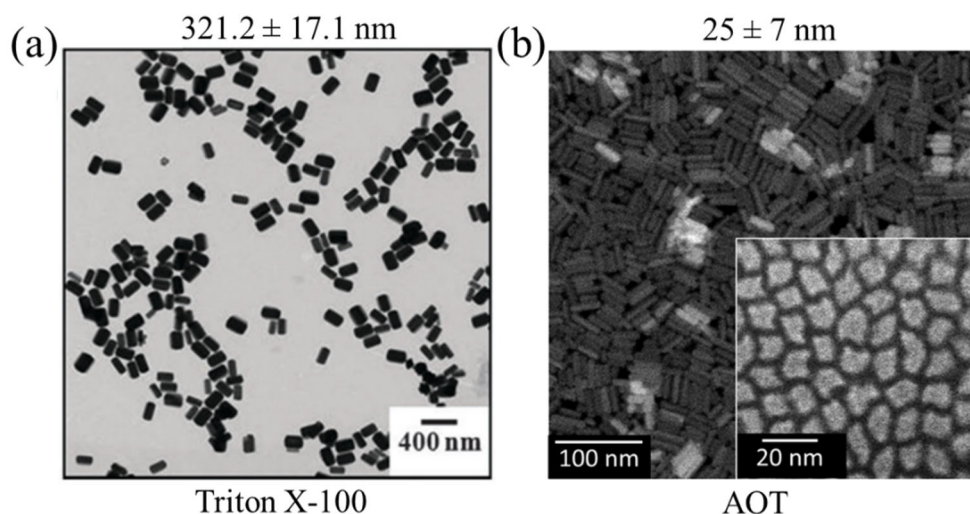


Figure 6. TEM images of $[Fe(Htrz)_2(trz)](BF_4)$ NPs synthesized under similar conditions but using Triton X-100 (a) or AOT (b) microemulsions. Extracted from 3,21

4.1.3.b. Reaction time and temperature

Increasing the reaction time, the number of micellar exchanges increases, obtaining bigger NPs, Figure 7.²² The temperature during the synthesis is another crucial factor, which linearly increases the particle length, Figure 7.²²

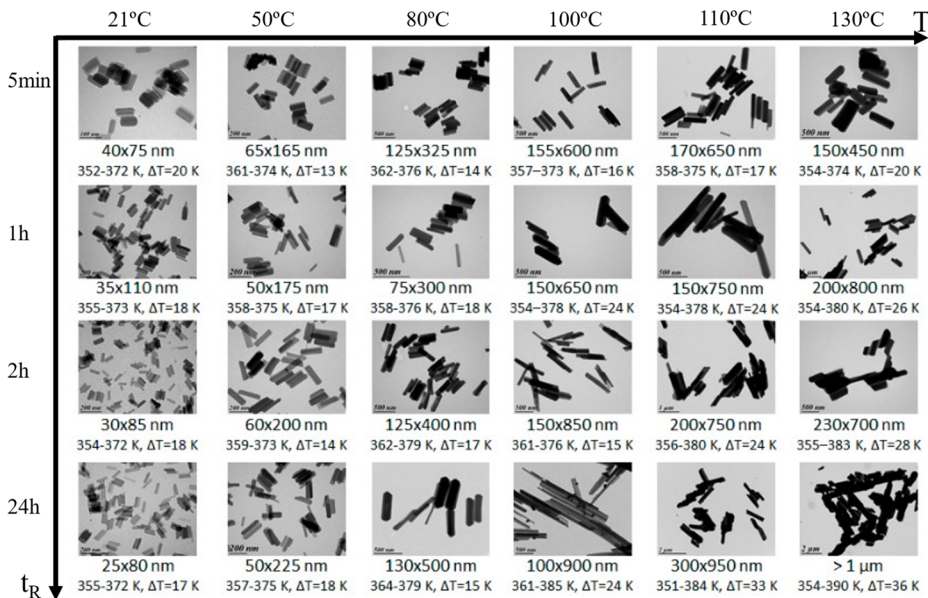


Figure 7. TEM images of [Fe(Htrz)₂(trz)](BF₄) NPs synthesized at different temperatures and reaction times. Adapted from 22

4.1.3.c. Concentration of precursors

The concentration of metal (Fe²⁺) and ligand (Htrz) also affects the resulting NPs size. A larger concentration means more nucleation centers, hence, smaller NPs, while the reverse scenario produces bigger NPs, Figure 8.²¹

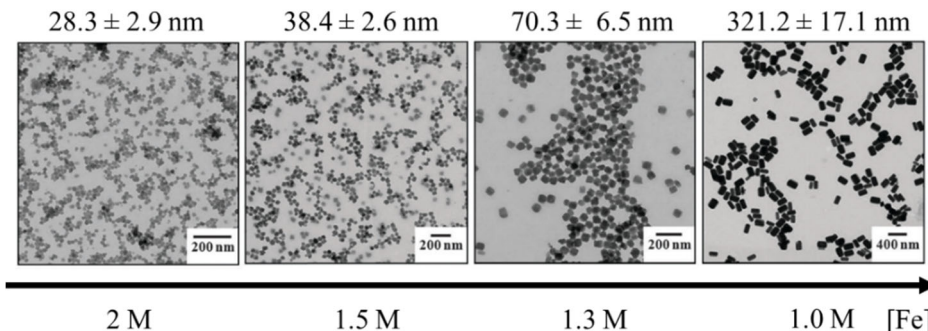


Figure 8. TEM images of [Fe(Htrz)₂(trz)](BF₄) NPs synthesized at different concentrations of precursors. Figure extracted from 21

4.1.3.d. ω parameter

By playing with the ratio of water/surfactant, it is also possible to modulate the water pool size, which contains the precursors;^{3,23} hence, the size of the final NPs. An example of this was the synthesis of $[\text{Fe}(\text{Htrz})_2(\text{trz})](\text{BF}_4)$ NPs with AOT as the surfactant. By varying ω from 5 to 9, NPs with sizes from 4 to 16 nm are obtained, Figure 9.³

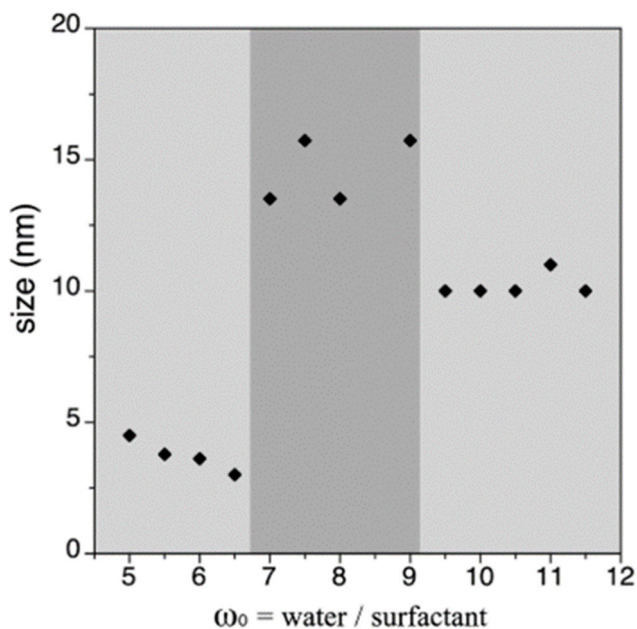


Figure 9. Plot of the $[\text{Fe}(\text{Htrz})_2(\text{trz})](\text{BF}_4)$ NPs size synthesized with AOT at different ω ratios. Figure extracted from 3

4.2.4. $[\text{Fe}(\text{Htrz})_2(\text{trz})](\text{BF}_4)@\text{SiO}_2$

As pointed out before, some disadvantages arise with the downsizing of SCO systems, such as the quenching of the cooperativity and their chemical instability.^{2,24} To overcome these limitations, in 2011, Mallah et al. covered $[\text{Fe}(\text{pz})(\text{Pt}(\text{CN})_4)]$ 10 nm NPs with a thin silica shell (3 nm) to increase their

stiffness and maintain the cooperativity in small nanostructures, increasing at the same time their chemical robustness, Figure 10a.⁸

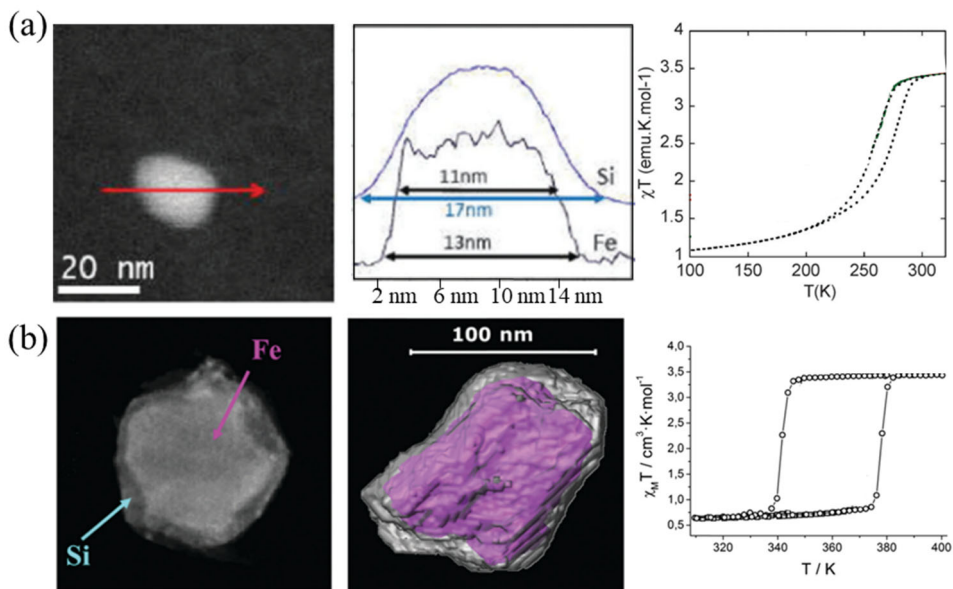


Figure 10. TEM images (left), energy dispersive X-ray profile, top, and tomography, bottom, (middle), and $\chi_M T$ plot of $[\text{Fe}(\text{pz})\text{Pt}(\text{CN})_4]@\text{SiO}_2$ (a) and $[\text{Fe}(\text{Htrz})_2(\text{trz})](\text{BF}_4)@\text{SiO}_2$ NPs (b) respectively. Figures extracted from 15,8

The silica shell was grown by adding tetraethylorthosilicate (TEOS) in the regular reverse micelle technique. TEOS is a well-known silica precursor that polymerizes in the presence of water, nucleating inside the micelle on top of the SCO NPs. As expected, the cooperativity of this system, which is destroyed for NPs smaller than 20 nm, is maintained in the silica-covered compound, Figure 10a.^{25,26}

Later, following a similar approach, Herrera and coworkers grew the same shell over $[\text{Fe}(\text{Htrz})_2(\text{trz})](\text{BF}_4)$ NPs. As a result, NPs ranging from 100 to 50 nm were synthesized with a 12 nm thick silica shell, Figure 10b.^{5,21} Although the shell provides some advantages,²⁷ some drawbacks need to be improved.

Thus, in these NPs the SCO is isolated from their environment, diminishing their potential as active component in electronic devices or mechanical actuators. In this matter, thinner shells are desirable.

4.3. Results and discussion

Herein, we describe the synthesis and size fine-tuning of the core-shell NPs $\text{Fe}(\text{Htrz})_2(\text{trz})(\text{BF}_4)@\text{SiO}_2$, named $\text{SCO}@\text{SiO}_2$, Figure 11. While Herrera et al. succeeded in the obtention of NPs of 50 nm with a thick silica shell (~12 nm), we have further explored the synthesis of smaller NPs with a thinner shell. This may increase the interaction of the core spin state with its environment without compromising its chemical stability.



Figure 11. (a) 1D structure of the $\text{Fe}(\text{Htrz})_2(\text{trz})(\text{BF}_4)$. (b) Scheme of the NPs $\text{Fe}(\text{Htrz})_2(\text{trz})(\text{BF}_4)@\text{SiO}_2$ synthesized in this thesis with different sizes and morphologies, ranging from nanorods to nanocubes.

The synthesis of these core@shell NPs was performed by slightly modifying the already mentioned reverse micelle technique, section 4.2.3. In this case, we blended two different microemulsions of $\text{Fe}(\text{BF}_4)_2$ (metal) and 1,2,4-Triazole (ligand), with the silica precursor TEOS, forming the $\text{Fe}(\text{Htrz})_2(\text{trz})(\text{BF}_4)@\text{SiO}_2$ inside the micelles. The microemulsions were formed by adding the aqueous solution of the metal or ligand into a mixture of cyclohexane (organic medium), hexanol (co-surfactant), triton X-100 (surfactant), and TEOS (silica precursor), called the organic phase. After the microemulsion was formed, the TEOS migrates inside the micelles and

polymerizes, producing SiO_2 , which wraps the on growing NPs, Figure 12. It must be noticed that in the initial recipe, the TEOS was added to the aqueous phase. However, we decided to add it in the organic phase to reduce the silica polymerization kinetics; hence, the shell thickness decreases to few nm (as the polymerization requires contact with the water of the aqueous phase).

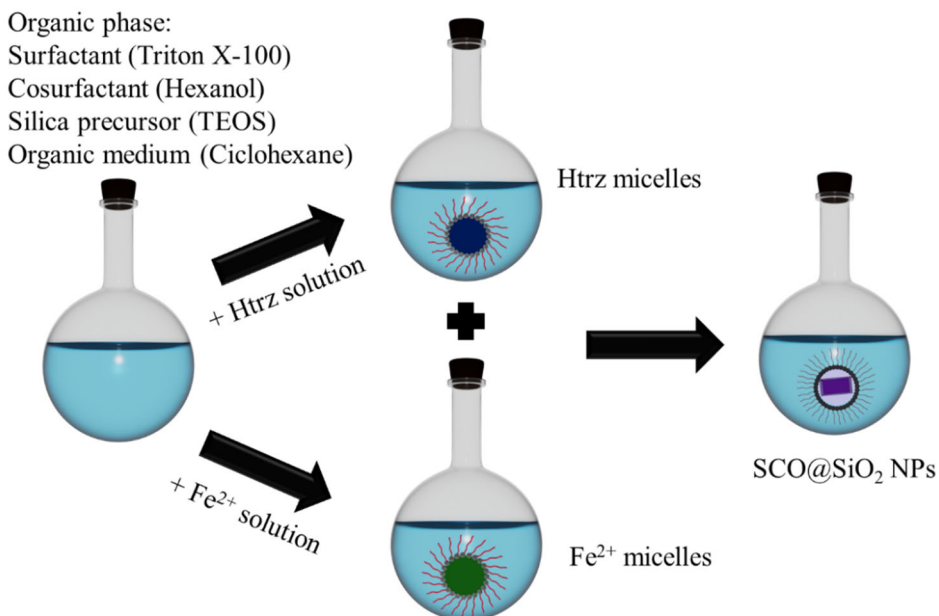


Figure 12. Scheme of the reverse micelle technique to synthesize SCO NPs.

4.3.1. Tuning the $\text{Fe}(\text{Htrz})_2(\text{trz})(\text{BF}_4)$ @ SiO_2 NPs size

To tune the size of the resulting NPs, we decided to play with the reaction time, the precursor concentration and the ω parameter. We chose these parameters because they are easily manipulated and modulates the size of the NPs in a broad range.

In this context, there were two different synthetic scenarios, i.e.: (i) The decrease of the reaction time and the precursor concentration and (ii) the decrease of water/surfactant ratio. In the first case, we could obtain NPs of 90

nm (SCO@SiO₂-1) or of 60 nm (SCO@SiO₂-2). In the second case, by fixing ω to 9 or 5, and keeping the rest of the synthetic parameters as in the synthesis of SCO@SiO₂-2, the NP size was further reduced to ~40 (SCO@SiO₂-3) and ~30 nm (SCO@SiO₂-4) respectively. All the synthetic parameters and the resulting sizes are summarized in table 1. It is important to note that attempts to used $\omega < 5$ resulted in unstable micellar suspensions.

The size of the resulting NPs was explored by Dynamic Light Scattering (DLS) and by TEM, Figure 13 and 14.

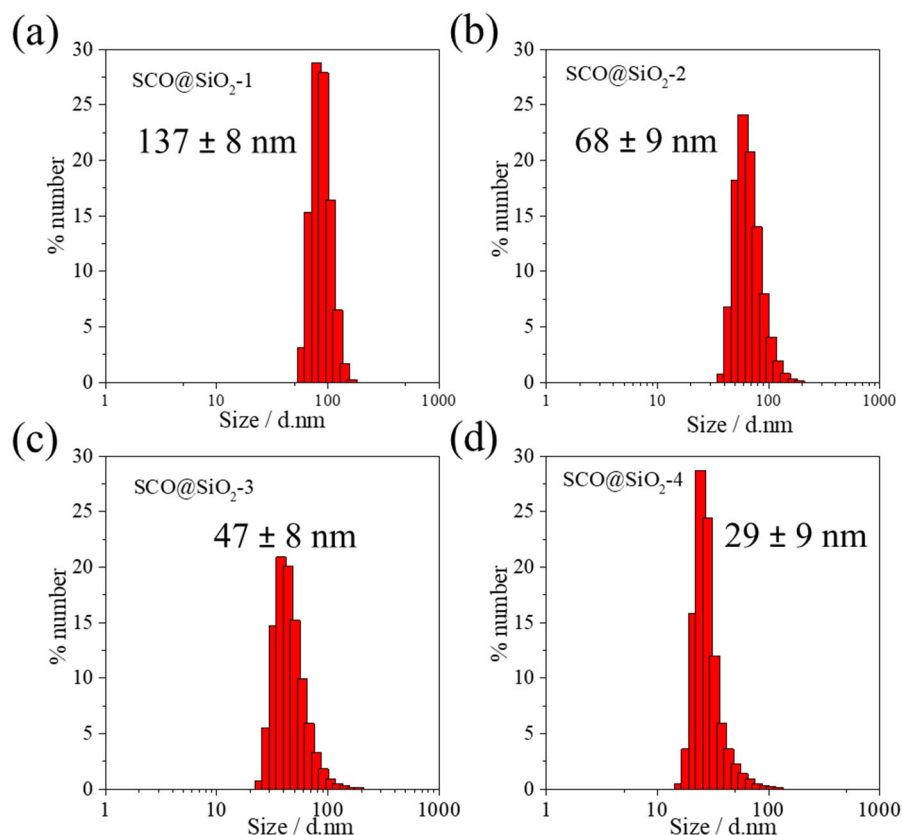


Figure 13. (a-d) Number-based particle size distribution for stable ethanolic suspensions of SCO@SiO₂-1 to 4 obtained by DLS analysis.

DLS is a technique that correlates the scattered light of a colloid with the size of the particles in suspension. Therefore, it provides valuable information about particle size and colloidal stability. For these measurements, dried samples of SCO@SiO₂-1 to 4 were measured after their redispersion in ethanol. The hydrodynamic diameter recorded for the different samples was 137 ± 8 and 68 ± 9 nm for SCO@SiO₂-1 and 2, and 47 ± 8 and 29 ± 9 nm for 3 and 4 (Figure).

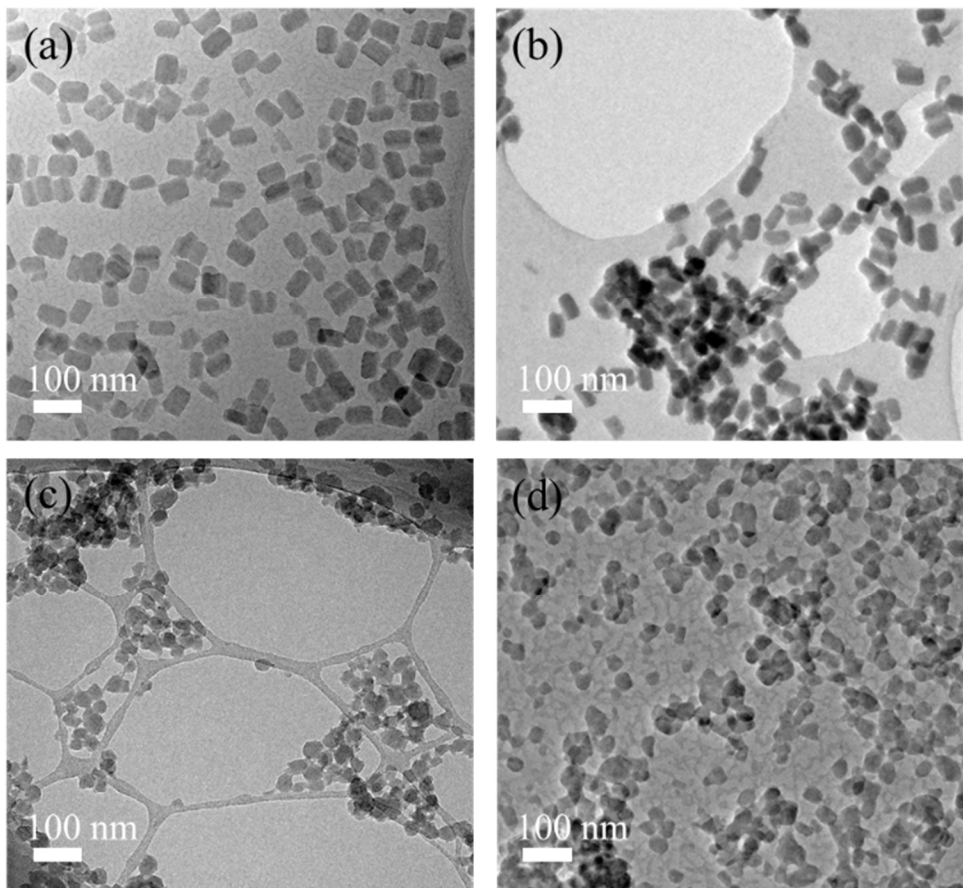


Figure 14. TEM images of SCO@SiO₂-1 (a), 2 (b), 3 (c), and 4 (d), deposited by drop casting on holey carbon film in (a) and (c), whereas a lacey carbon film is used in (b) and (c).

These values are consistent with the more precise size extracted by TEM, which additionally provides information on the morphology and composition. The hybrids SCO@SiO₂-1 and 2 present rod-like morphologies with average side lengths of 87 ± 8 and 60 ± 8 nm, respectively, whereas SCO@SiO₂-3 and 4 tended to be spherical with a diameter of 38 ± 7 and 28 ± 6 nm, respectively (Figure 14).

The small discrepancies in diameters between DLS and TEM are probably due to two factors. On the one hand, it is common that the size calculated by DLS is overestimated. This is because in DLS the obtained diameter is not the real one, but the hydrodynamic, which includes solvent molecules at the surface of the colloid and, more importantly, is calculated from the particles rotating in suspension. This provokes that for anisotropic NPs, like nanorods, the recorded size corresponds to the diameter of the rotating particle, which is larger than its length. On the other hand, larger NPs can be easily redispersed; thus, the signal obtained by DLS also may correspond to the bigger particles.

The above results could be understood as follows: by increasing the metal concentration in the aqueous phase, the number of nucleation centers increases, leading to decreased NPs final size. Then, by limiting the reaction time, the size can be further reduced. From the point of view of ω parameter, its modification alters the diameter of the micelle and thus, the NPs size. For the values shown in this thesis ($\omega = 9, 8$ and 5), the NPs sizes decrease accordingly with the ω value.

Table 1. Correlation between synthetic parameters and the particle size and composition for SCO@SiO₂ NPs.

| Sample | [Fe ²⁺] / M | ω | Time / h | TEM Length / nm | DLS / nm | Si/Fe ICP |
|-------------------------|----------------------------|----------|-------------|--------------------|-------------|--------------|
| SCO@SiO ₂ -1 | 1.25 | 9 | 24 | 87 ± 8 | 137 ± 8 | 0.7 |
| SCO@SiO ₂ -2 | 1.5 | 9 | 2 | 60 ± 8 | 68 ± 9 | 0.8 |
| SCO@SiO ₂ -3 | 1.5 | 8 | 2 | 38 ± 7 | 47 ± 8 | 0.8 |
| SCO@SiO ₂ -4 | 1.5 | 5 | 2 | 28 ± 6 | 29 ± 9 | 1.1 |

4.3.2. Stability and structure of the [Fe(Htrz)₂(trz)](BF₄)@SiO₂

It is common for this coordination polymer to present polymorphisms, which can affect its SCO properties.¹² Thus, the structure of the NPs was investigated by powder X-ray diffraction (PXRD). The diffractograms of the NPs revealed a single phase in all the samples, Figure 15a. This phase corresponds to the [Fe(Htrz)₂(trz)](BF₄) coordination polymer, as the simulated pattern shows, Figure 15a-black.

The thermogravimetric analysis (TGA) of the NPs displayed the same decomposition temperature despite the miniaturization. Indicating that Fe(Htrz)₂(trz)(BF₄)@SiO₂ miniaturization did not modify its stability significantly, Figure 15b.

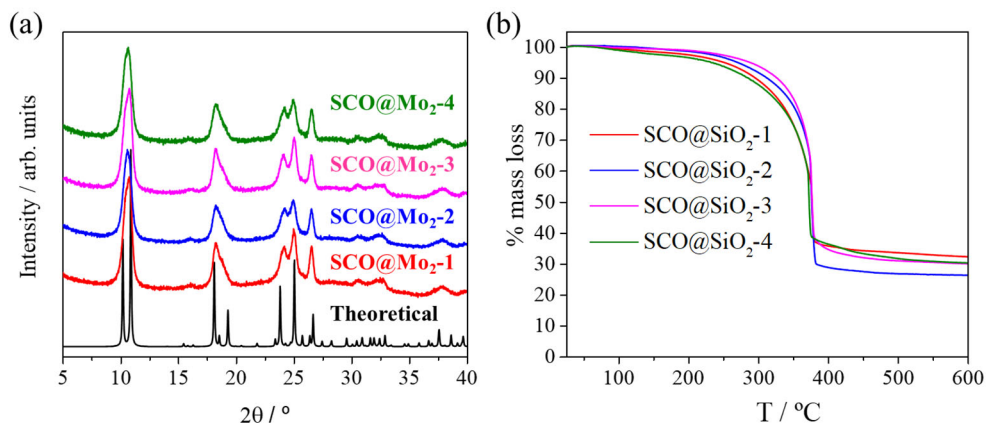


Figure 15. (a) X-ray diffraction patterns of powdered SCO@SiO_2 -1 to 4 and samples simulated pattern (black). (b) Thermogravimetric analysis of the same samples.

4.3.3. Thickness of the silica shell in $[\text{Fe}(\text{Htrz})_2(\text{trz})](\text{BF}_4)\text{@SiO}_2$

4.2.3.a. Inductively coupled plasma optical emission spectrometry

The amount of Si and Fe was quantified by inductively coupled plasma optical emission spectrometry (ICP-OES). In this technique, the NPs were digested under acidic conditions, and the Si and Fe contents were quantified directly. A molar ratio of Si/Fe comprised between 0.7 and 1.1 was obtained for SCO@SiO_2 -1 to 4, table 1, in agreement with the decrease of the core size.

4.2.3.b. Energy-dispersive X-ray spectroscopy mapping

To demonstrate the formation of SiO_2 around the SCO core EDX mappings of SCO@SiO_2 -1 to 4 were carried out with a scanning transmission microscope (STEM). In all cases, the presence of O and Si at the surface was evidenced, Figure . Nevertheless, only for SCO@SiO_2 -1 a sharp oxygen shell of ~3 nm was observed, (Figure a).

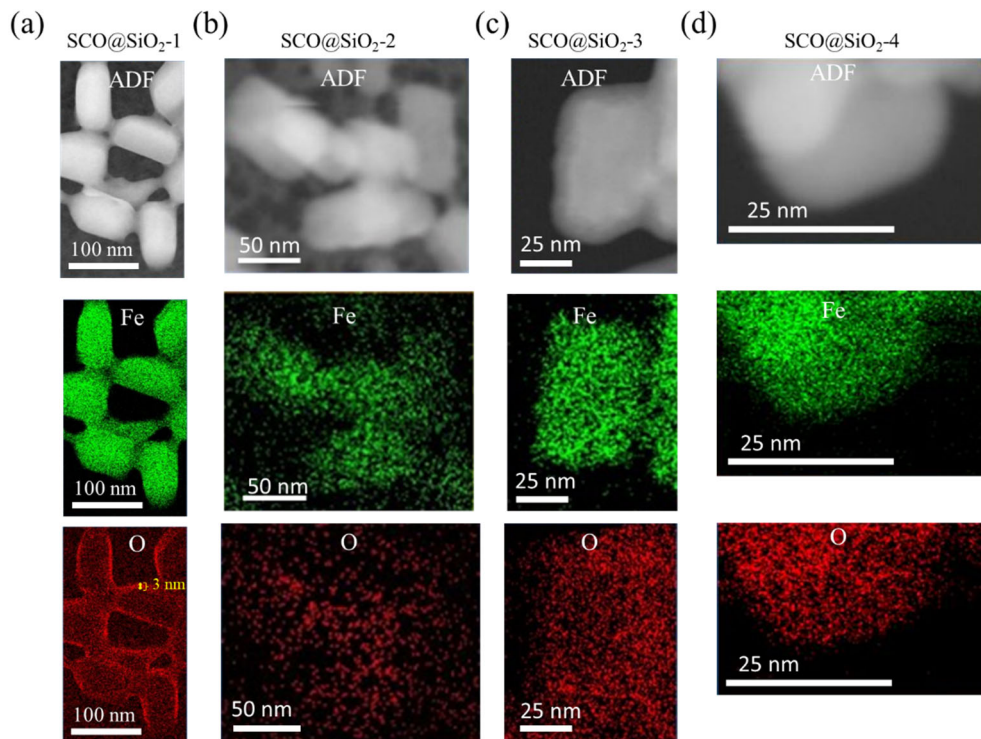


Figure 16. STEM elemental mapping of SCO@SiO₂-1 (a), SCO@SiO₂-2 (b), SCO@SiO₂-3 (c) and SCO@SiO₂-4 (d). Green points represent iron and red oxygen.

In the other samples a clear shell could not be distinguished due to residual oxygen contamination and its reduced thickness (Figure b,c and d). It must be noticed that to determine the thickness of the shell, we studied the oxygen mapping instead of the Si mapping due to persistent Si contamination in all the grids.

4.3.4. [Fe(Htrz)₂(trz)](BF₄)@SiO₂ size magnetic dependency

Magnetic properties of SCO@SiO₂-1 to 4 were studied to explore the downsizing effect in the spin transition. Figure 7 shows χ_{MT} vs T of the different samples. Remarkably all samples exhibited a characteristic abrupt spin transition centered above room temperature. Nevertheless, the hysteresis

width decreased upon size reduction. A 40% narrowing of the thermal hysteresis was observed from ca. 40 K in SCO@SiO₂-1 ($T_{1/2}^{HS} = 376$ K and $T_{1/2}^{LS} = 339$ K) to ca. 20 K in SCO@SiO₂-4 ($T_{1/2}^{HS} = 364$ K and $T_{1/2}^{LS} = 342$ K). Such a decrease was associated with a drop in the cooperativity due to downsizing, indicating that this thin shell did not increase the stiffness of the nanoparticle drastically.

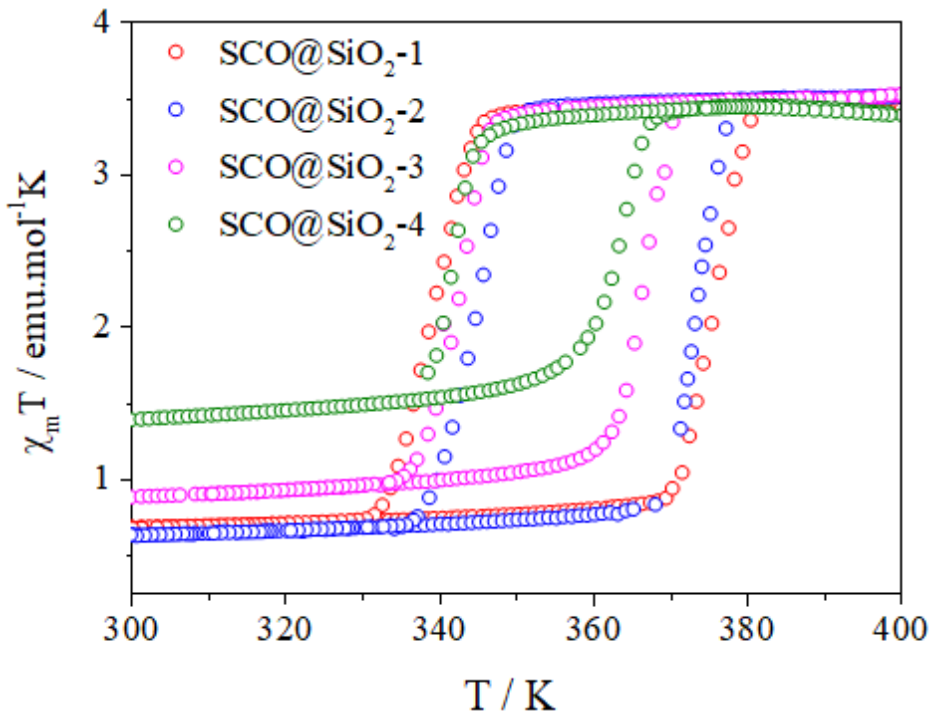


Figure 7. Comparison of the thermal variation of the χ_{MT} for the different core@shell NPs after two heating-cooling modes.

Another interesting feature was the increase in residual paramagnetic signal with miniaturization. Due to the size decrease, the percentage of metallic centers at the NPs surface with an incomplete coordination sphere increases. All these parameters are summarized in Table 2.

Table 2. Physical parameters of the thermally induced spin transition for [Fe(Htrz)₂(trz)](BF₄)@SiO₂ NPs.

| Sample | T ^{HS} _{1/2} (K) | T ^{LS} _{1/2} (K) | ΔT | HS (%) |
|-------------------------|------------------------------------|------------------------------------|----|--------|
| SCO@SiO ₂ -1 | 376 | 339 | 37 | 19 |
| SCO@SiO ₂ -2 | 373 | 344 | 29 | 18 |
| SCO@SiO ₂ -3 | 366 | 342 | 24 | 25 |
| SCO@SiO ₂ -4 | 364 | 342 | 22 | 41 |

4.4. Conclusions and perspectives

In this part of the thesis, we successfully modified the reverse micelle technique to control the size of the SCO compound [Fe(Htrz)₂(trz)(BF₄)@SiO₂. The size of the obtained NPs ranged from 90 to 28 nm, which is almost half the size already reported by Herrera et al.²¹ Even more, we succeeded on the obtention of a thinner silica shell, which for the biggest NPs was ~3nm, proving that it is possible to modulate also the shell thickness by acting over the polymerization kinetics. As has been established, the structure and the spin transition were maintained despite the miniaturization.

In the future, we will focus our efforts on the obtention of SCO NPs exhibiting a spin transition centred at room temperature, in order to reduce the energy required to induce the transition and facilitate their implementation in practical devices.

4.5. Bibliography

- (1) Coronado, E.; Galán-Mascarós, J. R.; Monrabal-Capilla, M.; García-Martínez, J.; Pardo-Ibáñez, P. Bistable Spin-Crossover Nanoparticles Showing Magnetic Thermal Hysteresis near Room Temperature. *Adv. Mater.* **2007**, *19* (10), 1359–1361.
- (2) Mikolasek, M.; Félix, G.; Nicolazzi, W.; Molnár, G.; Salmon, L.; Bousseksou, A. Finite Size Effects in Molecular Spin Crossover Materials. *New J. Chem.* **2014**, *38* (5), 1834–1839.
- (3) Giménez-Marqués, M.; García-Sanz De Larrea, M. L.; Coronado, E. Unravelling the Chemical Design of Spin-Crossover Nanoparticles Based on Iron(II)-Triazole Coordination Polymers: Towards a Control of the Spin Transition. *J. Mater. Chem. C* **2015**, *3* (30), 7946–7953.
- (4) Catala, L.; Volatron, F.; Brinzei, D.; Mallah, T. Functional Coordination Nanoparticles. *Inorg. Chem.* **2009**, *48* (8), 3360–3370.
- (5) Titos-Padilla, S.; Herrera, J. M.; Chen, X. W.; Delgado, J. J.; Colacio, E. Bifunctional Hybrid SiO₂ Nanoparticles Showing Synergy between Core Spin Crossover and Shell Luminescence Properties. *Angew. Chemie - Int. Ed.* **2011**, *50* (14), 3290–3293.
- (6) Faulmann, C.; Chahine, J.; Malfant, I.; De Caro, D.; Cormary, B.; Valade, L. A Facile Route for the Preparation of Nanoparticles of the Spin-Crossover Complex [Fe(Htrz)₂(Trz)](BF₄) in Xerogel Transparent Composite Films. *Dalt. Trans.* **2011**, *40* (11), 2480–2485.
- (7) Koo, Y. S.; Galán-Mascarós, J. R. Spin Crossover Probes Confer Multistability to Organic Conducting Polymers. *Adv. Mater.* **2014**, *26*

- (39), 6785–6789.
- (8) Raza, Y.; Volatron, F.; Moldovan, S.; Ersen, O.; Huc, V.; Martini, C.; Brisset, F.; Gloter, A.; Stéphan, O.; Bousseksou, A.; Catala, L.; Mallah, T. Matrix-Dependent Cooperativity in Spin Crossover Fe(Pyrazine)Pt(CN)₄ Nanoparticles. *Chem. Commun.* **2011**, 47 (41), 11501–11503.
- (9) Tokarev, A.; Long, J.; Guari, Y.; Larionova, J.; Quignard, F.; Agulhon, P.; Robitzer, M.; Molnár, G.; Salmon, L.; Bousseksou, A. Spin Crossover Polysaccharide Nanocomposites. *New J. Chem.* **2013**, 37 (11), 3420–3432.
- (10) Gonçalves, R. H.; Fiel, R.; Soares, M. R. S.; Schreiner, W. H.; Silva, C. M. P.; Leite, E. R. Single-Step Exfoliation and Covalent Functionalization of MoS₂ Nanosheets by an Organosulfur Reaction. *Chem. - A Eur. J.* **2015**, 21 (44), 15583–15588.
- (11) Galán-Mascarós, J. R.; Coronado, E.; Forment-Aliaga, A.; Monrabal-Capilla, M.; Pinilla-Cienfuegos, E.; Ceolin, M. Tuning Size and Thermal Hysteresis in Bistable Spin Crossover Nanoparticles. *Inorg. Chem.* **2010**, 49 (12), 5706–5714.
- (12) Grosjean, A.; Négrier, P.; Bordet, P.; Etrillard, C.; Péchev, S.; Lebraud, E.; Létard, J.; Grosjean, A.; Négrier, P.; Bordet, P.; Etrillard, C.; Mondieig, D. Crystal Structures and Spin Crossover in the Polymeric Material [Fe (Htrz)₂(Trz)](BF₄) Including Coherent-Domain Size Reduction Effects *European Journal of Inorganic Chemistry*, 2013(5-6), 796-802..

- (13) Rackwitz, S.; Klopper, W.; Schünemann, V.; Wolny, J. A. Quantification of Intramolecular Cooperativity in Polynuclear Spin Crossover Fe(II) Complexes by Density Functional Theory Calculations. *Phys. Chem. Chem. Phys.* **2013**, *15* (37), 15450–15458.
- (14) Durand, P.; Pillet, S.; Bendeif, E. E.; Carteret, C.; Bouazaoui, M.; El Hamzaoui, H.; Capoen, B.; Salmon, L.; Hébert, S.; Ghanbaja, J.; Aranda, L.; Schaniel, D. Room Temperature Bistability with Wide Thermal Hysteresis in a Spin Crossover Silica Nanocomposite. *J. Mater. Chem. C* **2013**, *1* (10), 1933–1942.
- (15) Zhao, T.; Cuignet, L.; Dîrtu, M. M.; Wolff, M.; Spasojevic, V.; Boldog, I.; Rotaru, A.; Garcia, Y.; Janiak, C. Water Effect on the Spin-Transition Behavior of Fe(II) 1,2,4-Triazole 1D Chains Embedded in Pores of MCM-41. *J. Mater. Chem. C* **2015**, *3* (30), 7802–7812.
- (16) Siddiqui, S. A.; Domanov, O.; Schafner, E.; Vejpravova, J.; Shiozawa, H. Synthesis and Size-Dependent Spin Crossover of Coordination Polymer [Fe(Htrz)₂(Trz)](BF₄). *J. Mater. Chem. C* **2021**, *9* (3), 1077–1084.
- (17) Piedrahita-Bello, M.; Ridier, K.; Mikolasek, M.; Molnár, G.; Nicolazzi, W.; Salmon, L.; Bousseksou, A. Drastic Lattice Softening in Mixed Triazole Ligand Iron(II) Spin Crossover Nanoparticles. *Chem. Commun.* **2019**, *55* (33), 4769–4772.
- (18) Pileni, M. P.; Zemb, T.; Petit, C. Solubilization by Reverse Micelles: Solute Localization and Structure Perturbation. *Chem. Phys. Lett.* **1985**, *118* (4), 414–420.

- (19) Pileni, M. P. Reverse Micelles as Microreactors. *J. Phys. Chem.* **1993**, *97* (27), 6961–6973.
- (20) Ranjan, S.; Dasgupta, N.; Lichtfouse, E. *Nanoscience in Food and Agriculture III*; 2016; Vol. 23.
- (21) Herrera, J. M.; Titos-Padilla, S.; Pope, S. J. A.; Berlanga, I.; Zamora, F.; Delgado, J. J.; Kamenev, K. V.; Wang, X.; Prescimone, A.; Brechin, E. K.; Colacio, E. Studies on Bifunctional Fe(II)-Triazole Spin Crossover Nanoparticles: Time-Dependent Luminescence, Surface Grafting and the Effect of a Silica Shell and Hydrostatic Pressure on the Magnetic Properties. *J. Mater. Chem. C* **2015**, *3* (30), 7819–7829.
- (22) Moulet, L.; Daro, N.; Etrillard, C.; Létard, J.-F.; Grosjean, A.; Guionneau, P. Rational Control of Spin-Crossover Particle Sizes: From Nano- to Micro-Rods of [Fe(Htrz)₂(Trz)](BF₄). *Magnetochemistry* **2016**, *2* (1), 10.
- (23) Forestier, T.; Kaiba, A.; Pechev, S.; Denux, D.; Guionneau, P.; Etrillard, C.; Daro, N.; Freysz, E.; Létard, J. F. Nanoparticles of [FeNH₂-Trz₃] Br₂·3H₂O (NH₂-Trz=2-Amino-1,2,4-Triazole) Prepared by the Reverse Micelle Technique: Influence of Particle and Coherent Domain Sizes on Spin-Crossover Properties. *Chem. - A Eur. J.* **2009**, *15* (25), 6122–6130.
- (24) Volatron, F.; Catala, L.; Rivière, E.; Gloter, A.; Stéphan, O.; Mallah, T. Spin-Crossover Coordination Nanoparticles. *Inorg. Chem.* **2008**, *47* (15), 6584–6586.

- (25) Linares, J.; Jureschi, C.; Boukheddaden, K. Surface Effects Leading to Unusual Size Dependence of the Thermal Hysteresis Behavior in Spin-Crossover Nanoparticles. *Magnetochemistry* **2016**, 2 (2), 24.
- (26) Félix, G.; Mikolasek, M.; Molnár, G.; Nicolazzi, W.; Bousseksou, A. Tuning the Spin Crossover in Nano-Objects: From Hollow to Core-Shell Particles. *Chem. Phys. Lett.* **2014**, 607, 1–4.
- (27) Holovchenko, A.; Dugay, J.; Giménez-Marqués, M.; Torres-Cavanillas, R.; Coronado, E.; van der Zant, H. S. J. Near Room-Temperature Memory Devices Based on Hybrid Spin-Crossover@SiO₂Nanoparticles Coupled to Single-Layer Graphene Nanoelectrodes. *Adv. Mater.* **2016**, 28 (33).

5

Design of bistable gold@spin crossover nanoparticles

R. Torres-Cavanillas, R. Sanchis-Gual, J. Dugay, M. Coronado-Puchau, M. Giménez-Marqués, E. Coronado. *Advanced Materials* 2019, 31, 27, 1900039

5.1. Motivation

As already introduced, SCO materials displaying a hysteretic spin transition are highly desirable since they can be useful as molecular nano switches, especially for electronic devices.^{1,2} In order to read out the spin state in these devices, materials displaying wide hysteresis loops near to room temperature are preferred, but even more important is the need for large electrical responses. Nevertheless, their high insulating nature is a great obstacle for this purpose, as discussed below. Herein, we look for an improvement in the electrical conductivity of the SCO compound $\text{Fe}(\text{Htrz})_2(\text{trz})(\text{BF}_4)$ by the synthesis of hybrid structures containing highly conductive materials in close contact with SCO systems.

5.2. Introduction

5.2.1. *Spin-crossover electrical devices*

The first example of an electronic device based on $[\text{Fe}(\text{Htrz})_2(\text{trz})](\text{BF}_4)$ NPs was reported in 2009 by Prins et al. In this work 11 nm NPs of the already mentioned SCO material were placed between two nanometer-spaced electrodes with a gap ranging from 5 to 10 nm.³ The thermal hysteresis in the conductance resembles that observed in the magnetic susceptibility, with a HS more conductive than the LS, Figure 1a.

Nevertheless, a low and poorly reproducible electrical signal was recorded by this approach due to the insulating nature of the material and the bad packing of the NPs between the electrodes. Therefore, to obtain a more efficient contact between electrodes and to improve the electrical signal, Rotaru et al. proposed the dielectrophoresis (DEP) technique as a suitable manner for packing the NPs in between fingerprint electrodes, Figure 1b.⁴ In

this methodology $\text{Fe}(\text{Htrz})_2(\text{trz})](\text{BF}_4)$ microrods are organized by applying an AC voltage between fingerprint electrodes with a 4 μm gap. Once the voltage is removed, the particles remain perfectly organized and well packed, increasing the stability of the setup.

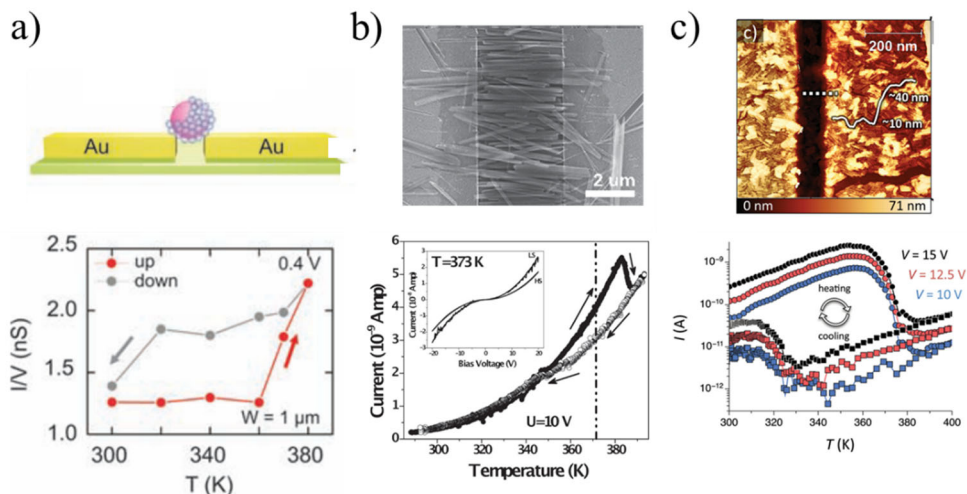


Figure 1. Top: electrical set up used in different works. (a) 11 nm $\text{Fe}(\text{Htrz})_2(\text{trz})(\text{BF}_4)$ NPs organized by μ -microcontact printing between electrodes with 5-10 nm gap.³ (b) 3 μm , organized by DEP between gold electrodes with a gap of 4 μm .⁴ (c) 44 NPs organized also by DEP between gold electrodes with a gap of 100 nm.⁵ Bottom: electrical response as function of the temperature of the same devices.

In contrast with Prins et al., the conductivity recorded by Rotaru et al., in the LS state was larger than that of the HS state, Figure 1b. This difference with respect to the single NPs device may be attributed to a different cooling contact due to the different sizes of the NPs and methods to organize them, which is translated in a different electron flow mechanism. Nevertheless, the performance of the device was still deficient.

Later in 2015 Dugay et al., followed the same procedure (DEP) but using electrodes with a smaller gap, 50 nm, and smaller nanorods, 10 x 25nm and 6

x 44nm.⁵ In this scenario, the electrical response was improved, exhibiting a two order of magnitude more conductive LS, Figure 1c.

A plausible explanation for the improved electrical response could be a better alignment due to the smaller NPs length, compared to Rotaru et al. This work is one of the first steps towards highly responsive electrical devices based on the SCO phenomenon.

5.2.2. $[Fe(Htrz)_2(trz)]BF_4@SiO_2$ based devices

Despite the efforts to improve their conductivity, the fatigue associated with the successive transitions, while a current is applied, still had to be faced.⁶

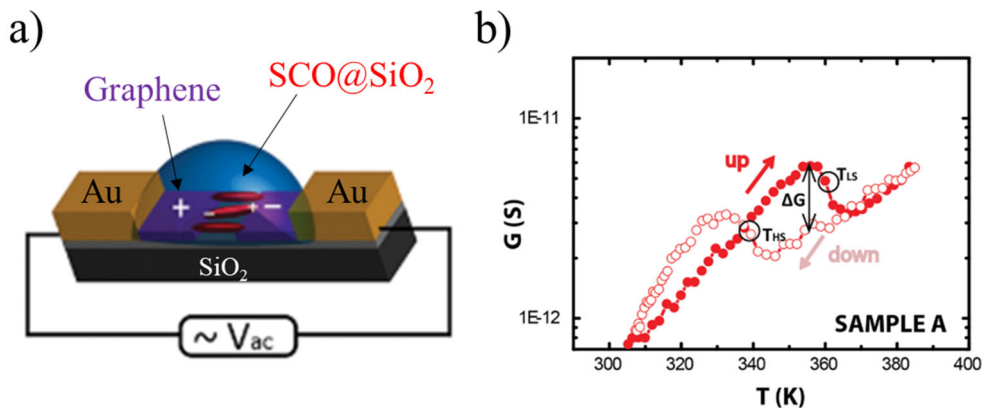


Figure 2. (a) Scheme of the $[Fe(Htrz)_2(trz)](BF_4)@SiO_2$ contacted between graphene electrodes. (b) Electrical response as a function of the temperature of the same device. Extracted from reference [7].

Therefore, to minimize degradation, a more robust device was prepared using silica wrapped $[Fe(Htrz)_2(trz)]BF_4$ nanorods contacted between graphene electrodes. In this setup, the graphene improved the contact with the NPs, while the silica coverage increases their robustness.

Remarkably, the graphene device exhibited the same electrical response of bare Fe(Htrz)₂(trz)]BF₄ (Figure 2) but minimizing the fatigability.

5.2.3. *Hybrids with conductive materials*

The insulating conductivity of this coordination polymer remains far from practical applications.^{4,8,9} For this reason, several researchers, focus their work on combining conductive materials with SCO compounds.

5.2.3.a. *Hybrids with conductive polymers*

In this line, Koo et al. incorporated [Fe(Htrz)₂(trz)]BF₄ powder into highly conducting Polypyrrole (ppy).¹⁰ The particularity of ppy conductivity is its pressure dependency. Under pressure, the distance between chains decreases, reducing the energy barriers and increasing the average electrical conductivity. This feature makes it an ideal candidate to couple its electrical response with the volumetric variation of SCO materials. For such a device, the room temperature conductivity of the films was nine orders of magnitude higher than the bare NPs. Above 387 K, the electrical conductivity increases abruptly towards a new highly conducting phase, obtaining four times higher conductivity in the HS, Figure 3a.

Similarly, Cheng et al. covered a constantan metallic alloy (an alloy of Cu and Ni) with a polycarbonate containing the same SCO system. As for the ppy, such alloy is strain sensitive.¹¹ Therefore, by recording the electrical conductivity of the constantan, a 0.075% lower electrical conductivity was found in the HS, indicating that the strain reduces the conductivity of the constantan, Figure 3b. Even more, by the difference in conductivity, the strain applied by the NPs could be estimated, corresponding with a value of *ca* $3.75 \cdot 10^{-2} \%$.

Finally, following the same approach, Rat et al. used ca. 20 nm NPs of $[\text{Fe}\{(\text{Htrz})_2(\text{trz})\}_{0.9}(\text{NH}_2\text{-trz})_{0.3}](\text{BF}_4)_{1.1}$ in poly(vinylidene fluoride-co-trifluoro-ethylene), (PVDF-TrFE), and poly(vinylidene fluoride) (PVDF) matrices to form macroscopic (cm-scale), freestanding, and flexible conductive nanocomposites.¹²

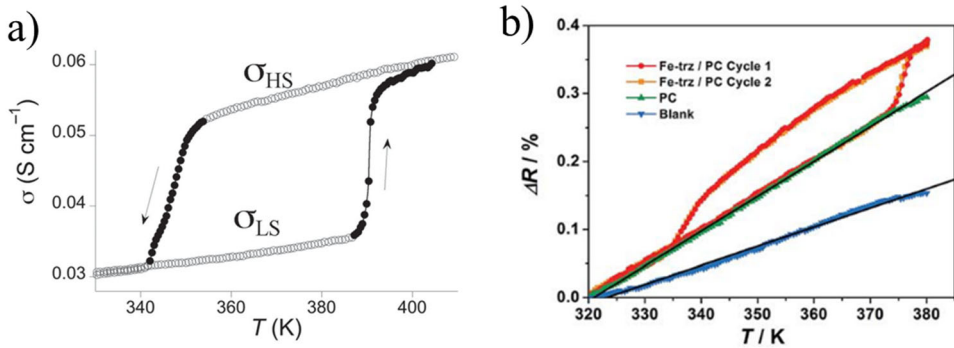


Figure 3. Electrical conductivity as function of the temperature for $[\text{Fe}(\text{Htrz})_2(\text{trz})](\text{BF}_4)$ embedded in ppy (a) and polycarbonate (b). Extracted from reference [10,11].

5.2.3.b. Hybrids with conductive 2D materials

Similar to the previous cases, the synthesis of highly conductive 2D combined with SCO compounds has attracted much interest, transferring the SCO phenomenon to flatland. In this context, the use of SCO materials to alter the electrical properties of graphene has been recently explored.^{13,14} In this context, Dugay et al. microprinted $[\text{Fe}(\text{Htrz})_2(\text{trz})]\text{BF}_4$ nanorods on a graphene sheet on top of a Si/SiO₂ device.¹⁴ In this case, the charge transport properties were explored using a four-probe field-effect configuration. With this setup, the authors were able to convincingly demonstrate that both the resistance and hole mobility of the graphene was reversibly affected by the spin state of the SCO NPs close to the Dirac cone, Figure 4. Calculations seem

to suggest that charge-carrier-scattering mechanisms in the graphene are influenced by the relative dielectric constants of the two spin states in the $[\text{Fe}(\text{Htrz})_2(\text{trz})]\text{BF}_4$ nanorods.^{15–17}

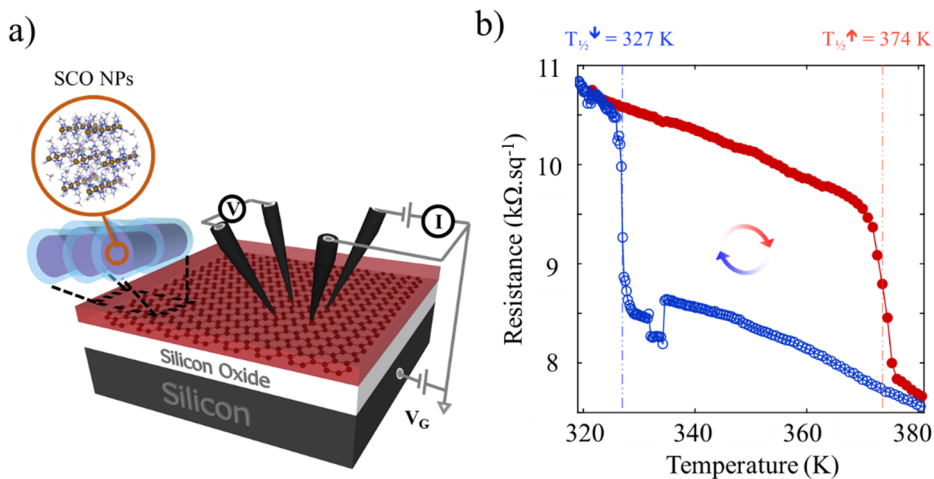


Figure 4. (a) Schematic of the device with CVD graphene on top of a silicon–silicon oxide substrate and after deposition of a bistable $[\text{Fe}(\text{Htrz})_2(\text{trz})]\text{BF}_4$ nanoparticles thin film prepared by μ -contact printing. (b) Resistance per square at the Dirac point of the graphene as a function of temperature for heating and cooling modes. Extracted from reference [14].

5.2.3.c. Hybrids with metallic nanostructures

Recently, several publications have explored the blending of gold NPs (Au NPs) with $[\text{Fe}(\text{Htrz})_2(\text{trz})](\text{BF}_4)$. Nevertheless, the target of almost all these works falls in the use of the metallic NPs as photothermal agents, ignoring its potential to boost the electrical conductivity of SCO materials.^{18,19} As photothermal agent, several works have proposed the system $[\text{Fe}(\text{Htrz})_2(\text{trz})](\text{BF}_4)@\text{SiO}_2$ as SCO system, in which Au NPs were anchored on the silica shell.^{20,21} In these works, the SiO_2 shell chemical reactivity is used to interact with gold NPs, through a bridging molecule. The silica shell is functionalized with a silanol molecule with amino or thiol terminal groups,

((3-Amino or mercapto propyl)triethoxysilane, called APTES or MPTES respectively), to ulteriorly anchor the gold NPs through the amine or thiol moieties, Figure 5a-b. By this approach and taking advantage of the Au strong photothermal effect, it has been possible to reduce the power required to complete the spin transition by laser irradiation around a 70%, measured by Raman spectroscopy.²¹ However, the thick shell and the bridging molecule are expected to reduce the synergy between the metallic and the SCO NPs. Therefore, more intimate contact between both compounds are expected to improve efficiency.

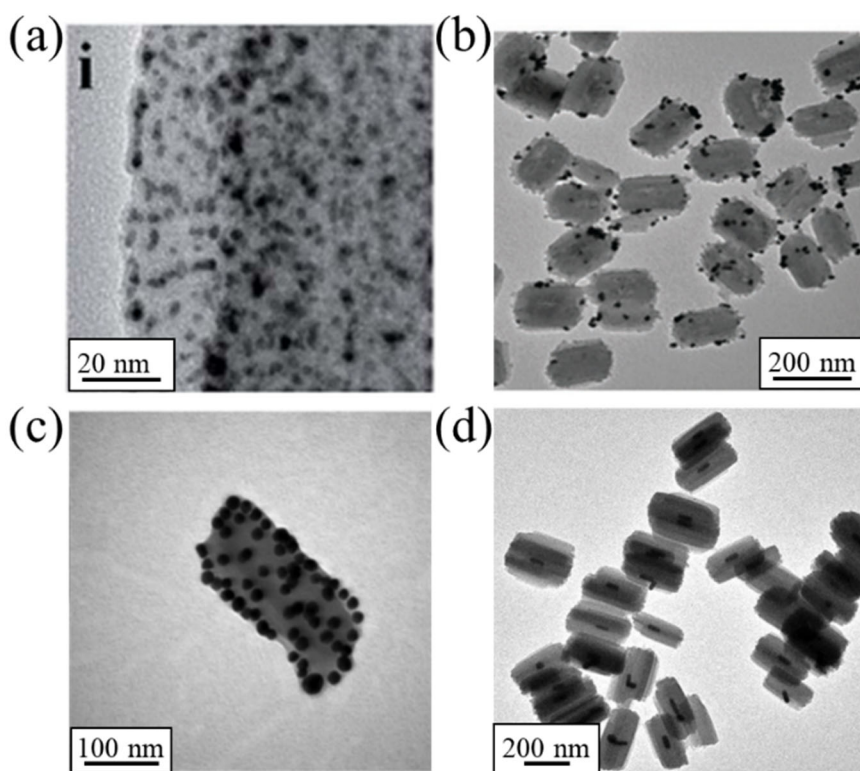


Figure 5. (a-b) TEM images of $[Fe(Htrz)_2(trz)](BF_4)@SiO_2$ NPs decorated with gold NPs. (c) Images of direct decoration of the gold NPs on $[Fe(Htrz)_2(trz)](BF_4)$ NPs. (d) Core@shell of gold and the same SCO material. Figure extracted from references [20-23].

To achieve this goal, the direct decoration of Au NPs via the nitrogen atoms from the triazoles located at the SCO NPs surface was reported in 2015 by Moulet et al., Figure 5c.²² Unfortunately, no photothermal effect was observed for this hybrid. It must be noticed that the authors measured the magnetic properties of the hybrid during irradiation. These measurements are less local than Raman, and the light intensity is lower; hence, both techniques cannot be compared.

Recently, this concept was expanded, embedding gold nanorods on $\text{Fe}(\text{Htrz})_2(\text{trz})(\text{BF}_4)$, Figure 5d,²³ where in contrast with the direct decoration, a real core@shell architecture was designed. Note that this work was carried out in parallel to the results presented in this thesis, following a similar synthetic approach, but reported one year later. In this hybrid, a well-defined thermo-induced switching with a broad hysteresis, achieving a photoconversion of the 55% upon light irradiation, was recorded (extracted from magnetic measurements).

5.3. Results and discussion

In this chapter, we present the chemical design of a core@shell system formed by a gold core and a $\text{Fe}(\text{Htrz})_2(\text{trz})(\text{BF}_4)$ shell. Once more, we chose this SCO material because of its high cooperativity, permitting the preparation of ultrathin shells, which retains the spin transition. Later the chemical stability of the shell is explored. Even more, we have investigated the use of different gold nanostructures as the core. In particular, nanospheres and nanostars. Figure 6.

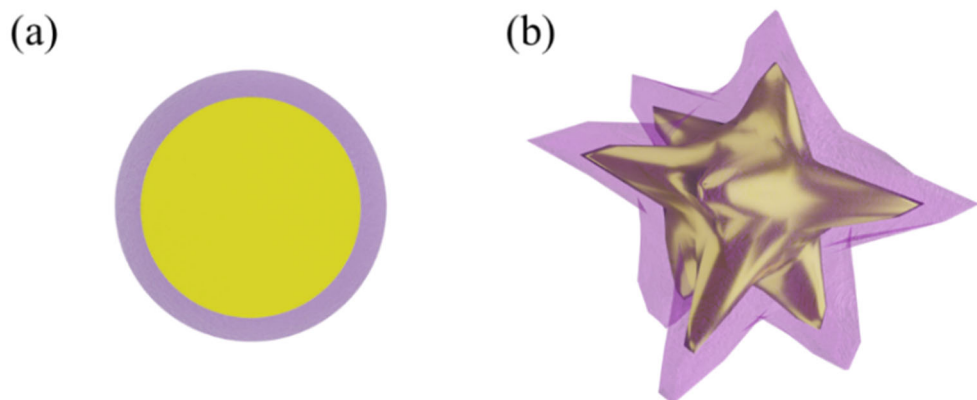


Figure 6. Sketch of core@shell NPs of gold nanospheres (a) and nanostars (b) capped with $\text{Fe}(\text{Htrz})_2(\text{trz})(\text{BF}_4)$.

5.3.1. Core@shell based on gold nanospheres

The Synthesis of the core@shell $\text{Au}@(\text{Fe}(\text{Htrz})_2(\text{trz})(\text{BF}_4))$, $\text{Au}@(\text{SCO})$, consists of the Au nanospheres coated with a thin shell of $\text{Fe}(\text{Htrz})_2(\text{trz})(\text{BF}_4)$. The protocol relies on functionalized Au NPs with triazole ligands as nucleation seeds (Figure 7i), to ulteriorly grow the SCO compound $\text{Fe}(\text{Htrz})_2(\text{trz})(\text{BF}_4)$ (Figure 7ii).

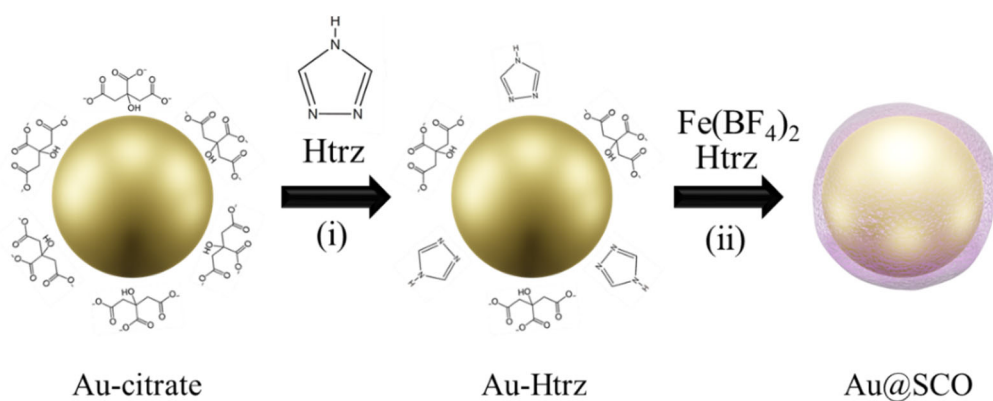


Figure 7. Scheme of the synthetic protocol followed to obtain the hybrid $\text{Au}@(\text{SCO})$ NPs.

5.3.1.a. synthesis of gold nanospheres

Firstly, to obtain colloiddally stable Au NPs with an accessible surface, citrate stabilized nanospheres of 12.6 ± 1.2 nm were synthesized following the Turkevich method, Figure 8a.²⁴ This method produces highly monodisperse NPs, which are colloiddally stable for months. To probe the colloiddal stability of these metallic NPs, we analyzed their zeta-potential (ζ -pot), which is an analytic method that provides information about the colloid electrostatic repulsion. Values up to ± 40 mV are considered colloiddally stable, which means that electrostatic repulsions are high enough to prevent the particles aggregation. In contrast, values down to ± 30 mV are provided by colloids that aggregate with time.²⁵ In our samples, the ζ -pot of Au NPs remained unaltered for weeks, maintaining a ζ -pot of -40.1 ± 9.5 mV.

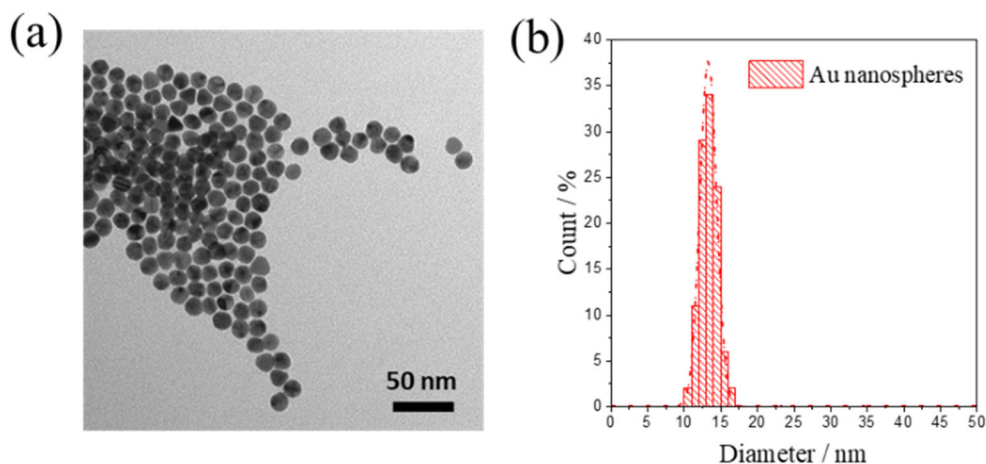


Figure 8. (a-b). TEM image of the Au nanospheres (a) with their diameter distribution (b)

Remarkably, Au nanostructures exhibit singular optical dependency with their size and shape. This is due to the collective oscillation of the free electrons in noble metal nanostructures at specific wavelengths. This

resonance, called localized surface plasmon resonance (LSPR), creates sharp spectral absorption, scattering peaks, and strong electromagnetic near-field enhancements.¹⁸ Therefore, depending on the size and shape, the LSPR wavelength differs.^{26,27} For instance, 12 nm gold nanospheres exhibit their LSPR at ~ 520 nm (Figure 9a), 80 nm nanostars at ~ 690 nm (Figure 9b), and 40x10 nm nanorods at ~ 810 nm (Figure 9c). The NPs employed in this part of the thesis are the 12 nm gold nanospheres, Figure 9a. The Au NPs were synthesized by Roger Sanchis-Gual at the ICMol. Even more, the LSPR position is extremely sensitive to its surrounding dielectric constant, permitting these nanostructures to act as a sensor.

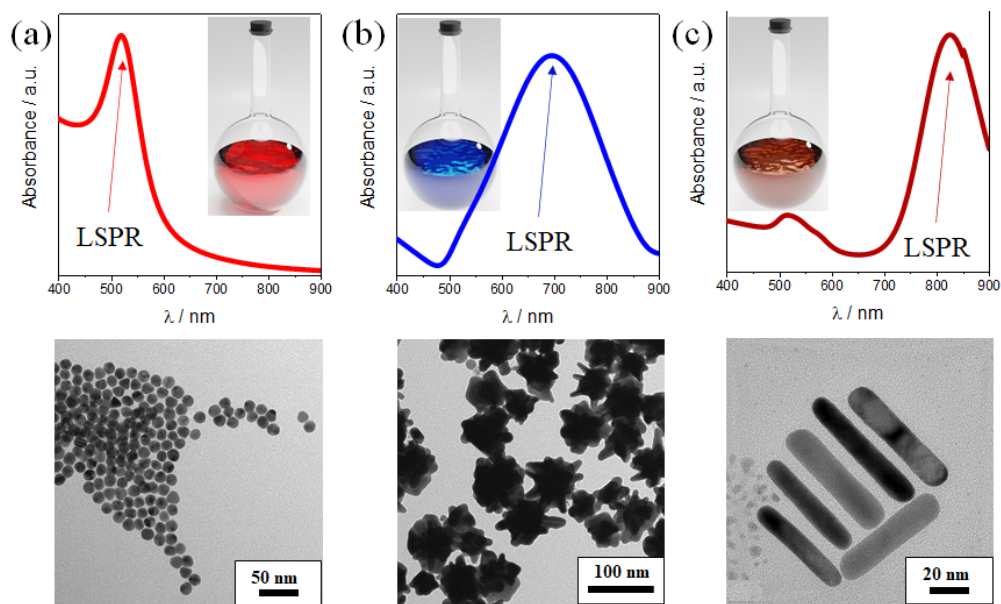


Figure 9. Top, LSPR measured by UV-VIS of Au nanospheres (a), nanostars (b), and nanorods (c); the insets are representations of the observed colours. Bottom, TEM images of the metallic nanostructures.

5.3.1.b. Ligand substitution

Once the Au seeds were synthesized, the growth of the SCO complex continues with the partial ligand substitution of the gold capping. As the first step occurs at the surface of the Au NPs a partial displacement of the citrate capping for triazole ligands is involved, affording some nucleation sites that act as anchors for the subsequent growth of the SCO shell, Figure 7i. The substitution occurs thanks to the relatively weak Au-citrate interaction,²⁸ and the triazole nitrogen affinity to the gold.²² Nevertheless, the triazole cannot effectively stabilize the Au NPs. Hence, a complete substitution provoked the NPs colloidal stability loss, preventing the SCO from growing homogeneously.

Therefore, fine control of the amount of Htrz ligands added was a critical parameter. In this context, we found that adding a 20% of triazole with respect to the initial moles of gold is sufficient to have some nucleation centers without altering their colloidal stability (ζ -pot remained intact -40.6 ± 6 mV), these NPs will be called Au-Htrz NPs. The presence of the ligand was proved by XPS analysis in the N1s region. In order to prepare the samples, Au-Htrz NPs were washed to remove the unreacted ligand and then drop casted on a Si/SiO₂ (285 nm) substrate. As Figure 10 shows, the signal coming from the Htrz is only visible in the modified Au-Htrz NPs.

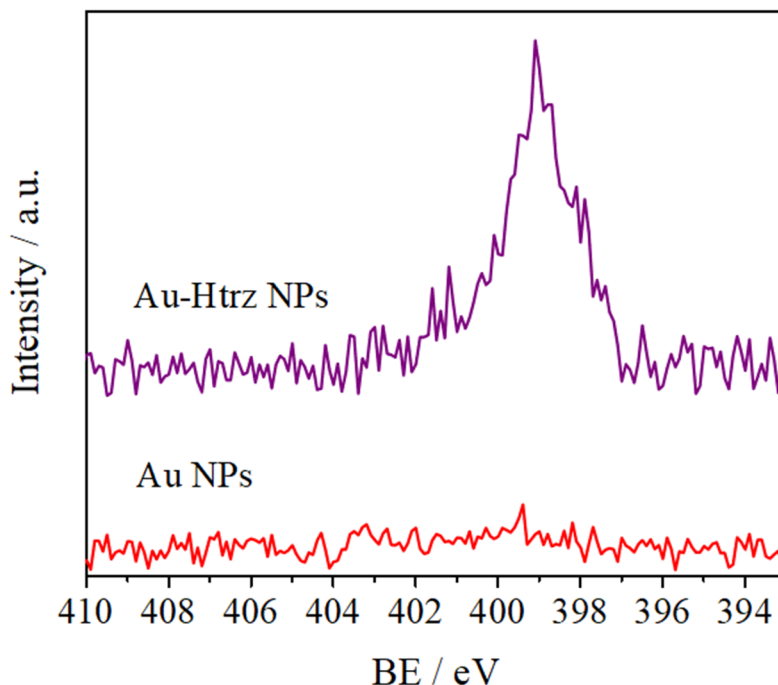


Figure 10. XPS spectra of NIs survey for Au NPs (red) and Au-Htrz NPs (purple).

5.3.1.c. Metal and ligand addition

The second key step of the protocol comprised the continuous growth of the SCO complex onto the pre-modified Au surface, Figure 7ii. This was achieved by adding SCO precursors in a controlled manner. Thus, aqueous solutions of the Fe^{2+} precursor and the Htrz ligand were simultaneously added to the Au-Htrz suspension at a constant rate ($4 \text{ mL}\cdot\text{h}^{-1}$). To avoid the aggregation of the colloid during the synthesis, highly diluted metal and ligand solutions had to be added ($1.6\cdot 10^{-4}$ and $5\cdot 10^{-4}$ M, respectively) into a highly diluted gold suspension ($1.6\cdot 10^{-4}$ M). The product of the reaction will be called Au@SCO-1.

The SCO overgrowth was monitored by following the particle size at different times, showing a continuous growth upon addition of reagents,

Figure 11. Hydrodynamic diameters ranging from ~13 nm at time zero to ~18 nm at 45 min were measured. Longer reaction time, adding more precursors led to aggregation.

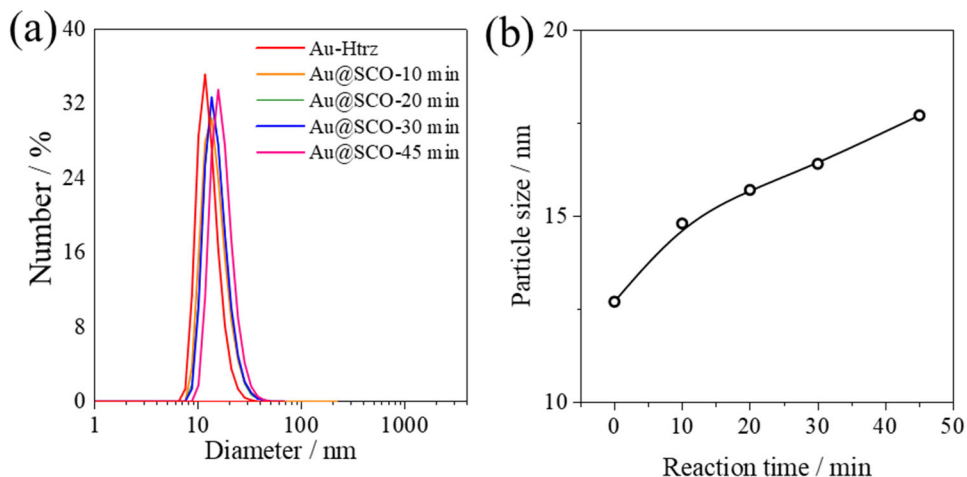


Figure 11. (a) DLS of the Au-Htrz NPs at different addition times. (b) Plot of the particle diameter versus the addition time.

Focusing on the ζ -pot, significant changes occur during the synthesis. A substantial modification from -40 ± 6 to -28 ± 4 mV took place from the Au-Htrz NPs to the Au@SCO-1, respectively. Therefore, we conclude that the ζ -pot of the Au-Htrz NPs was progressively neutralized for the growth of the SCO shell.

Once the reaction was completed, the morphology of the colloid was investigated by TEM. The images evidenced a uniform shell of 3.6 ± 1.0 nm surrounding the gold core, Figure 12. We conclude that a homogeneous coating is obtained by this synthetic approach, leading to Au NPs embedded in a SCO matrix.

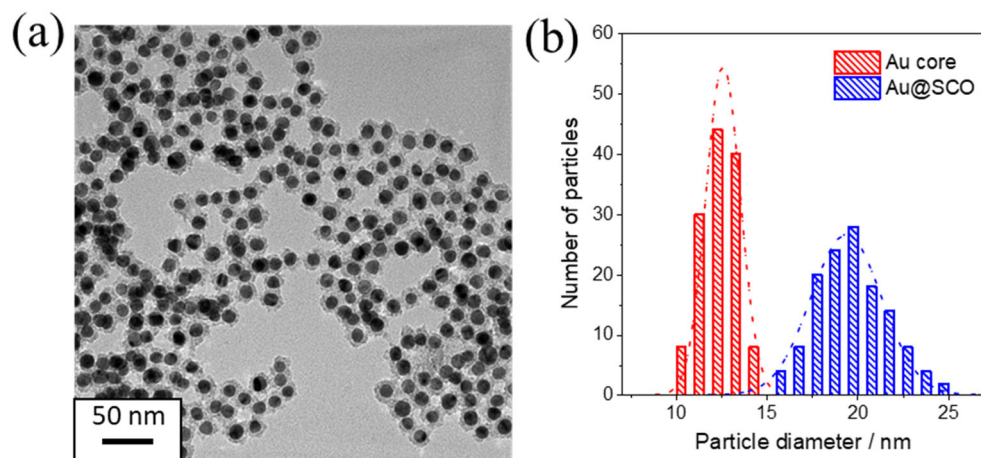


Figure 12. (a) TEM image of the Au@SCO-1 nanospheres. (b) Diameter distribution of the Au-core, in red, and core@shell, in blue (b).

Energy-dispersive X-ray spectroscopy (EDX) was used to estimate the metallic composition of the Au@SCO-1 NPs. Figure 13 shows a clear core@shell distribution with an estimated ratio $\text{Au/Fe} = 0.58$. A more accurate analysis of the metal content, establishing a ratio $\text{Au/Fe} = 0.62$, was performed by ICP-OES.

Interestingly, and in contrast with the other reported examples of SCO hybrids, these Au@SCO-1 NPs possess a naked surface (i.e., free from any organic moiety). Such surfactant-free configuration may turn out to be particularly convenient to conduct post-synthetic modification on the NPs surface.

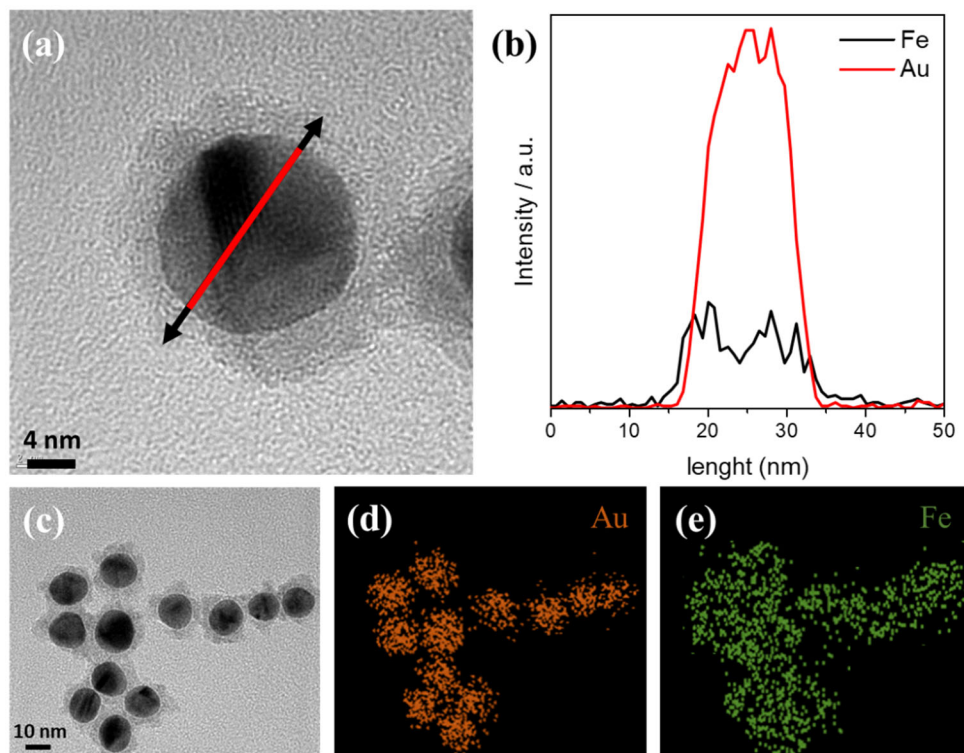


Figure 13. (a) TEM image and (b) EDX profile showing Au and Fe on a single NP; (c–e) EDX mapping of the metals present in the hybrids.

5.3.1.d. Optical properties

The optical absorption of this hybrid is reported in Figure 14 and compared with the bare gold NPs. It was observed that the localized LSPR was gradually red-shifted during the shell growth (up to 530 nm in the Au@SCO-1). This plasmon shift can be visually detected by the suspension colour change from red to pink. Besides, a subsequent increase in the plasmon band intensity was also observed. The mechanism at play may have its origin in the change of the dielectric properties at the Au NP surface upon the SCO shell overgrowth.²⁹

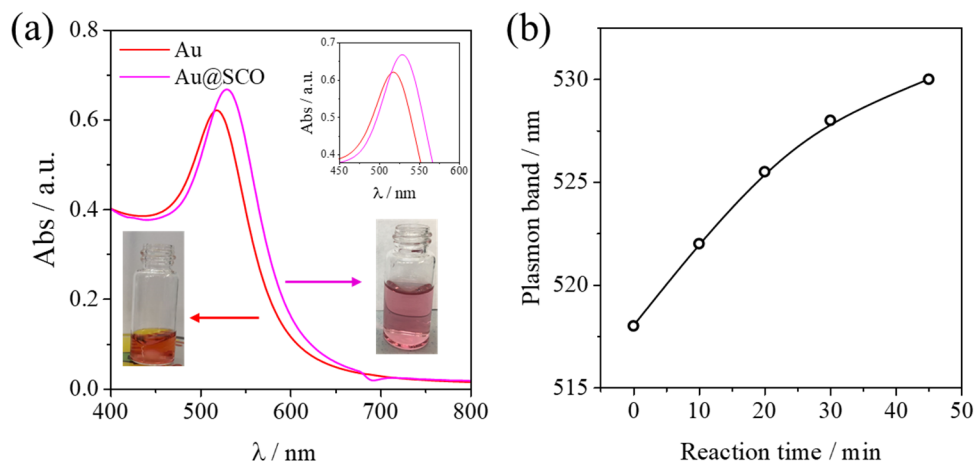


Figure 14. (a) UV-VIS spectra of Au and Au@SCO-1 NPs in the visible region. (b) Plot of the plasmon band at a function of the reaction time.

5.3.1.e. Chemical characterization

The hybrid material was investigated by XPS and X-ray diffraction to characterize the chemical composition and structure of the shell, Figure 15. The diffraction pattern of the Au@SCO-1 exhibits a unique peak at 38.2° characteristic of metallic gold, whereas the expected peaks for the $[\text{Fe}(\text{Htrz})_2(\text{trz})](\text{BF}_4)$ compound are absent, Figure 15a. Three possible causes can be responsible for this. (1) The small thickness of the SCO shell, which may be beyond the detection limit of the X-ray diffractometer. (2) The poor crystallinity of the SCO material. (3) The oxidation of the outer-shell surface due to its naked nature.

To clarify this and to obtain further insight into the elemental composition and oxidation state of the iron, we studied the XPS spectra. To do so, a solution of the Au@SCO-1 is drop casted on a Si/SiO₂ (285 nm) substrate, and the aggregates on top of the substrate were measured. Then, the Fe2p (from the SCO metal), N1p (from the SCO ligand), and F1s (from the SCO

counterion) regions were monitored. As Figure 15b-d shows, clear bands in the three regions are visible, indicating the presence of the metal, the ligand, and the counterion, thus, supporting the formation of the SCO compound on the outer shell.

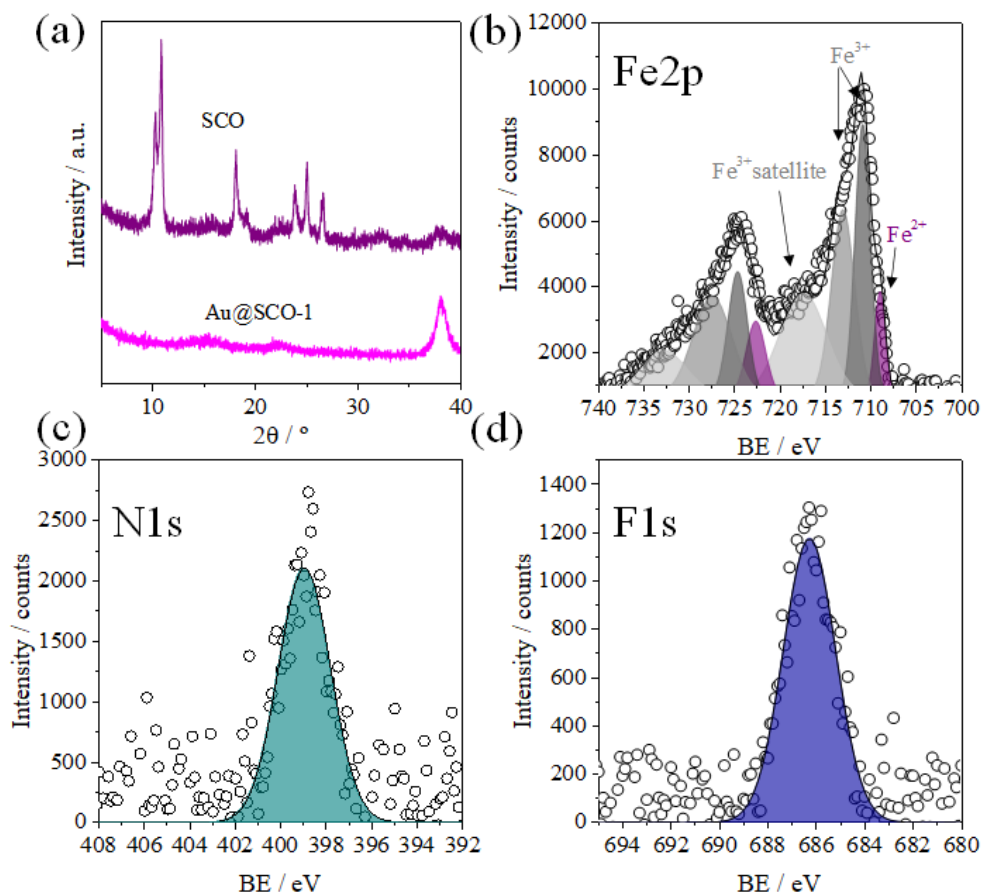


Figure 15. (a) Room temperature XRD for Au@SCO-1 (magenta) and SCO (purple) compounds. (b-d) XPS spectra of Fe2p, N1s and F1s regions for the Au@SCO-1.

Focusing on the iron region, three peaks can be deconvoluted. The first one at 708.8 eV was attributed to Fe²⁺ species, the other three at 710.8, 713.5, and 717.8 eV to the Fe³⁺ multiplete and its satellite. As can be seen in Figure

15d a majority of Fe^{+3} is present in Au@SCO-1. Accordingly, with the iron signal deconvolution, there is a ~9 % of Fe^{2+} . The atoms at the surface are known to be more reactive and susceptible to oxidize at ambient conditions. Therefore, the high number of metallic centers at the surface, combined with the lack of any protective capping or surfactant, makes this system highly unstable in the air. Finally, it must be noticed that the percentage of Fe^{2+} is just an approximation. The deconvolution of Fe^{2+} and Fe^{3+} is complicated due to the presence of multiple features and satellite peaks, making this calculation a rough estimation.

5.3.1.f. Au@SCO spin transition

Despite the limited number of Fe^{2+} centers that can undergo the spin transition, the spin transition of the core@shell was unambiguously confirmed by DSC measurements under N_2 atmosphere. Two well-defined peaks at 361 ($T_{1/2}^{\text{HS}}$) and 342 ($T_{1/2}^{\text{LS}}$) K in heating and cooling modes were observed, Figure 16a.

This result is in good agreement with the already reported spin transition values for 4 nm NPs of the same SCO compound.³⁰ Also, some heating and cooling cycles were carried out to cast light on the spin transition reversibility, Figure 16b. The material undergoes some fatigue with the successive cycles, as shown by the decrease the area under the peaks. This is quantified from the area under the endothermic and exothermic curves that change with the successive cycles. Being particularly visible in the exothermic signal, which experiments the larger quenching. This observation suggests an increase in the irreversibility of the process once it switches into the high spin state. In spite of the fatigue suffered by the shell, the different transition temperatures

in the heating and the cooling demonstrate the hysteresis retention in the reduced SCO shell.

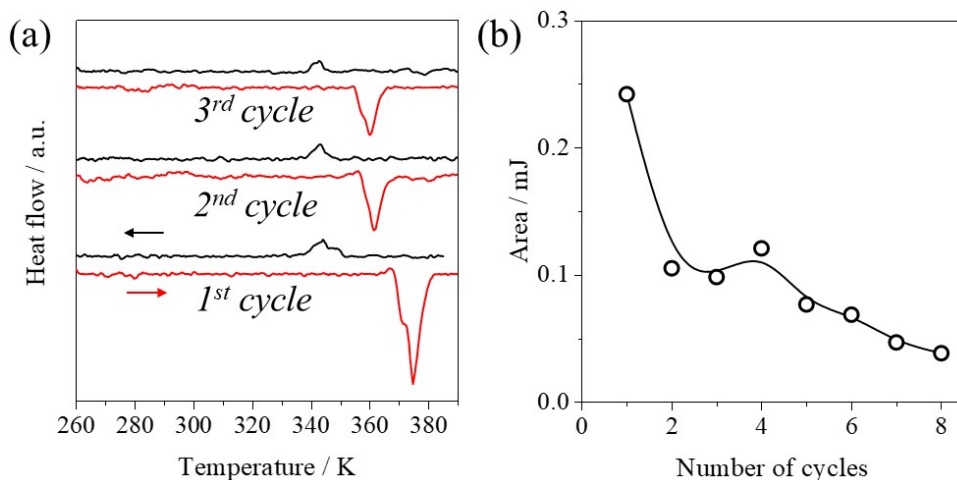


Figure 16. (a) Three DSC curves of Au@SCO-1, heating in red and cooling in black. (b) Plot of the area under the endothermic peak (red in a), as a function of the number of cycles performed.

5.3.1.g. Electrical characterization

The electrical properties of the Au@SCO-1 were investigated by organizing the NPs between gold interpenetrated fingerprint electrodes with a gap of 10 μm , Figure 17a. The organization was achieved by DEP, which is carried out by drop casting 5mM ethanolic solution of Au@SCO-1, between the electrodes and applying an AC voltage (for more information, see the experimental section). These measurements were carried out in collaboration with Julien Dugay at the ICMol. Scanning electron microscopy (SEM) and AFM images performed revealed a dense and thin assembly of NPs between the electrodes, Figure 17.

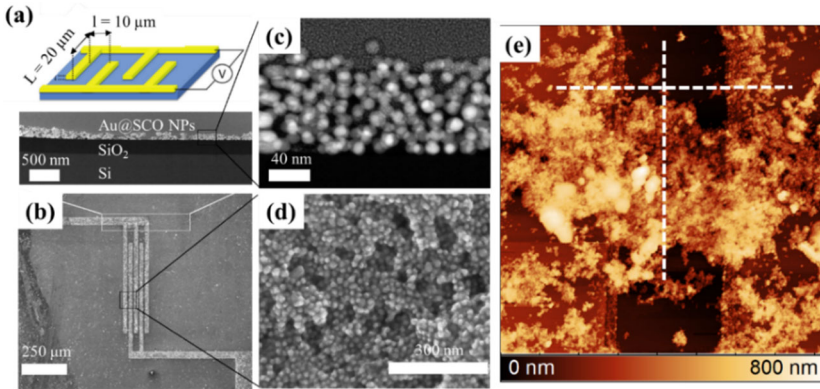


Figure 17. Au@SCO-I device for electrical characterization (a) Scheme and dimensions of the electrodes (top); STEM transversal cross-section of the device (bottom). A zoom of this image to show the packing of the NPs is displayed in (c). (b) SEM image of the device (top view). A zoom of this image is shown in (d). (e) AFM image of the particles between two electrodes.

To prove the proper NPs packing and contact with the electrodes, current-voltage (I–V) curves were recorded before and after the deposition, Figure 18a. After the deposition, two out of twelve devices (17%) displayed a clear increase in conductance compared to the empty gap, indicating that several particles in parallel were contacting the electrodes. The low percentage of success reflected the difficulty in preparing such devices.

The I–V curves in the LS and HS inside the hysteresis, at 325 K and 355 K, are shown in Figure 18b. Remarkably, the Au@SCO-1 exhibited a relatively higher current in the nA range in the LS state (red). These conductance values were well above the detection limit of the apparatus (in the pA range) and, therefore, were measured with good accuracy. As the current values were in the pA range in the HS state, the signal is less accurate and noisy (blue). It was observed that, despite the large gap between electrodes, the conductance values in the present device were comparable or

higher than those reported in previous works with much smaller gaps, table 3.

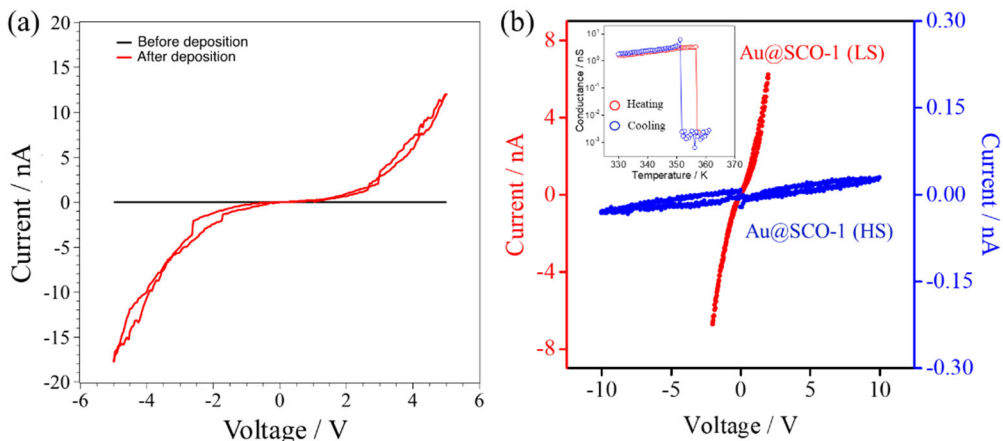


Figure 18. (a) Room temperature I - V curves before and after the electrophoresis of Au@SCO-1 are compared. Changes in the transport-characteristics can then be attributed to the presence of hybrid Au@SCO-1 in the gap. (b) I - V curves of the high-conductive (red) and low-conductive (blue) behaviours associated with the LS (325 K) and HS (355 K), respectively. Inset: Thermal variation of the electrical current for an applied voltage of 2 V in the heating and cooling modes at $1 \text{ K}\cdot\text{min}^{-1}$ scan rate.

Such improvement in the conductance is mainly attributed to the presence of the Au core, which does enhance the conductance of these core@shell NPs, thus facilitating the charge transport through the device.

Table 3. Summary of the already published conductance values of SCO NPs under similar conditions

| <i>Reference</i> | <i>NPs</i> | <i>Size (μm)</i> | <i>Gap (μm)</i> | <i>Voltage (V)</i> | <i>E (V/μm)</i> | <i>Conductance LS (S)</i> | <i>Conductance HS (S)</i> |
|-------------------|------------|--|---------------------------------------|--------------------|---------------------------------------|---------------------------|---------------------------|
| This work | Au@SCO | 0.02 | 10 | 2 | 0.2 | 3×10^{-9} | 2×10^{-12} |
| [³] | SCO@AOT | 0.01 | 0.01 | 0.4 | 40 | 0.5×10^{-9} | 0.9×10^{-9} |
| [³] | SCO@AOT | 0.01 | 0.01 | 0.4 | 40 | 2×10^{-11} | 6×10^{-11} |
| [³¹] | SCO | nanometric | - | 0.5 | - | 10^{-12} | - |
| [⁴] | SCO@AOT | ca. 0.030 | 0.1 | 10 | 100 | 0.2×10^{-9} | 0.1×10^{-9} |
| [⁴] | SCO-rods | 3 | 4 | 10 | 2.5 | 0.5×10^{-9} | 0.3×10^{-9} |
| [⁴] | SCO-rods | 0.25 | 4 | 10 | 2.5 | 0.4×10^{-11} | 0.1×10^{-11} |
| [³²] | SCO-rods | 2 | 4 | 20 | 5 | 1×10^{-12} | 1×10^{-13} |
| [⁶] | SCO-rods | 1 | 4 | 20 | 5 | 1×10^{-10} | 5×10^{-11} |
| [⁵] | SCO@AOT | 0.025 | 0.05 | 15 | 300 | 8×10^{-11} | 4×10^{-12} |

5.3.2. Optimization of the Fe^{2+} in the shell

The same synthetic protocol was carried out in a N_2 to increase the percentage of Fe^{2+} and, as a result, the atoms susceptible to switch their spin state. This hybrid is called from now on Au@SCO-2. The morphology of Au@SCO-2 was similar to its analogue synthesized in air, Figure 19a. To evaluate the amount of Fe^{2+} atoms, the XPS of Au@SCO-2 was carried out, Figure 19b-d. Focusing on the iron region, the Fe^{2+} peak at 708.9 eV was higher than the Fe^{3+} multiplet at 711.2 and 715.4 eV. This indicated a larger amount of Fe^{2+} in the SCO shell, which is quantified as a $\sim 36\%$.

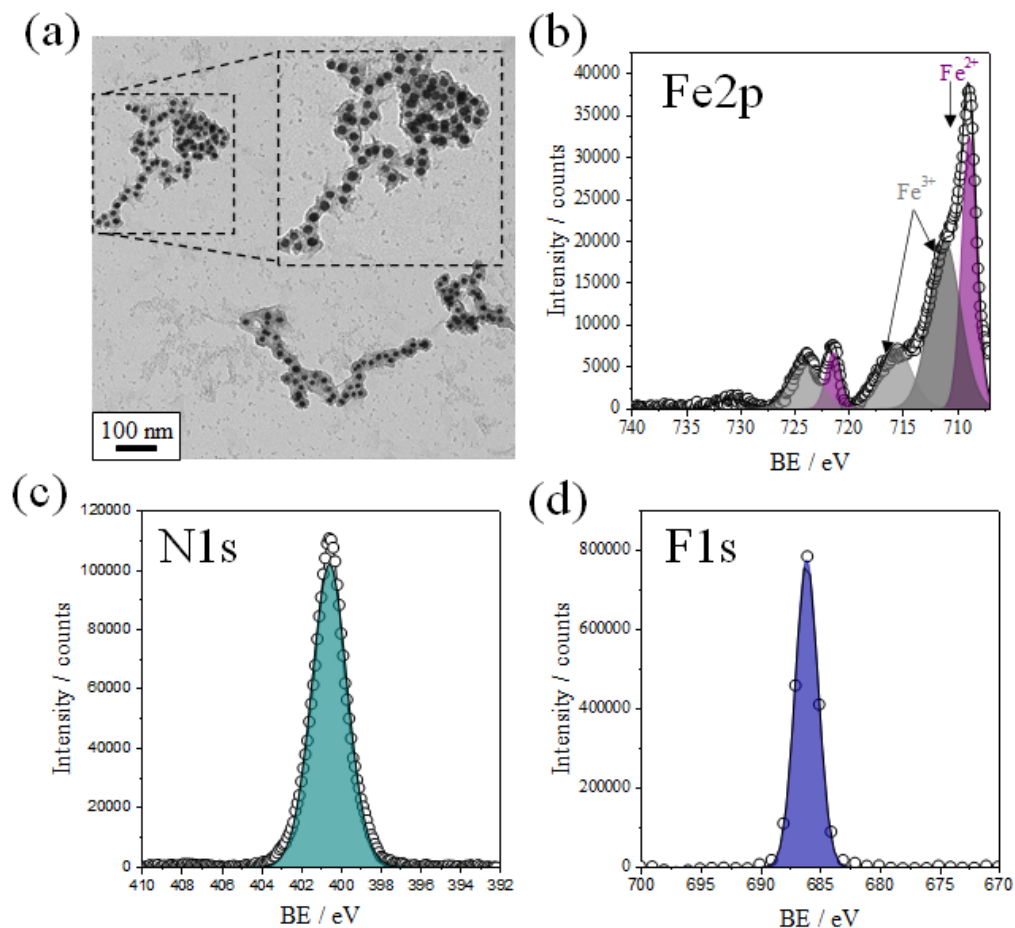


Figure 19. (a) TEM images of Au@SCO-2. (b-d) XPS spectra of Fe2p, N1s and F1s regions of the same NPs.

So far, no electrical characterization has been carried out for Au@SCO-2, but it will be done in the near future.

5.3.3. Hybrid system based on gold nanostars as core

The synthetic protocol explored in section 5.2.1. was expanded to other gold nanostructures under an inert atmosphere. In this context, we synthesized gold nanostars and used them as nucleation seeds to grow the SCO, Figure 20. Additionally, the stability of the iron shell was investigated by XPS.

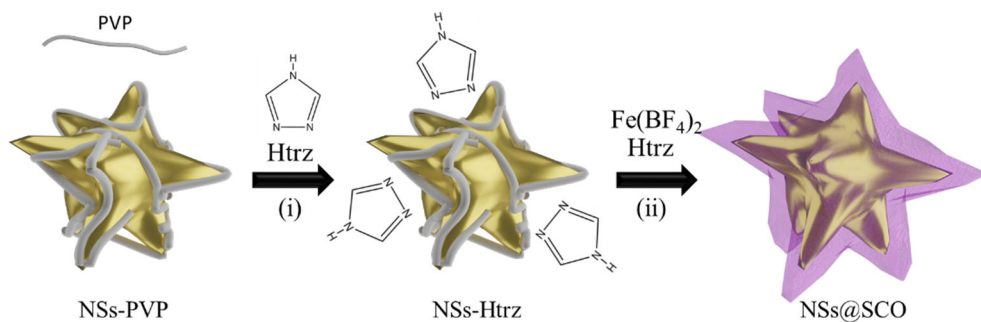


Figure 20. Scheme of the synthetic protocol followed to obtain the hybrid NSs@SCO NPs.

5.3.3.a. Synthesis of Gold nanostars

The synthesis of the nanostars, NSs, was done using nanospheres prepared by the turkevich method, followed by growing the branches. To do so, HAuCl₄ and AgNO₃ were added to the gold nanospheres (~12 nm) solution, followed by the addition of ascorbic acid to the mixtures. The ascorbic acid reduces the HAuCl₄ to metallic gold, which grows around the preformed nanospheres while the AgNO₃ forces the asymmetric growth.³³ Finally, a poly(vinylpolypyrrolidone) (PVP) solution was added to stabilize the NSs, thus, acting as capping.

The star-like morphology was confirmed by TEM, where nanostars of 74 ± 13 nm in diameter were obtained, Figure 21a. As has been previously introduced, the gold NSs optical response differs drastically with respect to that of the spheres, Figure 21b. Due to the different sizes and shapes, the LSPR of this structure was far more complex than for the classical spheres, showing a broader LSPR band located around 700 nm.

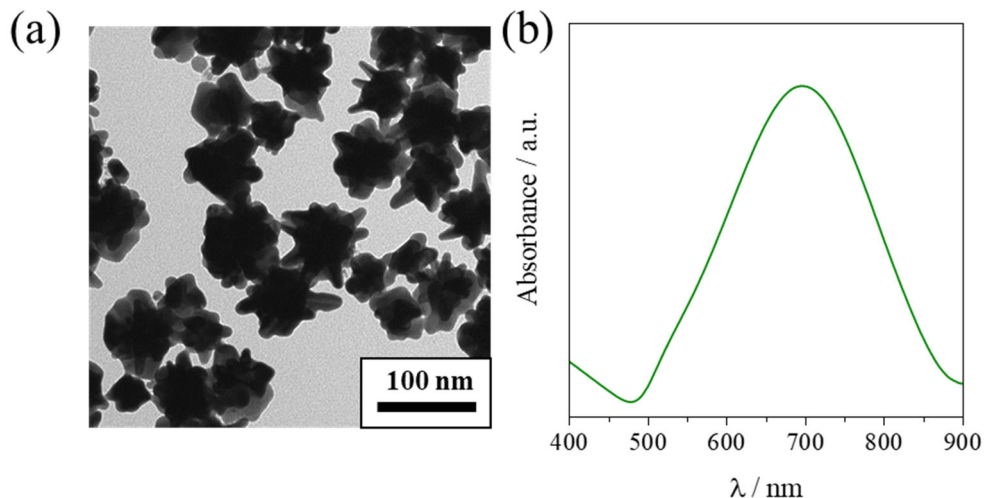


Figure 21. (a) TEM image of the Au NSs. (b) UV-VIS spectra of the same nanostructures suspended in water.

5.3.3.b. Synthesis of the $Fe(Htrz)_2(trz)$ shell

To cover the NSs with the SCO material, NSs@SCO, we added Htrz to the Au NSs solution to introduce the nucleation center, followed by the alternative addition of metal and ligand. All the steps were carried out under N_2 atmosphere.

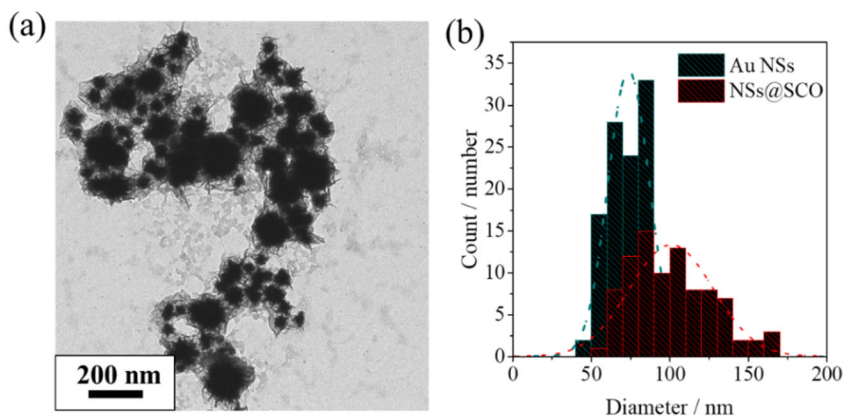


Figure 22. TEM image of NSs@SCO (a), and the diameter distribution of the core, in dark cyan, and core@shell, in red, (b).

Once the reaction was completed, the morphology of the resulting system was investigated by TEM. As Figure 22a-b shows, a clear shell ~14 nm grew around the Au NSs. Once more, the iron distribution in the core@shell was investigated by EDX mapping, showing the iron wrapping the gold core, Figure 23a-b. The change in dielectric constant around the gold feature was also evidenced by the plasmon band shift from ~700 nm, in the unmodified Au NSs, to 740 nm in the NSs@SCO, Figure 23c.

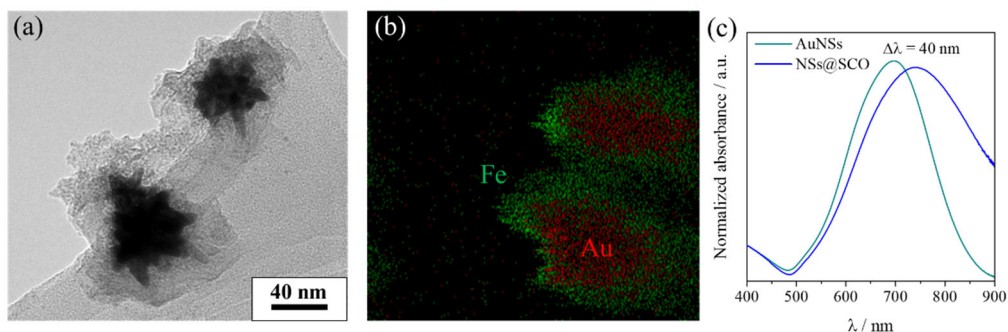


Figure 23. (a) NSs@SCO TEM image and (b) EDX mapping of the same image. In green the Fe, and red the Au. (c) UV-VIS of the Au NSs (green) and the NSs@SCO (blue).

5.3.3.c. NSs@SCO spin transition

The spin transition of the core@shell was investigated by DSC, Figure 24a-b. Focusing on the first heating process (red line), a clear endothermic peak at 376 K can be discerned. This band was attributed to the first spin transition from LS to HS. Similarly, when the material was cooled down, an exothermic peak appears at 339 K, associated with the LS recovery. This proved the presence of a SCO compound, and the transition temperatures matched with the $\text{Fe}(\text{Htrz})_2(\text{trz})(\text{BF}_4)$. After this first transition, the exothermic peak experienced a shift to lower temperatures (360 K). This is a general issue in this SCO compound, where the first transition occurs at

higher temperatures and with a broader hysteresis. This is attributed to the presence of solvent molecules in the structure or the fatigue associated with the transition that is more significant in the first cycle.³⁴ Interestingly the $T_{1/2}^{LS}$ was always maintained constant. Another important feature to consider is that, in contrast with the previously discussed Au@SCO-1, the NSs@SCO does not experience remarkable fatigue. The exothermic and endothermic bands of the NSs@SCO remain similar upon the first four thermal cycles, Figure 24b.

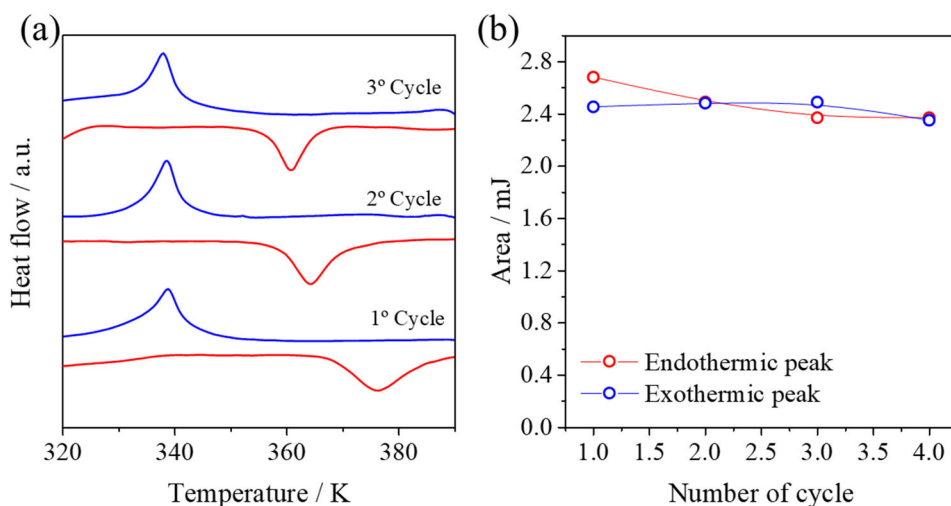


Figure 24. (a) three DSC curves of NSs@SCO, heating in red and cooling in black. (b) Plot of the area under the endothermic and exothermic peaks (red in a), as a function of the number of cycles performed.

From these results, we can conclude that the cooperativity of the system remains unaffected after the first spin transition, and it is improved with respect to the Au@SCO-1. This may be due to the thicker shell and the presence of a larger number of Fe^{2+} susceptible to switch their spin state.

5.3.3.d. NSs@SCO oxidation

To investigate the evolution of the shell in air, the amount of Fe^{2+} in NSs@SCO was quantified in freshly prepared samples and after one day in the air, Figure 25.

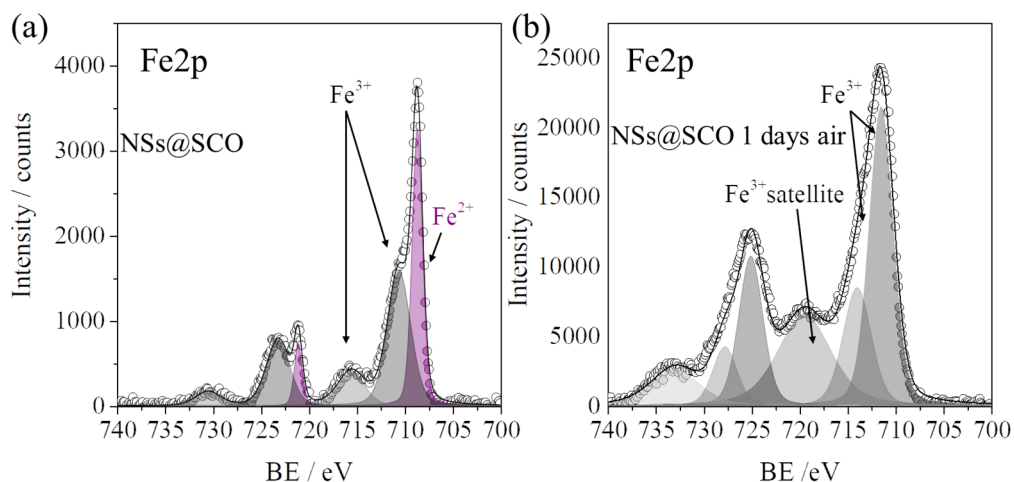


Figure 25. Fe2p XPS spectra of NSs@SCO (a) and NSs@SCO after 1 day in the air (b).

As shown in the Fe2p region, NSs@SCO freshly prepared display a prominent Fe^{2+} signal at 708.7 eV and a minor Fe^{3+} multiplet at 710.6 and 715.6 eV. After one day in open air, the spectrum of this sample changed completely, vanishing the Fe^{2+} signal. This indicates that after one day of O_2 exposure, the oxidation of the shell is complete. The estimated percentage of Fe^{2+} in freshly prepared NSs@SCO and after one day is ~ 43 vs 0 %,.. Therefore, we conclude that the SCO shell completely oxidizes after one day at ambient conditions.

5.4. Conclusions and perspectives

Herein, we have developed and explored a synthetic protocol to cover colloiddally stable gold nanostructures with the spin crossover compound $\text{Fe}(\text{Htrz})_2(\text{trz})(\text{BF}_4)$. This methodology permits the synthesis of heterostructures by using colloiddally stable nucleation seeds. In this thesis, we cover the use of gold nanospheres and nanostars as seeds, but this protocol can be expanded to other coordination polymers or metallic NPs. Therefore, it is presented as an exciting approach to synthesize hybrid metalorganic/inorganic core@shell structures with controlled shell thickness.

Focusing on the gold@SCO nanospheres treated in section 5.2.1. the hybrid system retains the spin switching even for shells as thin as 4 nm. Even more, the fact that the core@shell is capping free can facilitate its post-functionalization. From the electrical point of view, the hybrid exhibits a superior electrical performance, recording currents in the nA range when a voltage of 2 V is applied. This voltage is around one order of magnitude lower than the typical one employed to obtain similar values in the bare NPs. Nevertheless, the iron ions at the interphase of the core@shell are highly susceptible to oxidize. To improve this the synthesis has been carried out at inert atmosphere, obtaining a substantial increase of the Fe^{2+} in the shell, a ~10 % at air and a ~40% at inert environment. Additionally, this same synthesis has been expanded to gold nanostars as core, obtaining a thicker shell, which exhibits a clear and reproducible spin transition without fatigue signs.

In the future, this system will be encapsulated in protective polymers of capping agents to prevent the shell from oxidizing, and this synthetic approach will be applied to other metallic nanostructures as nucleation seeds.

5.5. Bibliography

- (1) Kahn, O.; Martinez, C. J. Spin-Transition Polymers: From Molecular Materials toward Memory Devices. *Science*. **1998**, *279* (5347), 44–48. <https://doi.org/10.1126/science.279.5347.44>.
- (2) Lefter, C.; Rat, S.; Costa, J. S.; Manrique-Juárez, M. D.; Quintero, C. M.; Salmon, L.; Séguy, I.; Leichle, T.; Nicu, L.; Demont, P.; Rotaru, A.; Molnár, G.; Bousseksou, A. Current Switching Coupled to Molecular Spin-States in Large-Area Junctions. *Adv. Mater.* **2016**, *28* (34), 7508–7514.
- (3) Prins, F.; Monrabal-Capilla, M.; Osorio, E. A.; Coronado, E.; Van Der Zant, H. S. J. Room-Temperature Electrical Addressing of a Bistable Spin-Crossover Molecular System. *Adv. Mater.* **2011**, *23* (13), 1545–1549.
- (4) Rotaru, A.; Dugay, J.; Tan, R. P.; Guralskiy, I. A.; Salmon, L.; Demont, P.; Carrey, J.; Molnár, G.; Respaud, M.; Bousseksou, A. Nano-Electromanipulation of Spin Crossover Nanorods: Towards Switchable Nanoelectronic Devices. *Adv. Mater.* **2013**, *25* (12), 1745–1749.
- (5) Dugay, J.; Giménez-Marqués, M.; Kozlova, T.; Zandbergen, H. W.; Coronado, E.; Van Der Zant, H. S. J. Spin Switching in Electronic Devices Based on 2D Assemblies of Spin-Crossover Nanoparticles. *Adv. Mater.* **2015**, *27* (7), 1288–1293.
- (6) Lefter, C.; Tan, R.; Tricard, S.; Dugay, J.; Molnár, G.; Salmon, L.; Carrey, J.; Rotaru, A.; Bousseksou, A. On the Stability of Spin

Crossover Materials: From Bulk Samples to Electronic Devices. *Polyhedron* **2015**, *102*, 434–440.

- (7) Holovchenko, A.; Dugay, J.; Giménez-Marqués, M.; Torres-Cavanillas, R.; Coronado, E.; van der Zant, H. S. J. Near Room-Temperature Memory Devices Based on Hybrid Spin-Crossover@SiO₂Nanoparticles Coupled to Single-Layer Graphene Nanoelectrodes. *Adv. Mater.* **2016**, *28* (33).
- (8) Senthil Kumar, K.; Ruben, M. Emerging Trends in Spin Crossover (SCO) Based Functional Materials and Devices. *Coord. Chem. Rev.* **2017**, *346*, 176–205.
- (9) Molnár, G.; Rat, S.; Salmon, L.; Nicolazzi, W.; Bousseksou, A. Spin Crossover Nanomaterials: From Fundamental Concepts to Devices. *Adv. Mater.* **2018**, *30* (5), 1–23.
- (10) Koo, Y. S.; Galán-Mascarós, J. R. Spin Crossover Probes Confer Multistability to Organic Conducting Polymers. *Adv. Mater.* **2014**, *26* (39), 6785–6789.
- (11) Chen, Y. C.; Meng, Y.; Ni, Z. P.; Tong, M. L. Synergistic Electrical Bistability in a Conductive Spin Crossover Heterostructure. *J. Mater. Chem. C* **2015**, *3* (5), 945–949.
- (12) Rat, S.; Piedrahita-Bello, M.; Salmon, L.; Molnár, G.; Demont, P.; Bousseksou, A. Coupling Mechanical and Electrical Properties in Spin Crossover Polymer Composites. *Adv. Mater.* **2018**, *30* (8), 1–6.
- (13) Qiu, D.; Ren, D. H.; Gu, L.; Sun, X. L.; Qu, T. T.; Gu, Z. G.; Li, Z. Spin Crossover-Graphene Nanocomposites: Facile Syntheses,

- Characterization, and Magnetic Properties. *RSC Adv.* **2014**, *4* (59), 31323–31327.
- (14) Dugay, J.; Aarts, M.; Gimenez-Marqués, M.; Kozlova, T.; Zandbergen, H. W.; Coronado, E.; Van Der Zant, H. S. J. Phase Transitions in Spin-Crossover Thin Films Probed by Graphene Transport Measurements. *Nano Lett.* **2017**, *17* (1), 186–193.
- (15) Bousseksou, A.; Molnár, G.; Demont, P.; Menegotto, J. Observation of a Thermal Hysteresis Loop in the Dielectric Constant of Spin Crossover Complexes: Towards Molecular Memory Devices. *J. Mater. Chem.* **2003**, *13* (9), 2069–2071.
- (16) Lefter, C.; Gural'skiy, I. A.; Peng, H.; Molnár, G.; Salmon, L.; Rotaru, A.; Bousseksou, A.; Demont, P. Dielectric and Charge Transport Properties of the Spin Crossover Complex $[\text{Fe}(\text{Htrz})_2(\text{Trz})](\text{BF}_4)$. *Phys. Status Solidi. Rapid Res. Lett.* **2014**, *8* (2), 191–193.
- (17) Lefter, C.; Davesne, V.; Salmon, L.; Molnár, G.; Demont, P.; Rotaru, A.; Bousseksou, A. Charge Transport and Electrical Properties of Spin Crossover Materials: Towards Nanoelectronic and Spintronic Devices. *Magnetochemistry* **2016**, *2* (1), 18.
- (18) Mayer, K. M.; Hafner, J. H. Localized Surface Plasmon Resonance Sensors. *Chem. Rev.* **2011**, *111* (6), 3828–3857.
- (19) Miller, M. M.; Lazarides, A. A. Sensitivity of Metal Nanoparticle Surface Plasmon Resonance to the Dielectric Environment. *J. Phys. Chem. B* **2005**, *109* (46), 21556–21565.

- (20) Qiu, D.; Gu, L.; Sun, X. L.; Ren, D. H.; Gu, Z. G.; Li, Z. SCO@SiO₂@Au Core-Shell Nanomaterials: Enhanced Photo-Thermal Plasmonic Effect and Spin-Crossover Properties. *RSC Adv.* **2014**, 4 (106), 61313–61319.
- (21) Suleimanov, I.; Sánchez Costa, J.; Molnár, G.; Salmon, L.; Bousseksou, A. The Photothermal Plasmonic Effect in Spin Crossover@silica–Gold Nanocomposites. *Chem. Commun.* **2014**, 50 (86), 13015–13018.
- (22) Moulet, L.; Daro, N.; Mornet, S.; Vilar-Vidal, N.; Chastanet, G.; Guionneau, P. Grafting of Gold onto Spin-Crossover Nanoparticles: SCO@Au. *Chem. Commun.* **2016**, 52 (90), 13213–13216.
- (23) Palluel, M.; Tran, N. M.; Daro, N.; Buffière, S.; Mornet, S.; Freysz, E.; Chastanet, G. The Interplay between Surface Plasmon Resonance and Switching Properties in Gold@Spin Crossover Nanocomposites. *Adv. Funct. Mater.* **2020**, 2000447, 1–9.
- (24) Turkevich, J. Colloidal Gold. *Gold Bull.* **1985**, 18 (4), 125–131.
- (25) Kumar, A.; Dixit, C. K. Methods for Characterization of Nanoparticles. *Adv. Nanomedicine Deliv. Ther. Nucleic Acids* **2017**, 44–58.
- (26) Chen, H.; Kou, X.; Yang, Z.; Ni, W.; Wang, J. Shape- and Size-Dependent Refractive Index Sensitivity of Gold Nanoparticles. *Langmuir* **2008**, 24 (10), 5233–5237.
- (27) Lee, K. S.; El-Sayed, M. A. Gold and Silver Nanoparticles in Sensing and Imaging: Sensitivity of Plasmon Response to Size, Shape, and

- Metal Composition. *J. Phys. Chem. B* **2006**, *110* (39), 19220–19225.
- (28) Park, J. W.; Shumaker-Parry, J. S. Structural Study of Citrate Layers on Gold Nanoparticles: Role of Intermolecular Interactions in Stabilizing Nanoparticles. *J. Am. Chem. Soc.* **2014**, *136* (5), 1907–1921.
- (29) Chaffin, E. A.; Bhana, S.; O'Connor, R. T.; Huang, X.; Wang, Y. Impact of Core Dielectric Properties on the Localized Surface Plasmonic Spectra of Gold-Coated Magnetic Core-Shell Nanoparticles. *J. Phys. Chem. B* **2014**, *118* (49), 14076–14084.
- (30) Giménez-Marqués, M.; García-Sanz De Larrea, M. L.; Coronado, E. Unravelling the Chemical Design of Spin-Crossover Nanoparticles Based on Iron(II)-Triazole Coordination Polymers: Towards a Control of the Spin Transition. *J. Mater. Chem. C* **2015**, *3* (30), 7946–7953.
- (31) Rotaru, A.; Gural'skiy, I. A.; Molnár, G.; Salmon, L.; Demont, P.; Bousseksou, A. Spin State Dependence of Electrical Conductivity of Spin Crossover Materials. *Chem. Commun.* **2012**, *48* (35), 4163–4165.
- (32) Lefter, C.; Tan, R.; Dugay, J.; Tricard, S.; Molnár, G.; Salmon, L.; Carrey, J.; Rotaru, A.; Bousseksou, A. Light Induced Modulation of Charge Transport Phenomena across the Bistability Region in [Fe(Htrz)₂(Trz)](BF₄) Spin Crossover Micro-Rods. *Phys. Chem. Chem. Phys.* **2015**, *17* (7), 5151–5154.
- (33) Barbosa, S.; Agrawal, A.; Rodríguez-Lorenzo, L.; Pastoriza-Santos,

- I.; Alvarez-Puebla, R. A.; Kornowski, A.; Weller, H.; Liz-Marzán, L. M. Tuning Size and Sensing Properties in Colloidal Gold Nanostars. *Langmuir* **2010**, *26* (18), 14943–14950.
- (34) Brooker, S. Spin Crossover with Thermal Hysteresis: Practicalities and Lessons Learnt. *Chem. Soc. Rev.* **2015**, *44* (10), 2880–2892.
- (35) Galán-Mascarós, J. R.; Coronado, E.; Forment-Aliaga, A.; Monrabal-Capilla, M.; Pinilla-Cienfuegos, E.; Ceolin, M. Tuning Size and Thermal Hysteresis in Bistable Spin Crossover Nanoparticles. *Inorg. Chem.* **2010**, *49* (12), 5706–5714.
- (36) Herrera, J. M.; Titos-Padilla, S.; Pope, S. J. A.; Berlanga, I.; Zamora, F.; Delgado, J. J.; Kamenev, K. V.; Wang, X.; Prescimone, A.; Brechin, E. K.; Colacio, E. Studies on Bifunctional Fe(II)-Triazole Spin Crossover Nanoparticles: Time-Dependent Luminescence, Surface Grafting and the Effect of a Silica Shell and Hydrostatic Pressure on the Magnetic Properties. *J. Mater. Chem. C* **2015**, *3* (30), 7819–7829.

5.6. Experimental section

5.6.1. Equipment

X-ray Photoelectron Spectroscopy (XPS): Samples are analyzed *ex-situ* at the X-ray Spectroscopy Service at the Universidad de Alicante using a K-ALPHA Thermo Scientific spectrometer. All spectra are collected using Al K α radiation (1486.6 eV), monochromatized by a twin crystal monochromator, yielding a focused X-ray spot (elliptical in shape with a major axis length of 400 μ m) at 30 mA and 2 kV. The alpha hemispherical analyzer is operated in the constant energy mode with survey scan pass energies of 200 eV to measure the whole energy band and 50 eV in a narrow scan to selectively measure the particular elements. Charge compensation is achieved with the system flood gun that provides low energy electrons and low energy argon ions from a single source.

Scanning transmission electron microscopy (STEM): EDS experiments of SCO@SiO₂ are performed using an Oxford Instruments X-MaxN 100TLE detector. The elemental maps are produced by collecting an EDS spectrum for each position of the electron beam in the scanned area. This scanned area is selected from an Annular Dark Field (ADF) STEM image. Carbon contamination was excluded or minimized using a MEMS heating device to remove water from the sample. The SiN support film of the MEMS heater was previously removed with etching to enable mapping of NPs suspended above a hole. Sample preparation was done placing a drop of the NPs suspended in a solvent on a carbon coated copper grid obtained from Agar Scientific.

High-resolution transmission electron microscopy (HR-TEM) and transmission electron microscopy (TEM): HR-TEM studies are carried out on a Technai G2 F20 microscope operating at 200 kV and TEM studies on a JEM-1010 operating at 100 kV. Samples are prepared by dropping suspensions on lacey formvar/carbon copper grids (300 mesh).

Dynamic light scattering (DLS) and Zeta Potential (ξ pot): Both values are determined in suspension at room temperature with a Zetasizer Nano ZS instrument (Malvern Instruments Ltd.).

Zeta Potential (ξ pot) measurements: ξ -pot values are measured at room temperature with a Zetasizer Nano ZS instrument (Malvern Instruments Ltd.).

Thermogravimetric analyses (TGA): Samples are measured using a TGA 550 (TA Instruments) at a heating rate of 5 °C/min from 25-700 °C under air.

Transport measurements: All transport measurements have been performed in a Physical Properties Measurement System (Quantum Design, PPMS-9) in the temperature range of 280 K

to 400 K, under vacuum. Disc-shaped pressed powder pellets of the different samples are prepared by applying ca. 0.05 MPa and measured in a two probes configuration. The pellets are contacted through silver paste and Pt wires, maintaining a very close geometry in all samples. Electrical measurements are performed using a Keithley 6517B electrometer as voltage source and to measure current. Conductivity values are calculated as $\sigma = (G \cdot l)/(t \cdot w)$, where G is the measured conductance, l is the distance between electrodes, w the electrodes length, and t the thickness of the pellets. Optical microscopy has been used to estimate these values.

Inductively Coupled-Plasma Optical Emission Spectrometry (ICP-OES): ICP-OES analysis is conducted at the Universidad of Valencia. Samples are digested in nitric acid using a high-pressure microwave oven.

Magnetic susceptibility (SQUID): Magnetic susceptibility measurements are performed on powdered samples with a Quantum Design MPMS-XL-5 SQUID susceptometer. The susceptibility data are corrected from the diamagnetic contributions and deduced by using Pascal's constant tables. The data are collected in the range 300–400 K upon recording several heating-cooling cycles at a constant rate of $1 \text{ K} \cdot \text{min}^{-1}$ with an applied field of 0.1 T.

UV/Vis Spectroscopy: UV-vis absorption spectra are recorded on a Jasco V-670 spectrophotometer in baseline mode from 400 to 800 nm range, using 1.000-cm-optical-path plastic cuvettes.

5.6.2. Methods

Materials. All chemical reagents are purchased and used without further purification: Tetraethyl orthosilicate 98% (Sigma-Aldrich), Triton X-100 (Sigma-Aldrich), ascorbic acid (Sigma-Aldrich), 1,2,4-triazole (Sigma-Aldrich), iron tetrafluoroborate hexahydrate (Sigma-Aldrich), *n*-hexanol (Sigma-Aldrich), cyclohexane (Sigma-Aldrich), ethanol absolute (Sigma-Aldrich) ultra-pure water (18.2 M Ω). SiO₂ (285 nm)/Si substrates are bought from NOVA Electronic Materials LLC, Flower Mound, TX. (Sigma-Aldrich), chloroauric acid (Sigma-Aldrich), sodium citrate tribasic dihydrate (Sigma-Aldrich), silver nitrate (Sigma-Aldrich), Sodium borohydride (Sigma-Aldrich), and Polyvinylpyrrolidone 40000 wt (Sigma-Aldrich).

5.6.3. Fe(Htrz)₂(trz)(BF₄)@SiO₂ core-shell NPs

SCO@SiO₂-1

An aqueous solution of Fe(BF₄)₂·6H₂O (0.5 mL, 1.25 M) and tetraethyl orthosilicate (TEOS) (0.1 mL) is added to a freshly prepared mixture containing Triton X-100 (1.8 mL, ω = 9), n-hexanol (1.8 mL), cyclohexane (7.5 mL). A microemulsion of this mixture is obtained by stirring at room temperature for 15 minutes. Then, an aqueous solution of 1,2,4-1H-triazole (0.5 mL, 3.75 M) ligand containing the TEOS (0.1 mL) is added to a similarly prepared organic solution and stirred at room temperature for 15 min. In order to permit a micellar exchange, both microemulsions are combined and stirred for 24 h. The formed nanoparticles are isolated by precipitation upon addition of acetone and collected by centrifugation (12000 rpm, 10 min), followed by washing with ethanol (x4 times), to remove the excess of surfactant, and acetone (x1 time). Finally, the powdered samples are dried at 70°C for 2 h.

SCO@SiO₂-2

SCO@SiO₂-2 were prepared following the same synthetic procedure as in NP 1, but adding Fe(BF₄)₂·6H₂O (0.5 mL, 1.5 M), and 1,2,4-1H-triazole (0.5 mL, 4.5 M). Later the NPs precipitation is carried out after 2 h of micellar exchange.

SCO@SiO₂-3

The synthesis of SCO@SiO₂-3 is performed like 2 but using 2 mL of Triton X.100.

SCO@SiO₂-4

The smallest NPs are synthesised like 2 but using 2.7 mL of Triton X.100.

Gold nanospheres

Citrate-stabilized gold NPs of 12.4 ± 1.0 nm are synthesized following the Turkevich method by Roger Sanchis-Gual.

Gold nanostars

100 μl of the previously prepared gold NPs are added on 10 ml of HAuCl_4 (0.25 mM). Later, 10 μl of HCl (1M) is added to the mixture. Finally, 50 μl of ascorbic acid (0.1 M), and 100 μl of AgNO_3 (3 mM) are added to growth the branches, followed by the addition of and 100 μl of PVP (10g/l) to stabilize the NPs.

Au@SCO-1

Into 3ml of an aqueous solution of citrate-stabilized Au NPs ($0.16 \cdot 10^{-3}$ M) a solution of Htrz ligand ($0.5 \cdot 10^{-3}$ M) is added, and let it react for 30 min. Later an aqueous solution of the $\text{Fe}(\text{BF}_4)_2$ ($0.16 \cdot 10^{-3}$ M) precursor and Htrz ligand ($0.5 \cdot 10^{-3}$ M) are simultaneously added at a constant rate of 4 mL h^{-1} , at room temperature and under stirring.

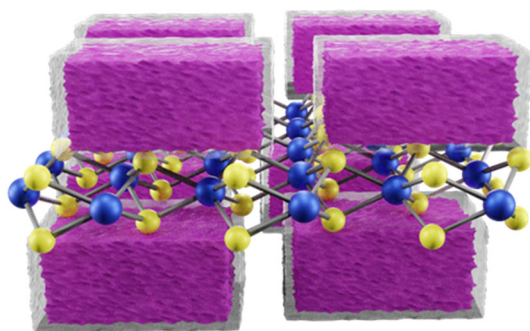
Au@SCO-2

An analogue synthesis than Au@SCO-1 is carried out under N_2 atmosphere.

NSs@ SCO-1

NSs@SCO-1 is synthesized like Au@SCO-1 but adding as nucleation center Gold NSs.

PART III



6

INTRODUCTION TO MoS₂ STRAIN ENGINEERING

6.1. 2D materials

Two dimensional (2D) materials are defined as crystalline solids that can be isolated as one atom or few atoms thick layers, exhibiting quantum confinement effects. These materials present many advantages with respect to their bulk counterparts.^{1,2} For instance, the in-plane electron confinement provides singular electronic properties.^{3–6} Also, due to the covalent nature of the in-plane bonds and their atomic thickness, they exhibit exceptional mechanical strength, flexibility, and optical transparency.^{7,8} Another important advantage intrinsic to their 2D nature is the large surface area, which provides a high exposure of the atoms at the surface.^{8,9} Due to this last feature, the properties of the 2D materials can be easily tuned through chemical functionalization, elemental doping, creation of defects, or strain engineering.^{10–14}

The flagship of the 2D world is graphene, an atom thick carbon layer that was first isolated in 2004 by micromechanical cleavage of graphite, Figure 1.¹⁵ Despite the expected instability of graphene, it was proved to be highly inert. Even more, their electrical properties differed dramatically from their 3D counterpart, becoming a zero-bandgap semimetal.^{16,17} The very high-charge carrier mobility at room temperature, $\sim 10\,000\text{ cm}^2\text{ V}^{-1}\text{ s}^{-1}$, optical transparency, and robustness made graphene a desirable material for several electronic applications.^{1,18}

This break-through motivated the researchers to expand the exfoliation methodologies developed for graphene to other layered materials. Indeed, several 2D materials have been isolated over the past years from their bulk crystals (top-down approaches)²⁰ or even directly synthesized (bottom-up

approaches).^{8,19,20} They range from mono-atomically thick layers like, boron nitride, to more complex structures, like the transition metal dichalcogenides.⁸ Remarkably, the different materials exhibit entirely different properties, displaying a high degree of versatility from the point of view of their applications in practical devices.

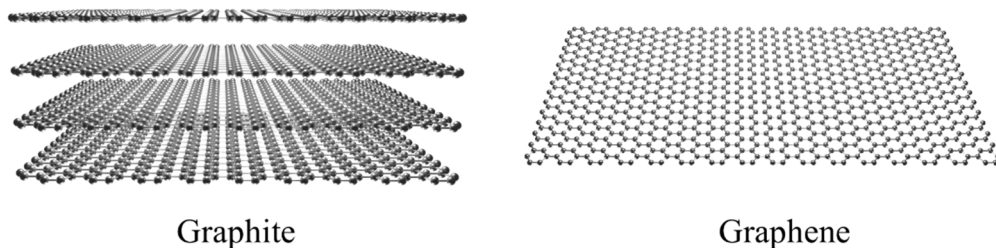


Figure 1. Scheme of graphite (left) and graphene (right)

6.2. Transition metal dichalcogenides

Transition metal dichalcogenides (TMDCs) are layered compounds with the general chemical formula MX_2 , where M is a transition metal element (M= groups 4 to 10) and X represents a chalcogen (X = S, Se, and Te) in the oxidation states +4 and -2, respectively. Each TMDC layer consists of a three atoms thick slab, where a transition metal layer is sandwiched between two chalcogen layers, displaying a thickness of $\sim 6\text{-}7 \text{ \AA}$, Figure 2.²¹ The intra-layer M–X bonds are predominantly covalent, whereas like in graphene weak van der Waals forces couple the layers. This weak interaction can be easily broken, isolating a single layer while the in-plane bonds remain intact. The absence of dangling bonds in the basal plane renders stability against degradation or oxidation, despite their high exposure.

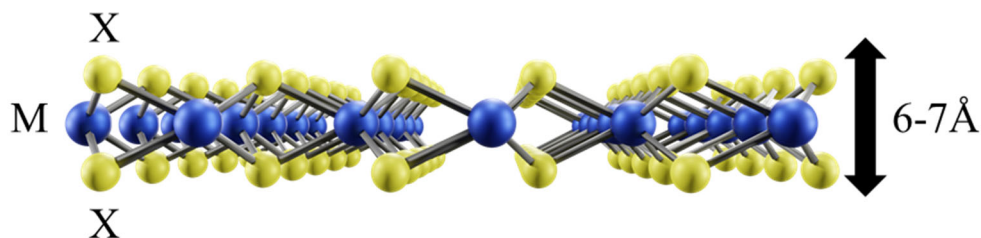


Figure 2. MX_2 single layer structure, X in yellow, and M in blue.

6.2.1. Crystalline phase

Generally, TMDCs can be presented in different phases or polytypes, where an alphanumeric code names each one. In this code, a letter indicates the crystal symmetry (T = Tetragonal, H = Hexagonal, R = Rhombohedral), while a number refers to the number of X-M-X layers per unit cell. The most common polytypes are the hexagonal phase, 2H, the rhombohedral, 3R, or the tetragonal, 1T. In the different polytypes, the metallic centers can present either octahedral in 1T, or trigonal prismatic coordination in 2H and 3R, Figure 3.¹³

In the octahedral form, the d orbitals of the transition metal centers are split into the triple degenerated d_{yz} , d_{xz} , d_{xy} , and the double degenerate d_z^2 , $d_{x^2-y^2}$ levels, Figure 3 (1T-phase). In contrast, in the trigonal prismatic coordination three subsets, d_z^2 ; $d_{x^2-y^2}$, d_{xy} ; and d_{xz} , d_{yz} are formed, Figure 3 (2H-phase). As can be seen in Figure 3b, the difference between 2H and 3R is the symmetry of the stacked layers. Therefore, single layers of TMDCs can only be in either H or T phase.

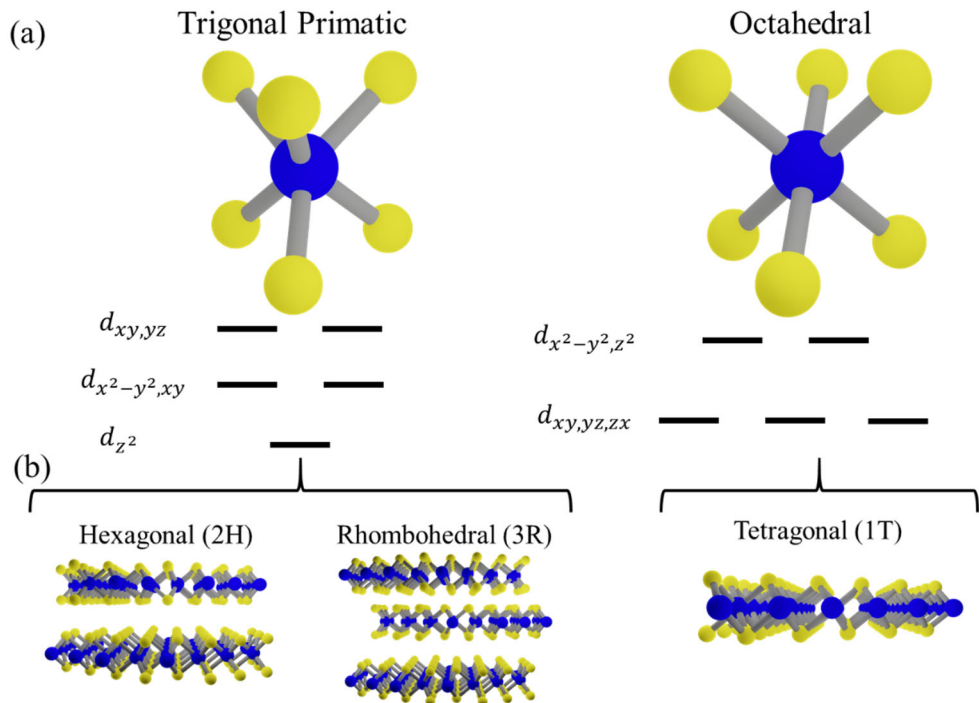


Figure 3. Scheme of atomic structure for TMDCs a) *d*-orbital splitting depending on the coordination. b) TMDCs polytypes.

Regarding the more stable coordination environment, it mainly depends on the transition metal *d*-electron count, table 1. Group 4 TMDCs (M^{4+} having d^0 electrons) prefer the octahedral coordination, whereas both octahedral and trigonal prismatic phases can be seen in group 5 ($M^{4+} = d^1$). Group 6 ($M^{4+} = d^2$) prefers the trigonal prismatic geometry, and group 7 ($M^{4+} = d^3$) a distorted octahedral structure, 1T'. Finally, Group 10 ($M^{4+} = d^6$) are all in a pure octahedral structure. This dependence is due to the progressive filling of the molecular orbitals, which stabilize one or other phase.²²

Table 1. Summary of phases and electrical properties of the TMDCs depending on the group of the metal. Extracted from 22.

| Group | M | X | Phase | Properties |
|-------|------------|-----------|-------|---|
| 4 | Ti, Hf, Zr | S, Se, Te | 2H | Semiconductors |
| 5 | V, Nb, Ta | S, Se, Te | 1T/2H | Metals or semimetals |
| 6 | Mo, W | S, Se, Te | 2H | Semiconductors, except tellurides that are semimetals |
| 7 | Tc, Re, | S, Se, Te | 1T' | Small-gap semiconductors |
| 10 | Pd, Pt | S, Se, Te | 1T | Semiconductors, except tellurides that are metallic |

The importance of knowing the adopted coordination environment arises from the fact that it defines the physical properties of the TMDC. For instance, TMDCs with partially filled orbitals (like 2H-NbSe₂ or 1T-ReS₂) exhibit metallic conductivity, while those with fully occupied orbitals (like 1T-HfS₂ or 2H-MoS₂) are semiconductive, table 1.²³

6.3. Molybdenum disulfide

Among all the TMDCs Molybdenum disulfide (MoS₂) is the most studied one. For many years, it has been used as a lubricant,²⁴ catalysts for hydrodesulfurization,²⁵ or electrocatalysis.²⁶ As Mo is a group 6 transition metal, the trigonal prismatic coordination is favourable (2H), being in bulk an indirect bandgap semiconductor, with a gap of ~ 1.2 eV.²⁷

6.3.1. Exfoliated 2H-MoS₂

Like graphene and the rest of layered materials, when the 2H-MoS₂ is exfoliated down to the monolayer, it changes its physical properties.²⁸ To understand this dependency, an insight into its band structure is required. In

bulk, MoS₂ bandgap is located between the conduction-band at the K and the Γ -point of the valence-band, Figure 4. The conduction-band states are mainly formed by d orbitals of the Mo atoms. These orbitals are located in between the chalcogen layers, and they are relatively unaffected by the interlayer coupling. In contrast, the states of the valence band near the Γ -point are mainly formed by p_z orbitals of the S hybridized with Mo d orbitals. These p_z orbitals are located at the surface of the layer, and they are strongly affected by the interlayer coupling.²⁹ As can be seen in Figure 4, in the case of 2H-MoS₂ monolayer the Γ -point changes due to the lack of interlayer coupling, becoming a direct gap semiconductor, ~1.9 eV.

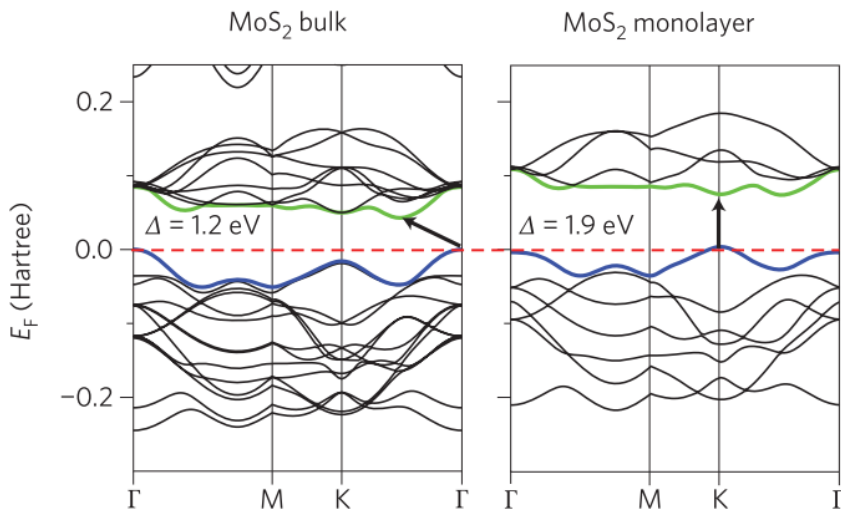


Figure 4. Band structure of 2H-MoS₂ bulk and 2H-MoS₂ single layer, left and right, respectively. Adapted from reference 28.

6.3.2. Exfoliated 1T-MoS₂

Although 2H polytype is the thermodynamically stable, it is possible to obtain the 1T polytype by phase engineering. Remarkably, 1T-MoS₂ presents completely different electrical and optical properties compared with its

hexagonal counterpart.^{30,31} Accordingly, with their band structure (Figure 5) bulk, and exfoliated 1T-MoS₂ are metals.^{32–34}

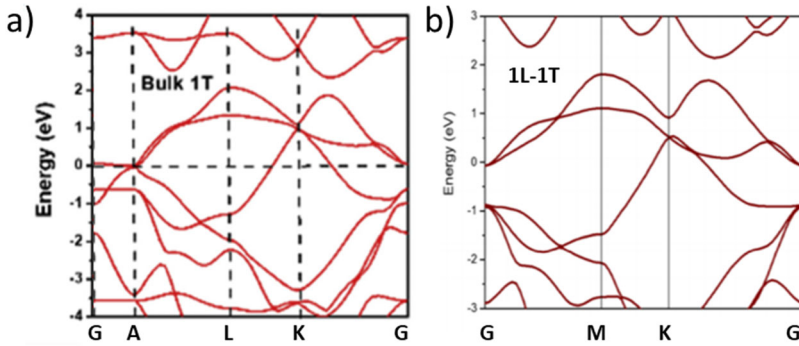


Figure 5. Band structure of bulk 1T-MoS₂ and single layer, a and b, respectively. Adapted from references 32,33.

Therefore, in electrochemical reactions and energy storage applications, the 1T phase presents a superior performance, as the electrical resistance is dramatically reduced with respect to the 2H phase.^{31,35,36} Besides, its semi-transparency offers new opportunities for the development of transparent 2D electronic conductors. For all these reasons, the synthesis of bulk and exfoliated 1T-MoS₂ is highly desirable. Nevertheless, the obtainment and stabilization of the metallic 1T-MoS₂ are still challenging.

6.4. From bulk to single layer

As has been commented, MoS₂ properties are highly dependent on the number of layers and polytype. Thus, for the further study of their physical and chemical properties, precise control on the thickness and phase is mandatory. In this context, several methodologies have been developed in the past years to control the thickness and polytype of the resulting MoS₂.²⁸ Depending on the mechanism employed to obtain the 2D material, the

techniques can be divided into two categories, called the top-down and the bottom-up methodologies.

The top-down approach involves all the procedures in which the 2D layer is exfoliated from a parent crystal.⁸ In this category, we can find the classical mechanical cleavage, as other liquid phase techniques like mechanical force-assisted exfoliation, ion intercalation-assisted exfoliation, ion exchange-assisted exfoliation, oxidation-assisted exfoliation, or selective etching-assisted exfoliation

In contrast, the bottom-up approach relies on the reaction of a certain precursor to form the 2D layer, while the experimental conditions control the dimensionality.⁸ Good examples of this approach are the CVD growth, the wet-chemical synthesis, and the thermal decomposition of a precursor.

In this thesis, we focus on the ion intercalation-assisted liquid exfoliation (top-down), to obtain thin sheets of MoS₂. Thus, only this technique will be explained in more detail below.

6.4.1. Ion intercalation-Assisted Liquid Exfoliation

This is the most employed technique to exfoliate 2H-MoS₂ in solution. The underlying idea is the weakening of the van der Waals interactions between layers via the intercalation of ions into the 2H-MoS₂ interlayer space.³⁷ The intercalated compound will significantly expand the space between layers decreasing the interlayer coupling. At the same time, that can inject charges inside the layers leading to chemically reduced layers. For these reasons, the intercalated mixture can be easily exfoliated into single- or few-layers under mild sonication for a short time.^{38,39}

The most used compound, and the one used during this thesis, is the *n*-butyl lithium (*n*-BuLi), which reduces the MoS₂ layers (creating negatively charged layers) and provides Li⁺ cations that are integrated between the layers. The exfoliation protocol is shown in Figure 6, where 2H-MoS₂ bulk is firstly intercalated with *n*-BuLi to form the compound Li_xMoS₂. The intercalation weakens the coupling between the layers, facilitating their splitting. Later the intercalated Li_xMoS₂ is dispersed in water and exfoliated under mild sonication.

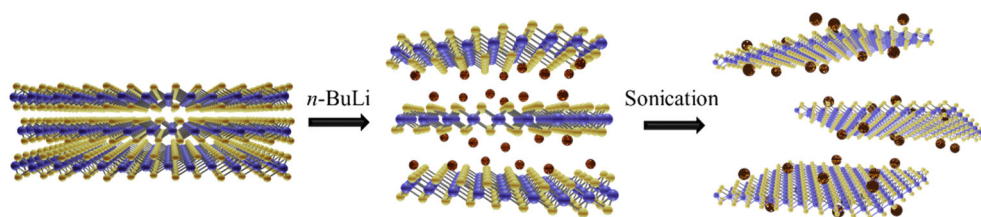


Figure 6. Scheme of the MoS₂ exfoliation.

The main advantage of this technique is the high yield of single- and few-layers. Even more, the resulting suspension is colloidally stable for weeks due to the presence of negative charges in the MoS₂ layers. Remarkably, the phase of the MoS₂ is changed to 1T during the intercalation.

6.5. Functionalization of chemically exfoliated MoS₂

An interesting approach to modify the physical and chemical properties of exfoliated MoS₂ relies on its molecular functionalization. Several researchers have focused on this topic because the MoS₂ functionalization can be used to protect the exfoliated material from oxidation or degradation, improve its processability, or prepare multifunctional materials.^{40,42}

In this sense, there are two main types of functionalization depending on the bonding or interaction that maintains together the MoS₂ and the molecule used to functionalize it: via non-covalent and covalent interactions, Figure 7.⁴³

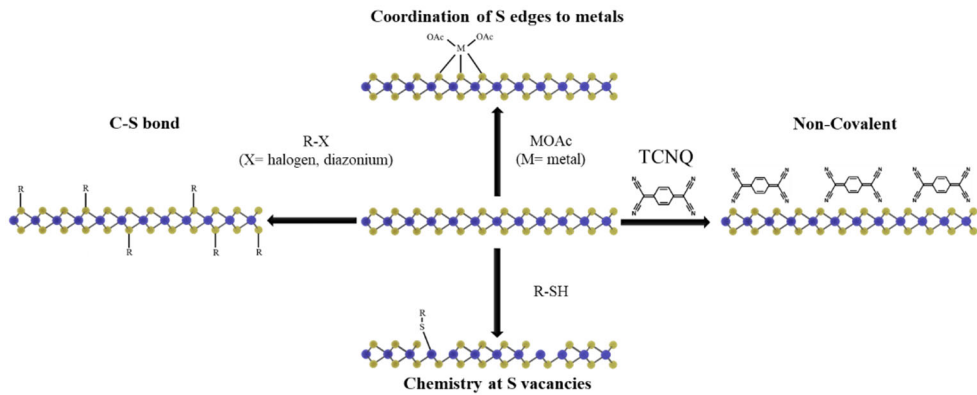


Figure 7. Scheme of the different types of MoS₂ functionalizations: Non-Covalent, Covalent forming C-S bonds, Chemistry at S vacancies, and Coordination of S edges to metals.

6.5.1. Non-covalent functionalization

The non-covalent molecular functionalization involves the attachment of the molecules via weak van der Waals, or electrostatic interactions, Figure top. This approach has been vastly employed to alter the physical and chemical properties of exfoliated 2H-MoS₂.⁴³ For instance, by depositing on top of the 2D material molecules like tetracyanoquinodimethane (TCNQ),^{44,45} tetracyanoethylene (TCNE),¹⁰ tetrathiafulvalene (TTF),¹⁰ benzyl viologen (BV),⁴⁶ Cs₂CO₃,⁴⁷ fullerenes,⁴⁸ or phthalocyanides,⁴⁹ a charge transfer between the molecule and the MoS₂ occurs, doping negatively or positively the MoS₂. This alters its electrical and optical response. The main disadvantage of this approach is its fragility due to the weak interaction between molecule and MoS₂.

6.5.2. Covalent functionalization

The covalent approach involves forming covalent bonds between the 2D layer and the selected molecules to obtain a strong interaction between both systems, Figure . Therefore, to develop strategies for the edge and in-plane covalent functionalization, three main approaches have been explored: (1) direct C-S bond formation (2) coordination of S edges to metals (3) chemistry at S vacancies.

6.5.2.a. C-S bond formation

The S at the 2D interphase and edges have a modest nucleophilic character, which can be used to react with electrophiles to form new bonds. In this context, mainly two types of molecules have been used as electrophiles, organohalides, and diazonium salts. Unfortunately, the MoS₂ basal plane in the 2H phase tends to be rather inert; thus, examples of this kind are scarce.⁵⁰ It is worth to mention, that recently a soft approach to functionalize the basal plane of exfoliated 2H-MoS₂ has been developed by Emilio Pérez et al.^{50,51} The approach is based on the use of maleimide derivatives as electrophiles, which can react with soft nucleophiles like 2H-MoS₂, obtaining efficiencies of the 4%.⁵²

In contrast to the 2H phase functionalization, exfoliated 1T-MoS₂ via *n*-BuLi treatment is far more reactive thanks to the negative charges at the MoS₂ surface that increase the nucleophilicity of the basal plane S. For the case of the organohalides, the reaction occurs between these nucleophilic S and the electrophile carbon bonded to the halide, C-X (X = Br or I).⁵³⁻⁵⁷ Using these molecules and 1T-MoS₂, functionalization as high as ~20% can be achieved. Noticeably, the physical properties of the MoS₂ are seriously affected by the

functionalization. This was unequivocally proved by Voiry et al., where the metallic 1T-MoS₂ recovered its semiconductive behaviour after the reaction with 2-iodoacetamide.⁵³

Moving to the use of diazonium salts, these types of molecules have been widely employed to functionalize graphene or carbon nanotubes, thanks to the possibility to form a free radical from the diazonium salt, which attacks the sp² carbons forming a covalent bond.⁵⁸ This same protocol was successfully applied on 1T-MoS₂ by several authors, forming covalent bonds between the diazonium molecule and the 2D layer.^{59–62} However, the functionalization efficiency seems to be lower (only a~7%).

6.5.3.b. Coordination of S edges to metals

This approach relies on coordinating the MoS₂ to metals through the sulphur atoms, Figure bottom. For instance, the coordination of metallic complexes by 2H-MoS₂ was explored by Bakes et al. mixing exfoliated 2H-MoS₂ with M(OAc)₂ (M=Zn, Cu, Ni, and OAc= acetate), leading to (2H) MoS₂-M(OAc)₂.⁶³ Similarly, Pramoda et al. decorated 1T-MoS₂ with the Zeolitic imidazolate framework-8 (ZIF-8), a metal-organic framework based on Zn.⁶⁴ In this work, the authors suggested that the 1T-MoS₂ permits more efficient coordination of the Zn centers.

6.5.3.c. Chemistry at S vacancies

This last approach consists of filling the S vacancies occupancy by organothiols. Organothiols can covalently interact^{65,66} or just get physisorbed^{67,68} on S vacancies, leading to MoS₂ functionalized with the organic molecule.^{10,69–71}

6.6. Phase engineering

The MoS₂ physical properties can be modified by tuning the 2D polytype, called phase engineering.¹⁴ The switch from 1T to 2H is easily achieved by heating, aging, irradiation with NIR or microwaves, Figure 8.^{72–75} This is due to the higher stability of the hexagonal MoS₂ phase.

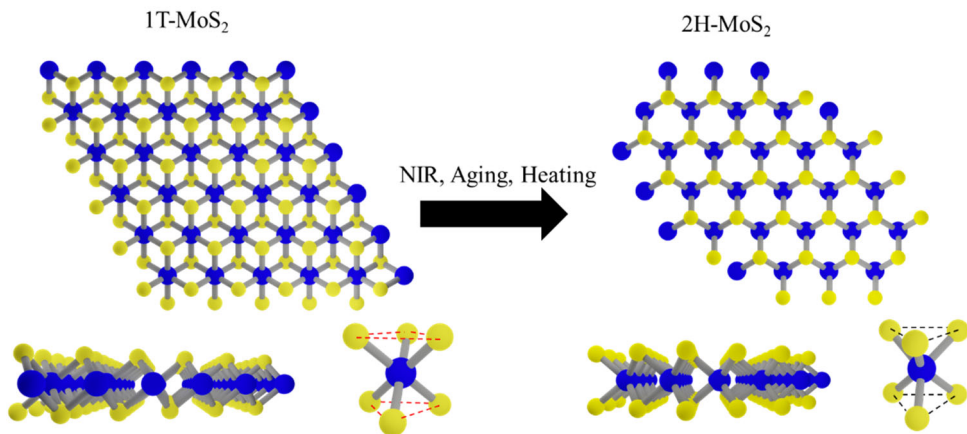


Figure 8. Interconversion from 1T to 2H. Top and side view of 2H-MoS₂ and 1T-MoS₂, top and down, respectively.

In contrast, the reverse process is more challenging. Several researchers have studied the phase transition from 2H to 1T by different techniques.^{13,14,76} All of them are based on the increase of electron density in the metal or on the direct mechanical deformation of the layer. The most important techniques can be divided into five groups, strain engineering, creation of S-vacancies, chemical intercalation, electron injection, and chemical induce phase transition, Figure 9.⁷⁶

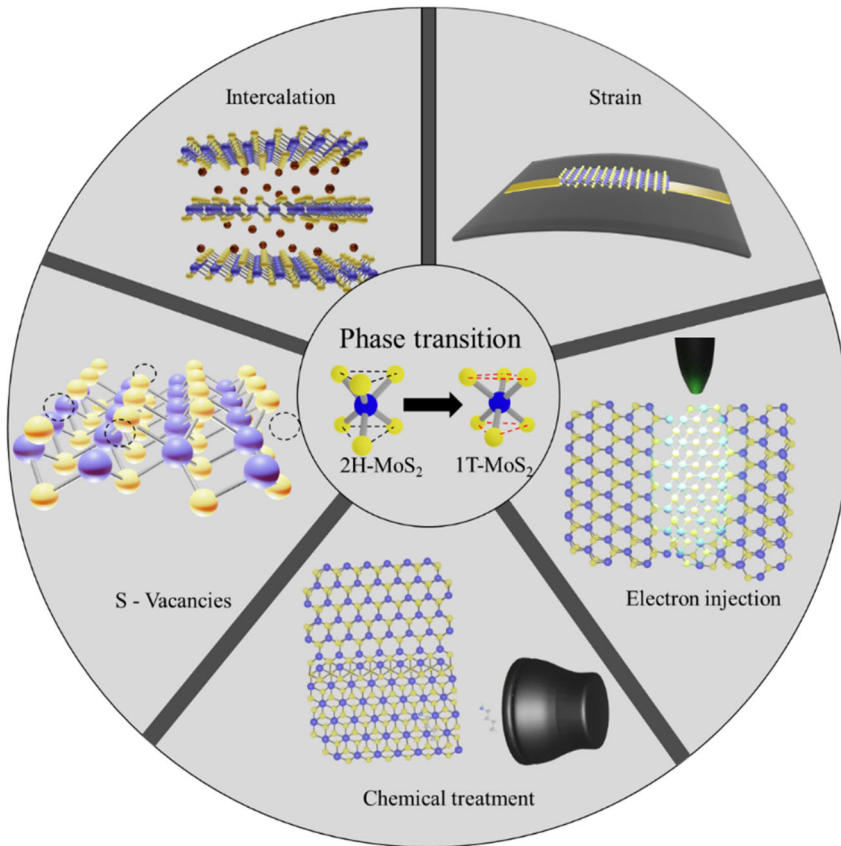


Figure 9. Scheme of the main phase transition techniques used on MoS₂ to switch between 2H and 1T phase.

6.6.1. Strain Engineering

The band structure of semiconductors can be strongly perturbed by mechanical strain, giving rise to the possibility of using mechanical deformation to tune their electronic and photonic performance.⁷⁷ This principle, known as strain engineering, has been used for a long time in semiconductor device manufacturing.

From the point of view of MoS₂, the introduction of strain originates an elongation or shortening of the atomic Mo-S bonds, altering the lattice symmetry. As a result, the electronic structure of the material is changed.^{78,79}

For instance, the application of tensile strain increases the Mo-Mo and Mo-S length, reducing the orbital hybridization and hence the bandgap (Figure 10).⁸⁰ Accordingly to theoretical calculations, under the application of a 1-2% of tensile strain, the direct bandgap of 2H-MoS₂ turns into indirect, and over the 10% to metallic.⁸¹ It must be noticed that MoS₂ can sustain in-plane strain levels as high as 11%, making possible the isolation of the metallic phase before the fracture of the 2D layer.⁸²

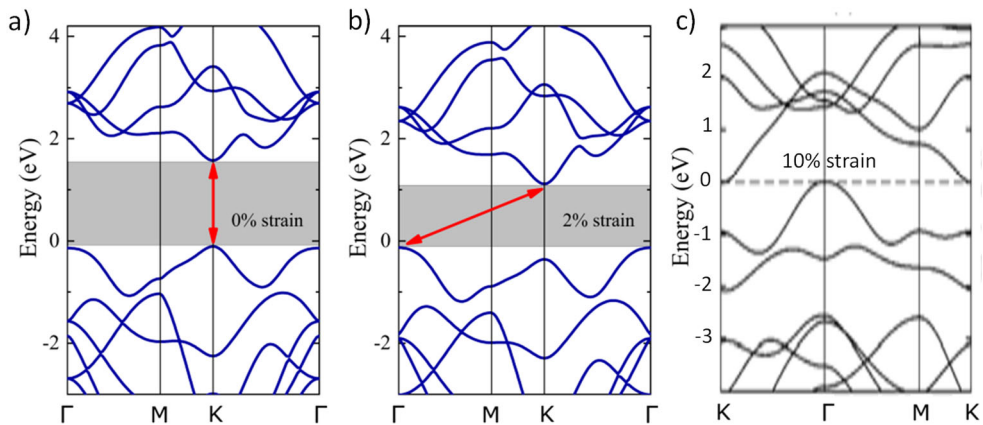


Figure 6. 2H-MoS₂ Energy band structures under different tensile strains: 0, 2, and 10% (a, b and c, respectively). Adapted from references 81,83.

One of the major drawbacks of the 2D strain engineering is the method to apply strain, which often requires indirect stress produced by a substrate or a probe.⁸³⁻⁸⁹ This limits the amount of material susceptible to be stressed, which difficult its practical application in real devices. There are few examples in the literature that overcome this limitation by straining exfoliated MoS₂ by

means of molecular systems.^{90,91} For instance, 2H-MoS₂ layers have been rolled up via N-(2-aminoethyl)-3 α -hydroxy-5 β -cholan-24-amide self-assembly on the surface of the 2D layer. During the self-assembly, the S-plane is glided, inducing the transition to 1T. Ratios of 1T of 58% have been achieved by this technique. Therefore, strain engineering through molecular compounds is presented as an efficient alternative to strain MoS₂.

6.6.2. S vacancies induction

It has been proposed that the H-to-T conversion can be triggered via n-type doping.¹¹ The controlled creation of sulfur vacancies (S_v) dopes the layers negatively due to the S_v acting as electron donors, inducing the phase transition. In this context, mainly two approaches have been employed to produce S_v in MoS₂. The first one is based on introducing S defects by gas treatment; Ar, or O.^{92,93} This treatment can lead to a 40% conversion. The second alternative is the creation of vacancies on MoS₂ nanosheets by a solvothermal treatment or synthesis. The mechanism of the defect creation is still not clear, but by playing with some synthetic parameters, a certain percentage of 1T phase during the synthesis of the MoS₂ or posterior solvothermal treatment is possible.⁹⁴⁻⁹⁸ The maximum conversion obtained by solvothermal treatment falls around 25%.

6.6.3. Chemical/electrochemical intercalation

The layered properties of MoS₂ allow its intercalation with organic molecules, alkali metals, or other systems that fit in the interlayer space.⁹⁹ If the intercalate is an electron donor, it can tune the electron occupancy of the metallic center, thus inducing the conversion to 1T. Plenty of experimental methods have been developed in this line, using different electron donors to

intercalate.¹⁰⁰ Among them, the most widely used is the direct immersion of the 2H-MoS₂ crystals in a solution of the intercalates.^{101,102} Typically, alkali metals are used as intercalants, generating a high ratio of 1T MoS₂. From the point of view of phase transition, DFT calculation has been carried out, showing that at least 12% of the donor needs to be present to trigger the complete conversion from 2H to 1T.^{103,104} Typically, high ratios of 1T conversion (~70-80%) are achieved by this technique.^{96,105,106} Another useful option is the electrochemical intercalation of alkali ions similarly to the chemical intercalation. 1T-MoS₂ fabrication via electrochemical intercalation relies on the interaction of alkali ions (Li⁺ and Na⁺) with the MoS₂ layers stimulated by an external voltage.^{107,108} Using this technique, it is possible to control the intercalation degree precisely and thus, the 1T/2H ratio.

6.6.4. Electron injection

Above, it has been mentioned that the electron transfer from a metal to 2H-MoS₂ plays a key role in the conversion to 1T phase. Recent studies have revealed that electron injections in different forms are also able to trigger this phase transition on mono- or few-layer MoS₂.^{109,110,111} The straightforward method to inject electrons onto 2H-MoS₂ is based on the direct electron beam irradiation. The irradiation will cause the electronic enrichment in the marked area causing the phase transition to 1T.¹⁰⁹

Another interesting approach is the use of hot electrons, coming from a plasmonic NP, to provoke the charge transfer. This has been done by depositing gold NPs on 2H-MoS₂ and irradiating the sample at the wavelength of the NPs localized plasmon resonance.^{110,111}

6.6.5. Chemical induced phase transition

Through the exposure of 2H-MoS₂ to chemical vapours of strong electron donors (e.g., butylamine, or triethylamine) the phase transition to 1T also occurs. In this case, the stabilization of the 1T phase is caused by the electron donation of the vapours to the metallic center.¹¹²

6.7. Bibliography

1. Jagadish, C. & Weber, E. R. *2D materials: Properties and devices*. (2011).
2. Stanford, M. G., Rack, P. D. & Jariwala, D. Emerging nanofabrication and quantum confinement techniques for 2D materials beyond graphene. *npj 2D Mater. Appl.* **2**, (2018).
3. Geim, A. K. & Novoselov, K. S. The rise of graphene. *Nanosci. Technol. A Collect. Rev. from Nat. Journals* 11–19 (2009)
4. Li, X. *et al.* Graphene and related two-dimensional materials: Structure-property relationships for electronics and optoelectronics. *Appl. Phys. Rev.* **4**, (2017).
5. Chhowalla, M., Jena, D. & Zhang, H. Two-dimensional semiconductors for transistors. *Nat. Rev. Mater.* **1**, 1–15 (2016).
6. Li, S. L., Tsukagoshi, K., Orgiu, E. & Samori, P. Charge transport and mobility engineering in two-dimensional transition metal chalcogenide semiconductors. *Chem. Soc. Rev.* **45**, 118–151 (2016).
7. Lee, C., Wei, X., Kysar, J. W. & Hone, J. Measurement of the elastic properties and intrinsic strength of Monolayer Graphene. **321**, 385–

- 388 (2008).
8. Tan, C. *et al.* Recent Advances in Ultrathin Two-Dimensional Nanomaterials. *Chem. Rev.* **117**, 6225–6331 (2017).
 9. Stoller, M. D., Park, S., Yanwu, Z., An, J. & Ruoff, R. S. Graphene-Based ultracapacitors. *Nano Lett.* **8**, 3498–3502 (2008).
 10. Nguyen, E. P. *et al.* Electronic Tuning of 2D MoS₂ through Surface Functionalization. *Adv. Mater.* **27**, 6225–6229 (2015).
 11. Luo, P. *et al.* Doping engineering and functionalization of two-dimensional metal chalcogenides. *Nanoscale Horizons* **4**, 26–51 (2019).
 12. Chen, X. & McDonald, A. R. Functionalization of Two-Dimensional Transition-Metal Dichalcogenides. *Adv. Mater.* **28**, 5738–5746 (2016).
 13. Voiry, D., Mohite, A. & Chhowalla, M. Phase engineering of transition metal dichalcogenides. *Chem. Soc. Rev.* **44**, 2702–2712 (2015).
 14. Shi, S., Sun, Z. & Hu, Y. H. Synthesis, stabilization and applications of 2-dimensional 1T metallic MoS₂. *J. Mater. Chem. A* **6**, 23932–23977 (2018).
 15. Novoselov, K. S. *et al.* Two-dimensional atomic crystals. *Proc. Natl. Acad. Sci. U. S. A.* **102**, 10451–10453 (2005).
 16. Novoselov, K. S. *et al.* Two-dimensional gas of massless Dirac fermions in graphene. *Nature* **438**, 197–200 (2005).
 17. Castro Neto, A. H., Guinea, F., Peres, N. M. R., Novoselov, K. S. & Geim, A. K. The electronic properties of graphene. *Rev. Mod. Phys.*

- 81**, 109–162 (2009).
18. K. S. Novoselov, A. K. Geim, S. V. Morozov, D. Jiang, Y. Zhang, S. V. Dubonos, I. V. G. and A. A. F. Electric Field Effect in Atomically Thin Carbon Films. **306**, 666–669 (2016).
 19. Mas-Ballesté, R., Gómez-Navarro, C., Gómez-Herrero, J. & Zamora, F. 2D materials: To graphene and beyond. *Nanoscale* **3**, 20–30 (2011).
 20. Nicolosi, V., Chhowalla, M., Kanatzidis, M. G., Strano, M. S. & Coleman, J. N. Liquid exfoliation of layered materials. *Science*. **340**, 72–75 (2013).
 21. Wilson, J. A. & Yoffe, A. D. The transition metal dichalcogenides discussion and interpretation of the observed optical, electrical and structural properties. *Adv. Phys.* **18**, 193–335 (1969).
 22. Chhowalla, M. *et al.* The chemistry of two-dimensional layered transition metal dichalcogenide nanosheets. *Nat. Chem.* **5**, 263–275 (2013).
 23. Kolobov, A. V & Tominaga, J. *Two-Dimensional Transition-Metal Dichalcogenides*. (Springer, 2016).
 24. Lansdown, A. R. *Molybdenum disulphide lubrication*. (1999).
 25. Mom, R. V., Louwen, J. N., Frenken, J. W. M. & Groot, I. M. N. In situ observations of an active MoS₂ model hydrodesulfurization catalyst. *Nat. Commun.* **10**, 1–8 (2019).
 26. Laursen, A. B., Kegnaes, S., Dahl, S. & Chorkendorff, I. Molybdenum sulfides - Efficient and viable materials for electro - And

- photoelectrocatalytic hydrogen evolution. *Energy Environ. Sci.* **5**, 5577–5591 (2012).
27. Kuc, A., Zibouche, N. & Heine, T. Influence of quantum confinement on the electronic structure of the transition metal sulfide TS₂. *Phys. Rev. B - Condens. Matter Mater. Phys.* **83**, 1–4 (2011).
 28. Wang, Q. H., Kalantar-Zadeh, K., Kis, A., Coleman, J. N. & Strano, M. S. Electronics and optoelectronics of two-dimensional transition metal dichalcogenides. *Nat. Nanotechnol.* **7**, 699–712 (2012).
 29. Splendiani, A. *et al.* Emerging photoluminescence in monolayer MoS₂. *Nano Lett.* **10**, 1271–1275 (2010).
 30. Acerce, M., Voiry, D. & Chhowalla, M. Metallic 1T phase MoS₂ nanosheets as supercapacitor electrode materials. *Nat. Nanotechnol.* **10**, 313–318 (2015).
 31. Lukowski, M. A. *et al.* Enhanced hydrogen evolution catalysis from chemically exfoliated metallic MoS₂ nanosheets. *J. Am. Chem. Soc.* **135**, 10274–10277 (2013).
 32. He, H. *et al.* Structural Properties and Phase Transition of Na Adsorption on Monolayer MoS₂. *Nanoscale Res. Lett.* **11**, 0–7 (2016).
 33. Jayabal, S., Wu, J., Chen, J., Geng, D. & Meng, X. Metallic 1T-MoS₂ nanosheets and their composite materials: Preparation, properties and emerging applications. *Mater. Today Energy* **10**, 264–279 (2018).
 34. Zhao, W. *et al.* Metastable MoS₂: Crystal Structure, Electronic Band Structure, Synthetic Approach and Intriguing Physical Properties.

- Chem. - A Eur. J.* **24**, 15942–15954 (2018).
35. Tan, C. *et al.* Preparation of High-Percentage 1T-Phase Transition Metal Dichalcogenide Nanodots for Electrochemical Hydrogen Evolution. *Adv. Mater.* **30**, 1–9 (2018).
 36. Li, Y. *et al.* MoS₂ nanoparticles grown on graphene: An advanced catalyst for the hydrogen evolution reaction. *J. Am. Chem. Soc.* **133**, 7296–7299 (2011).
 37. Dines, M. B. Lithium intercalation via n-Butyllithium of the layered transition metal dichalcogenides. *Mater. Res. Bull.* **10**, 287–291 (1975).
 38. Joensen, P., Frindt, R. F. & Morrison, S. R. Single-layer MoS₂. *Mater. Res. Bull.* **21**, 457–461 (1986).
 39. Morant-Giner, M. *et al.* Prussian Blue@MoS₂ Layer Composites as Highly Efficient Cathodes for Sodium- and Potassium-Ion Batteries. *Adv. Funct. Mater.* **28**, 1–11 (2018).
 40. Zhang, X., Lai, Z., Tan, C. & Zhang, H. Solution-Processed Two-Dimensional MoS₂ Nanosheets: Preparation, Hybridization, and Applications. *Angew. Chemie - Int. Ed.* **55**, 8816–8838 (2016).
 41. Liu, K. K. *et al.* Growth of large-area and highly crystalline MoS₂ thin layers on insulating substrates. *Nano Lett.* **12**, 1538–1544 (2012).
 42. Bertolazzi, S., Gobbi, M., Zhao, Y., Backes, C. & Samorì, P. Molecular chemistry approaches for tuning the properties of two-dimensional transition metal dichalcogenides. *Chem. Soc. Rev.* **47**, 6845–6888

- (2018).
43. Stergiou, A. & Tagmatarchis, N. Molecular Functionalization of Two-Dimensional MoS₂ Nanosheets. *Chem. - A Eur. J.* **24**, 18246–18257 (2018).
 44. Jing, Y., Tan, X., Zhou, Z. & Shen, P. Tuning electronic and optical properties of MoS₂ monolayer via molecular charge transfer. *J. Mater. Chem. A* **2**, 16892–16897 (2014).
 45. Mouri, S., Miyauchi, Y. & Matsuda, K. Tunable photoluminescence of monolayer MoS₂ via chemical doping. *Nano Lett.* **13**, 5944–5948 (2013).
 46. Kiriya, D., Tosun, M., Zhao, P., Kang, J. S. & Javey, A. Air-stable surface charge transfer doping of MoS₂ by benzyl viologen. *J. Am. Chem. Soc.* **136**, 7853–7856 (2014).
 47. Lin, J. D. *et al.* Electron-doping-enhanced trion formation in monolayer molybdenum disulfide functionalized with cesium carbonate. *ACS Nano* **8**, 5323–5329 (2014).
 48. Baek, J. *et al.* Formation and Photodynamic Behavior of Transition Metal Dichalcogenide Nanosheet–Fullerene Inorganic/Organic Nanohybrids on Semiconducting Electrodes. *Chem. - A Eur. J.* **24**, 1561–1572 (2018).
 49. Choi, J., Zhang, H. & Choi, J. H. Modulating optoelectronic properties of two-dimensional transition metal dichalcogenide semiconductors by photoinduced charge transfer. *ACS Nano* **10**, 1671–1680 (2016).

50. Vera-Hidalgo, M., Giovanelli, E., Navío, C. & Pérez, E. M. Mild Covalent Functionalization of Transition Metal Dichalcogenides with Maleimides: A ‘click’ Reaction for 2H-MoS₂ and WS₂. *J. Am. Chem. Soc.* **141**, 3767–3771 (2019).
51. Quirós-Ovies, R. *et al.* Controlled Covalent Functionalization of 2 H-MoS₂ with Molecular or Polymeric Adlayers. *Chem. - A Eur. J.* (2020).
52. Vázquez Sulleiro, M. *et al.* Covalent Cross-Linking of 2H-MoS₂ Nanosheets. *Chem. - A Eur. J.* **27**, 2993–2996 (2021).
53. Voiry, D. *et al.* Covalent functionalization of monolayered transition metal dichalcogenides by phase engineering. *Nat. Chem.* **7**, 45–49 (2015).
54. Vishnoi, P., Sampath, A., Waghmare, U. V. & Rao, C. N. R. Covalent Functionalization of Nanosheets of MoS₂ and MoSe₂ by Substituted Benzenes and Other Organic Molecules. *Chem. - A Eur. J.* **23**, 886–895 (2017).
55. Pramoda, K. *et al.* Nanocomposites of C₃N₄ with Layers of MoS₂ and Nitrogenated RGO, Obtained by Covalent Cross-Linking: Synthesis, Characterization, and HER Activity. *ACS Appl. Mater. Interfaces* **9**, 10664–10672 (2017).
56. Kurapati, R. *et al.* Enzymatic Biodegradability of Pristine and Functionalized Transition Metal Dichalcogenide MoS₂ Nanosheets. *Adv. Funct. Mater.* **27**, (2017).
57. Vishnoi, P. *et al.* Covalently Linked Heterostructures of Phosphorene with MoS₂/MoSe₂ and Their Remarkable Hydrogen Evolution

- Reaction Activity. *ACS Appl. Mater. Interfaces* **11**, 27780–27787 (2019).
58. Georgakilas, V. *et al.* Functionalization of graphene: Covalent and non-covalent approaches, derivatives and applications. *Chem. Rev.* **112**, 6156–6214 (2012).
59. Knirsch, K. C. *et al.* Basal-Plane Functionalization of Chemically Exfoliated Molybdenum Disulfide by Diazonium Salts. *ACS Nano* **9**, 6018–6030 (2015).
60. Pramoda, K., Gupta, U., Ahmad, I., Kumar, R. & Rao, C. N. R. Assemblies of covalently cross-linked nanosheets of MoS₂ and of MoS₂-RGO: Synthesis and novel properties. *J. Mater. Chem. A* **4**, 8989–8994 (2016).
61. Benson, E. E. *et al.* Balancing the Hydrogen Evolution Reaction, Surface Energetics, and Stability of Metallic MoS₂ Nanosheets via Covalent Functionalization. *J. Am. Chem. Soc.* **140**, 441–450 (2018).
62. Tuci, G. *et al.* Surface Engineering of Chemically Exfoliated MoS₂ in a ‘click’: How to Generate Versatile Multifunctional Transition Metal Dichalcogenides-Based Platforms. *Chem. Mater.* **30**, 8257–8269 (2018).
63. Backes, C. *et al.* Functionalization of liquid-exfoliated two-dimensional 2H-MoS₂. *Angew. Chemie - Int. Ed.* **54**, 2638–2642 (2015).
64. Pramoda, K., Kaur, M., Gupta, U. & Rao, C. N. R. Nanocomposites of 2D-MoS₂ nanosheets with the metal-organic framework, ZIF-8. *Dalt.*

- Trans.* **45**, 13810–13816 (2016).
65. Makarova, M., Okawa, Y. & Aono, M. Selective adsorption of thiol molecules at sulfur vacancies on MoS₂(0001), followed by vacancy repair via S-C dissociation. *J. Phys. Chem. C* **116**, 22411–22416 (2012).
 66. Cho, K. *et al.* Electrical and Optical Characterization of MoS₂ with Sulfur Vacancy Passivation by Treatment with Alkanethiol Molecules. *ACS Nano* **9**, 8044–8053 (2015).
 67. Chen, X., Berner, N. C., Backes, C., Duesberg, G. S. & McDonald, A. R. Functionalization of Two-Dimensional MoS₂: On the Reaction Between MoS₂ and Organic Thiols. *Angew. Chemie* **128**, 5897–5902 (2016).
 68. Ding, Q. *et al.* Basal-Plane Ligand Functionalization on Semiconducting 2H-MoS₂ Monolayers. *ACS Appl. Mater. Interfaces* **9**, 12734–12742 (2017).
 69. Chou, S. S. *et al.* Ligand conjugation of chemically exfoliated MoS₂. *J. Am. Chem. Soc.* **135**, 4584–4587 (2013).
 70. Kim, J. S., Yoo, H. W., Choi, H. O. & Jung, H. T. Tunable volatile organic compounds sensor by using thiolated ligand conjugation on MoS₂. *Nano Lett.* **14**, 5941–5947 (2014).
 71. Wang, T. *et al.* Direct detection of DNA below ppb level based on thionin-functionalized layered MoS₂ electrochemical sensors. *Anal. Chem.* **86**, 12064–12069 (2014).

72. Reshmi, S., Akshaya, M. V., Satpati, B., Basu, P. K. & Bhattacharjee, K. Structural stability of coplanar 1T-2H superlattice MoS₂ under high energy electron beam. *Nanotechnology* **29**, (2018).
73. Eda, G. *et al.* Photoluminescence from chemically exfoliated MoS₂. *Nano Lett.* **11**, 5111–5116 (2011).
74. Fan, X. *et al.* Fast and Efficient Preparation of Exfoliated 2H MoS₂ Nanosheets by Sonication-Assisted Lithium Intercalation and Infrared Laser-Induced 1T to 2H Phase Reversion. *Nano Lett.* **15**, 5956–5960 (2015).
75. D. Yang, S. Jiménez Sandoval, W.M.R. D ivigalpitiya, J. C. I. and R. F. F. Structure of single-molecular layers MoS₂. *Phys. Rev. B* **43**, 53–56 (1991).
76. Wang, R. *et al.* Strategies on Phase Control in Transition Metal Dichalcogenides. *Adv. Funct. Mater.* **28**, 1–17 (2018).
77. Sun, Y., Thompson, S. E. & Nishida, T. *Strain effect in semiconductors: Theory and device applications. Strain Effect in Semiconductors: Theory and Device Applications* (2010).
78. Sun, Y. & Liu, K. Strain engineering in functional 2-dimensional materials. *J. Appl. Phys.* **125**, (2019).
79. Johari, P. & Shenoy, V. B. Tuning the electronic properties of semiconducting transition metal dichalcogenides by applying mechanical strains. *ACS Nano* **6**, 5449–5456 (2012).
80. He, K., Poole, C., Mak, K. F. & Shan, J. Experimental demonstration

- of continuous electronic structure tuning via strain in atomically thin MoS₂. *Nano Lett.* **13**, 2931–2936 (2013).
81. Scalise, E., Houssa, M., Pourtois, G., Afanas'ev, V. & Stesmans, A. Strain-induced semiconductor to metal transition in the two-dimensional honeycomb structure of MoS₂. *Nano Res.* **5**, 43–48 (2012).
 82. Bertolazzi, S., Brivio, J. & Kis, A. Stretching and breaking of ultrathin MoS₂. *ACS Nano* **5**, 9703–9709 (2011).
 83. Petó, J. *et al.* Moderate strain induced indirect bandgap and conduction electrons in MoS₂ single layers. *npj 2D Mater. Appl.* **3**, 1–6 (2019).
 84. Roldán, R., Castellanos-Gomez, A., Cappelluti, E. & Guinea, F. Strain engineering in semiconducting two-dimensional crystals. *J. Phys. Condens. Matter* **27**, (2015).
 85. Ouyang, B., Lan, G., Guo, Y., Mi, Z. & Song, J. Phase engineering of monolayer transition-metal dichalcogenide through coupled electron doping and lattice deformation. *Appl. Phys. Lett.* **107**, (2015).
 86. Lloyd, D. *et al.* Band Gap Engineering with Ultralarge Biaxial Strains in Suspended Monolayer MoS₂. *Nano Lett.* **16**, 5836–5841 (2016).
 87. Dhakal, K. P. *et al.* Local Strain Induced Band Gap Modulation and Photoluminescence Enhancement of Multilayer Transition Metal Dichalcogenides. *Chem. Mater.* **29**, 5124–5133 (2017).
 88. Conley, H. J. *et al.* Bandgap engineering of strained monolayer and bilayer MoS₂. *Nano Lett.* **13**, 3626–3630 (2013).

89. Manzeli, S., Allain, A., Ghadimi, A. & Kis, A. Piezoresistivity and Strain-induced Band Gap Tuning in Atomically Thin MoS₂. *Nano Lett.* **15**, 5330–5335 (2015).
90. Hwang, D. Y., Choi, K. H., Park, J. E. & Suh, D. H. Highly thermal-stable paramagnetism by rolling up MoS₂ nanosheets. *Nanoscale* **9**, 503–508 (2017).
91. Hwang, D. Y., Choi, K. H., Park, J. E. & Suh, D. H. Highly efficient hydrogen evolution reaction by strain and phase engineering in composites of Pt and MoS₂ nano-scrolls. *Phys. Chem. Chem. Phys.* **19**, 18356–18365 (2017).
92. Yang, C. Y. *et al.* Phase-driven magneto-electrical characteristics of single-layer MoS₂. *Nanoscale* **8**, 5627–5633 (2016).
93. Zhu, J. *et al.* Argon Plasma Induced Phase Transition in Monolayer MoS₂. *J. Am. Chem. Soc.* **139**, 10216–10219 (2017).
94. Yang, S. *et al.* Hierarchical 1T-MoS₂ nanotubular structures for enhanced supercapacitive performance. *J. Mater. Chem. A* **5**, 23704–23711 (2017).
95. Cai, L. *et al.* Vacancy-induced ferromagnetism of MoS₂ nanosheets. *J. Am. Chem. Soc.* **137**, 2622–2627 (2015).
96. Zhang, P. *et al.* Structural Phase Transition Effect on Resistive Switching Behavior of MoS₂-Polyvinylpyrrolidone Nanocomposites Films for Flexible Memory Devices. *Small* **12**, 2077–2084 (2016).
97. Chang, K. *et al.* Targeted Synthesis of 2H- and 1T-Phase

- MoS₂ Monolayers for Catalytic Hydrogen Evolution. *Adv. Mater.* **28**, 10033–10041 (2016).
98. Cai, L. *et al.* High-Content Metallic 1T Phase in MoS₂-Based Electrocatalyst for Efficient Hydrogen Evolution. *J. Phys. Chem. C* **121**, 15071–15077 (2017).
99. Rao, G. V. S. & Shafer, M. W. Intercalation in Layered Transition Metal Dichalcogenides. *Intercalated Layer. Mater.* 99–199 (1979)
100. Friend, R. H. & Yoffe, A. D. Electronic properties of intercalation complexes of the transition metal dichalcogenides. *Adv. Phys.* **36**, 1–94 (1987).
101. Zhou, L., He, B., Yang, Y. & He, Y. Facile approach to surface functionalized MoS₂ nanosheets. *RSC Adv.* **4**, 32570–32578 (2014).
102. Papageorgopoulos, C. A. & Jaegermann, W. Li intercalation across and along the van der Waals surfaces of MoS₂(0001). *Surf. Sci.* **338**, 83–93 (1995).
103. Enyashin, A. N. & Seifert, G. Density-functional study of Li_xMoS₂ intercalates ($0 \leq x \leq 1$). *Comput. Theor. Chem.* **999**, 13–20 (2012).
104. Kan, M. *et al.* Structures and phase transition of a MoS₂ monolayer. *J. Phys. Chem. C* **118**, 1515–1522 (2014).
105. Voiry, D. *et al.* Conducting MoS₂ nanosheets as catalysts for hydrogen evolution reaction. *Nano Lett.* **13**, 6222–6227 (2013).
106. Nurdiwijayanto, L., Ma, R., Sakai, N. & Sasaki, T. Insight into the structural and electronic nature of chemically exfoliated molybdenum

- disulfide nanosheets in aqueous dispersions. *Dalt. Trans.* **47**, 3014–3021 (2018).
107. Zeng, Z. *et al.* An effective method for the fabrication of few-layer-thick inorganic nanosheets. *Angew. Chemie - Int. Ed.* **51**, 9052–9056 (2012).
108. Ejigu, A., Kinloch, I. A., Prestat, E. & Dryfe, R. A. W. A simple electrochemical route to metallic phase trilayer MoS₂: Evaluation as electrocatalysts and supercapacitors. *J. Mater. Chem. A* **5**, 11316–11330 (2017).
109. Lin, Y. C., Dumcenco, D. O., Huang, Y. S. & Suenaga, K. Atomic mechanism of the semiconducting-to-metallic phase transition in single-layered MoS₂. *Nat. Nanotechnol.* **9**, 391–396 (2014).
110. Kang, Y. *et al.* Plasmonic Hot Electron Induced Structural Phase Transition in a MoS₂ Monolayer. *Adv. Mater.* **26**, 6467–6471 (2014).
111. Milekhin, A. G. *et al.* Giant gap-plasmon tip-enhanced Raman scattering of MoS₂ monolayers on Au nanocluster arrays. *Nanoscale* **10**, 2755–2763 (2018).
112. Friedman, A. L. *et al.* Evidence for Chemical Vapor Induced 2H to 1T Phase Transition in MoX₂ (X = Se, S) Transition Metal Dichalcogenide Films. *Sci. Rep.* **7**, 1–9 (2017).

7

REVERSIBLE MoS₂ MOLECULAR STRAIN ENGINEERING

R. Torres-Cavanillas, M. Morant-Giner, G. Escorcía-Ariza, J. Dugay, J. Canet-Ferrer, S. Tatay, S. Cardona-Serra, M. Giménez-Márquez, M. Galbiati, A. Forment-Aliaga, E. Coronado. ChemRxiv. Preprint, 2020. chemrxiv.12664799.v1

7.1. Motivation

As has been introduced in section 3.2.6, SCO NPs can be used as sources of mechanical strain due to their volume changes upon the spin transition.¹⁻³ In this context, several authors have employed crystals or SCO NPs to perform microelectromechanical systems (MEMS)⁴⁻⁷ in which an external stimulus is translated into mechanical motion due to the spin transition. Therefore, these molecular systems can be used to mechanically stress at the nanoscale 2D materials like exfoliated MoS₂, via the appropriate functionalization of the 2D system to link with the SCO compound. Herein, we propose the synthesis of hybrid heterostructures of [Fe(Htrz)₂(trz)](BF₄)@SiO₂ NPs (SCO@SiO₂ NPs) and MoS₂ as an efficient manner to reversibly strain the 2D layer thanks to the volume change of the NPs during the spin transition.

7.2. Introduction

To the best of our knowledge, the first example of a molecular actuator driven by a SCO material was provided by J. Sheperd et al. in 2013, who successfully fabricated actuators with a bilayer cantilever architecture of four different SCO materials: single crystal of {Fe(3-CNpy)[Au(CN)₂]₂, particles of Na_{0.53}[Co_{1.32}Fe(CN)₆] and two polymorphs of the compound [Fe(Htrz)₂(trz)](BF₄) embedded in a PMMA matrix.⁵ The spin transition was studied for all the compounds as a function of the temperature and light by following the deflection of the cantilever caused by the volume change, Figure 1. Nevertheless, the processability of these gadgets and their performance were limited due to the large dimensions of the SCO systems.

Therefore, later the same devices, but based on SCO NPs, were explored to obtain a more efficient mechanical coupling.

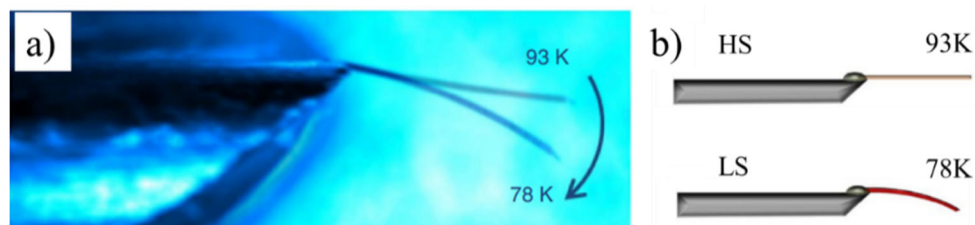


Figure 1. (a) Comparison of the aluminium cantilever at 93 and 78 K, highlighting the SCO-induced actuation of a $\{Fe(3-CNpy)[Au(CN)_2]_2\}$ crystal. (b) Scheme of the cantilever movement as a function of the spin state. Extracted from reference 5.

With this in mind, Manrique-Juarez et al., embedded 85 nm $[Fe(Htrz)_2(trz)]BF_4$ NPs in a polymeric matrix of SU-8 (an epoxy-based photoresistor), to integrate them on silicon cantilevers by spray-coating.⁸ Then, the device was cycled between 293 and 423 K recording the deflection of the cantilever, Figure 2a. An abrupt downward bending after heating up to ~ 380 K was observed, which corresponds to the spin transition temperature from LS into HS. This modification was followed by the recovery of the initial cantilever position during the HS to LS transition during the cooling process, ~ 340 K. This device exhibited a moderated strain of around 1%.

Independently, Dugay et al. used Si microresonators as spin sensors. In this work, the sensitivity of oscillating Si MEMs cantilevers was exploited to study a set of hybrid core-shell $[Fe(Htrz)_2(trz)]BF_4@SiO_2$ NPs.⁷ The microcantilevers were coated with thin films of the hybrid $SCO@SiO_2$ NPs by drop-casting. When the cores of these hybrid $SCO@SiO_2$ NPs switched from LS to HS, a reversible increase in the cantilever resonance frequency

was recorded, Figure 2b. The hysteretic behaviour was attributed to the variations of the surface stress caused by the NPs volume change.

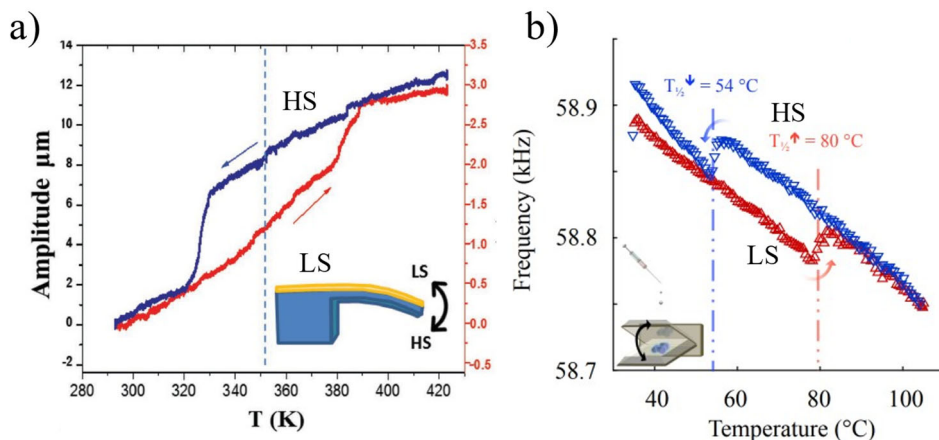


Figure 2. (a) Temperature dependence of the static piezoresistance change and the corresponding actuation amplitude in silicon MEMS microcantilevers covered by the SCO/SU-8 composite film. (b) Thermal hysteresis loops detected in the fundamental resonance frequency of the resonators with drop casted SCO@SiO₂ NPs. Extracted from references 7 and 8.

7.3. Results and discussion

To attach SCO@SiO₂ NPs to a MoS₂ surface, a two-step protocol was developed. It involves the use of (3-iodopropyl)trimethoxysilane (IPTS) as a bridging molecule to anchor the SCO@SiO₂ NPs covalently through the silica shell. Therefore, the first step involved the functionalization of chemically exfoliated MoS₂ (ce-MoS₂) with IPTS, Figure 3i. Next, by putting together the functionalized 2D layers and the SCO@SiO₂ NPs, the grafting occurred due to the reaction of the silane with the SiO₂ shell, Figure 3ii. The synthesis was performed with NPs of different sizes, i.e.: 40, and 70 nm. Moreover, different degrees of coverage were studied for the hybrids based on 40 nm NPs. The preparation of this family of hybrid materials permitted

the evaluation of the strain applied on the 2D layers as a function of the size and number of NPs. Once the synthesis was complete, the electrical and optical properties of the different heterostructures were investigated in detail by measuring the electrical behaviour of the hybrids and by Raman spectroscopy.

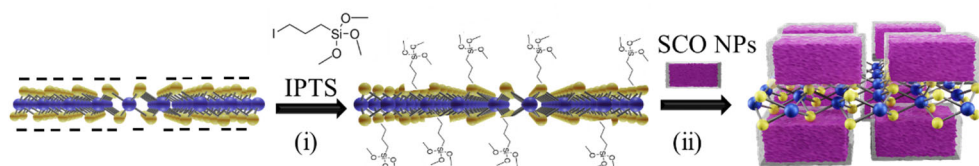


Figure 3. Schematic representation of the synthetic approach to prepare the hybrid heterostructures. (i) $ce\text{-MoS}_2$ is functionalized with propyl(trimethoxysilane) (PTS); (ii) SCO@SiO_2 NPs are covalently attached to the functionalized MoS_2 layers through a chemical reaction between the silane group and the SiO_2 shell.

7.3.1. MoS_2 Chemical exfoliation

Ultrathin $ce\text{-MoS}_2$ flakes were prepared by the already explained $n\text{-BuLi}$ exfoliation protocol by Marc Morant Giner at the ICMol.⁹ The colloidal stability of the $ce\text{-MoS}_2$ in water was confirmed by ζ -potential analysis, which presents a value around -45 mV. Regarding the lateral size of the flakes, the exfoliation led to sheets ranging from 0.2 to 1.2 μm , Figure 4a. Additionally, the presence of Mo and S in the flakes was evidenced by EDX (Figure 4b).

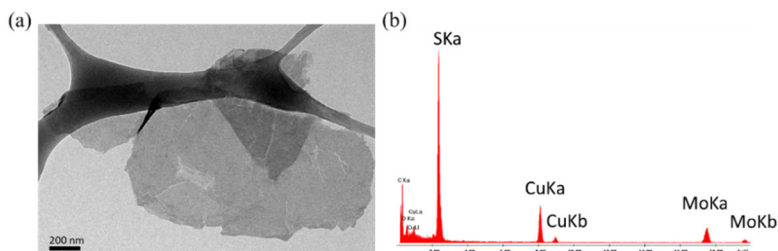


Figure 4. TEM image of $ce\text{-MoS}_2$ layers, (a), and EDX of the same flakes, (b).

The average flakes thickness was investigated by AFM topographic analysis of ce-MoS₂ spin-coated on a Si/SiO₂ (285nm) substrate. From the image profile, we observe MoS₂ flakes that range from monolayers to 5 layers thick, Figure 5. All this indicated the high quality of the exfoliation, which leads to large and thin flakes.

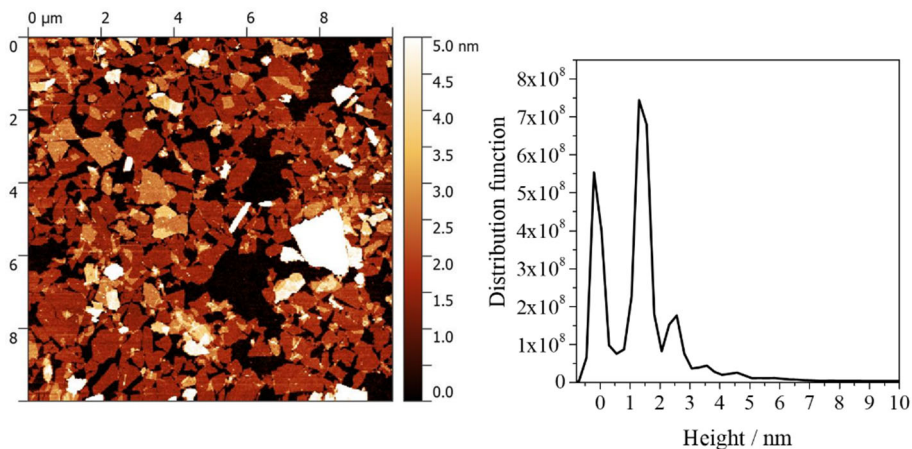


Figure 5. (a) AFM topographic image of ce-MoS₂ layers spin coated on a Si/SiO₂ substrate. (b) Height histogram of the same image.

7.3.2. Silane functionalized MoS₂

After the exfoliation, the reaction between the ce-MoS₂ and the IPTS gave rise to the covalent functionalization of the layers (PTS-MoS₂), which was rendered by mixing overnight an aqueous suspension of ce-MoS₂ with an ethanolic solution of IPTS, Figure 3i. Thanks to the excess of negative charge located at the ce-MoS₂ surface, the flakes displayed a pronounced nucleophilic character. Therefore, by adding an electrophile (like the C atom bonded to the I atom in the IPTES), the ce-MoS₂ functionalization was easily achieved.

Noticeably, the PTS-MoS₂ was colloiddally unstable in the mixture H₂O:EtOH. This was accounted by the ζ -pot reduction, which for the PTS-MoS₂ was close to 0, while the ce-MoS₂, with the same H₂O:EtOH ratio, exhibited a value of \sim 30 mV, Figure 6. This is caused by the neutralization of charges at the 2D surface due to its reaction with the IPTS. Later, to remove the unreacted IPTS, the functionalized sheets were washed with EtOH several times. Remarkably, despite the lack of PTS-MoS₂ colloidal stability in aqueous media, the same material was easily resuspended in EtOH, remaining stable for days.

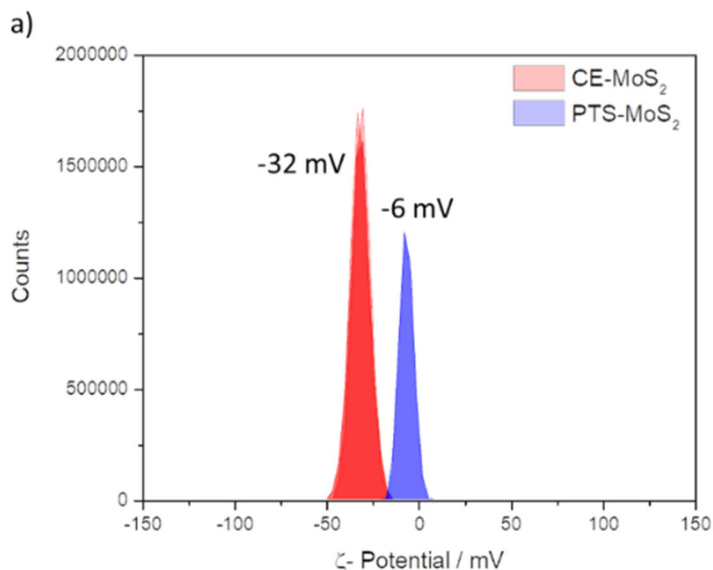


Figure 6. ζ -pot of ce-MoS₂ and PTS-MoS₂ in a mixture H₂O:EtOH, 2:1.

As the TEM images show, the morphology of the flakes remained unaltered after their functionalization, Figure 7a. EDX confirmed the presence of Si (\sim 1KeV) from the PTS, while the iodine signal was absent (\sim 4 keV), Figure 7b. This observation supported the formation of C-S bonds at the expense of the original C-I bonds in the IPTS molecule.

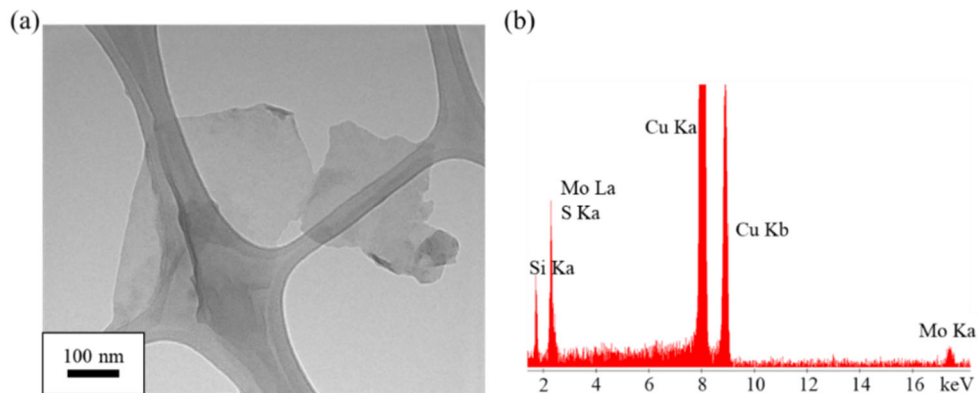


Figure 7. (a) TEM image of the functionalized *ce*-MoS₂ layers, PTS-MoS₂. (b) EDX of the PTS-MoS₂.

The degree of functionalization was estimated by thermogravimetric analysis (TGA), Figure 8. The mass loss of the PTS-MoS₂, at 400 °C, compared with the *ce*-MoS₂ indicated a ~30% of functionalization.

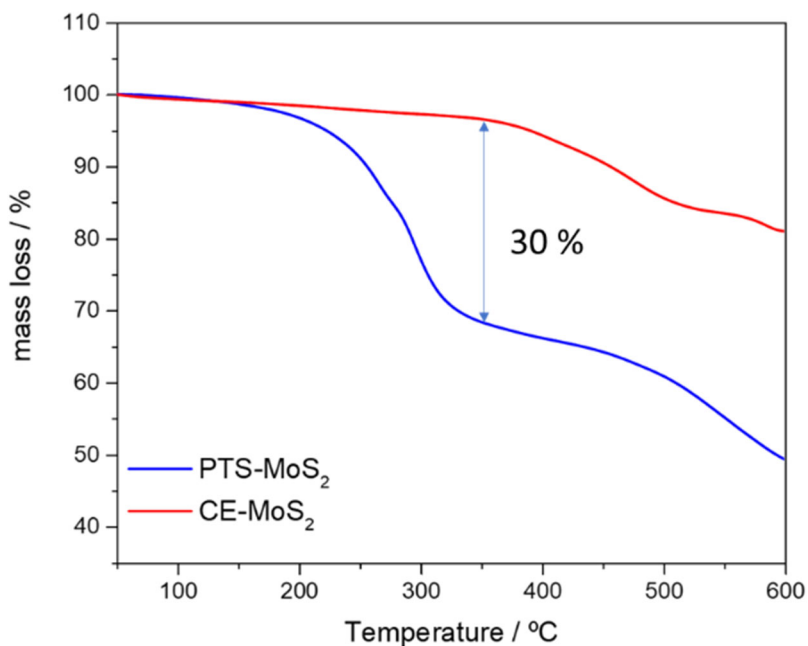


Figure 8. TGA of the *ce*-MoS₂ and PTS-MoS₂.

7.3.3. Anchoring SCO@SiO_2 NPs to the MoS_2

To decorate the 2D layers with the SCO material, we took advantage of the reactivity provided by the silica shell with the silane groups in the PTS- MoS_2 hybrid. The covalent bond between silanes and SiO_2 is well known in the field of SAMs, where it has been widely used to functionalize SiO_2 substrates with different molecules across the years.^{10–12} The reaction occurs through the dangling bonds at the surface of the SiO_2 that can react with the silane. We took advantage of this knowledge to graft the NPs on the 2D surface. Thus, the last synthetic step involved mixing the core@shell NPs SCO@SiO_2 with the PTS- MoS_2 (SCO/MoS_2), Figure 3ii.

7.2.3.a. Tuning the surface coverage

The first NPs used to decorate the 2D layers were cubic shape~40 nm NPs of SCO@SiO_2 (SCO@SiO_2 -40), Figure 9a.

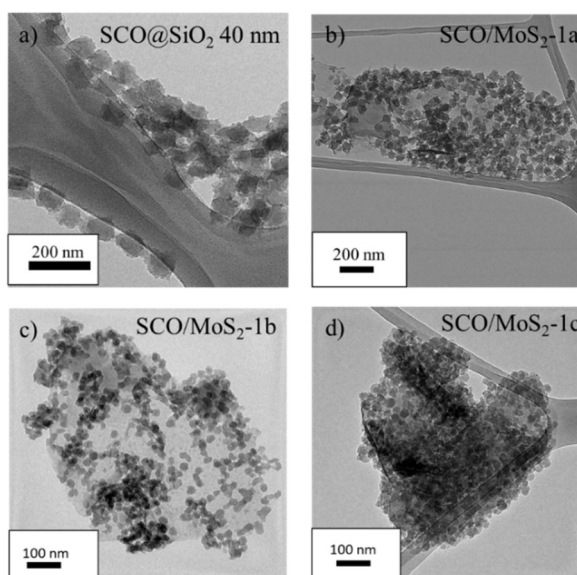


Figure 9. (a-d) TEM images of the bare SCO@SiO_2 -40 nm NPs, and hybrid SCO/MoS_2 -1a, b, and c materials, respectively.

We played with the concentration of SCO@SiO₂-40 NPs to modulate the final number of grafted NPs. To synthesize the different heterostructures, ethanolic suspensions of SCO@SiO₂-40 NPs; 25 Mm, 2.5 mM, or 50 mM, were added into a 5 mM PTS-MoS₂ ethanolic dispersion, giving rise to SCO/MoS₂-1a, b, and c, respectively. After two days, the mixture was washed by three centrifugation steps. Figure 9b, c, and d show the TEM images that reflect the different coverage degrees reached. In table 1 the degrees of coverage extracted from several TEM images are summarized. For SCO/MoS₂-1a the coverage was around 80%, while for SCO/MoS₂-1b and c, they were 50 and ~100%, respectively.

Table 1. Summary of the coverage extracted from TEM images, the ratio Fe/Mo measured by ICP, and the molecular formula estimated from the Fe/Mo ratio.

| Samples | Coverage / % | Ratio Fe/Mo | Molecular formula |
|--------------------------|--------------|-------------|---|
| SCO/MoS ₂ -1a | 82 ± 3 | 1.8 | MoS ₂ [Fe(Htrz) ₂ (trz)(BF ₄)@SiO ₂] _{1.8} |
| SCO/MoS ₂ -1b | 50 ± 2 | 0.4 | MoS ₂ [Fe(Htrz) ₂ (trz)(BF ₄)@SiO ₂] _{0.4} |
| SCO/MoS ₂ -1c | 100 | 5 | MoS ₂ [Fe(Htrz) ₂ (trz)(BF ₄)@SiO ₂] _{5.0} |
| SCO/MoS ₂ -2 | 78 ± 2 | 1.8 | MoS ₂ [Fe(Htrz) ₂ (trz)(BF ₄)@SiO ₂] _{1.8} |

The quantification was carried out by calculating the uncovered area of the total surface. It must be noticed that the quantification was done ignoring the thickness and number of layers of the flakes, only considering their visible

surface. Hence, the values extracted here cannot be related to the amount of Mo and Fe, but to the coverage of the flakes.

To estimate the molecular formula of the different heterostructures, the ratio Fe/Mo was measured by ICP. Ratios of 1.8, 0.4, and 5 for SCO/MoS₂-1a, b, and c were obtained (table 1).

7.2.3.b. Anchoring SCO@SiO₂ NPs of different sizes

The synthesis of SCO/MoS₂-1a was adapted to use prismatic ca. 70 nm NPs instead of the 40 nm ones, called SCO@SiO₂-70 NPs. Thus, a 25 mM suspension of SCO@SiO₂-70 NPs was added into a 5 mM PTS-MoS₂ dispersion, and it was stirring for two days, giving rise to the hybrid material named SCO/MoS₂-2, Figure 10.

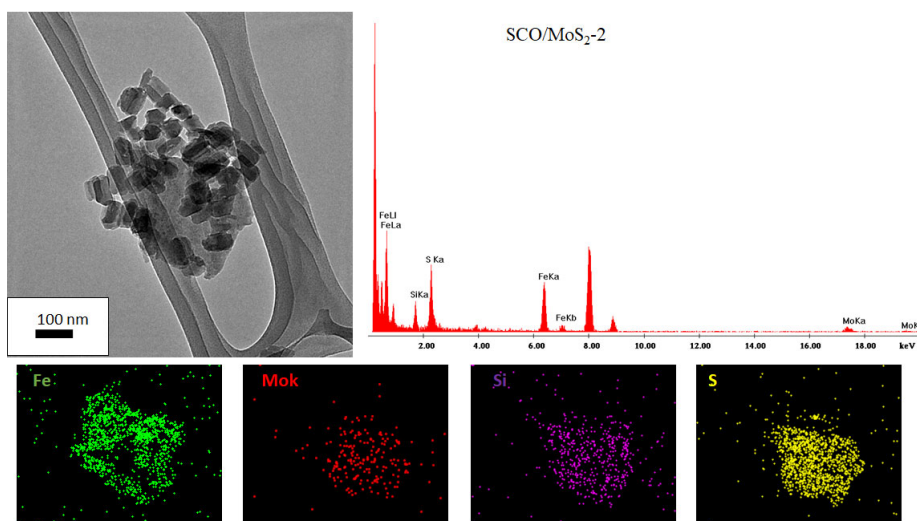


Figure 10. a) TEM image of SCO-MoS₂-2. b) EDX spectrum and, c) EDX mapping of Fe, Mo, Si and S of the same flake.

The coverage of the SCO/MoS₂-2 was ~78% with a ratio Fe/Mo of 1.8, Table 1. For SCO/MoS₂-2 EDX mapping of a decorated layer showed the

presence of Fe localized in the NPs and Si over the entire flake, due to the presence of PTS, Figure 10.

7.3.4. *MoS₂ Phase*

As has been previously discussed, the *n*-BuLi exfoliation usually leads to the interconversion from 2H to 1T-MoS₂ phase. As the phase of the MoS₂ determines its physical properties, knowing the phase after each synthetic step is mandatory. However, the preservation or conversion of 1T to 2H phase during the functionalization is an interesting and controversial question. Some authors suggest that the 1T phase is maintained after the covalent functionalization,^{13,14} but exhibiting a semiconductive behaviour, while others support a complete or partial phase transition¹⁵⁻¹⁷. In order to clarify this issue for our systems we studied the MoS₂ by X-ray photoelectron spectroscopy (XPS), X-ray absorption spectroscopy (XAS), and Raman spectroscopy after each synthetic step.

7.2.4.a. *X-ray photoelectron spectroscopy*

XPS is one of the most employed techniques to investigate the MoS₂ polytype. Looking at the bands of the Mo3d and S2p regions, relevant information of the Mo and S electronic signature of the MoS₂ can be obtained.

In this context, each MoS₂ phase presents Mo3d and S2p bands at specific energies, being the bands in 1T phase shifted ~0.9 eV to lower binding energies than in the 2H phase. Therefore, we analyzed the Mo3d and S2p of bulk-MoS₂ (as the reference of 2H-MoS₂), ce-MoS₂ (reference of 1T-MoS₂), PTS-MoS₂, SCO/MoS₂-1a, and SCO/MoS₂-2.

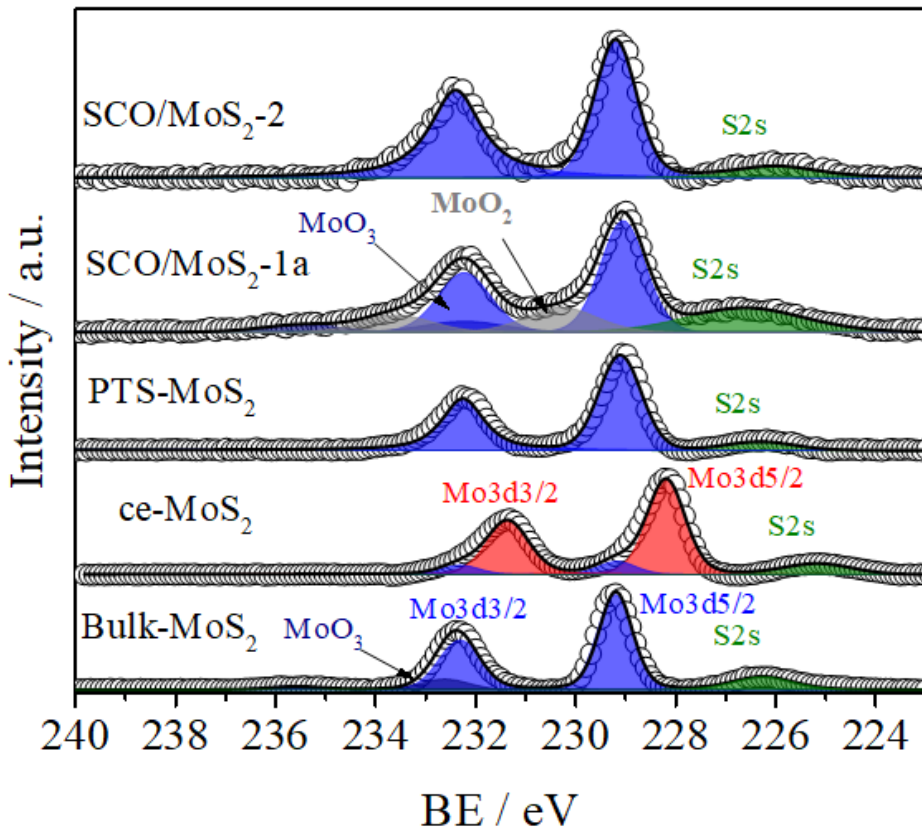


Figure 11. Mo3d XPS spectra of bulk-MoS₂, ce-MoS₂, PTS-MoS₂, SCO/MoS₂-1a, and SCO/MoS₂-2.

Three signals were discerned with the Mo 3d region of bulk-MoS₂, i. e. a singlet and two doublets, Figure 11. The singlet at 226.4 eV corresponds to the S2s level of the MoS₂. The main doublet at 229.2 eV (Mo3d5/2) and 232.3 eV (Mo3d3/2) can be assigned to the 2H-MoS₂, while the secondary doublet at 232.8 eV (Mo3d5/2) and 235.4 eV (Mo3d3/2) corresponds to MoO₃ species. Moving to the ce-MoS₂, important changes with respect to the bulk were visible. On the one hand, the S2s singlet is shifted to 225.1 eV (green). On the other hand, two doublets corresponding to 1T-MoS₂, 228.3 eV (Mo 3d5/2) and 231.3 eV (Mo3d3/2), and 2H-MoS₂, 229.2 eV (Mo3d5/2) and

232.5 eV (Mo3d3/2), can be seen. It must be noticed that, even if the conversion from 2H to 1T is not complete, the 1T-MoS₂ percentage deduced from the areas of 1T-MoS₂ Mo3d5/2, and 2H-MoS₂ Mo3d5/2 is close to 80%.

After the functionalization, the Mo3d region of the PTS-MoS₂, SCO/MoS₂-1a, and SCO/MoS₂-2 spectra resembled that of the 2H-MoS₂ bulk, Figure 11. Thus, the main doublet at 229.1 and ~232.3 eV (blue) has been deconvoluted in the three samples. All the peak contributions of the XPS fitting are summarized in table 2.

Table 2. Summary of the main peaks of the Mo3d regions of the different samples.

| | S2s | Mo3d 2H | Mo3d 1T | MoO ₂ | MoO ₃ |
|--------------------------|----------|--|--|--|--|
| Bulk MoS ₂ | 226.4 eV | 229.2 eV (Mo3d5/2) 232.3 eV (Mo3d3/2) | - | - | 232.8 eV (Mo3d5/2) 235.4 eV (Mo3d3/2) |
| ce-MoS ₂ -1T | 225.1 eV | 229.2 eV (Mo3d5/2) 232.5 eV (Mo3d3/2) | 228.3 eV (Mo3d5/2) 231.3 eV (Mo3d3/2) | - | - |
| PTS-MoS ₂ | 226.3 eV | 229.1 eV (Mo3d5/2) 232.3 eV (Mo3d3/2) | - | - | - |
| SCO/MoS ₂ -1a | 226.5 eV | 229.1 eV (Mo3d5/2) 232.2 eV (Mo3d3/2) | - | 230.4 eV (Mod5/2) 233.7 eV (Mod3/2) | 232.3 eV (Mo3d5/2) 235.8 eV (Mo3d3/2) |
| SCO/MoS ₂ -2 | 226.0 eV | 229.2 eV (Mo3d5/2) 232.4 eV (Mo3d3/2) | - | - | - |

Now, moving to the S2p region, bulk-MoS₂ presents a doublet with its component S2p3/2 located at 162.1 eV and the 2p1/2 at 163.2 eV, Figure 12. The ce-MoS₂ displays a more complex spectrum. The main S2p doublet, S2p3/2 at 161.0 eV and S2p1/2 at 162.1 eV, is attributed to 1T-MoS₂, while a small contribution of non-converted 2H is evidenced by the presence of a doublet with the S2p3/2 at 162.2 eV and S2p1/2 at 163.3 eV, Figure 12.

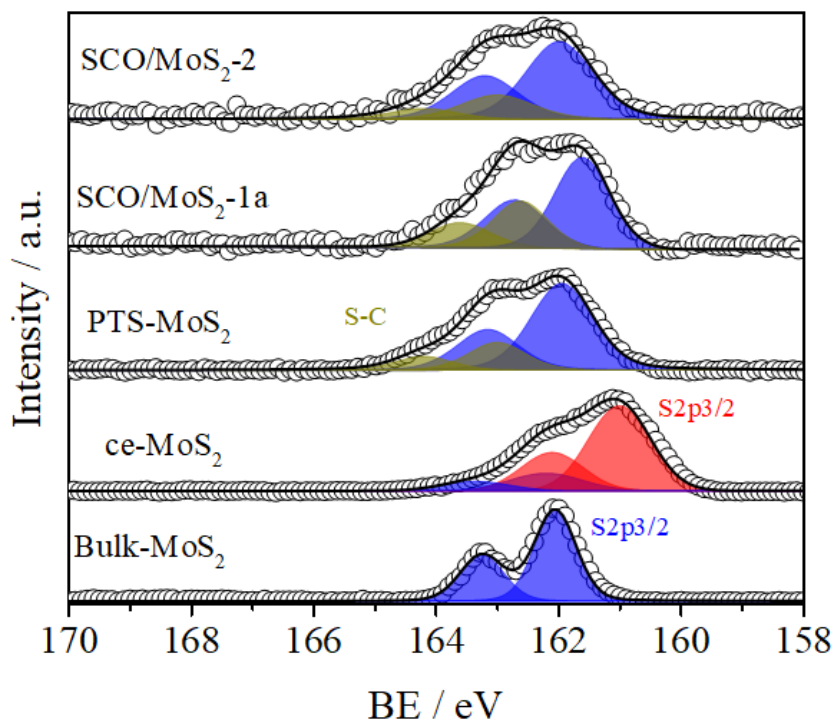


Figure 12. $S2p$ XPS of bulk- MoS_2 , $ce-MoS_2$, $PTS-MoS_2$, SCO/MoS_2-1a , and SCO/MoS_2-2 .

In contrast with the $ce-MoS_2$, the main contribution to the $S2p$ region in the $PTS-MoS_2$ spectrum corresponds to a $S2p_{3/2}$ peak at 161.9 eV and $S2p_{1/2}$ peak at 163.2 eV, positions closer to the 2H- MoS_2 . Additionally, there is a small doublet at higher binding energy with the $S2p_{3/2}$ peak at 163 eV and the $S2p_{1/2}$ at 164.3 eV. According to the literature, this last doublet could be related to the S-C species coming from the functionalization.¹⁸ Looking at the relative area of the S-C doublet, a ~25 % of functionalization is estimated, in good agreement with the TGA.

From the XPS analysis, we can conclude that after the functionalization, the binding energies of $Mo3d$ and $S2p$ levels are closer in energies to the 2H- MoS_2 phase.

Table 3. Summary of the main peaks of S2p regions of the different samples.

| | S2p 2H | S2p 1T | S2p S-C |
|--------------------------|--|--|--|
| Bulk MoS ₂ | 162.1 eV (S2p _{3/2}) 163.2 eV (S2p _{3/2}) | - | - |
| ce-MoS ₂ -1T | 162.2 eV (S2p _{3/2}) 163.3 eV (S2p _{3/2}) | 161.0 eV (S2p _{3/2}) 162.1 eV (S2p _{3/2}) | - |
| PTS-MoS ₂ | 161.9 eV (S2p _{3/2}) 163.2 eV (S2p _{3/2}) | - | 163.0 eV (S2p _{3/2}) 164.3 eV (S2p _{3/2}) |
| SCO/MoS ₂ -1a | 161.9 eV (S2p _{3/2}) 162.8 eV (S2p _{3/2}) | - | 162.7 eV (S2p _{3/2}) 163.8 eV (S2p _{3/2}) |
| SCO/MoS ₂ -2 | 161.9 eV (S2p _{3/2}) 163.2 eV (S2p _{3/2}) | - | 163.1 eV (S2p _{3/2}) 164.4 eV (S2p _{3/2}) |

7.2.4.b. X-ray absorption spectroscopy

XAS corroborated the experimental results of XPS. This technique is based on the excitation of core electrons using X-ray irradiation. When the irradiated energy is high enough to promote an electron from the core into an unoccupied level, an absorption edge appears. Depending on the excited electronic level, the edges are called K, L, and M, corresponding to levels with the principal quantum number 1, 2, and 3, respectively.

The edge shape and energy position are related to the oxidation state and the local environment. Therefore, XAS is a powerful tool to characterize the MoS₂ polytype. In this context, XAS spectrum of S K-edge of bulk-MoS₂, ce-MoS₂, PTS-MoS₂, and Mo K-edge of bulk-MoS₂, ce-MoS₂, PTS-MoS₂, SCO/MoS₂-1a, and -2 were studied (measured in the beamlines Deimos and SAMBA of synchrotron Soleil).

- *S K-edge*

The MoS₂ S K-edge appears around 2470 eV, corresponding to the excitation of 1s electrons to 3p levels.¹⁹ Like for XPS, the S-K edge of bulk-MoS₂ and ce-MoS₂, were used as references of 2H and 1T-MoS₂, respectively. Focusing on bulk-MoS₂, three peaks are observed, that we named a_H, b_H and c_H, around 2.47, 2.48, and 2.49 keV, Figure 13. Focussing on the first peak, a clear asymmetry is observed. Actually, a_H peak is formed by two bands, a₁ and a₂, that correspond to the excitation into 3Sp_x, 3p_y, and 3p_z orbitals, respectively. While 3p_y and 3p_x are degenerated, the 3p_z shifts to higher energies due to the S3p_z-Mo4d hybridization.^{20,21}

After the exfoliation, the S-K edge differed drastically to the 2H-bulk, Figure 13. The ce-MoS₂ exhibits three peaks named a_T, b_T, and c_T, at ~2.47, 2.48, and 2.50 KeV. Noticeably, the intensity of the a_T peak in ce-MoS₂ is lower than its bulk counterpart, and the asymmetry of the 2H-MoS₂ vanishes due to the lower energy separation of the 3Sp_{x,p_y}, and 3Sp_z in 1T-MoS₂, merging both peaks in one.²² Therefore, an efficient manner to distinguish the polytype is to search for the asymmetry of the a_H peak. Moving to the functionalized PTS-MoS₂, the absorption edge strongly resembles the one of the 2H-MoS₂. As shown in Figure 13, the main peak at 2.47 eV displays the asymmetry and absorption intensity expected for the hexagonal polytype.

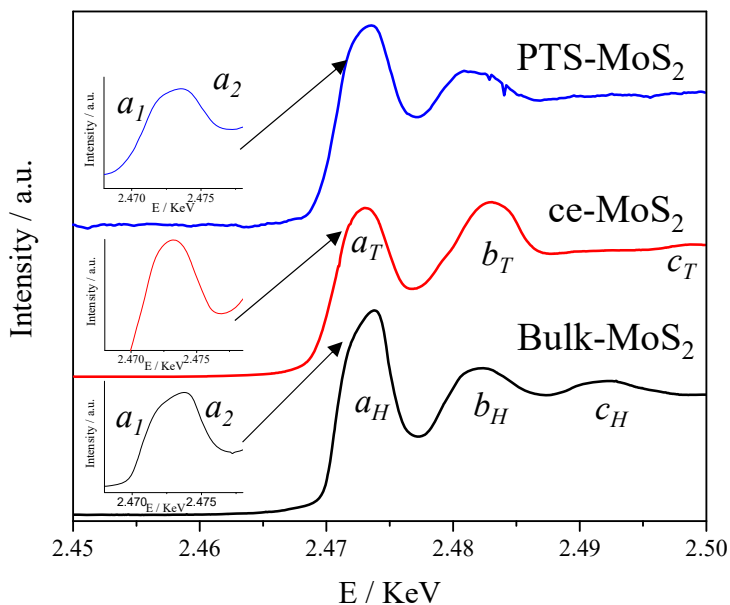


Figure 13. S K-edge spectra of bulk-, ce- and PTS-MoS₂ (black, red, and blue, respectively).

- Mo K-edge

Mo K-edge corresponds to the excitation from the Mo 1s to 5p orbitals. In the bulk-MoS₂, four clear peaks are distinguished: d, e, f and g, located at ~20.01, 20.03, 20.08, and 20.14 keV, respectively (Figure 15). In contrast, the exfoliated 1T layers do not present the d peak. Therefore, monitoring the d peak is possible to cast light on the MoS₂ phase.²³ Looking at the Mo K- edge, after the functionalization, in PTS-MoS₂, SCO/MoS₂-1a, and SCO/MoS₂-2 spectra, the d peak is restored, Figure 14. Therefore, the S and Mo K edges seem to support the phase transition after the MoS₂ covalent functionalization with IPTS.

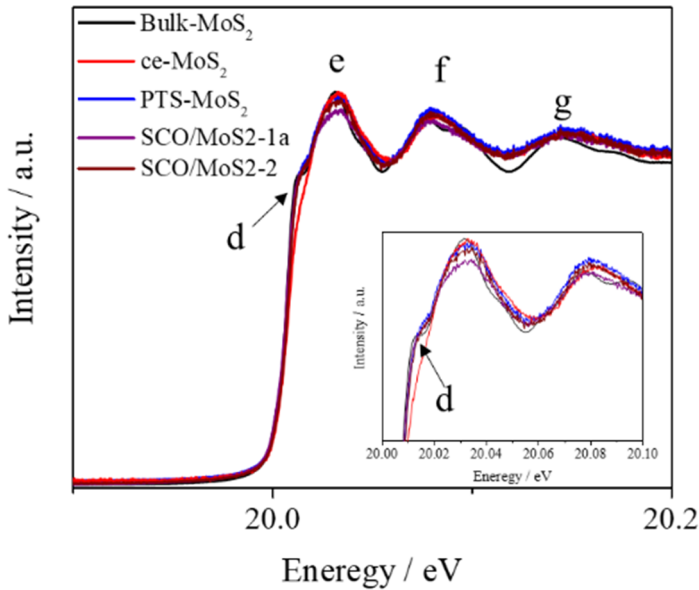


Figure 14. Mo K-edge spectra of bulk (black), ce-MoS₂ (red), and PTS-MoS₂ (blue), SCO/MoS₂-1a (purple), and SCO/MoS₂-2 (wine). Inset: zoom of the first peak region.

7.2.4.c. Raman spectroscopy

Finally, the MoS₂ phase was also investigated by Raman spectroscopy. TMDCs and particularly the MoS₂, exhibit characteristic features depending on the phase and the number of layers.²⁴ Therefore, it is possible to distinguish the polytype and thickness.

Raman spectrum of bulk 2H-MoS₂ is dominated by two peaks, at ~381 and 406 cm⁻¹, which are assigned to the in-plane E_{2g}¹ and out-of-plane A_{1g} vibrational modes, Figure 15. In contrast, a more complex spectrum is observed in the ce-MoS₂. It must be noticed that to measure the Raman of the exfoliated MoS₂ a colloidal suspension of the layers is spin-coated in a Si/SiO₂ (285nm) substrate. Later, the substrate region is carefully selected and measured, avoiding the large aggregates of restacked MoS₂.

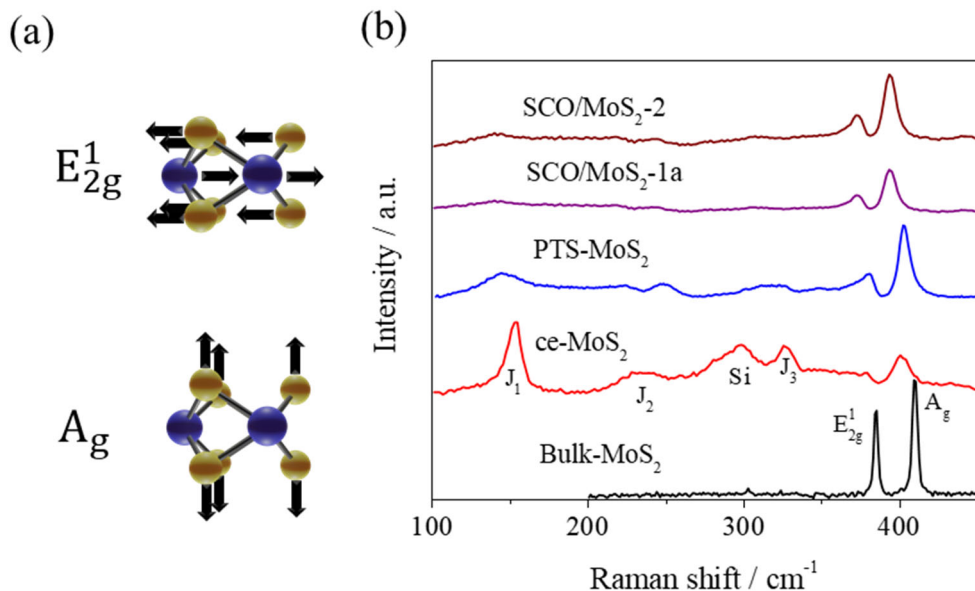


Figure 15. a) E_{2g}^1 and A_{1g} vibrational modes of MoS₂. b) Raman spectrum of bulk-MoS₂ (black), ce-MoS₂ (red), PTS-MoS₂ (blue), SCO/MoS₂-1a (purple), and SCO/MoS₂-2 (wine). The Raman measurements were carried out with the 532 nm excitation wavelength.

For this material, in addition to the E_{2g}^1 and A_{1g} modes, the so-called J peaks are seen in the ce-MoS₂, Figure 15. The presence of J_1 , J_2 , and J_3 peaks (located at ~ 152 , 226 , and 327 cm^{-1} , respectively) are characteristic of 1T-MoS₂. They arise from the 1T-MoS₂ longitudinal acoustic phonon modes.^{25,26} In the PTS-MoS₂, SCO/MoS₂-1a, and -2, the J peaks decrease at the expense of the E_{2g}^1 and A_{1g} signals, Figure 15. These observations support the recovery of the semiconductive 2H phase.

Additionally, the energy of the bandgap can also be monitored by Raman spectroscopy to confirm the phase of the MoS₂. 1T-MoS₂ is metallic without bandgap, while a single layer of 2H-MoS₂ is a direct gap semiconductor with a gap of ~ 1.9 eV, called A peak.²⁷ Therefore, following the photoluminescence (PL) of the different materials in the range between 1.6

and 2.1 eV is possible to distinguish both phases. The main advantage of using this technique instead of a conventional fluorimeter is its high sensitivity and local character, which permits the localization and study of individual flakes.²⁸

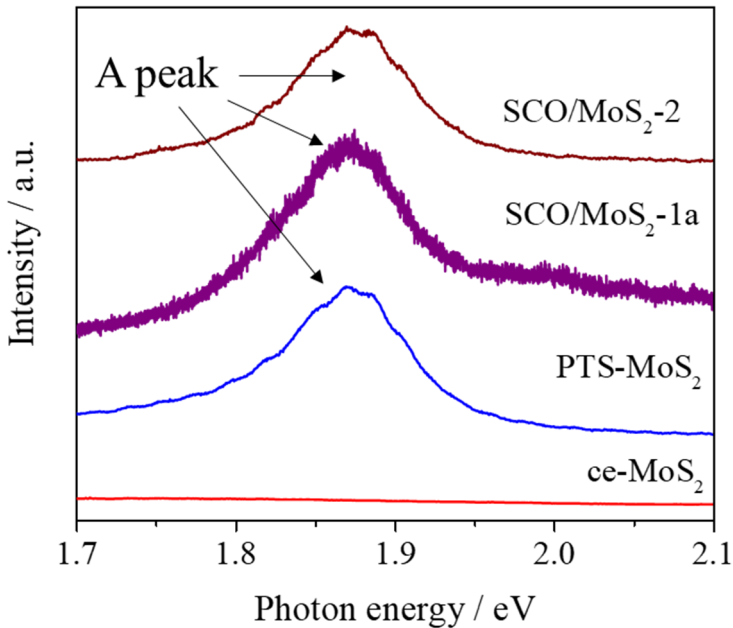


Figure 16. PL measurements of *ce-MoS₂* (red) and *PTS-MoS₂* (blue), *SCO/MoS₂-1a* (purple), and *SCO/MoS₂-2* (wine). The measurements were carried out with 532 nm excitation wavelength.

As can be seen in Figure 16, *ce-MoS₂* does not display PL, due to the metallic nature of the 1T-*MoS₂*. In contrast, *PTS-MoS₂*, *SCO/MoS₂-1a*, and -2 clearly exhibit the A peak expected for the semiconductive 2H-*MoS₂*, Figure 16.²⁷ Therefore, the absence of J peaks and the presence of PL support the recovery of the semiconductive phase after the functionalization.

All this indicates that the 2H-phase seems to be recovered after the covalent functionalization in our particular case.

7.3.5. SCO/MoS₂ spin transition

To study the spin transition persistence in the heterostructure, the oxidation state of the iron, and the χ_{MT} vs T plot of the SCO@SiO₂-40 and -70 NPs and the hybrids SCO/MoS₂-1a, and -2 were measured and compared. Focusing on the XPS, at the region comprised between 700 and 740 eV, the presence of Fe²⁺ was discerned in all the samples, Figure 17.

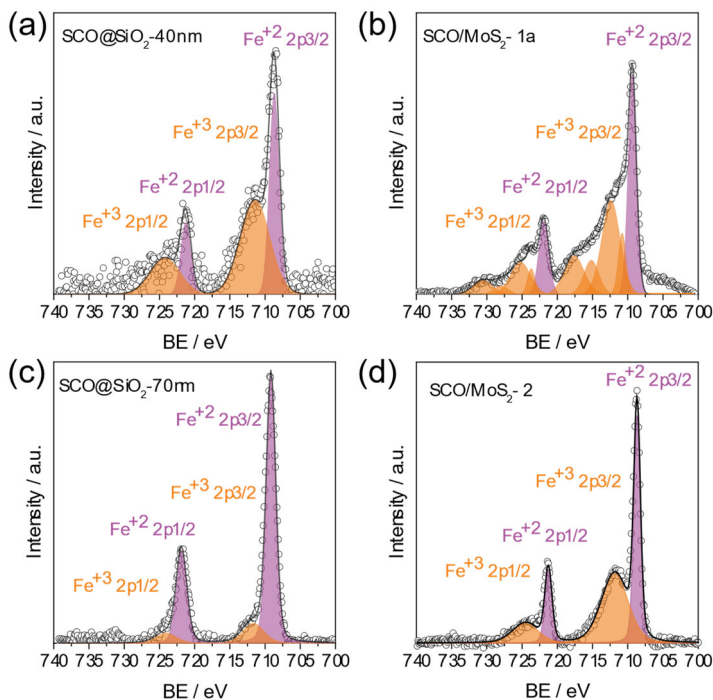


Figure 17. Fe2p XPS region of SCO@SiO₂-40nm (a), SCO/MoS₂-1a (b), SCO@SiO₂-70nm (c), and SCO/MoS₂-2 (d).

The shape of the Fe 2p_{3/2} and Fe 2p_{1/2} of both hybrids matched well with the parent NPs, showing the presence of Fe²⁺ (magenta), and extra bands that we associated with Fe³⁺ (orange). Remarkably, the amount of Fe³⁺ seemed to increase in SCO/MoS₂-1a, and -2 respect the bare NPs, pointing out to a partial oxidation of the NPs during the synthetic protocol.

This slight increase in Fe^{3+} is also reflected in the $\chi_{\text{M}}T$ of the SCO/MoS₂-1a, and -2 Figure 18. Thus, the hybrid material exhibits a higher $\chi_{\text{M}}T$ at room temperature than the bare NPs, Table 3.

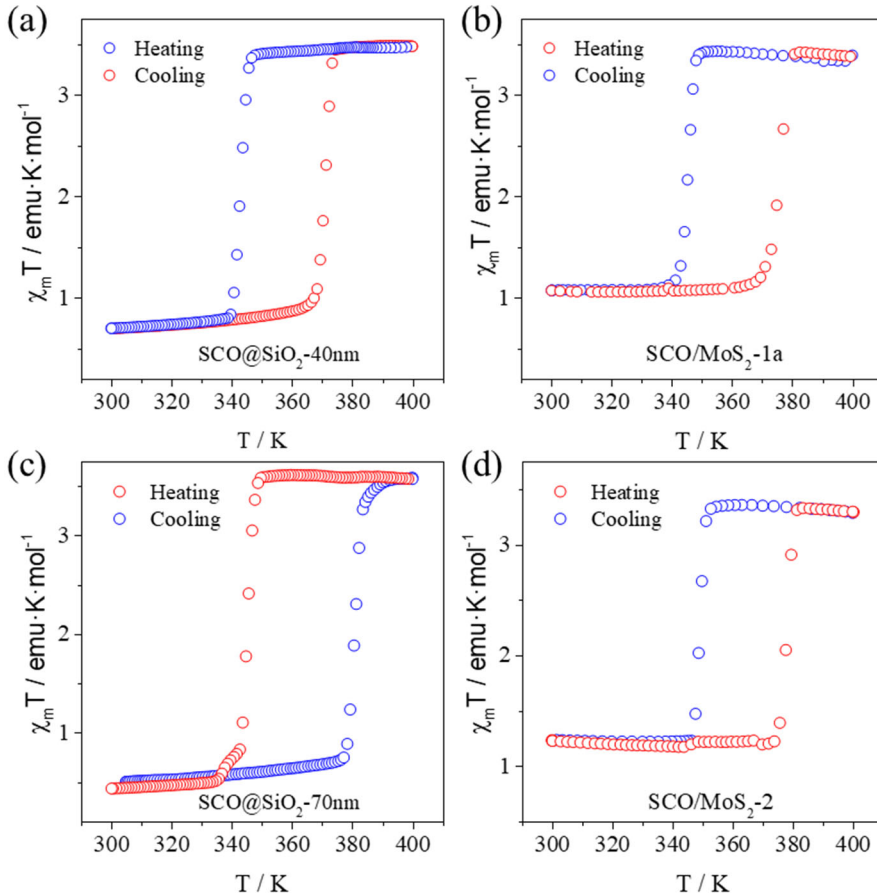


Figure 18. $\chi_{\text{M}}T$ vs T of SCO@SiO₂-40nm (a), SCO/MoS₂-1a (b), SCO@SiO₂-70nm (c), and SCO/MoS₂-2 (d). The measurements have been carried out at 1K/min.

This analysis points out to an increase in the paramagnetic species after the attachment onto the MoS₂ layers. Nevertheless, the transition temperatures remain constant, preserving the same hysterical behaviour at the same transition temperatures than the parents SCO@SiO₂ NPs, Table 4.

Table 4. Physical parameters of the thermally induced spin transition for the different samples.

| | Paramagnetic residue / emu·K·mol ⁻¹ | T _{1/2} ^{HS} / K | T _{1/2} ^{LS} / K | ΔT / K |
|-----------------------------|--|------------------------------------|------------------------------------|--------|
| SCO@SiO ₂ -40 nm | 0.7 | 371 | 343 | 28 |
| SCO@SiO ₂ -70 nm | 0.5 | 380 | 345 | 35 |
| SCO/MoS ₂ -1a | 1.1 | 376 | 345 | 31 |
| SCO/MoS ₂ -2 | 1.2 | 378 | 347 | 31 |

7.3.6. MoS₂ electrical dependency on the NPs spin state

The electrical conductance of the heterostructures as a function of the spin state has been the main tool used in this thesis to elucidate the spin transition effect over the MoS₂. As we have previously proved, the MoS₂ in the hybrid heterostructure was in a semiconductive phase; thus, the band structure of the 2D material can be altered by strain engineering with the aid of the SCO@SiO₂ NPs.

To explore this, the temperature-dependent electrical conductance of disc-shaped pressed pellets of the different materials is investigated. All the measurements are done in a two-probe configuration and a close geometry. These measurements were carried out in collaboration with Julien Dugay and Marta Galbiati at the ICMol.

7.2.6.a. MoS_2 references

It must be noticed that ce- MoS_2 electrical behaviour experienced remarkable changes after its functionalization. Thus, to understand the electrical properties of the hybrid heterostructures, compressed pellets of ce- MoS_2 (1T), annealed ce- MoS_2 (which undergoes a phase transition to 2H), and covalently functionalized ce- MoS_2 , were used as reference samples. The last reference should be the PTS- MoS_2 . However, due to the polymerization at the ambient condition of the silane group, the electrical characterization could not be properly done. Therefore, we functionalized ce- MoS_2 with 1-iodooctadecane, and used it as a reference for covalently functionalized ce- MoS_2 . We call this sample C18- MoS_2 .

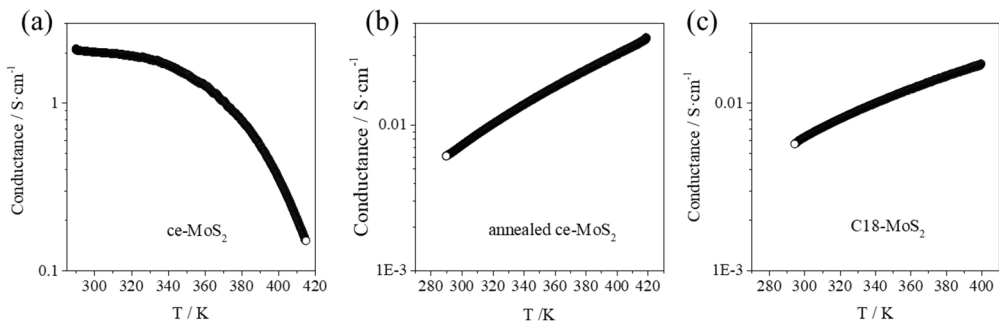


Figure 19. Conductivity as function of the temperature, of ce- MoS_2 , annealed- MoS_2 and C18- MoS_2 , a, b and c, respectively. All the samples were measured at 1K/min.

Figure 19 shows the temperature dependence of the conductance for three reference samples mentioned above. ce- MoS_2 exhibits high conductivity and the typical trend of a metal, where conductivity decreases while the temperature increases, Figure 19a. Moreover, an abrupt decrease occurred over 360 K, which can be associated with the thermal phase transition from 1T to 2H, which begins around 363 K.²⁸

In contrast, the annealed ce-MoS₂ sample at 200°C for 1 h, exhibits a conductance two orders of magnitude lower than the ce-MoS₂, Figure 19b. Additionally, a semiconductor trend is observed for the annealed ce-MoS₂, where conductivity increased almost linearly with the temperature. Finally, the functionalized C18-MoS₂, displays a similar conductivity and trend than for the annealed ce-MoS₂, Figure 19c.

7.2.6.b. SCO/MoS₂

First of all, to properly understand the electrical response of the SCO/MoS₂ samples, raw 40 nm SCO@SiO₂ NPs were characterized. Therefore, a compressed pellet of SCO@SiO₂ NPs was electrically studied as a function of the temperature. As shown in Figure 20a, the SCO@SiO₂ NPs exhibited two jumps in conductance at the transition temperatures. On the one hand, from LS to HS, at ~380 K ($T_{1/2}^{HS}$), and abrupt decrease in conductance was recorded, followed by the reverse scenario upon the transition from HS to LS, at ~340 K ($T_{1/2}^{LS}$). Remarkably, the low value of conductance proved the highly insulating nature of these silica protected NPs (conductance of 10⁻¹¹ at 298 K).

- Effect of the surface coverage

Once all the reference samples and the bare SCO@SiO₂ NPs were investigated, we explored the samples SCO/MoS₂-1a to c made with 40 nm NPs but with different coverages, Figure 20. Starting with SCO/MoS₂-1a (80% coverage) the first interesting feature was its high electrical conductance compared with the bare NPs, i.e.: 10⁻¹¹ S·cm⁻¹ for the NPs and 10⁻⁶ S·cm⁻¹ for the hybrid at 298 K, Figure 20b. This enhanced electrical response suggests that the flakes were connected in the pellet, permitting the

electron flow through the MoS₂ instead of the insulating NPs. Even more, a clear hysteresis loop at the transition temperatures was recorded, measuring an abrupt increase in conductance at ~ 380 K ($T_{1/2}^{HS}$) and a decrease at ~ 340 K ($T_{1/2}^{LS}$). Remarkably, this is the opposite behaviour to that observed in the bare SCO@SiO₂ NPs. This can be attributed to the strain provoked by the spin transition of the NPs to the connected flakes, increasing its average conductance.

For the SCO/MoS₂-1b (50% coverage) a more significant improvement in the electrical response was obtained, exhibiting a conductance as high as 10^{-4} S·cm⁻¹ at 298 K, Figure 20c. Unfortunately, no spin-dependent electrical transport was recorded. This may be attributed to the lower coverage, which improves the contact between flakes at the expense of the strain applied by the NPs.

Finally, SCO/MoS₂-1c (100% coverage) was the most insulating of the three hybrids, displaying a conductance of 10^{-8} S·cm⁻¹ at 298 K, Figure 20d. This indicates that due to the high coverage, there was no contact between flakes. Thus, the main obstacle for the electronic delocalization was the NPs. This is confirmed by the presence of hysteresis with the same trend than bare SCO@SiO₂ NPs (a LS state more conductive than the HS state).

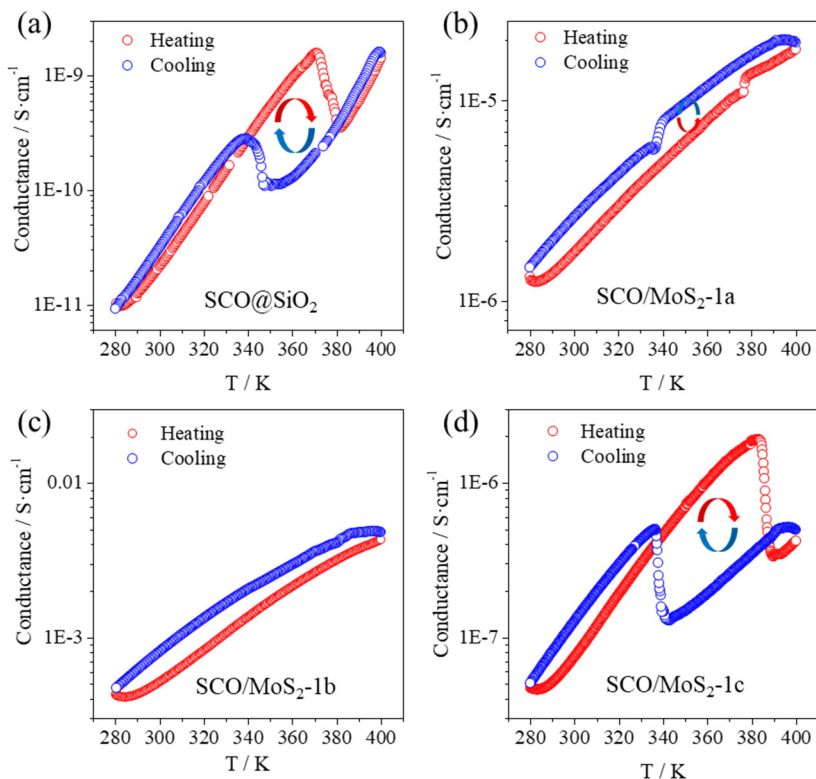


Figure 20. (a-d) Comparison of conductivities as a function of the temperature of SCO@SiO₂ NPs, SCO/MoS₂-1a, b and c respectively. All the samples were measured at 1K/min.

In summary, we have proposed that for SCO/MoS₂-1c, the high coverage isolates the flakes, forcing the electrons to cross through the insulating SCO/SiO₂ NPs, Figure 21c. In contrast, SCO/MoS₂-1b exhibits the highest conductivity due to an effective contact between flakes. Still, if the concentration of NPs is too low the spin transition detection is not possible, Figure 21b.

Finally, SCO/MoS₂-1a is the most interesting sample, presenting a spin state electrical modulation, which has the opposite sign that in the bare NPs. This can be explained considering that the coverage of this sample still

permits the interflake contact, while the number of NPs is high enough to stress the MoS₂. Therefore, the electrical response is mainly obtained from the connected sheets that are mechanically deformed after the spin transition, increasing their conductivity, Figure 21a.

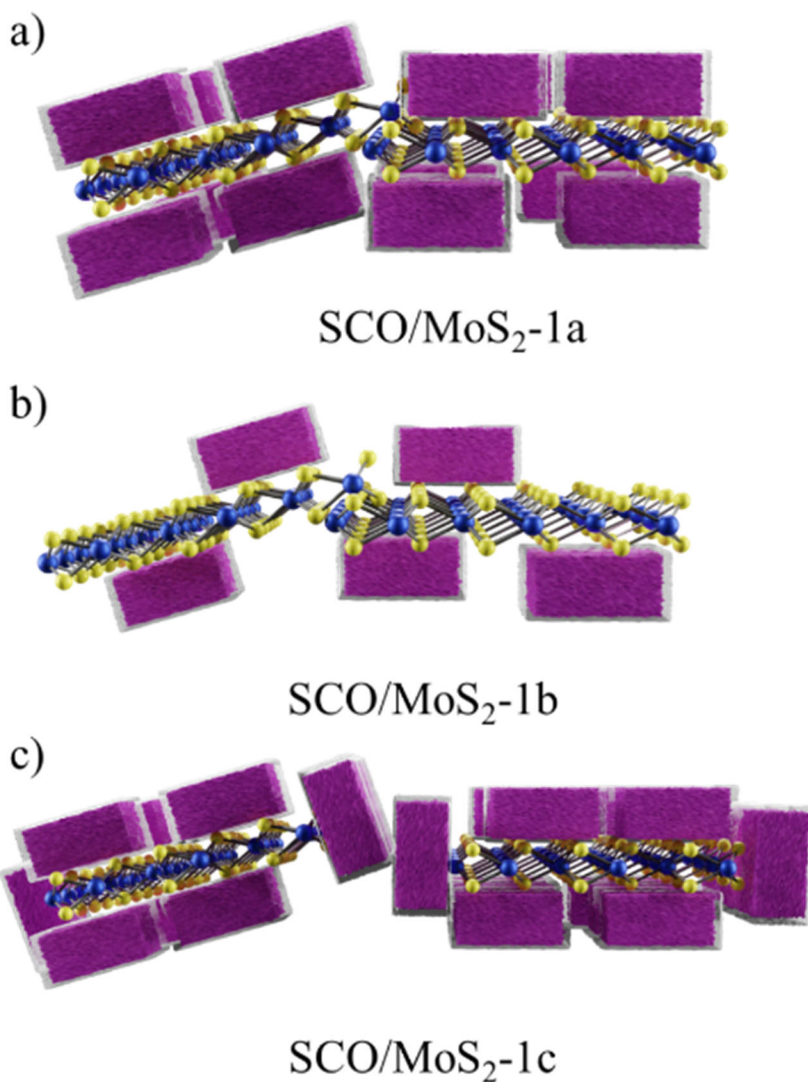


Figure 21. Scheme of the expected contact between MoS₂ layers in the different samples

- SCO@SiO₂ NPs size effect

To investigate the NPs size effect, we also studied the electrical response of SCO/MoS₂-2 (70 nm NPs) with an analogous coverage and ratio of Fe/Mo than SCO/MoS₂-1a. As Figure 22 shows, SCO/MoS₂-2 exhibits a large spin-dependent electrical response, displaying abrupt conductivity increase due to the NPs transition from LS to HS and decrease from HS to LS.

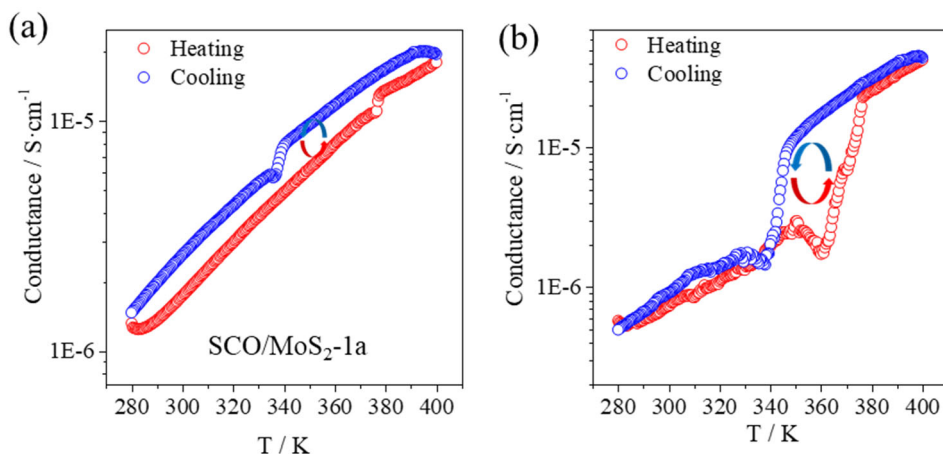


Figure 22. Conductivity vs temperature of SCO-MoS₂-1a, and -2. All the samples were measured at 1K/min.

From the point of view of conductance at 298 K, the two samples exhibit similar values, close to 10^{-6} S·cm⁻¹, suggesting a similar interflake connectivity. Focussing on the trend of the temperature dependence conductance, the same trend is displayed by both samples, with HS being more conductive than LS, Figure 22. Once more, this supported the strain of interconnected flakes as a source of the electronic modulation.

Remarkably, the intensity of the modulation depends on the NPs size. For instance, SCO/MoS₂-2 displays the most extensive electrical modulation, ca. 900% of change, while SCO/MoS₂-1a provides a response of ca. 100%.

Therefore, it is evident that the NPs size plays a role in the mechanical deformation sensed by the MoS₂. These last results point out that, when the relative quantity of SCO:MoS₂ is maintained, there is a more relevant effect induced on the 2D material by the size and shape of the nanoparticles (whose axial elongation increases as their size does), than by their number.

7.3.7. Piezoresistivity

Finally, we estimated the strain sensed by the 2D layer in the SCO/MoS₂ hybrids by using the conductance results, section 7.2.6. The strain was calculated by applying the formula,

$$\varepsilon = \frac{\Delta R}{G \cdot R_0} \quad \text{Eq 1}$$

where ε is the applied strain, R_0 is the electrical resistance of the non-strained material, ΔR is the resistance change inside the hysteresis, and G the gauche factor, which is unique for each material. Accordingly, with the literature, the G value of MoS₂ composites based on chemically exfoliated material can be considered as $G \approx -150$.^{29,30} Therefore, applying equation 1, the estimated strain provoked by the NPs is a 0.2% for the 40 nm NPs (SCO/MoS₂-1a), and 0.6% for the 70 nm (SCO/MoS₂-2), table 5.

Table 5. Summary of SCO/MoS₂ composites strains applied by the NPs.

| | Size / nm | $\Delta R \cdot R_0^{-1}$ | $\varepsilon / \%$ |
|--------------------------|-------------|---------------------------|--------------------|
| SCO/MoS ₂ -1a | ca. 40 x 40 | 0.33 ± 0.03 | 0.22 ± 0.01 |
| SCO/MoS ₂ -2 | ca. 70 x 50 | -0.9 ± 0.2 | 0.60 ± 0.10 |

7.3.8. Spin-dependent optical bandgap

As has been previously presented, because of the direct gap semiconductor nature of the MoS₂ monolayers (2H phase), it may be possible to gain direct information on their bandgap energy through PL measurements. It is well known that when a tensile strain is applied to a MoS₂ layer, its PL redshifts and weakens its intensity due to the bandgap narrowing accompanied by the transition from direct to indirect bandgap semiconductor.^{29,31–36} Therefore, the strain applied by the NPs can be followed by recording the PL as a function of the temperature.

7.2.8.a. SCO@SiO₂ NPs thermally induced spin transition

First of all, the spin transition of the SCO@SiO₂ NPs (70 nm) was investigated by Raman spectroscopy. This coordination compound exhibits three characteristic peaks in the region between 100–300 cm⁻¹, belonging to different Fe-N vibrational modes, and their Raman shift values depend on the spin state, Figure 23.^{1,37} The low spin state signals are located at 133, 205, and 289 cm⁻¹, while the ones of the HS state are at 105, 140, and 180 cm⁻¹.

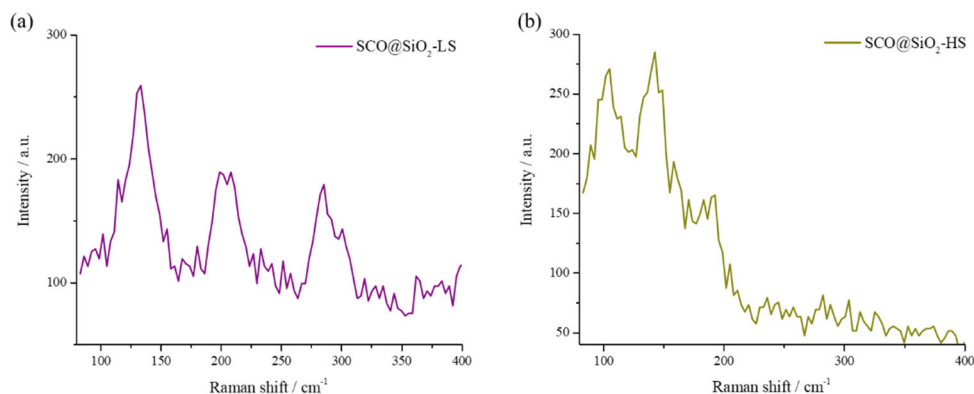


Figure 23. Raman spectra of the SCO@SiO₂ NPs in the LS (298 K) and the HS state (393 K), a and b, respectively.

The spin transition as a function of the temperature was monitored, and it is shown in Figure 24. The bistability region between 340–380 K measured by Raman spectroscopy was in good agreement with the magnetic measurements.

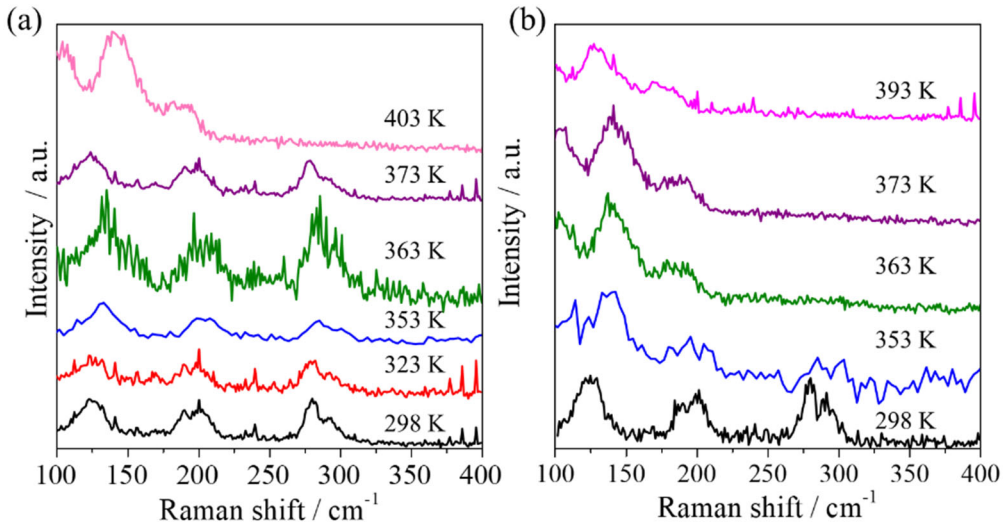


Figure 24. Raman spectra of the SCO@SiO₂ NPs as a function of the temperature in the heating and the cooling processes, a and b, respectively.

7.2.8.b. ce-MoS₂ (2H) photoluminescence thermal dependency

Once the spin transition of the raw SCO@SiO₂ NPs was proved by Raman spectroscopy, we investigated the temperature dependence of annealed ce-MoS₂ to distinguish the PL thermal shift from PL shift caused by the mechanical effect of the NPs volume change. To do so, ce-MoS₂ (1T) was spin-coated on a Si/SiO₂ (285 nm) substrate and heated at 200 °C for 1 h under an inert atmosphere to provoke the phase transition to 2H phase, ce-MoS₂ (2H).

As shown in Figure 25, a linear dependency of the A peak energy with the temperature is displayed by the ce-MoS₂ (2H). Remarkably, by doing a complete cyclic heating-cooling process, no hysteresis is detected.

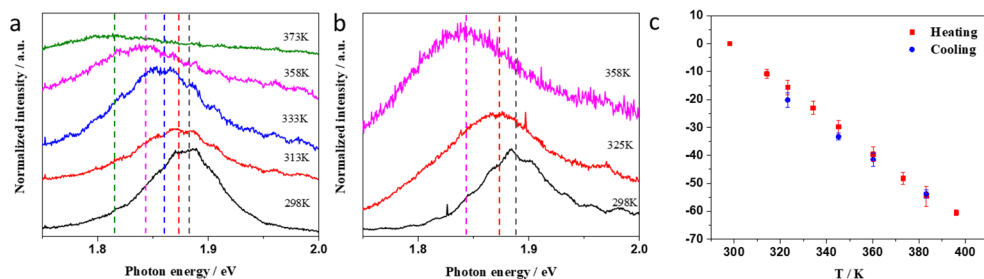


Figure 25. Evolution of the position of the PL emission maximum with temperature of ce-MoS₂ (2H) during the heating (a) and the cooling (b). Excitation power at 0.08 mW. c) PL maximum shift as a function of temperature (red dots, heating, and blue dots, cooling).

7.2.8.c. SCO/MoS₂ photoluminescence thermal dependency

Finally, the same thermal study was done for SCO/MoS₂-1a and -2. The measurements were also carried out over Si/SiO₂ (285 nm) covered with the heterostructures. Figure 26 shows the temperature dependence Raman spectra of both samples. As for the ce-MoS₂ (2H), the A peak shifts to lower energies while the temperature is increased. However, remarkably, in the spin transition range, the A peak in the cooling process is shifted to lower energies for both samples.

To investigate this change in more detail, the A peak maximum as a function of the temperature is plotted, Figure 27a-b. Noticeably, a hysteresis that resembles the one of the SCO@SiO₂ NPs is recorded in both composites. Even more, at the same temperature but in the LS or HS states, we can see a shift of ~9 meV and 40 meV for SCO/MoS₂-1a and 2, respectively, Figure 27c-d. It must be noticed that for the SCO/MoS₂-1a, the error bars of the

heating and the cooling points in the hysteresis overlap, making difficult the precise determination of the shift.

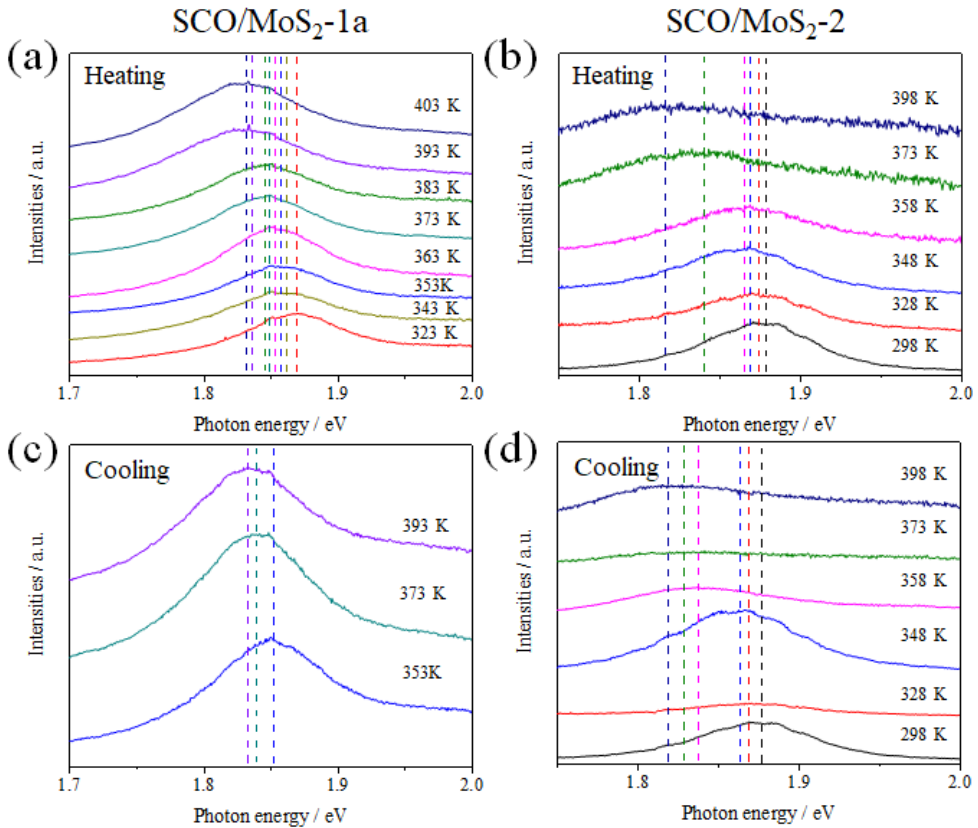


Figure 26. Evolution of the PL emission maxima with the temperature of the SCO/MoS₂-1a and -2 during the heating (a,b) and the cooling (c,d) processes. Excitation power at 0.08 mW.

According to the literature, this A peak redshift inside the hysteresis correspond to a tensile strain of a 0.1% for the SCO/MoS₂-1a and a 0.6% for the SCO/MoS₂-2.³⁶ Noticeably, the calculated tensile strain matches pretty well with the one estimated from the electrical measurements in section 7.2.7. Additionally, the PL intensity seems to decrease in the HS state, which could

be associated with the increase in its indirect bandgap behaviour provoked by the spin transition strain.

These results corroborate that the modulation of the MoS₂ electrical conductance is mainly caused by the pressure applied for the SCO@SiO₂ NPs. Moreover, we have observed that the larger effect is obtained using bigger NPs, which opens the door to tuning the tensile strain applied by playing with the NPs size.

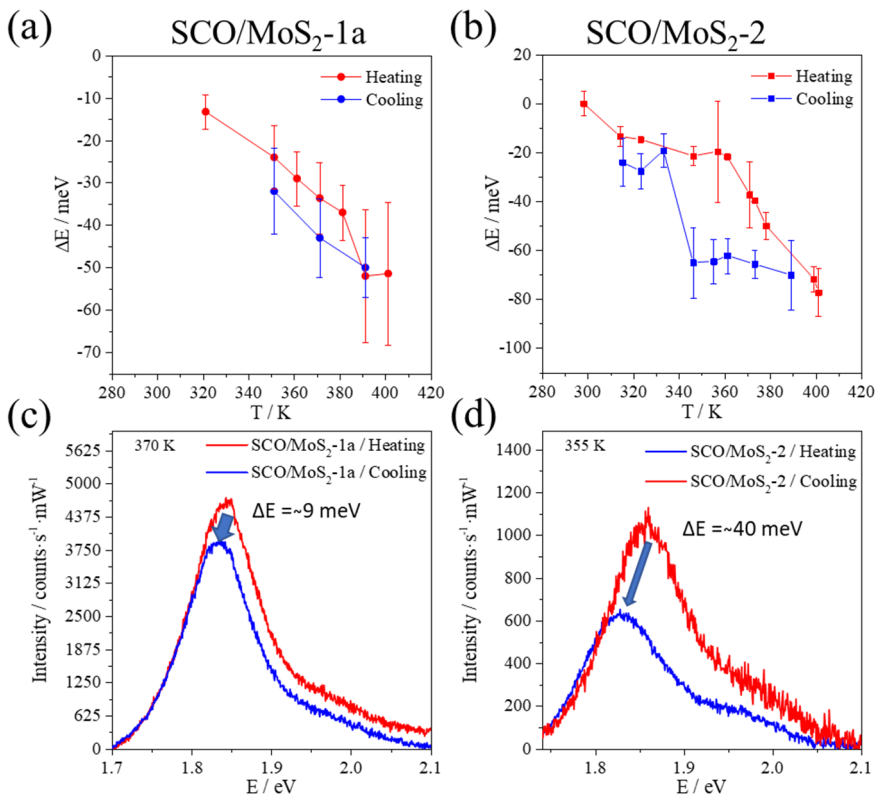


Figure 27. PL shift as a function of temperature (red dots, heating, and blue dots, cooling) of the SCO/MoS₂-1a (a), and 2 (b). (c) PL spectra of SCO/MoS₂-1a at LS, red line (heating), and HS states, blue line (cooling), taken at 370 K. (d) PL spectra of SCO/MoS₂-2 at LS, red line (heating), and HS states, blue line (cooling), taken at 355 K. Raman measurements done with the 532 nm excitation wavelength an 0.08 mW power.

7.2.8.d. *SCO/MoS₂ spin transition under continuum light irradiation*

Since the spin transition of the nanoparticles can be triggered tuning the intensity of irradiating light, the use of an optical source to drive strain modulation in the hybrid materials can also be possible.³⁸ As shown in Figure 28a the spin transition of 70 nm SCO@SiO₂ NPs powder can be triggered by increasing the excitation intensities of the laser from 0.08 to 0.8 mW. The LS features are displayed at the lower excitation (0.08mW) intensity, while the HS is predominant at the higher intensity (0.8 mW). Higher intensities are not possible to be applied because of the damaging of the NPs.

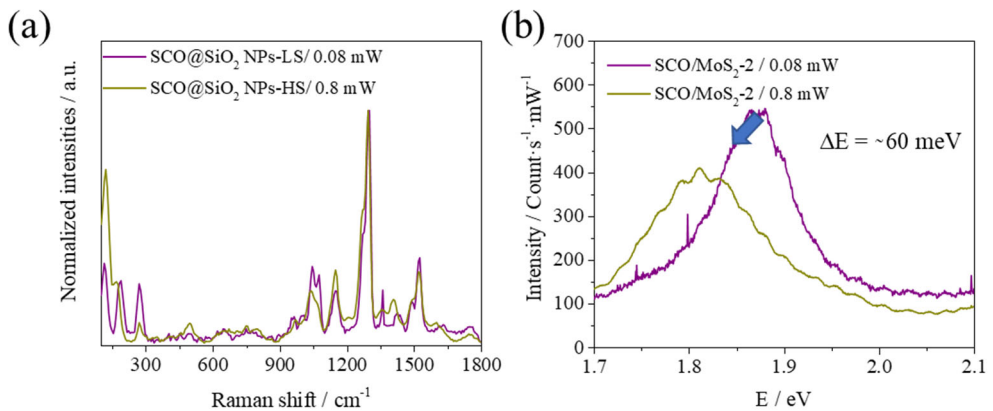


Figure 28. Raman spectra at two different laser intensities (0.8mW, yellow and 0.08 mW, purple) of 70 nm SCO@SiO₂ NPs (a) and SCO/MoS₂-2 (b).

The same methodology has been applied to the hybrid material, SCO/MoS₂-2. At the laser intensities where the spin transition is expected to be in HS, the A_{1g} peak shifted ~ 60 meV and the intensity is decreased, Figure 28b. Comparing these results with the thermally induced spin transition, higher movement of the A_{1g} peak is achieved by light-induced spin transition, ca. 20 meV larger shift. This suggests a cooperative effect between the NPs

heating due to laser irradiation, and the strain induced by the spin transition. To prove this idea, we characterize two reference samples at the two intensities, ce-MoS₂ (2H), and MoS₂ decorated with SiO₂ NPs. This new hybrid material was synthesized by following a similar protocol that the one used for SCO/MoS₂ but by adding pure SiO₂ NPs³⁹ (SiO₂/MoS₂).

Interestingly, the A peak of ce-MoS₂ (2H) does not present any dependence with the laser intensity used in this work, 0.8 and 0.08 mW, (Figure 29a), indicating that the laser does not heat the MoS₂ under these experimental conditions. However, as can be seen in Figure 29b, the A peak of the SiO₂/MoS₂ is shifted ~30 meV and decreases its relative intensity at 0.8 mW irradiation. From these results, we conclude that around ~30 meV of the energy shift exhibited by the SCO/MoS₂-2 could be thermal in origin.

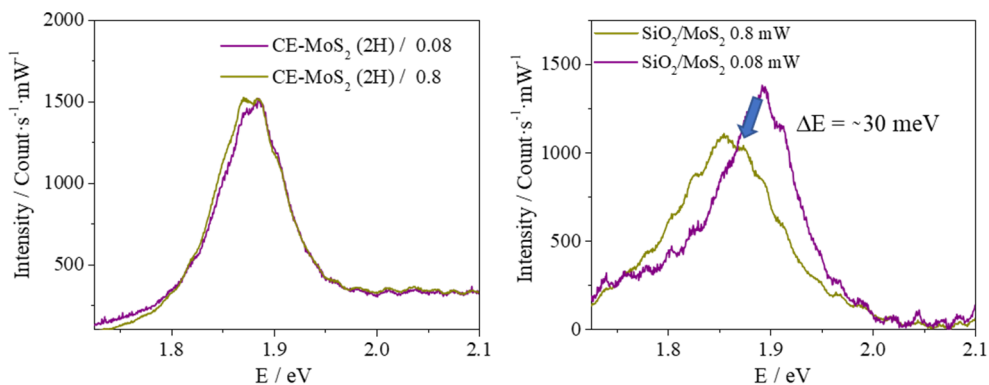


Figure 29. PL spectra at two different laser intensities (0.8 mW, green and 0.08 mW, purple) of reference sample ce-MoS₂/2H (a) and SiO₂/MoS₂ (b).

These results prove that we can optically induce the spin transition by increasing the power of the excitation laser, straining the MoS₂ at room temperature by light irradiation.

7.4. Conclusions and perspectives

In this part of the thesis, we have explored the strain engineering of the MoS₂ bandgap by coupling chemically exfoliated MoS₂ with 40 and 70 nm SCO@SiO₂ NPs in order to obtain a self-stainable composite.

The composite was synthesized by a two-step protocol in solution. In a first step, CE-MoS₂ flakes (metallic 1T-phase) were covalently functionalized with an organic molecule (IPTS), which dramatically altered their electrical and optical properties and restored the semiconducting 2H-MoS₂ phase. Then, by means of the use of the attached molecules as grafting points, the SCO@SiO₂-NPs were homogeneously anchored on these semiconducting MoS₂ layers. The robust synthetic methodology developed permitted to obtain a family of SCO/MoS₂ covalently-linked heterostructures in which control over the size of the nanoparticles and the degree of surface coverage could be achieved.

The change in volume of the SCO@SiO₂ NPs induced by the spin transition upon varying the temperature or by light irradiation, generated a tensile strain on the MoS₂ layers, which has been reflected by sharp changes in their electrical and optical properties. The strain could be tuned depending on the coverage and size of the anchored SCO@SiO₂ NPs. Hence, we have taken advantage of the intrinsic properties of the SCO component to induce strain in TMDCs by the application of temperature or light. In the future, this idea would be expanded to other 2D materials and with the aim of tuning their physical properties via the SCO phenomenon, opening new frontiers for strain engineering towards their application in multifunctional devices beyond conventional electronics.

7.5. Bibliography

- (1) Urakawa, A.; Van Beek, W.; Monrabal-Capilla, M.; Galán-Mascarós, J. R.; Palin, L.; Milanesio, M. Combined, Modulation Enhanced X-Ray Powder Diffraction and Raman Spectroscopic Study of Structural Transitions in the Spin Crossover Material [Fe(Htrz)₂(Trz)](BF₄). *J. Phys. Chem. C* **2011**, *115* (4), 1323–1329.
- (2) Grosjean, A.; Négrier, P.; Bordet, P.; Etrillard, C.; Péchev, S.; Lebraud, E.; Létard, J.; Grosjean, A.; Négrier, P.; Bordet, P.; Etrillard, C.; Mondieig, D. Crystal Structures and Spin Crossover in the Polymeric Material [Fe(Htrz)₂(Trz)](BF₄) Including Coherent-Domain Size Reduction Effects *European Journal of Inorganic Chemistry*, 2013(5-6), 796-802. .
- (3) Chemistry, C. *Spin Crossover in Transition Metal Compounds I*; 2004.
- (4) Manrique-Juárez, M. D.; Rat, S.; Salmon, L.; Molnár, G.; Quintero, C. M.; Nicu, L.; Shepherd, H. J.; Bousseksou, A. Switchable Molecule-Based Materials for Micro- and Nanoscale Actuating Applications: Achievements and Prospects. *Coord. Chem. Rev.* **2016**, *308*, 395–408.
- (5) Shepherd, H. J.; Gural'Skiy, I. A.; Quintero, C. M.; Tricard, S.; Salmon, L.; Molnár, G.; Bousseksou, A. Molecular Actuators Driven by Cooperative Spin-State Switching. *Nat. Commun.* **2013**, *4*, 1–9.
- (6) Gural'Skiy, I. A.; Quintero, C. M.; Costa, J. S.; Demont, P.; Molnár, G.; Salmon, L.; Shepherd, H. J.; Bousseksou, A. Spin Crossover Composite Materials for Electrothermomechanical Actuators. *J. Mater. Chem. C* **2014**, *2* (16), 2949–2955.

-
- (7) Dugay, J.; Giménez-Marqués, M.; Venstra, W. J.; Torres-Cavanillas, R.; Sheombarsing, U. N.; Manca, N.; Coronado, E.; Van Der Zant, H. S. J. Sensing of the Molecular Spin in Spin-Crossover Nanoparticles with Micromechanical Resonators. *J. Phys. Chem. C* **2019**, *123* (11).
- (8) Manrique-Juárez, M. D.; Mathieu, F.; Laborde, A.; Rat, S.; Shalabaeva, V.; Demont, P.; Thomas, O.; Salmon, L.; Leichle, T.; Nicu, L.; Molnár, G.; Bousseksou, A. Micromachining-Compatible, Facile Fabrication of Polymer Nanocomposite Spin Crossover Actuators. *Adv. Funct. Mater.* **2018**, *28* (29), 1–7.
- (9) Joensen, P.; Frindt, R. F.; Morrison, S. R. Single-Layer MoS₂. *Mater. Res. Bull.* **1986**, *21* (4), 457–461.
- (10) Wang, M.; Liechti, K. M.; Wang, Q.; White, J. M. Self-Assembled Silane Monolayers: Fabrication with Nanoscale Uniformity. *Langmuir* **2005**, *21* (5), 1848–1857.
- (11) Singh, J.; Whitten, J. E. Adsorption of 3-Mercaptopropyltrimethoxysilane on Silicon Oxide Surfaces and Adsorbate Interaction with Thermally Deposited Gold. *J. Phys. Chem. C* **2008**, *112* (48), 19088–19096.
- (12) Coronado, E.; Forment-Aliaga, A.; Pinilla-Cienfuegos, E.; Tatay, S.; Catala, L.; Plaza, J. A. Nanopatterning of Anionic Nanoparticles Based on Magnetic Prussian-Blue Analogues. *Adv. Funct. Mater.* **2012**, *22* (17), 3625–3633.
- (13) Paredes, J. I.; Munuera, J. M.; Villar-Rodil, S.; Guardia, L.; Ayán-Varela, M.; Pagán, A.; Aznar-Cervantes, S. D.; Cenis, J. L.; Martínez-

- Alonso, A.; Tascón, J. M. D. Impact of Covalent Functionalization on the Aqueous Processability, Catalytic Activity, and Biocompatibility of Chemically Exfoliated MoS₂ Nanosheets. *ACS Appl. Mater. Interfaces* **2016**, *8* (41), 27974–27986.
- (14) Voiry, D.; Goswami, A.; Kappera, R.; Silva, C. D. C. C. E.; Kaplan, D.; Fujita, T.; Chen, M.; Asefa, T.; Chhowalla, M. Covalent Functionalization of Monolayered Transition Metal Dichalcogenides by Phase Engineering. *Nat. Chem.* **2015**, *7* (1), 45–49.
- (15) Pramoda, K.; Gupta, U.; Chhetri, M.; Bandyopadhyay, A.; Pati, S. K.; Rao, C. N. R. Nanocomposites of C₃N₄ with Layers of MoS₂ and Nitrogenated RGO, Obtained by Covalent Cross-Linking: Synthesis, Characterization, and HER Activity. *ACS Appl. Mater. Interfaces* **2017**, *9* (12), 10664–10672.
- (16) Vishnoi, P.; Pramoda, K.; Gupta, U.; Chhetri, M.; Balakrishna, R. G.; Rao, C. N. R. Covalently Linked Heterostructures of Phosphorene with MoS₂/MoSe₂ and Their Remarkable Hydrogen Evolution Reaction Activity. *ACS Appl. Mater. Interfaces* **2019**, *11* (31), 27780–27787.
- (17) Pramoda, K.; Gupta, U.; Ahmad, I.; Kumar, R.; Rao, C. N. R. Assemblies of Covalently Cross-Linked Nanosheets of MoS₂ and of MoS₂-RGO: Synthesis and Novel Properties. *J. Mater. Chem. A* **2016**, *4* (23), 8989–8994.
- (18) Voiry, D.; Goswami, A.; Kappera, R.; Silva, C. D. C. C. E.; Kaplan, D.; Fujita, T.; Chen, M.; Asefa, T.; Chhowalla, M. Covalent Functionalization of Monolayered Transition Metal Dichalcogenides by Phase Engineering. *Nat. Chem.* **2015**, *7* (1), 45–49.

- (19) Li, D.; Bancroft, G. M.; Kasrai, M.; Fleet, M. E.; Feng, X. H.; Tan, K. H. Polarized X-Ray Absorption Spectra and Electronic Structure of Molybdenite (2H-MoS₂). *Phys. Chem. Miner.* **1995**, *22* (2), 123–128.
- (20) Garcia-Basabe, Y.; Peixoto, G. F.; Grasseschi, D.; Romani, E. C.; Vicentin, F. C.; Villegas, C. E. P.; Rocha, A. R.; Larrude, D. G. Phase Transition and Electronic Structure Investigation of MoS₂-Reduced Graphene Oxide Nanocomposite Decorated with Au Nanoparticles. *Nanotechnology* **2019**, *30* (47), 0–1.
- (21) Guay, D.; Divigalpitiya, W. M. R.; Bélanger, D.; Feng, X. H. Chemical Bonding in Restacked Single-Layer MoS₂ by X-Ray Absorption Spectroscopy. *Chem. Mater.* **1994**, *6* (5), 614–619.
- (22) Yang, S.; Zhang, K.; Wang, C.; Zhang, Y.; Chen, S.; Wu, C.; Vasileff, A.; Qiao, S. Z.; Song, L. Hierarchical 1T-MoS₂ Nanotubular Structures for Enhanced Supercapacitive Performance. *J. Mater. Chem. A* **2017**, *5* (45), 23704–23711.
- (23) Huang, Y.; Sun, Y.; Zheng, X.; Aoki, T.; Pattengale, B.; Huang, J.; He, X.; Bian, W.; Younan, S.; Williams, N.; Hu, J.; Ge, J.; Pu, N.; Yan, X.; Pan, X.; Zhang, L.; Wei, Y.; Gu, J. Atomically Engineering Activation Sites onto Metallic 1T-MoS₂ Catalysts for Enhanced Electrochemical Hydrogen Evolution. *Nat. Commun.* **2019**, *10* (1), 1–11.
- (24) Li, H.; Zhang, Q.; Yap, C. C. R.; Tay, B. K.; Edwin, T. H. T.; Olivier, A.; Baillargeat, D. From Bulk to Monolayer MoS₂: Evolution of Raman Scattering. *Adv. Funct. Mater.* **2012**, *22* (7), 1385–1390.
- (25) Saito, R.; Tatsumi, Y.; Huang, S.; Ling, X.; Dresselhaus, M. S. Raman

- Spectroscopy of Transition Metal Dichalcogenides. *J. Phys. Condens. Matter* **2016**, *28* (35).
- (26) Jiménez Sandoval, S.; Yang, D.; Frindt, R. F.; Irwin, J. C. Raman Study and Lattice Dynamics of Single Molecular Layers of MoS₂. *Phys. Rev. B* **1991**, *44* (8), 3955–3962.
- (27) Mak, K. F.; Lee, C.; Hone, J.; Shan, J.; Heinz, T. F. Atomically Thin MoS₂: A New Direct-Gap Semiconductor. *Phys. Rev. Lett.* **2010**, *105* (13), 2–5.
- (28) Eda, G.; Yamaguchi, H.; Voiry, D.; Fujita, T.; Chen, M.; Chhowalla, M. Photoluminescence from Chemically Exfoliated MoS₂. *Nano Lett.* **2011**, *11* (12), 5111–5116.
- (29) Manzeli, S.; Allain, A.; Ghadimi, A.; Kis, A. Piezoresistivity and Strain-Induced Band Gap Tuning in Atomically Thin MoS₂. *Nano Lett.* **2015**, *15* (8), 5330–5335.
- (30) Bicca, S.; Boland, C. S.; Odriscoll, D. P.; Harvey, A.; Gabbett, C.; Osuilleabhain, D. R.; Griffin, A. J.; Li, Z.; Young, R. J.; Coleman, J. N. Negative Gauge Factor Piezoresistive Composites Based on Polymers Filled with MoS₂ Nanosheets. *ACS Nano* **2019**, *13* (6), 6845–6855.
- (31) Scalise, E.; Houssa, M.; Pourtois, G.; Afanas'ev, V.; Stesmans, A. Strain-Induced Semiconductor to Metal Transition in the Two-Dimensional Honeycomb Structure of MoS₂. *Nano Res.* **2012**, *5* (1), 43–48.
- (32) Li, H.; Contryman, A. W.; Qian, X.; Ardakani, S. M.; Gong, Y.; Wang,

- X.; Weisse, J. M.; Lee, C. H.; Zhao, J.; Ajayan, P. M.; Li, J.; Manoharan, H. C.; Zheng, X. Optoelectronic Crystal of Artificial Atoms in Strain-Textured Molybdenum Disulphide. *Nat. Commun.* **2015**, *6* (May).
- (33) Mangu, V. S.; Zamiri, M.; Brueck, S. R. J.; Cavallo, F. Strain Engineering, Efficient Excitonic Photoluminescence, and Exciton Funnelling in Unmodified MoS₂ Nanosheets. *Nanoscale* **2017**, *9* (43), 16602–16606.
- (34) Carrascoso, F.; Lin, D.-Y.; Frisenda, R.; Castellanos-Gomez, A. Biaxial Strain Tuning of Interlayer Excitons in Bilayer MoS₂. *J. Phys. Mater.* **2019**, *3* (1), 015003.
- (35) Gant, P.; Huang, P.; Pérez de Lara, D.; Guo, D.; Frisenda, R.; Castellanos-Gomez, A. A Strain Tunable Single-Layer MoS₂ Photodetector. *Mater. Today* **2019**, *27* (August), 8–13.
- (36) Pető, J.; Dobrik, G.; Kukucska, G.; Vancsó, P.; Koós, A. A.; Koltai, J.; Nemes-Incze, P.; Hwang, C.; Tapasztó, L. Moderate Strain Induced Indirect Bandgap and Conduction Electrons in MoS₂ Single Layers. *npj 2D Mater. Appl.* **2019**, *3* (1), 1–6.
- (37) Faulmann, C.; Chahine, J.; Malfant, I.; De Caro, D.; Cormary, B.; Valade, L. A Facile Route for the Preparation of Nanoparticles of the Spin-Crossover Complex [Fe(Htrz)₂(Trz)](BF₄) in Xerogel Transparent Composite Films. *Dalt. Trans.* **2011**, *40* (11), 2480–2485.
- (38) Guillaume, F.; Tobon, Y. A.; Bonhommeau, S.; Létard, J. F.; Moulet, L.; Freysz, E. Photoswitching of the Spin Crossover Polymeric

Material [Fe(Htrz)₂(Trz)](BF₄) under Continuous Laser Irradiation in a Raman Scattering Experiment. *Chem. Phys. Lett.* **2014**, *604*, 105–109.

- (39) Stöber, W.; Fink, A. Controlled Growth of Monodisperse Silica Spheres in the Micron Size Range. *J. Colloid Interface Sci.* **1968**, *26*, 62–69.

7.5. Experimental section

7.5.1. Characterization techniques: Equipment and experimental conditions.

High-resolution transmission electron microscopy (HR-TEM) and transmission electron microscopy (TEM): HR-TEM studies are carried out on a Technai G2 F20 microscope operating at 200 kV and TEM studies on a JEM-1010 operating at 100 kV. Samples are prepared by dropping suspensions on lacey formvar/carbon copper grids (300 mesh).

Dynamic light scattering (DLS) and Zeta Potential (ξ pot): Both values are determined in suspension at room temperature with a Zetasizer Nano ZS instrument (Malvern Instruments Ltd.).

Zeta Potential (ξ pot) measurements: ξ -pot values are measured at room temperature with a Zetasizer Nano ZS instrument (Malvern Instruments Ltd.).

Thermogravimetric analyses (TGA): Samples are measured using a TGA 550 (TA Instruments) at a heating rate of 5 °C/min from 25-700 °C under air.

Attenuated total reflectance Fourier-transform infrared spectra (ATR-FTIR): Samples are measured using an ALPHA II FTIR Spectrometer (Bruker) in the 4000-400 cm^{-1} range with a resolution of 4 cm^{-1} .

X-ray Photoelectron Spectroscopy (XPS): Samples are analyzed *ex-situ* at the X-ray Spectroscopy Service at the Universidad de Alicante using a K-ALPHA Thermo Scientific spectrometer. All spectra are collected using Al $K\alpha$ radiation (1486.6 eV), monochromatized by a twin crystal monochromator, yielding a focused X-ray spot (elliptical in shape with a major axis length of 400 μm) at 30 mA and 2 kV. The alpha hemispherical analyzer is operated in the constant energy mode with survey scan pass energies of 200 eV to measure the whole energy band and 50 eV in a narrow scan to selectively measure the particular elements. XPS data are analyzed with Avantage software, and plotted with the software Origin. A smart background function is used to approximate experimental backgrounds.

Charge compensation is achieved with the system flood gun that provides low energy electrons and low energy argon ions from a single source.

Transport measurements: All transport measurements have been performed in a Physical Properties Measurement System (Quantum Design, PPMS-9) in the temperature range of 280 K to 400 K, under vacuum. Disc-shaped pressed powder pellets of the different samples are prepared by applying ca. 0.05 MPa and measured in a two probes configuration. The pellets are contacted through silver paste and Pt wires, maintaining a very close geometry in all samples. Electrical measurements are performed using a Keithley 6517B electrometer as voltage source and to measure current. Conductivity values are calculated as $\sigma = (G \cdot l) / (t \cdot w)$, where G is the measured conductance, l is the distance between electrodes, w the electrodes length, and t the thickness of the pellets. Optical microscopy has been used to estimate these values.

Inductively Coupled-Plasma Optical Emission Spectrometry (ICP-OES): ICP-OES analysis is conducted at the Universidad of Valencia. Samples are digested in nitric acid using a high-pressure microwave oven.

Magnetic susceptibility (SQUID): Magnetic susceptibility measurements are performed on powdered samples with a Quantum Design MPMS-XL-5 SQUID susceptometer. The susceptibility data are corrected from the diamagnetic contributions and deduced by using Pascal's constant tables. The data are collected in the range 300–400 K upon recording several heating-cooling cycles at a constant rate of $1 \text{ K} \cdot \text{min}^{-1}$ with an applied field of 0.1 T.

Raman measurements: the Raman measurements are carried out with a Horiba-MTB Xplora. All the samples are measured under continuous waveoperation (CW), exciting the sample at 532 nm wavelength. The excitation power is 0.8 or 0.08 mW. The light is focused on the sample using a regular microscope objective (100x magnification, Olympus brand, with a working distance of 0.21 mm). The power is measured placing a laser power meter (Maxlab-TOP from Coherent Inc.) below the objective. SCO@SiO₂-NPs, and SCO/MoS₂-1 spectra are measured on powdered samples, while

the MoS₂ and the SCO/MoS₂-1 are spin-coated on silicon substrates and the largest and most isolated flakes are chosen. The temperature dependent Raman characterization has been carried out by adapting the sample holder of our confocal setup for holding a ceramic resistor of 20 W with one inch² area. The sample is located at the centre of the resistor and held with silver paste. The temperature of the system is monitored with a platinum resistance and controlled with feedback electronics. A stabilization time of five minutes is left between consecutive measurements in the temperature sweep to minimize eventual thermal drifts.

UV/Vis Spectroscopy: UV-vis absorption spectra are recorded on a Jasco V-670 spectrophotometer in baseline mode from 400 to 800 nm range, using 1.000-cm-optical-path plastic cuvettes.

Atomic Force Microscopy (AFM). The substrates are imaged with a Digital Instruments Veeco Nanoscope IVa AFM microscope in tapping and contact mode. Silicon tips with natural resonance frequency of 300 kHz and with an equivalent constant force of 40 N/m are used. Gwyddion software is used to process the obtained images

Synchrotron X-Ray Absorption spectroscopy. X-ray data of powder or dropped casted material on Si/SiO₂ or glass substrates are collected at the Beamlines Deimos (proposal 20181583) and SAMBA (proposal 20191609) at Soleil synchrotron.

7.5.2. Methods

Materials. All chemical reagents are purchased and used without further purification: (3-Iodopropyl)trimethoxysilane, 1-Iodooctadecane (Sigma-Aldrich), Tetraethyl orthosilicate 98% (Sigma-Aldrich), Triton X-100 (Sigma-Aldrich), ascorbic acid (Sigma-Aldrich), 1,2,4-triazole (Sigma-Aldrich), iron tetrafluoroborate hexahydrate (Sigma-Aldrich), n-hexanol (Sigma-Aldrich), cyclohexane (Sigma-Aldrich), ethanol absolute (Sigma-Aldrich) ultra-pure water (18.2 MΩ). Molybdenum(IV) sulfide (Alfa Aesar), *n*-butyllithium solution 1.6 M in hexane (Sigma-Aldrich),

anhydrous hexane (Sigma-Aldrich). SiO₂ (285 nm)/Si substrates are bought from NOVA Electronic Materials LLC, Flower Mound, TX. (Sigma-Aldrich), chloroauric acid (Sigma-Aldrich), sodium citrate tribasic dihydrate (Sigma-Aldrich), Sodium borohydride (Sigma-Aldrich).

7.5.3. Self-strainable MoS₂ composite

Chemical exfoliation MoS₂ (CE-MoS₂).

The chemical exfoliation of MoS₂ is carried out according by Marc Morant-Giner.¹

Chemical exfoliated MoS₂ in 2H-phase.

CE-MoS₂ flakes retrieved by centrifugation is spin coated on SiO₂ (285 nm)/Si substrates and heated up at 200°C for 2 h under an inert atmosphere (O₂ < 0.1 ppm, H₂O < 0.1 ppm), to induce the 1T-to-2H-phase transition

70 x 50 nm [Fe(Htrz)(trz)(BF₄)]@SiO₂ Nanoparticles.

An aqueous solution of Fe(BF₄)₂·6H₂O (0.5 mL, 1.25 M) and tetraethyl orthosilicate (TEOS) (0.1 mL) is added to a freshly prepared mixture containing Triton X-100 (1.8 mL, ω = 9), n-hexanol (1.8 mL), cyclohexane (7.5 mL). A microemulsion of this mixture is obtained by stirring at room temperature for 15 minutes. Then, an aqueous solution of 1,2,4-1H-triazole (0.5 mL, 4.5 M) ligand containing the TEOS (0.1 mL) is added to a similarly prepared organic solution and stirred at room temperature for 15 min. In order to permit a micellar exchange, both microemulsions are combined and stirred for 2 h. The formed nanoparticles are isolated by precipitation upon addition of acetone and collected by centrifugation (12000 rpm, 10 min), followed by washing with ethanol (x4 times), to

remove the excess of surfactant, and acetone (x1 time). Finally, the powdered samples are dried at 70°C for 2 h.

40 x 40 nm [Fe(Htrz)(trz)(BF₄)]@SiO₂ NPs.

The synthesis of the smallest NPs follows the same procedure as for the 70 nm but using 2 mL of Triton X.100.

30 x 30 nm Fe(Htrz)(trz)(BF₄)]@SiO₂ NPs.

The synthesis of the smallest NPs follows the same procedure as for the 70 nm but using 2.7 mL of Triton X.100.

MoS₂ IPTS functionalised (PTS-MoS₂).

Firstly, a 5 mM aqueous suspension of CE-MoS₂ flakes is prepared from the mother one. Independently, a solution of 3-iodopropyl(trimethoxysilane) (IPTS), 0.1 M in ethanol is prepared. Later the IPTS solution is slowly added over the aqueous suspension in water:ethanol ratio, 2:1, under strong stirring, and let it react for 12h. Finally, the functionalized nanosheets are washed by several cycles of centrifugation (at 7000 rpm, 15 min) and dispersed in water:ethanol, 2:1 (x3 times), and in ethanol (x3 times).

SCO/MoS₂-1a-c.

The functionalized PTS-MoS₂ is suspended in ethanol under vigorous stirring in a concentration of 5 mM. Later, a colloidal suspension of 40 nm SCO-NPs, 10, 1, and 20 mg·ml⁻¹, is added and leave it

to react for 48 h, SCO/MoS₂-1a, b, and c, respectively. Finally, several cycles of centrifugation and dispersion at different rates are carried out until the supernatant has no residues of SCO-NPs.

SCO/MoS₂-2.

The functionalized PTS-MoS₂ is suspended in ethanol under vigorous stirring in a concentration of 5 mM. Later, a colloidal suspension of 70 nm SCO-NPs, 10 mg·ml⁻¹, is added and leave it to react for 48 h. Finally, several cycles of centrifugation and dispersion at different rates are carried out until the supernatant has no residues of SCO-NPs.

SCO/MoS₂-3.

An analogues synthesis than SCO/MoS₂-2 is carried out but adding ~30 nm NPs.

8. General Conclusions

In this thesis, we have investigated three different molecular systems to obtain multifunctional hybrid materials. Later these same hybrids were implemented in electrical devices as a proof of concept for their use as active components.

Firstly, in chapters 1 and 2 we explored the use of a chiral peptide, LBT, coordinating a metallic cation, Tb and Y, as a spin filter. The coordination compound was formed in solution by mixing a buffered solution with the peptide and a solution containing the cation. In the case of the Tb, the proper coordination was proved by PL spectroscopy, measuring the light emission of the complex after 280 nm irradiation, which is characteristic of the Tb coordination by the LBT. Then a SAM of the complex was formed on gold-covered substrates, thanks to the LBT terminal cysteine. The correct anchoring of the peptide was studied by MALDI-TOF, XPS, and PL spectroscopy, where the presence of the peptide and the coordinated Tb were demonstrated. The formed SAM was found to be a well-packed monolayer, according with the AFM and QMCD results. Finally, the spin-dependent electrical conductivity of the TbLBT and YLBT were investigated by wet and dry techniques and using an external magnetic field to magnetize a functionalized ferromagnetic substrate (Ni/Au). On the one hand, the spin filtering of the SAM was investigated by using the functionalized substrate as the working electrode in an electrochemical cell and following the redox reaction of a $\text{Fe}^{2+}/\text{Fe}^{3+}$ solution. For this technique, a clear spin polarization of the $\sim 3\%$ was recorded for the TbLBT, while for the YLBT was a $\sim 2\%$. On the other hand, these same results were corroborated by solid-state electrical conductivity using liquid contacts.

Therefore, we concluded that the coordinated atom plays a role in the spin filtering capabilities of these types of SAMs, opening the door to its reinforcement by exchanging the coordinated cation.

In chapters 3, 4, and 5, we focused our attention on the synthesis of hybrid nanostructures of the SCO compound $[\text{Fe}(\text{Htrz})_2(\text{trz})](\text{BF}_4)$. Two hybrids were explored during this thesis. The first one in chapter 4 consisted of the wrap of $[\text{Fe}(\text{Htrz})_2(\text{trz})](\text{BF}_4)$ NPs with a SiO_2 shell to provide an anchoring point for post functionalization at the same time that increases the robustness of the system. While this system has already been reported, we targeted to synthesize smaller NPs than the already reported and with a thinner shell to improve the interaction of the core with its environment. To do so, we synthesized the NPs by the reverse micelle techniques, and by tuning some crucial parameters, we could obtain NPs ranging from ~ 90 to ~ 28 nm. It must be noticed that the smaller NPs reported till now of this $\text{SCO}@\text{SiO}_2$ compound were of ~ 50 nm. We also succeeded in decreasing the shell thickness, obtaining a shell of ~ 3 nm for the bigger NPs, while the previous publications produced a shell of ~ 12 nm.

The second hybrid, in chapter 5, was also a $\text{core}@\text{shell}$ nanoarchitecture with Au NPs as core and a $[\text{Fe}(\text{Htrz})_2(\text{trz})](\text{BF}_4)$ shell. The main interest of developing this type of metallic-SCO heterostructures resides in improving the SCO electrical responses, which hampers their implementation in practical devices due to their high insulating nature. The synthetic protocol developed during this thesis consisted of the progressive grown of the SCO shell around the Au core by alternative addition of the metal and the ligand, which, thanks to Au's great affinity for the N, from the triazole, grows covering the metallic nanostructures. This protocol could be applied for two

different Au nanoarchitectures, nanospheres or nanostars, proving the versatility of the method. Then the electrical performance of the core@shell made with Au nanospheres was tested, obtaining a system several orders of magnitude more conductive than the bare SCO NPs, and with a larger on/off ratio.

The last chapters, 6-7, deal with the strain engineering of MoS₂ as a manner to alter its electrical and optical response. To do so, in chapter 7 we explored the use of the SCO@SiO₂ NPs described in chapter 4 as a source of reversible mechanical strain. In this context, chemically exfoliated MoS₂ was functionalized with a silanol molecule that can later react with the silica shell of the NPs, leading to flakes decorated with the SCO@SiO₂ NPs. Remarkably, in contrast with other publications, the original semiconductive phase of the MoS₂ was restored after its functionalization, as XPS, XAS, Raman and PL spectroscopy shows. Later the electrical response of the SCO/MoS₂ heterostructure was explored, recording a spin state electrical modulation that depended on the degree of coverage and size of the anchored NPs. The electrical tuning was attributed to a closure of the MoS₂ bandgap due to the strain applied by the NPs spin transition. This was further proved by studying the PL signal of the MoS₂ as a function of the temperature, observing a shift to lower energies in the HS state, indicating that the spin transition was causing the MoS₂ bandgap closure.

Resumen en castellano

En los pasados 50 nuestro mundo ha experimentado unos avances tecnológicos sin precedentes en la historia. Entre los múltiples motivos de esto, uno de los más importantes es la progresiva miniaturización de componentes electrónicos, que ha permitido la obtención de dispositivos cada vez más pequeños, eficientes y baratos. In este sentido los materiales utilizados típicamente para estos fines, especialmente el Silicio, están llegando a un plateau en lo que a eficiencia con respecto a su miniaturización se refiere. Esto es debido a que sus propiedades se ven gravemente afectadas cuando sus dimensiones son reducidas. Una solución muy interesante para superar esta limitación podría ser el desarrollo de materiales moleculares como componentes activos de estos dispositivos. Debido a su naturaleza molecular pueden conservar sus propiedades intactas incluso a escala monomolecular, representando el máximo exponente en el desarrollo de tecnologías a la nanoescala.

Por este motivo el objetivo de esta tesis ha sido el desarrollo de materiales híbridos, basados en materiales moleculares, cuyos componentes combinados den lugar a una modulación o incluso la aparición de nuevas propiedades, y que finalmente puedan emplearse en dispositivos electrónicos. Además, eligiendo apropiadamente los materiales que se combinan también se pueden desarrollar materiales multifuncionales que sean útiles para otros fines. Teniendo esto en mente, durante esta tesis doctoral se desarrollaron tres tipos de híbridos moleculares basados en componentes de distintas dimensionalidades. En primer lugar, en la parte I de la tesis se sintetizaron híbridos moleculares basados en oligopéptidos

de 1.6 nm de diámetro coordinado diferentes cationes sobre superficies metálicas, oro, y ferromagnéticas, oro/niquel, buscando el uso de estas moléculas como filtros de spin en espintrónica.

Es bien sabido que los electrones en movimiento son sistemas quirales, de forma que cuando interactúan con otros sistemas quirales interesantes fenómenos ocurren. Uno de los más interesantes para el desarrollo de dispositivos electrónicos es el acoplamiento de la quiralidad del electrón debido a su espín con la quiralidad de las biomoléculas, derivada de su helicidad. Debido a que los electrones fluyen a través del cuerpo central de este tipo de biomoléculas helicoidales, la quiralidad de esta puede acoplar con el espín del electrón, especialmente si la molécula está apropiadamente orientada, facilitando el paso de corriente en un sentido para un determinado espín (espín-arriba o abajo). Con esto se pueden conseguir corrientes polarizadas en espín, pudiendo convertirse en perfectos filtros de espín para dispositivos spintrónicos. Desde su descubrimiento este efecto ha sido conocido como chiral induce spin selectivity, efecto CISS, y aunque es un efecto interesante y con aplicaciones claras, su eficiencia se encuentra aun muy por debajo de los requisitos que demandan los dispositivos spintrónicos actuales. Por este motivo en esta parte de la tesis nos centramos en intentar mejorar el filtrado de espín de un oligopéptido perteneciente a una familia de biomoléculas llamadas Lanthanide Binding tags (LBT) coordinándolo con diferentes cationes metálicos y estudiamos el rol del catión coordinado en el filtrado de espín del sistema. El motivo por el que la presencia de átomos pesados, el catión coordinado por la biomolécula debería afectar al filtrado

de espín es debido a que la interacción del electrón circulando por la cadena debería incrementarse al introducir elementos con un gran peso atómico. Con este fin decidimos usar dos tipos de cationes para coordinar a la biomolécula, Y^{3+} y Tb^{3+} , los cuales presentan diferentes pesos atómicos ($Z=39$ y 65 , respectivamente) pero la misma carga y coordinan de forma análoga. También presentan propiedades magnéticas completamente diferentes, siendo el primero diamagnético ($S=0$) y el segundo paramagnético ($S=5/2$), esto añade otro grado de libertad al sistema, obteniendo diferentes comportamientos magnéticos, que, además, idealmente pueden llegar a jugar también un rol en el filtrado de espín.

Con esto en mente, lo primero que hicimos fue seleccionar el oligopéptido adecuado de la familia de los LBT, y para nuestros fines decidimos usar la siguiente secuencia YIDTNNDGWYEGDEL_C. Este oligopéptido presenta múltiples carbonilos terminales que coordinan fuertemente cationes como el Y^{3+} y el Tb^{3+} , además de presentar una intensa luminiscencia en el caso de la coordinación con el Tb^{3+} , lo puede usarse para demostrar la formación del complejo. El péptido presenta también 1.5 hélices, de forma que por su carácter helicoidal es capaz de filtrar espines, pero además presenta una cisteína terminal, cuyo grupo SH terminales es idóneo para anclar el péptido a superficies metálicas (gracias a la fuerte interacción de los S a metales). Después de elegir el péptido adecuado diseñamos el entorno químico adecuado para que los diferentes cationes pudieran ser coordinado por la molécula, y en el caso del complejo de Tb^{3+} lo comprobamos siguiendo la intensa luminiscencia que presenta a 550 nm

después de su coordinación y lo llamamos TbLBT. Una vez se obtuvo el complejo en disolución se procedió a su anclaje en un sustrato de oro. Este paso se realizó para estudiar la estructura que adquiriría el péptido una vez se depositaba en una superficie, siendo esto la antesala a la producción de un dispositivo espintrónico real, y se eligió el oro como punto de anclaje por los fuertes enlaces que forma con el S. Después de la incubación toda la noche del sustrato de oro en una disolución del complejo de TbLBT pudimos demostrar la presencia de péptido en la superficie metálica por MALDI-TOF, donde se pudo distinguir el fragmento completo del péptido, y la presencia del péptido fue demostrada por XPS, donde los característicos picos Tb3d eran perfectamente visibles. Para demostrar que la coordinación se había mantenido en nuestro sustrato de oro recubierto estudiamos la luminiscencia del mismo, observando una ligera emisión de luz proveniente del sustrato que demostraba la presencia de Tb³⁺ coordinados por el péptido. Todas estas pruebas sugieren fuertemente que nuestro protocolo sintético permite el recubrimiento de sustratos de oro con TbLBT sin afectar ni la estructura ni la coordinación del sistema, desde ahora el sustrato de oro modificado con el complejo será llamado Au/TbLBT.

Después estudiamos el porcentaje de recubrimiento y la topografía del sustrato mediante QMCD y AFM. El QMCD nos permitió estimar que la incubación del sustrato en la disolución del TbLBT daba lugar a monocapas de péptido en el sustrato metálico. Esta caracterización estaba en consonancia con las medidas de AFM de la topografía, donde no se veían cambios apreciables en la rugosidad del sustrato después del

recubrimiento, lo cual indica que el empaquetamiento de las moléculas es tan eficiente que no se puede distinguir de la rugosidad del sustrato.

Todo esto también fue corroborado con técnicas más sofisticadas como el XPS, donde el pico Au4f del oro se investigó antes y después de haber eliminado la monocapa de complejo mediante exposición a un tratamiento de Ar. De acuerdo con el aumento de la intensidad del oro, el complejo forma una monocapa de 1.6 nm, lo cual cuadra perfectamente con el tamaño del péptido, se pudo estimar.

Una vez se demostró que se podía anclar el TbLBT sobre superficies metálicas, procedimos a anclarlo a una superficie ferromagnética para estudiar su potencial como filtro de espín. Como superficie ferromagnética elegimos un sustrato de Ni recubierto con Au 5 nm de oro. El Au juega en este sistema un doble papel, por un lado, sirve como superficie ideal de anclaje para el péptido, mientras que protege al Ni de oxidarse.

El crecimiento se realizó de forma análoga al sustrato de Au pero en atmósfera inerte, obteniendo el sistema llamado Ni/Au/TbLBT o Ni/Au/YLBT, dependiendo del complejo usado para modificar el sustrato ferromagnético.

Después del recubrimiento del Ni/Au con los diferentes complejos estudiamos la eficiencia de estos como filtros de espín mediante dos técnicas la primera basada en procesos electroquímicos y la segunda en conductividad eléctrica en estado sólido. En el primer caso estudiamos la oxidación y reducción de una disolución de Fe^{2+}/Fe^{3+} donde el Ni/Au/TbLBT o Ni/Au/YLBT se usaron como electrodos de trabajo

mientras se le aplicaba un campo magnético externo. De esta forma introducíamos electrones polarizados en espín a través del sustrato los cuales al presentar la misma quiralidad el TbLBT experimentarían menor resistencia y favorecerían la reducción y oxidación de los Fe, presentando picos Redox más intenso y más cercanos a potenciales de 0V. De hecho estas medidas indicaron que en efecto ambos complejos presentaban una modesta polarización de espín, donde los espines abajo tienen la misma quiralidad que la biomolécula, exhibiendo los picos REDOX más intensos. Remarcablemente, el sistema de Ni/Au/TbLBT presentaba una polarización de espín un 1% mayor que su análogo de Y. Para descartar que esto pudiera ser debido a degradación o a un error sistemático en estas medidas por la agresividad de los altos voltajes empleados, se estudio este mismo sistema mediante EIS, la cual permite seguir el mismo proceso REDOX, pero a voltajes ordenes de magnitud menores. Los resultados obtenidos por EIS encajaban perfectamente con los obtenidos por las típicas voltamperometrías cíclicas, confirmando que el cation juega un rol en el filtrado de la monocapa.

Finalmente, se midió la conductividad en función del campo magnético externo de ambos sistemas usando un contacto líquido, para minimizar cortocircuitos. Los resultados obtenidos, una vez soportaban el papel no inocente del catión coordinado, presentando un filtrado de espín del 70% para el Ni/Au/TbLBT y un 50% para el Ni/Au/YLBT. Como se puede ver en este caso el filtrado obtenido es de 1 orden de magnitud más que los registrados por electroquímica. Esto es debido al carácter local de estas medidas.

En el futuro se investigará más en profundidad el efecto de las propiedades magnéticas del catión en la selectividad de espín, diseñando complejos de Fe^{2+} que pueden pasar de un estado paramagnético a diamagnético con la aplicación de estímulo externo y así poder investigar el rol del magnetismo para un peso atómico constante.

La parte II pasa de sistemas molecular (parte I), a un tipo muy particular de polímeros de coordinación 1D que presentan el llamado fenómeno de la transición de espín. El objetivo de esta parte fue la síntesis de estructuras core@shell basadas en compuestos de transición de espín para modificar o mejorar su rendimiento físico.

La transición de espín es uno de los fenómenos moleculares más espectaculares, donde un complejo de coordinación de un metal de transición del grupo d4-d7 puede estar en dos estados electrónicos, llamados bajo espín (LS) y alto espín (HS) diferentes en un mismo rango de un estímulo externo, como temperatura, luz, moléculas de gases o presión (a esto se le llama cooperatividad). Ambos estados electrónicos exhiben propiedades físicas completamente diferentes. Por ejemplo, la conductividad del HS difiere dramáticamente del LS, o el tamaño del HS puede ser hasta un 10% mayor que en el LS, debido a la elongación de los enlaces entre el metal y el ligando por el llenado de orbitales antienlazantes. Esto hace que sean sistemas muy interesantes como interruptores moleculares, no obstante, hay algunos impedimentos que hay que superar antes de poder usarlos en dispositivos reales. Los dos problemas que enfrentamos en esta tesis son su fragilidad frente a oxidación o degradación y su carácter aislante.

El primer punto es un problema general a todos los compuestos de transición de espín, ya que al nanoestructurarlo el número de centros metálicos en la superficie aumenta, y puestos que estos son metales con esferas de coordinación incompletas son altamente reactivos y fácilmente oxidables. Además, la miniaturización afecta a la cristalinidad del sistema eliminando la cooperatividad del sistema. Para mejorar esto una de las mejores opciones es el recubrimiento de las nanoestructuras de transición de espín con caparazones de silica para aumentar su robustez. Algunos trabajos en esta línea ya se desarrollaron anteriormente a esta tesis, y aquí nos dedicamos a explorar en detalle el protocolo sintético para obtener estas nanoestructuras corazón@caparazón, basadas en un corazón de transición de espín y un caparazón de silica, y poder modular el tamaño de la partícula total y de cada uno de sus componentes, el corazón y el caparazón. Como sistema de transición de espín elegimos el ampliamente conocido $[\text{Fe}(\text{Htrz})_2(\text{trz})](\text{BF}_4)$, el cual es presenta una transición de espín muy cooperativa, una histéresis de 40 K, encima de temperatura ambiente. Además el recubrimiento de nanopartículas de este sistema con silica ya fue reportado, sirviéndonos como punto de partida de esta parte de la tesis.

La síntesis de la nanoestructura corazón@caparazón se hizo mediante la técnica de la micela inversa, donde dos emulsiones una con el ligando y otra con el metal se juntan y se dejan reaccionar. En este protocolo las micelas actúan como nanoreactores controlando el crecimiento de las nanoestructuras. Para sintetizar las $[\text{Fe}(\text{Htrz})_2(\text{trz})](\text{BF}_4)@\text{SiO}_2$ juntamos una emulsión de $\text{Fe}(\text{BF}_4)_2$ y TEOS con otra de HTrz y TEOS. En este caso el TEOS actúa como precursor del SiO_2 reaccionando al contactar la fase

acuosa de las emulsiones. El control del tamaño de las nanopartículas resultantes se consiguió modificando el tiempo de reacción y el ratio agua: surfactante, consiguiendo nanopartículas de entre 28 nm a 90 nm. Además, pudimos obtener un caparazón mucho más fino que los reportados (12 nm en anteriores publicaciones, en esta tesis 4 nm) jugando con la cinética de la polimerización del TEOS. La estructura de las diferentes nanopartículas se estudió por difracción de rayos X de polvo y TGA, demostrando que la estabilidad de las nanopartículas era la misma que el material en masa. Finalmente se estudió el comportamiento magnético de las diferentes nanopartículas, observando que la cooperatividad se mantenía incluso para las más pequeñas, aunque es cierto que la histéresis se veía afectada por encogimiento, siendo de 20 K para las nanopartículas más pequeños. Esto indica que el caparazón formado no es rígido como se pensaba si no flexible, de forma que aunque proteja de la oxidación y aumente la estabilidad del corazón, no parece tener un efecto determinante en la cooperatividad del $[\text{Fe}(\text{Htrz})_2(\text{trz})](\text{BF}_4)$ sintetizado bajo nuestras condiciones sintéticas.

El segundo punto mencionado previamente, el carácter aislante eléctricamente hablando del material, se enfrente de sintetizando un híbrido entre el compuesto de transición de espín $[\text{Fe}(\text{Htrz})_2(\text{trz})](\text{BF}_4)$ y nanopartículas de oro, de forma que la alta conductividad eléctrica del oro pueda aumentar la respuesta electrónica del compuesto de transición de espín. De forma que diseñamos un protocolo sintético para obtener una estructura corazón@caparazón con un corazón de oro y un caparazón de $[\text{Fe}(\text{Htrz})_2(\text{trz})](\text{BF}_4)$. Este fue un enfoque totalmente novedoso, ya que, al

momento de la publicación del trabajo derivado de esta parte de la tesis, no había ningún sistema reportado de este tipo. Si que habían reportados trabajos donde se anclaban nanopartículas de oro a nanopartículas de transición de espín, pero todos estos sistemas presentaban pobres sinergias, además de no poder caracterizarse eléctricamente por el contacto entre oros. De hecho, el uso habitual de estas nanopartículas de transición de espín decoradas con oro era el aprovechamiento del efecto fototérmico del oro para inducir la transición de espín mediante irradiación a bajas potencias. En nuestro caso pensamos en la síntesis de una nanoestructura corazón@caparazón para maximizar la interacción entre ambos componentes.

El protocolo sintético esta basado en un proceso de dos etapas. La primera etapa consiste en la sustitución parcial del recubrimiento de citratos que tienen las nanopartículas de oro por Htrz. De esta forma estos Htrz se anclan al oro por la presencia de los grupos amino del Htrz. Estos Htrz actúan como centros de nucleación, donde después de la adición alternativa de Fe^{2+} y más Htrz acaban dando lugar a un recubrimiento homogéneo y progresivo de la nanopartícula de oro por el compuesto de transición de espín $[\text{Fe}(\text{Htrz})_2(\text{trz})](\text{BF}_4)$, llamado Au@SCO. Con este protocolo y jugando con los tiempos de reacción o concentraciones de precursores, caparazones de 2-4 nm pueden obtenerse rodeando las nanopartículas de oro. Desafortunadamente, debido a la gran exposición del fino caparazón al exterior una rápida oxidación ocurre durante la síntesis, dando lugar a un 8% de centros metálicos susceptibles de transitar entre los dos estados de espín. Además, mediante varios ciclos de

calentamiento y enfriamiento para inducir sucesivas transiciones de espín pudimos observar que el material sufría de una enorme fatiga, disminuyendo aún más con cada ciclo el número de centros metálicos susceptibles de transitar.

Una vez el Au@SCO estaba completamente caracterizado, se preparó un dispositivo para estudiar la respuesta eléctrica de este en función de la temperatura. Para ello las nanopartículas fueron depositadas en electrodos Interdigitados mediante dielectroforesis, técnica que permite atrapar nanoestructuras entre electrodos mediante la aplicación de una corriente alterna. Tras obtener un contacto óptico, pudimos medir una corriente de unos pocos nA a voltajes muy bajos, obteniendo una respuesta eléctrica muy superior a todos los demás sistemas reportados hasta la fecha de spin-crossover. Esto está claramente relacionado con la alta conductividad que proporciona el corazón de oro. Además se pudo ver como al calentar por encima de la temperatura de transición una abrupta caída en la corriente registrada se observa y al enfriar a la temperatura de recuperación del LS, esta volvía a su valor inicial. Dibujando claramente la histéresis típica de este compuesto de transición de espín.

Posteriormente este protocolo sintético fue expandido a otras nanoformas, y no solo a nanopartículas de oro, si no también a nanoestrellas de Au. Usar estrellas tiene varias ventajas respecto a las típicas esferas, por un lado, sus propiedades ópticas son mucho más ricas, abriendo nuevas posibilidades para estudiar el efecto de la transición de espín sobre el plasmon del Au. Por otro lado, estas nanoformas de Au son coloidalmente mucho más estables, al estar estabilizadas con polímeros voluminosos,

permitiendo el trabajar en concentraciones mucho mayores y pudiendo escalar la síntesis o crecer un caparazón más gordo. Con esta idea en mente conseguimos sintetizar un caparazón de unos 14 nm, que como el DSC mostraba no presentaba ningún tipo de degradación después de los primeros ciclos. En el futuro esta síntesis se expandirá a otras nanoformas (nanotriángulos o nanorods) o incluso materiales (plata) y se estudiará el efecto fototérmico de la nanoestructura plasmonica sobre la transición de espín, buscando obtener transiciones de espín a temperatura ambiente.

Finalmente, la parte III traslada esta tesis a planilandia, estudiando el uso de nanopartículas de transición de espín como actuadores mecánicos para estresar materiales 2D y así poder modular sus propiedades físicas. Los materiales 2D son compuestos que pueden ser estabilizados como mono o pocas capas presentando fenómenos de confinamiento cuántico. Por esto presentan propiedades físicas muy exóticas, como el grafeno que es un semimetal in contraste con el grafito. Desde el punto de vista del estrés mecánico, los materiales semiconductores son especialmente sensibles a este, de forma que elegimos como material 2D para estresar el MoS₂. Este esta formado por lamines de Mo encapsuladas con dos laminas de S. Lo interesante de este material es que en masa el MoS₂ es un semiconductor indirecto con un ancho en su estructura de bandas de 1.2 eV, mientras que al exfoliarse hasta la monocapa cambia su comportamiento y pasa a ser directo con un ancho de banda de 1.9 eV. Remarcablemente es especialmente sensible al estrés mecánico, y por ese motivo varios estudios se han hecho estresando el material por medios mecánicas aplicando tensión directamente con un AFM o con sustratos flexibles. En

esta tesis planteamos una aproximación totalmente diferente, basada en el uso del cambio de volumen que experimentan las nanopartículas de transición de espín para estresar MoS₂ exfoliado mecánicamente y producir un material auto-estresable.

La preparación de la heteroestructura transición de espín/MoS₂ (SCO/MoS₂) se realizó mediante la modificación química del MoS₂ para después anclar las nanopartículas mediante una molécula puente anclada al compuesto 2D y al de transición de espín. Como compuesto de transición de espín utilizamos las nanopartículas sintetizadas en la parte II de [Fe(Htrz)₂(trz)](BF₄)@SiO₂. La ventaja de este sistema es la presencia del caparazón de silica que es fácilmente funcionalizable, y que usaremos para anclar la nanopartícula al MoS₂. Por otro lado, el MoS₂ se exfolio químicamente mediante la intercalación con n-BuLi, la cual produce nanohojas de μm de dimensiones laterales y entre 1-6 nm de espesor. No obstante debido a la donación de carga provocada por el n-BuLi el MoS₂ cambia de politopo, pasando del termodinámicamente estable 2H al metaestable 1T. Este cambio de fase aumenta la reactividad del plano basal del MoS₂ permitiendo que reaccione fácilmente con electrófilos. En esta tesis nos aprovechamos de esto para hacer reaccionar el MoS₂ exfoliado con IPTS, una molécula con un enlace C-I, cuyo carbono es altamente electrófilo y por ende susceptible de reaccionar con el MoS₂, y un grupo funcional silanol que puede reaccionar covalentemente con el caparazón de silica de las nanopartículas [Fe(Htrz)₂(trz)](BF₄)@SiO₂. De esta forma la decoración del MoS₂ con [Fe(Htrz)₂(trz)](BF₄)@SiO₂ se puede conseguir fácilmente. De hecho, modificando ligeramente el protocolo

podimos jugar con el porcentaje de recubrimiento (50%, 80% y 100% de recubrimiento) o anclar nanopartículas de diferentes tamaños (40 y 70 nm) y de esa forma jugar con la presión aplicada por el compuesto de transición de espín. El polítopo del MoS₂ después de la decoración fue estudiado cuidadosamente por múltiples técnicas (XPS, XAS, Raman, medidas de fotoluminiscencia) y todas ellas indican que la fase semiconductor se recupera después de la funcionalización con el IPTS, sugiriendo que la molécula es capaz de sustraer el exceso de carga negativo donado por el n-BuLi.

Finalmente se investigo el efecto de la transición de espín en el MoS₂ mediante el estudio de la conductividad eléctrica de las diferentes heteroestructuras, con diferentes recubrimientos y tamaños, en función del estado de espín de las nanopartículas. Enfocándonos en la heteroestructura hecho con nanopartículas de 40 nm con diferentes recubrimientos podemos ver comportamientos completamente diferentes para las tres muestras. La primera con 50% de recubrimiento presenta una alta conductividad eléctrica (compatible con un MoS₂ funcionalizado) pero sin ningún tipo de dependencia con el estado de espín, indicando que el estrés es insuficiente para afectar al MoS₂. La segunda muestra con 80% de recubrimiento es un poco más aislante, debido al mayor número de nanopartículas en la heteroestructura, pero en este caso una clarísima dependencia con el estado de espín se puede observar, donde al contrario de las nanopartículas el HS es más conductor que el LS, además de que presenta varios ordenes de magnitud mayor conductividad eléctrica. Este sería el escenario ideal, donde las nanopartículas están estresando al MoS₂

y alterando su comportamiento eléctrico, presumiblemente por estar modificando su estructura de bandas y acercando el máximo de la banda de valencia y el mínimo de la de conducción. Pasando ahora a la muestra con el 100% de recubrimiento, en este caso observamos un comportamiento análogo a las nanopartículas solas, indicando que en este caso el recubrimiento es demasiado grande y el MoS₂ está aislado por las nanopartículas.

De forma que se observó que el ratio óptimo para obtener una respuesta adecuada era 80%, así que la decoración con las nanopartículas de 70 nm se hizo buscando este mismo recubrimiento. En este caso al medir la conductividad eléctrica con la temperatura se observó un comportamiento similar a su análogo con 40 nm, pero con unas diferencias en conductividad entre el LS y el HS muy superior a lo registrado con las nanopartículas de menor tamaño. Sugiriendo que de hecho al ser más grandes son capaces de transmitir el estrés al 2D más eficientemente.

De acuerdo a estimaciones teóricas la tensión sentida por el MoS₂ con las nanopartículas de 40 nm era de ~0.2%, mientras que para las de 70 nm de ~0.6%,

Para comprobar estos resultados se investigó la fotoluminiscencia de las heteroestructuras óptimas con 40 y 70 nm en función del estado de espín, para cuantificar directamente el cerramiento de las bandas del MoS₂. Los resultados obtenidos coincidían perfectamente con lo medido eléctricamente, obteniendo un estrés aproximado del ~0.1% para las nanopartículas de 40 nm y un ~0.6% para las de 70 nm. Corroborando que

los cambios observados en las propiedades eléctricas del 2D son debidos a la alteración de la estructura de bandas del MoS₂ causada por la tensión aplicada por las nanopartículas después de cambiar su estado de espín.

En el futuro este protocolo se expandirá a otros 2D que puedan ser más sensibles al estrés o a 2D exfoliados mecánicamente que tienen menos defectos y por lo tanto los efectos mecánicos serán más eficientes.